The relevance of root growth for spatiotemporal patterns of chemical gradients in the rhizosphere

Dissertation zur Erlangung des Doktorgrades
der Naturwissenschaften (Dr. rer. nat.)

Der

Naturwissenschaftlichen Fakultät III

Agrar- und Ernährungswissenschaften,

Geowissenschaften und Informatik

der Martin-Luther-Universität Halle-Wittenberg

vorgelegt von

Frau Eva Lippold

Gutachter:

Prof.Dr. Doris Vetterlein

Dr. Steffen Schlüter

Prof.Dr. Karsten Kalbitz

Datum der Verteidigung : 25.11.2024

Abstract

We trample it underfoot, it may seem unimportant to many, but it is indispensable - the soil beneath our feet. The soil as an ecosystem provides space for complex and interacting biochemical and biophysical processes, which in their entirety, for example in the form of agricultural systems, ensure human nutrition. In such systems, plants naturally play a decisive role, on the one hand in the production of usable biomass, and on the other hand as the centre of biological activity and associated processes, which are usually concentrated around plant roots. This area influenced by plants is also known as the rhizosphere. As plant roots play a dominant role in the regulation of many soil processes, alongside a number of other soil organisms, they are increasingly becoming the focus of research. The overall thematic framework of this work is provided by the DFG priority programme 2089 "Spatio-temporal organisation of the rhizosphere - a key to rhizosphere functions", which aims at a deeper understanding of the complex feedback loops between plant resource acquisition, microbiome-related plant health, soil carbon sequestration and soil structure development. This dissertation consists of five chapters, which contribute to this deeper understanding by answering individual research questions. At the centre of the work is the question of I) whether spatial and temporal nutrient gradients develop as a result of the interaction of roots with the soil. In order to answer this research question, an overarching understanding of the underlying processes is necessary: II) To what extent does the absence of root hairs influence the root architecture of maize plants (*Zea mays* L.) under field conditions, and to what extent does this depend on the soil texture (loam or sand)? This leads directly to the methodological challenge of reconciling complementary information obtained at different scale levels and poses the following questions: III) To what extent does local heterogeneity of the soil texture influence different root properties, and IV) To what extent are results transferable from laboratory experiments to those gained from field experiments?

Two genotypes of *Zea mays* L. were used to investigate the influence of root hairs on the plasticity of root architecture; the wild-type (WT) and a root hairless mutant (*rth3*), which is defective in the formation of root hairs. Two substrates with different textures (loam and sand) were used in this project to take the soil structure into account.

A central methodological technique described in this work is X-ray computed tomography (X-ray CT), which allows the measurement of true spatial 3D patterns of root and soil structure and the derivation of secondary information such as root age or root position. This secondary information is essential because the study of in-situ processes in the rhizosphere requires spatial information on physical and chemical properties under undisturbed conditions. In the context of this work, a correlative image-based workflow for targeted sampling of roots in their 3D context was developed in order to assess the influence of roots on the chemical properties of the root-soil contact zone in the µm to mm range. Although the presented method works in principle, it is bound to certain conditions of sampling. For example, the use of non-invasive methods (X-ray-CT) during the growth phase is currently required to determine the age of the root and to enable targeted sampling according to root age and type. In addition, the need for a homogeneously distributed substrate means that the proposed procedure can only be applied in laboratory experiments. In such experiments only a limited soil volume is available. On the basis of which plant growth can only be observed in the first three weeks up to the point at which the available space is completely accessed by the roots. In the laboratory experiment, no plastic adaptation of the architecture of the root system to the absence of root hairs could be observed, which resulted in reduced nutrient uptake, especially in the loam. Both maize genotypes showed a clear response to the substrate. This was clearly reflected in the spatial and temporal development of the rhizosphere volume fraction, but above all in the response of the root diameter to the substrate, irrespective of the genotype. Despite repeated application of X-ray CT, no impairment of growth by radiation could be detected. A reason for this could be that for the first time, a lead shield was used to protect the non-scanned areas from scattered radiation. A significant reduction in radiation dose by the lead shield was confirmed with dosimeters.

In the field experiment, a further level of structural heterogeneity was generated in the form of loam aggregates. In order to quantify this effect and to ensure the applicability of field and laboratory experiments with regard to this structural effect, the reaction of the two genotypes to the presence of larger loam aggregates was investigated in a further laboratory experiment.

The presence of aggregates led to an increase in the length of the roots and the number of branches around the aggregates, while only a few roots were able to grow into the aggregates. Wild-type and *rth3* were affected in the same way, but aboveground biomass was not affected by the presence of macroaggregates, in contrast to controls with homogeneously distributed loam. Macroaggregation of loam in sandy soils had little effect on maize growth, due to local adaptation of the root architecture to the heterogeneity of nutrient availability and penetration resistance caused by the aggregates. This knowledge allowed the comparison of the laboratory results with those of a field trial where the same soil heterogeneity was present.

In the field experiment, the root-hairless mutant *rth3* of *Zea mays* L. and its wild-type were grown on sand and loam for two years. The presence of hairs promoted shoot growth and the uptake of phosphorus and potassium by the plants at all stages of growth. The differences between the genotypes were greater on loam than on sand up to tassel emergence, probably because the additional nutrient utilisation by the hairs is greater on loam. Compensation for the lack of root hairs by increased root growth was hypothesized, but not observed. The ratio of root to shoot was higher in *rth3* than in the wild-type. The root

characteristics showed a high plasticity in response to the soil texture, independent of the genotype. This reaction manifested itself in the form of a larger mean root diameter in sand. The same observation was also made in the laboratory experiments. However, in contrast to the plants in the field experiment, the plants in the laboratory showed a lower root growth in sand and a higher aboveground biomass at a growth stage comparable to that in the field. The lower root length density in sand can be partly explained by the higher and evenly distributed content of plant-available nutrients in the homogeneous substrate used in laboratory experiments. Due to the progressive drying of the soil in the field, additional root growth was shifted to greater soil depths, while the plants in the laboratory found a uniform water supply, making further soil exploration unnecessary.

The growth differences between the two genotypes were consistent both in the laboratory and in the field in the sense that the root-hairless mutant was always slightly smaller than its hairy counterpart. These results underline the high capability of adaptation of both genotypes and a general capacity for plastic adaptation in response to different soil textures.

In summary, this work provides an insight into the complex field of soil-plant interactions at different scales. In addition to new scientific insights, a new approach for the almost non-destructive investigation of chemical gradients in the 3D context of the rhizosphere is presented. The combination of targeted sampling in the soil-root system and correlative microscopy opens up new ways to unravel processes in the rhizosphere *in situ* and explain phenomena observed at the field scale.

Zusammenfassung

Wir treten ihn mit unseren Füßen, er erscheint manchem unwichtig und ist doch unersetzlich - der Boden unter unseren Füßen. Das Ökosystem Boden bietet Raum für komplexe und ineinandergreifende biochemische und biophysikalische Prozesse, die in ihrer Gesamtheit z.B. in Form von Agrarsystemen die Ernährung des Menschen sichern. In solchen Systemen spielen Pflanzen naturgemäß eine entscheidende Rolle, zum einen hinsichtlich der Produktion verwertbarer Biomasse, zum anderen als Zentrum biologischer Aktivität und damit verbundener Prozesse, die sich meist um die Pflanzenwurzeln konzentrieren. Dieser von den Pflanzen beeinflusste Bereich wird auch als Rhizosphäre bezeichnet. Da die Pflanzenwurzeln neben einer Vielzahl anderer Bodenlebewesen eine dominante Rolle bei der Regulation vieler Bodenprozesse spielen, rücken sie zunehmend in den Fokus der Forschung. Den übergeordneten thematischen Rahmen dieser Arbeit bildet das DFG-Schwerpunktprogramm 2089 "Rhizosphere spatiotemporal organization - a key to rhizosphere functions", das auf ein tieferes Verständnis der komplexen Rückkopplungen zwischen dem Ressourcenerwerb von Pflanzen, der mikrobiombezogenen Pflanzengesundheit, der Kohlenstoffbindung im Boden und der Entwicklung der Bodenstruktur abzielt. Die Dissertation besteht aus fünf Einzelkapiteln, die durch die Beantwortung einzelner Forschungsfragen zu diesem tieferen Verständnis beitragen. Im Zentrum der Arbeit steht die Frage, I) inwieweit sich räumliche und zeitliche Nährstoffgradienten als Folge der Interaktion von Wurzeln mit dem Boden ausbilden. Zur Beantwortung dieser Forschungsfrage ist zunächst ein übergeordnetes Prozessverständnis notwendig: II) Inwieweit beeinflusst das Fehlen von Wurzelhaaren die Wurzelarchitektur von *Zea Mays* L. unter Feldbedingungen und inwieweit hängt dies von der Bodentextur (Lehm oder Sand) ab? Dies führt direkt zu der methodischen Herausforderung unterschiedlicher Skalenebenen und den sich daraus ergebenden Fragen III) inwieweit lokale Heterogenität der Bodentextur unterschiedliche Wurzeleigenschaften beeinflusst und IV) inwieweit Ergebnisse aus Laborversuchen auf solche aus Feldversuchen übertragbar sind.

Zwei Genotypen von *Zea mays* L. wurden verwendet, um den Einfluss von Wurzelhaaren auf die Plastizität der Wurzelarchitektur zu untersuchen. Zum einen wurde der Wildtyp verwendet, zum anderen eine wurzelhaarlose Mutante *(rth3*), die in der Bildung von Wurzelhaaren beeinträchtigt ist. Um die Bodenstruktur zu berücksichtigen, wurden in diesem Projekt zwei Substrate mit unterschiedlicher Textur (Lehm und Sand) verwendet.

Eine zentrale Technik in dieser Arbeit ist die Röntgen-Computertomographie (Röntgen-CT), die es ermöglicht, echte räumliche 3D-Muster der Wurzel- und Bodenstruktur zu messen und daraus sekundäre Informationen wie das Wurzelalter oder die Wurzelposition abzuleiten. Diese Sekundärinformationen sind essentiell, da die Untersuchung von *in-situ* Prozessen in der Rhizosphäre räumliche Informationen über physikalische und chemische Eigenschaften unter ungestörten Bedingungen erfordert. Obwohl das in dieser Arbeit vorgestellte Verfahren zur Messung chemischer Gradienten grundsätzlich funktioniert, ist es gleichzeitig an bestimmte Bedingungen der Probenahme gebunden. So ist der Einsatz nicht-invasiver Methoden (Röntgen-CT) während der Wachstumsphase bisher Voraussetzung, um das Wurzelalter zu bestimmen und eine gezielte Probenahme nach Wurzelalter und -typ zu ermöglichen. Da zudem ein homogen verteiltes Substrat erforderlich ist, kann der vorgestellte Arbeitsablauf bisher nur in Laborversuchen angewendet werden. Dort steht nur ein begrenztes Bodenvolumen zur Verfügung, so dass das Pflanzenwachstum nur in den ersten drei Wochen beobachtet werden kann. Im Laborversuch konnte keine plastische Anpassung der Architektur des Wurzelsystems an das Fehlen der Wurzelhaare festgestellt werden, was zu einer verminderten Nährstoffaufnahme, insbesondere im Lehm, führte. Beide Maisgenotypen zeigten eine deutliche Reaktion auf das Substrat. Dies spiegelte sich deutlich in der räumlich-zeitlichen Entwicklung des Rhizosphärenvolumenanteils wider, vor allem aber in der Reaktion des Wurzeldurchmessers auf das Substrat, unabhängig vom Genotyp. Trotz des wiederholten Einsatzes von Röntgen-CT konnte keine signifikante Veränderung des Pflanzenwachstums festgestellt werden. Ein Grund dafür könnte sein, dass zum ersten Mal ein Bleischirm verwendet wurde, um die nicht gescannten Bereiche vor Streustrahlung zu schützen. Mit Dosimetern konnte eine signifikante Reduktion der Strahlendosis gemessen werden. Um die Ergebnisse aus dem Labor auch im größeren Maßstab, im Feld, anwenden zu können, wurde zunächst ein weiteres Laborexperiment durchgeführt, um die Reaktion der beiden Genotypen auf das Vorhandensein von größeren Lehmaggregaten zu untersuchen.

Das Vorhandensein von Aggregaten führte zu einer Zunahme der Wurzellänge und der Verzweigungsdichte um die Aggregate herum, während nur wenige Wurzeln in die Aggregate hineinwachsen konnten. Wildtyp und *rth3* wurden in gleicher Weise beeinflusst. Die oberirdische Biomasse wurde jedoch nicht durch das Vorhandensein von Makroaggregaten beeinflusst, im Gegensatz zu Kontrollen mit homogen verteiltem Lehm. Die Makroaggregation von Lehm in Sandböden hat nur einen geringen Einfluss auf das Maiswachstum, was auf lokale Anpassungen der Wurzelarchitektur an die durch die Aggregate verursachte Heterogenität der Nährstoffverfügbarkeit und des Eindringwiderstandes zurückzuführen ist. Diese Erkenntnis ermöglichte den Vergleich der Laborergebnisse mit denen eines Feldversuchs, bei dem die gleiche Bodenheterogenität vorlag.

Im Feld wurden die Wurzelhaarmutante *rth3* von *Zea mays* L. und der entsprechende Wildtyp zwei Jahre lang auf einem sandigen und einem lehmigen Boden angebaut. Das Sprosswachstum und die Phosphor- und Kaliumaufnahme der Pflanzen wurden durch das Vorhandensein von Haaren in allen Wachstumsstadien gefördert. Die Unterschiede zwischen den Genotypen waren bis zur Blüte auf Lehm größer als auf Sand, wahrscheinlich weil die zusätzliche

Nährstoffausnutzung durch die Haare auf Lehm größer ist. Eine Kompensation des Fehlens von Wurzelhaaren durch verstärktes Wurzelwachstum wurde nicht beobachtet. Das Verhältnis von Wurzel zu Spross war bei *rth3* höher als beim Wildtyp. Die Wurzelmerkmale zeigten eine hohe Plastizität als Reaktion auf die Bodentextur, wobei das auffälligste Merkmal wie in den Laborversuchen ein größerer mittlerer Wurzeldurchmesser in Sand war, unabhängig vom Genotyp. Im Gegensatz zu den Pflanzen im Feldversuch zeigten die Pflanzen im Labor jedoch ein geringeres Wurzelwachstum im Sand und gleichzeitig eine größere oberirdische Biomasse in einem Wachstumsstadium, das mit dem im Feld vergleichbar war.

Die geringere Wurzellängendichte in Sand lässt sich teilweise durch den höheren und gleichmäßig verteilten Gehalt an pflanzenverfügbaren Nährstoffen in dem homogenen Substrat erklären, welches in den Laborversuchen verwendet wurde. Durch die fortschreitende Austrocknung des Bodens im Feld wurde zusätzliches Wurzelwachstum in größere Bodentiefen verlagert, während die Pflanzen im Labor eine gleichmäßige Wasserversorgung vorfanden, die eine weitere Bodenerkundung unnötig machte.

Die Wachstumsunterschiede zwischen den beiden Genotypen waren sowohl im Labor als auch im Freiland in dem Sinne konsistent, dass die wurzellose Mutante stets etwas kleiner war als ihr behaartes Gegenstück. Diese Ergebnisse unterstreichen die hohe Anpassungsfähigkeit beider Genotypen und eine generelle Fähigkeit zur plastischen Anpassung als Reaktion auf unterschiedliche Bodentexturen.

Zusammenfassend bietet diese Arbeit einen Einblick in das komplexe Feld der Boden-Pflanzen-Interaktion auf verschiedenen Skalenebenen. Neben neuen wissenschaftlichen Erkenntnissen wird ein neuer Ansatz zur nahezu zerstörungsfreien Untersuchung chemischer Gradienten im 3D-Kontext der Rhizosphäre vorgestellt. Die Kombination aus CT-Bild gesteuerter Probenahme im Boden-Wurzel-System und korrelativer Mikroskopie eröffnet neue Wege, um Prozesse in der Rhizosphäre *in situ* zu entschlüsseln und Phänomene zu erklären, die auf der Feldskala beobachtet werden.

Contents

Abstract i

Zusammenfassung v

Contents ix

List of figures xiii

List of tables xvii

Acronyms and abbreviations xix

1 Introduction 1

- 1.1 Scope of the thesis 1
  - 1.1.1 Chemical gradients in the rhizosphere 1
  - 1.1.2 Roots hairs and nutrient gradients 3
  - 1.1.3 Soil and texture shaping rhizosphere gradients 4
  - 1.1.4 Transferability of small-scale measurements 4

- 1.2 Objectives 4
- 1.3 Outline 6

2 Root hairs matter at field scale for maize shoot growth and nutrient uptake, but root trait plasticity is primarily triggered by texture and drought 9

- 2.1 Abstract 9
- 2.2 Introduction 9
  - 2.2.1 Root hairs 10
  - 2.2.2 Plasticity of root traits 10
  - 2.2.3 Exploration and exploitation – the integration of root traits 11

- 2.3 Materials and Methods 12
  - 2.3.1 Experimental design 12
  - 2.3.2 Shoot biomass sampling 14
  - 2.3.3 Root sampling 14
  - 2.3.4 Mycorrhization 15
  - 2.3.5 Rating of root hairs 15
  - 2.3.6 Ratio of root cortex: vascular bundle 15
  - 2.3.7 Root to shoot ratio 15
  - 2.3.8 Water use efficiency (WUE) 15
  - 2.3.9 Statistics 16

- 2.4 Results 16
  - 2.4.1 Environmental conditions 16

2.4.2 Shoot growth, shoot nutrient concentrations, content and nutrient uptake 17
2.4.3 Root traits 20
2.4.4 Root to shoot ratio and water use efficiency 24

2.5 Discussion 26
2.5.1 Do hairs matter at field scale for biomass production and nutrient uptake, in particular for loam as mobility of nutrients is low? 27
2.5.2 Do root hairs contribute to water acquisition by plants, especially under drought stress, and is this effect more important in sandy substrates? 28
2.5.3 Is the root hair mutant rth3 showing plasticity in other root traits to compensate for the lower surface? What is the relevance for rhizodeposition /carbon partitioning? 29
2.5.4 Root traits 29
2.5.5 Root to shoot ratio 30
2.5.6 Root length density 30
2.5.7 Root diameter 31
2.5.8 Arbuscular mycorrhiza (AM) formation 31
2.5.9 What explains the texture related differences in root traits beyond differences in nutrient supply? 32

2.6 Conclusion and Outlook 33
3 In soil measurement of radiation dose caused by X-ray computed tomography 35
3.1 Abstract 35
3.2 Introduction 36
3.3 Materials and methods 36
3.4 Results and discussion 38
3.4.1 The effect of absorbing material on the measured dose 38
3.4.2 The effect of shielding on the measured dose 39

3.5 Conclusions 39
4 Macroaggregates of loam in sandy soil show little influence on maize growth, due to local adaptations of root architecture to soil heterogeneity 41
4.1 Abstract 41
4.2 Introduction 42
4.3 Materials and Methods 43
4.3.1 Experimental design 43
4.3.2 Substrates varying in aggregation 43
4.3.3 Shoot biomass sampling and nutrient analysis 44
4.3.4 Destructive sampling of roots and substrate 44
4.3.5 Leaf area 44

4.3.6 X-ray µCT 45
4.3.7 Segmentation of roots 45
4.3.8 Segmentation of Aggregates 45
4.3.9 Analysis of local changes in root growth 45
4.3.10 Random root distribution 47
4.3.11 Statistics 47

4.4 Results 47
4.4.1 Influence on total plant and root growth 47
4.4.2 Local adaption of root traits in aggregated soil 48

4.5 Discussion 53
4.5.1 Local adaption of root growth to overcome soil heterogeneity 53
4.5.2 The importance of root hairs 55

4.6 Conclusions 55
5 Does the lack of root hairs alter root system architecture of Zea mays? 57
5.1 Abstract 57
5.2 Introduction 58
5.3 Materials and Methods 59
5.4 Results 66
5.5 Discussion 74
5.6 Conclusions 80
6 Correlative Imaging of the Rhizosphere - A Multimethod Workflow for Targeted Mapping of Chemical Gradients 81
6.1 Abstract 81
6.2 Synopsis 81
6.3 Introduction 82
6.4 Materials and Methods 85
6.4.1 Growth system, X-ray CT scanning, localisation of subsamples, and sample extraction 85
6.4.2 Chemical fixation and embedding 88
6.4.3 Thin section preparation for chemical imaging 89
6.4.4 Sequence of imaging 90
6.4.5 Micro X-ray fluorescence spectroscopy 91
6.4.6 Nanoscale secondary ion mass spectrometry 91
6.4.7 Laser-ablation isotope ratio mass spectrometry 92
6.4.8 Image registration 93
6.4.9 Image analysis 94

6.5 Results and Discussion 95
6.5.1 Imaging of 2D radial gradients 95
6.5.2 Structural integrity 98
6.5.3 Registration of 2D radial gradients in 3D context 98

7 Synthesis and conclusion 101
7.1 Summary and discussions 101
7.2 Upscaling and downscaling 108
8 Future work 109
Appendices 111
8.1 Appendices for Chapter 2 111
8.2 Appendices for Chapter 3 118
8.3 Appendices for Chapter 4 119
8.4 Appendices for Chapter 5 128
Bibliography 133
List of publications 157
Curriculum vitae 161
Eidesstattliche Erklärung / Declaration under oath 163
Danksagung/Acknowledgement 164

List of figures

2.1 Time course of plant available water during the growing season. 17

2.2 Impact of substrate and maize genotype on plant nutrient status at different stages of plant development 18

2.3 Impact of substrate and maize genotype on shoot dry weight at different stages of plant development 19

2.4 Impact of substrate and maize genotype on shoot P content and P uptake per unit root surface at different stages of plant development 20

2.5 Impact of substrate and maize genotype on root length density distribution with depth at different stages of plant development 21

2.6 Impact of substrate and maize genotype on mean root diameter in different depths, at different stages of plant development 22

2.7 Impact of substrate and maize genotype on the ratio of cortex width to width of the vascular bundle (left) and the degree of aerenchyma formation (centre) in 20-40 cm depth at two growth stages 23

2.8 Impact of substrate and maize genotype on the colonisation of roots by arbuscular mycorrhiza for different depths at different growth stages 24

2.9 Impact of substrate and maize genotype on root to shoot dry weight ratio at different stages of plant development 25

2.10 Impact of substrate and maize genotype on water use efficiency at different stages of plant development 26

2.11 Graphical summary with schematic representation of the response of shoot and root growth of maize wild-type and root hair mutant rth3 to texture...27

3.1 Schematic top view of the pot setup 37

3.2 Schematic representation of the experimental setup 38

4.1 Workflow for the segmentation of aggregates. 47

4.2 Rendered 3D images of root system 48

4.3 Roots in different locations 49

4.4 Root distribution around aggregates 52

4.5 Scheme of root and aggregate distribution within columns........................54

5.1 Sketch of a soil column indicating X-ray CT-scanned depth 62

5.2 Impact of substrate and maize genotype on plant traits 67

5.3 Root system architecture derived from X-ray CT scanning at 7, 14 and 21 days after planting 68

5.4 Change of root length density with depth for 7, 14 and 21 days after planting 69

5.5 Depth distribution of roots younger than 7 days at 14 days and 21 days after planting 70

5.6 Change of mean root diameter with depth for 7, 14 and 21 days after planting 71

5.7 a) Root distance maps. b) root distance histograms 72

5.8 Depth profile of mean root distance for 7, 14 and 21 days after planting 73

5.9 Depth profile of rhizosphere volume fraction for 7, 14 and 21 days after planting 74

6.1 Workflow for imaging of radial 2D chemical rhizosphere gradients in a 3D structural context 85

6.2 Device for extraction of subsamples 88

6.3 Examples of best practise and failures during sample fixation, embedding, slicing, and polishing 89

6.4 a) NanoSIMS results of ^{15}N and ^{13}C isotopic ratios b) light microscopy image with the root-soil interface indicated by the white line c) NanoSIMS images of root tissue and corresponding values of LA-IRMS measurements d) correspondence between average ^{13}C enrichment in a NanoSIMS map 93

6.5 a) Slice of segmented co-registered root system; b) Euclidean distance map (EDT) done on 2D image ignoring hidden roots outside of microscopy plane; c) EDT calculated on 3D image r. 95

6.6 a) Light microscopy image with co-registered µXRF images b) Calcium (Ca) and sulphur (S) counts with increasing distance from the root surface 95

AF.1 Daily precipitation and mean daily temperature during the 2019 and 2020 growing seasons at the Bad Lauchstädt research station 115

AF.2 Impact of substrate and maize genotype on root length density distribution with depth at different stages of plant development 115

AF.3 Impact of substrate and maize genotype on the fraction of roots showing root hairs 116

AF.4 Impact of substrate and maize genotypeon shoot K content at different stages of plant development 116

AF.5 Root length in different root diameter classes 117

AF.6 Root size distribution of the two genotypes within the two substrates (sieved and aggregated) 119

AF.7 Correlation of root length derived using WinRhizo and root length derived using X-ray CT 119

AF.8 Distribution of root traits and aggregate volume 120

AF.9 Concentration of phosphorous in macroaggregates and the sandy soil matrix 120

AF.10 Image-J script 127

AF.11 Impact of X-ray CT scanning on shoot and root growth 128

AF.12 Root recovery with destructive sampling as compared to root recovery with non-invasive X-ray CT scanning 129

AF.13 Change of root length density with depth for 22 days after planting for two maize genotypes 129

AF.14 Root length in different root diameter classes (class width 100 µm) 22 days after planting 130

AF.15 3D rendering of root networks 131

AF.16 Change of RVF with time for different root length scenarios. 132

AF.17 Scatter plot of RVF versus RLD for all time points and treatments 132

List of tables

1.1 Overview of the chapters of this thesis 8

4.1 Pooled continuous distance in distinctive distance classes 52

5.1 Physico-chemical properties of the substrates ‘loam’, ‘sand’. 61

5.2 Fertiliser application [mg nutrient kg^{-1}] to the substrates ‘loam’, ‘sand’. 61

6.1 Sequence, required sample preparation steps and purpose of X-ray CT, light microscopy, µXRF, SEM, NanoSIMS, and LA-IRMS fulfilled within the correlative imaging workflow 84

AT.1 Selected characteristics of the substrates loam and sand from 5-10 cm depth after establishment of soil plot experiment 111

AT.2 Substrate specific fertilisation of soil plot experiments 112

AT.3 Impact of substrate (loam, sand) and maize genotype (wild-type—WT, root hair mutant rth3–rth3) on nutrient removal by above ground biomass at different stages of plant development 112

AT.4 Impact of substrate (loam, sand) and maize genotype (wild-type - WT, root hair defective mutant rth3 – rth3) on mycorrhizal colonisation of roots 22 days after planting. 128

AT.5 Share or root length in diameter classes > 0.5 mm for two different bulk densities in loam for root hair defective mutant rth3 and its corresponding wild-type 128

Acronyms and abbreviations

AMF	Arbuscular Mycorrhizal Fungus
BBCH	BBCH-scale is a system for a uniform coding of phenologically similar growth stages of all mono- and dicotyledonous plant species
C	Carbon
Ca	Calcium
CEC	Cation Exchange Capacity
CT	Computed Tomography
DAP	Days After Planting
EDT	Euclidean Distance Transformation
LA-IRMS	Laser-Ablation Isotope Ratio Mass Spectrometry
L	Loam
µXRF	micro X-Ray Fluorescence spectroscopy
NanoSIMS	Nanoscale Secondary Ion Mass Spectrometry
N	Nitrogen
P	Phosphorus
RLD	Root Length Density
RD	Root Diameter
RDW	Root Dry Weight
RV	Root Volume
rth3	root hair mutant RooTHairless3
S	Sand
WR	WinRhizo
WT	Wild-Type
WUE	Water Use Efficiency

1 Introduction

1.1 Scope of the thesis

The stability of ecosystems and their ability to function under changing conditions has always preoccupied people. Especially with regard to agroecosystems, there is an urgent need to understand the underlying mechanisms and processes, as human nutrition is directly affected. For a long time, the focus for many arable crops was primarily on the directly visible and accessible, above-ground part of plants, as it is usually equated with crop health and yield. The below ground root biomass is inherently more difficult to sample and analyse than the above ground biomass and has largely been overlooked. Since the development of technologies for scanning and measuring roots has improved, over time the underground part has increasingly become the focus of farmers, breeders and researchers. This goes hand in hand with soil research, which also challenges researchers due the complexity of soil as a medium to be analysed. It is well known that soil and roots feed back on one another and form highly-dynamic environments where organic compounds, solutes, gases, and (micro)organisms drive the biogeochemical cycling of elements [1,2].

In this work, the focus is primarily on the part of the soil influenced by the plant roots [3], the rhizosphere. Life on earth is sustained by this small volume of soil that surrounds the roots [4]. All substances that are absorbed from and released into the soil must pass through the rhizosphere, and their flow, transport and reactions depend on rhizosphere-specific and time-dependent properties [5].

Understanding the rhizosphere in all its complexity is challenged by the fact that physical, chemical and biological processes occur at different spatial and temporal scales (from nm to cm and from minutes to months) [5], where they interactively affect each other and dynamically determine the rhizosphere properties [6].

To overcome these challenges, experimental platforms are needed that allow the integration of all these factors in the same experiment, but also at different points in time [7].

1.1.1 Chemical gradients in the rhizosphere

Properties of the rhizosphere are directly controlled or influenced by the roots, making the root system the most important factor in the formation of chemical and physical gradients in the rhizosphere. It is well known that the extent of the rhizosphere is spatially and temporally variable and differs for each parameter considered, such as soil bulk density, rhizodeposit concentration, nutrient depletion, microbial activity, etc.[8]. The expansion of biochemical and physical properties of the rhizosphere on the micrometer to centimeter scale is expected to be controlled by temporal changes in root properties. For this reason, it is first necessary to gain knowledge of the nutrient uptake of the entire plant, as well as the extent of the root system, in order to be able to interpret the gradients that develop.

Most of our knowledge on rhizosphere properties is based on operationally defined ways of sampling the rhizosphere, such as brushing, shaking, or washing off soil adhering to the roots after extracting them from bulk soil. These approaches do not refer to a certain distance from the root surface, although nutrient gradients are reported to extend over less than one mm up to several cm [8–11]. Current knowledge with respect to chemical gradients in rhizosphere soil has primarily been based on models which ignore the radial geometry of transport to and from roots such as rhizobox or split-compartment experiments [5]. Not accounting for this geometry in planar experimental setups leads to an amplification of the extent and magnitude of gradients [5,12]. In addition, chemical gradients change with time of interaction [13] and depend on root type and age [14,15], as well as soil texture and mineral composition. Therefore, both factors (soil and roots properties) are supposed to be a crucial parameter for the extent of physical and chemical gradients [16]. Thanks to novel technologies and experimental approaches, rhizosphere-scale processes can be imaged or characterized with an unprecentented spatial resolution [12] with only minimal to no disturbances of the spatial arrangement within the rhizosphere [17].

Since soil is inherently opaque, X-ray CT can be used to visualise the root in the soil during the growth period in 3D. From the obtained images, true 3D spatial patterns of root and soil structure could then be measured, as well as the derivation of secondary information such as root age, distance maps, and bulk density maps. This information can ultimately be used to interpret chemical gradients around individual root segments on a microscopic scale.

Most chemical and biological microscopy techniques in intact soil can only be performed on exposed two-dimensional soil surfaces. This introduces severe biases since spatial information outside of the imaging plane is unavailable [18], including all roots that are out of plane. For this reason, there is a need for correlative imaging methods that combine 3D structural information with 2D biochemical information to integrate this spatial context.

A methodological challenge is the combination of observed patterns in the rhizosphere of various imaging sources that all operate on different scales, with different resolution and different dimensionality (2D, 3D). Therefore, a prerequisite for the combination of different imaging techniques is that the spatial resolution and the imaged areas are harmonised as much as possible. This so-called image registration or co-registration has been demonstrated for combinations of 3D X-ray computed tomography (X-ray CT) with several different techniques such as scanning electron microscopy (SEM) coupled with energy-dispersive X-ray spectroscopy to reveal elemental maps [19,20], fluorescence microscopy to assess bacterial distributions [18,21], zymography to unravel enzyme release patterns [22] or light and near infrared spectroscopy to account for the spatial distribution of organic matter [23]. In this thesis, a workflow for the combination of 3D and 2D information is presented to overcome the mentioned artifacts of rhizobox systems and to determine chemical rhizosphere gradients for root segments of known type and age.

1.1.2 Roots hairs and nutrient gradients

The root system in its entirety and the associated ability to react plastically to external influences forms a characteristic root system architecture. High plasticity in response to environmental conditions is a key property of roots and crucial for resource acquisition [24,25]. The open questions include how a large number of traits are affected by environmental perturbation [26–28], and - when a particular trait is missing - which traits will be modified. For root traits, the spatial extent of patterns, such as depletion zones for a particular chemical element, is expected to vary with the presence of root hairs [5].

Root hairs are a morphological characteristic that plays an important role in adaptation to environmental conditions, alongside the size and architecture of the root system. They may be regarded as a small-scale subsystem of roots foraging for nutrients, in particular for nutrients with low mobility like phosphorus (P) [29,30]. In addition, root hairs are thought to be important for anchorage during establishment and root tip penetration into the soil [31,32]. Root hair formation as an anatomical feature is just one root trait among many which enables plants to adapt to environmental conditions such as low nutrient availability, limited water supply or unfavourable physical conditions [33]. Other plastic root morphological traits include changes in root diameter (diameter distribution, specific root length) or an overall change in root distribution in space. In summary, alterations in the root system architecture enable an extremely flexible response to soil physical factors and to limited or heterogeneous distribution of resources in time and space [25,34]. How the different traits are coordinated and whether some are mutually exclusive is currently poorly understood [27]. Root hair mutants can be used to address the plasticity of root traits in response to root hairs under different soil physical conditions, i.e. mutants that show reduced density and length of root hairs or normal root hair initiation but disturbed elongation [35,36]. The monogenic mutant *rth3* is transposon induced and shows normal root hair initiation but disturbed hair elongation. The mutant shows no apparent aberrant shoot phenotype, but yield is reduced by 20 to 40% compared to the wildtype under field conditions [36]. The mutated gene encodes a GPI-anchored COBRA-like cell wall protein RTH3 that is involved in the organization of the synthesized cellulose [37]. The *rth3* mutants are genetically highly homozygous because they have been backcrossed to the inbred line B73 for more than eight generations. In direct comparison with the maize wild-type (WT), the root hair mutant *rth3* is used in this thesis to investigate the plasticity of roots on different scale levels (rhizosphere, single plant, field scale).

1.1.3 Soil and texture shaping rhizosphere gradients

Soils are heterogeneous and complex mixtures of organic matter, mineral particles, and pore space. Their functionality is determined by the spatial arrangement of these components on different scales, i.e. by the soil structure [38–41]. The most prominent soil property influencing water and nutrient fluxes and hence spatial patterns of parameters is texture [42]. Relevant for the formation of gradients are, for example, the number of sorption sites as well as the textural fractions which shape the pore network [43]. For this reason, all experiments in this thesis were carried out with two contrasting substrates, a loam (L) and a sand (S).

1.1.4 Transferability of small-scale measurements

A major challenge in rhizosphere research lies in scaling up from the individual root to the root system, up to the entire soil profile [5,7]. Physiological properties are often studied under controlled conditions in the laboratory to eliminate uncertainties caused by fluctuating environmental parameters (e.g. temperature, light, water availability). Therefore, most of our current knowledge about the processes in the rhizosphere comes from young plants at the age of two to six weeks. Growth limitation in small pots is recognized as a possible artefact [44] . Most laboratory experiments have a high root length density and are therefore not comparable to the field situation in terms of the potential benefits of resource extraction strategies. A coordinated design and sampling scheme of field and laboratory experiments can help to overcome these challenges [3].

The challenges of different scale levels within this thesis result in a causal sequence in which the field scale serves to answer the overarching hypotheses, a holistic observation of numerous factors over time in a larger spatial context, but does not provide a detailed understanding of the process. Since the underlying processes are difficult to capture in the complex environment and dimensions of a field experiment, the path leads to controlled laboratory experiments that can be harmonised with the field data.

1.2 Objectives

The following questions arise in this context and are answered in this work:

i. How does an absence of root hairs, as well as different soil textures, influence plant growth
    i. over the duration of an entire growing season under field conditions? Is there a plastic adaptation to the absence of root hairs?

    ii. in the laboratory in structured soil? Does root growth react to the existing heterogeneity?

    iii. under laboratory conditions with homogenized substrate? How comparable are rhizosphere processes observed in laboratory experiments to data obtained under field conditions?

ii. How can spatial gradients in the rhizosphere be linked to root development? Can the spatial extent of gradients be determined using coordinated, nested sampling schemes for the joint analysis of 2D and 3D physical, chemical and biological properties at comparable spatial scales?

To answer these questions, the present work employs a two factorial, randomised design with six replications. The term replicates refers to individual soil columns (laboratory experiments) or fields plots (field experiment). Factor one is substrate (texture) with two levels (loam (L), sand (S)). Factor two is the *Zea mays* genotype with two levels comprising wild-type (WT), and the root hair mutant (*rth3*). The substrate loam was obtained by excavating 700 t of a haplic Phaeozem soil (from 0 to 50 cm depth) in Schladebach, Germany (51°18'31.41" N; 12°6'16.31" E). The substrate sand was obtained by repeated mixing and sieving of the loam with quartz sand (550 t, WF 33, Quarzwerke Weferlingen, Germany).

As part of a field experiment, the largest of the presented scale levels, the role of root hairs was examined in Chapter 2 [45] under field conditions with the substrates used throughout this work: loam (L) and sand (S) as well as a root hairless mutant (*rth3*) of Zea mays and the corresponding wild-type (WT). With this experiment, the laboratory experiment described in Chapter 4 [46] and 5 [47] was extended to less controllable environmental conditions with all the challenges that come with upscaling laboratory results.

Chapters 4 [46] and 5 [47] present the respective laboratory experiments, which represent the downscaled version of the field experiment. The set-up used largely allowed for the spatial complexity of the root system, in contrast to frequently used approaches that work on the 2D level. Chapter 4 [46] then considers how the architecture of the root system reacts to local heterogeneity, especially when two or more environmental factors vary spatially. This chapter builds a bridge between Chapters 2 [45] and 5 [47], since the sand substrate with its typical loamy aggregates from the field trial is compared with its finely sieved counterpart used in the laboratory experiments. As a result, the effect of heterogeneity is addressed with the presence of loamy macroaggregates. This was because it was not technically possible to sieve the substrates in the field to 1 mm in the same way as was done in the laboratory. Although all of the experiments presented here have the same mixing ratio of loam and sand in substrate S, there are larger loam aggregates in the field, as in the laboratory experiment in Chapter 5 [47].

Despite that, the pot experiments were carried out with the same treatments as in the field. What all the laboratory studies presented have in common is that the temporal-spatial organisation of the rhizosphere was investigated using X-ray computed tomography. The basic experimental setup was also the same in all the publications presented. The focus of the second chapter was on the measurement and reduction of the X-ray dose. Since it is already known from human medicine, but also from work in the field of rhizosphere research, that excessive radiation doses can lead to changes in the development of living organisms, in Chapter 3 [48] the radiation dose was measured for the first time with dosimeters used in human medicine at various positions during a column scan and the radiation was shielded as efficiently as possible outside the areas being scanned with the use of a lead shield.

Chapter 5 [47] examines the plasticity of the root architecture of *Zea mays* under conditions that allow the targeted, X-Ray CT Image guided, sampling of subsamples. By comparing a root hair defective mutant (*rth3*) and the corresponding wild-type siblings (WT), it was tested whether and how the mutant shows adaptation strategies in root growth and to what extent this depends on the substrate. Finally, in Chapter 6 [49], the focus is shifted from the complete root system to individual root types and segments. A workflow is presented that can be used to examine different characteristics of the rhizosphere on the same sample in the experimental setup of Chaper 5 [47]. Within this work, resin embedded subsamples were analysed by X-ray CT at high resolution for their 3D structure and chemical gradients around roots using micro X-ray fluorescence spectroscopy (µXRF), nanoscale secondary ion mass spectrometry (NanoSIMS), and laser-ablation isotope ratio mass spectrometry (LA-IRMS).

1.3 Outline

This thesis was written as a cumulative thesis. As a result, the following chapters each correspond to a publication published in a research journal. The topics already discussed are covered in the individual chapters. Only the formatting has been adapted to facilitate the flow of reading in this work. Chapter two is positioned at the beginning of this work because the determination of small-scale gradients and processes necessitates large-scale classification. Therefore, this work is referenced throughout the thesis, even if it is not a first-authored publication. The supporting information of the individual publications is listed at the end of this thesis in Chapter 8.

This work was part of the priority project 2089 "Rhizosphere spatiotemporal organization - a key to rhizosphere functions" funded by the German Research Foundation (project number 403801423).

The individual chapters are based on the following publications:

Chapter 2:	Vetterlein, D., Phalempin, M., Lippold, E., Schlüter, S., Schreiter, S., Ahmed, M.A., Carminati, A., Duddek, P., Jorda, H., Bienert, G.P., Bienert, M.D., Tarkka, M., Ganther, M., Oburger, E., Santangeli, M., Javaux, M., Vanderborght, J. (2022): Root hairs matter at field scale for maize shoot growth and nutrient uptake, but root trait plasticity is primarily triggered by texture and drought *Plant Soil* 478 (1-2), 119 – 141, DOI: 10.1007/s11104-022-05434-0

Chapter 3: Lippold, E., Kleinau, P., Blaser, S.R.G.A., Schlüter, S., Phalempin, M., Vetterlein, D. (2021): In soil measurement of radiation dose caused by X-ray computed tomography
J. Plant Nutr. Soil Sci. 184 (3), 343 – 345, DOI: 10.1002/jpln.202000276

Chapter 4: Lippold, E., Lucas, M., Fahrenkampf, T., Schlüter, S., Vetterlein, D. (2022):
Macroaggregates of loam in sandy soil show little influence on maize growth, due to local adaptations of root architecture to soil heterogeneity
Plant Soil 478 (1-2), 163 – 175, DOI: 10.1007/s11104-022-05413-5

Chapter 5: Lippold, E., Phalempin, M., Schlüter, S., Vetterlein, D. (2021): Does the lack of root hairs alter root system architecture of *Zea mays*?
Plant Soil 467 (1-2), 267 – 286, DOI: 10.1007/s11104-021-05084-8

Chapter 6: Lippold, E., Schlüter, S., Mueller, C.W., Höschen, C., Harrington, G., Kilian, R., Gocke, M.i., Lehndorff, E., Mikutta, R., Vetterlein, D. (2023):
Correlative imaging of the rhizosphere ─ A multimethod workflow for targeted mapping of chemical gradients
Environ. Sci. Technol. 57 (3), 1538 – 1549, DOI: 10.1021/acs.est.2c07340

In order to provide the reader with an overview of the individual hypotheses, methods and results, all publications are summarized in Table 1.1.

Table 1.1: Overview of the chapters of this thesis

	chapter 2	chapter 3	chapter 4	chapter 5	chapter 6
objective	Explore if and how bearing root hairs exhibited root growth adaptation strategies under field conditions on differing substrates.	Measurement and reduction of X-ray irradiation dose. Comparison of the results to the RadPro Calculator.	Investigate how different root traits are coordinated under local heterogeneity.	Explored if and how bearing root hairs exhibited root growth adaptation strategies and how dependent this is on substrate.	Development of a correlative imaging workflow for targeted root sampling in their 3D context.
methods	-*Zea mays* root hair defective mutant (*rth3*) and wild-type were grown on two substrates (loam and sand) with contrasting texture -experiment for two years under field conditions	-soil columns were irradiated in X-ray tomograph -the dose was measured with Radio-photoluminescence dosimeters	-pot experiment with *Zea mays* root hair defective mutant (*rth3*) and wild-type -changes in root growth and root distribution with respect to macroaggregates were investigated using X-ray computed tomography	-*Zea mays* root hair defective mutant (*rth3*) and wild-type were grown on two substrates (loam and sand) with contrasting texture -root system architecture was investigated using repeated X-ray CT	-pot experiment with ^{15}N- and ^{13}CO$_2$-isotope labeling -X-ray CT image-guided subsampling chemical gradients around roots in resin-embedded subsamples analysed using µXRF, NanoSIMS, LA-IRMS
results	-both genotypes showed a bigger root diameter in sand -higher shoot growth in loam than in sand -higher root growth in sand than in loam	-the dose in a typical single pot scan amounts to 1.2 Gy -efficient reduction of X-ray exposure by a lead shield	-increased root length and branch densities around aggregates; only a few roots were able to grow into them -no difference between wildtype and *rth3* -shoot growth was not affected	-both genotypes showed a bigger root diameter in sand -higher shoot growth in sand than in loam -lower root growth in sand than in loam	-gradients (Ca, S) with different extents identified by µXRF -^{13}C up to a distance of 100 µm from the root surface detected by NanoSIMS, LA-IRMS -^{15}N accumulated in root cells
conclusion	-plastic adaptation of root system architecture to substrate -role of hairs for nutrient uptake could be confirmed	-RadPro Calculator underestimates the measured dose -a lead shield efficiently reduced the X-ray exposure	-macroaggregation of loam in sandy soil shows little influence on maize growth -local adaptations of root architecture	-no plastic adaptation of root system architecture to the lack of root hairs but to substrate	-combining targeted sampling of the soil–root system and correlative microscopy opens new avenues for unravelling rhizosphere processes

2 Root hairs matter at field scale for maize shoot growth and nutrient uptake, but root trait plasticity is primarily triggered by texture and drought

2.1 Abstract

Aims: Root hairs are important for uptake, especially for nutrients with low mobility in soils with high sorption capacity. Mutants with defective root hairs are expected to have lower nutrient uptake, unless they compensate with more root growth. Since root hairs can also contribute to the plant's water uptake their importance could change over the course of a growing season. It was our objective to investigate the role of root hairs under field conditions.

Methods: The root hair mutant *rth3* of *Zea mays* and the corresponding wild-type were grown for two years under field conditions on sand and loam.

Results: Shoot growth and P and K uptake of the plants were promoted by the presence of hairs at all growth stages. Differences between genotypes were greater on loam than on sand until tassel emergence, presumably as additional exploitation by hairs is more relevant in loam. Compensation for the absence of root hairs by increased root growth was not observed in absolute terms. The root to shoot ratio was higher for *rth3* than for wild-type. Root traits showed high plasticity in response to texture, the most salient being a greater mean root diameter in sand, irrespective of genotype. The mechanism causing the increase in mean root diameter is still unknown. Root length density was higher in sand, which can be explained by a greater need for exploration than exploitation in this substrate.

Conclusion: The role of hairs for nutrient uptake could be confirmed under field conditions. The large impact of texture on root growth and consequences for carbon balance require further investigations.

Vetterlein, D., Phalempin, M., Lippold, E., Schlüter, S., Schreiter, S., Ahmed, M.A., Carminati, A., Duddek, P., Jorda, H., Bienert, G.P., Bienert, M.D., Tarkka, M., Ganther, M., Oburger, E., Santangeli, M., Javaux, M., Vanderborght, J. (2022):Root hairs matter at field scale for maize shoot growth and nutrient uptake, but root trait plasticity is primarily triggered by texture and drought, Plant Soil 478 (1-2), 119 – 141, DOI: 10.1007/s11104-022-05434-0

Introduction

2.1.1 Root hairs

It has been demonstrated numerous times in controlled condition experiments that root hairs are important for nutrient uptake, in particular for those with low mobility like phosphorus (P) and potassium (K) [29,30,50]. A favourable role of hairs for water uptake, in particular under conditions of limited water availability, has also been suggested, but with contradicting results [51–55]. Hairs increase the surface area for uptake and hence the soil volume influenced by an individual root at relatively low carbon costs [56,57]. They have been shown to increase the size of the depletion zone for immobile nutrients, to facilitate diffusion of exudates like organic acids or exoenzymes, and, as a result, to alter microbiome composition [55,58] and citations therein). It is therefore expected that root hairs improve crop tolerance to abiotic stress such as low water and nutrient availability. As pointed out by Marin et al. [55] most studies investigating the functions of root hairs have been conducted under controlled conditions, i.e. in sieved, homogenized soils, under artificial lighting, with limited soil volume, and for young growth stages only. Very few studies have attempted to validate these laboratory findings under field conditions [55,56,59–62] . Among those, only the one referred to by Marin et al. [55] and Ruiz et al. [62] covered a range of plant parameters throughout the whole growing season including data on climatic conditions and soil water availability. In their trial root hairs did not confer a notable advantage to barley under optimal (nutrients and water) conditions. Yet, under soil water deficit root hairs improved plant water status and stress tolerance, while promoting shoot P accumulation. There is still a pressing need to conduct further field studies addressing the function of root hairs while continuously monitoring plant growth as well as water and nutrient status of plants and soils, including the effect of soil texture on such relations. However, such experiments need to take the interplay of different root traits into account, including possible compensation measures. They also have to disentangle in more detail which traits contribute to soil exploration and which ones will rather improve soil exploitation. Such studies are now possible, utilizing root hair mutants.

2.1.2 Plasticity of root traits

High plasticity in response to environmental conditions is a key property of roots and crucial for resource acquisition [24,25]. The open questions include how a large number of traits are integrated upon environmental perturbation [26–28], and when a particular trait is missing - which traits will be modified. For the case of missing or short root hairs, some authors reported compensation by larger investment into root growth in general [63,64] or fine roots in particular [64]. In a laboratory experiment comparing two maize genotypes (wild-type to the corresponding root hair mutant *rth3*) in two soil textures, a shift in root to shoot ratio could be confirmed but no plastic adaptation of root system architecture to the lack of root hairs [47]. However, both genotypes showed large plasticity of root architecture and in particular root diameter in response to texture. Whether these findings would hold under field conditions with unrestricted soil volume and fluctuating water supply is an open question.

2.1.3 Exploration and exploitation – the integration of root traits

Some root traits alter soil exploration, i.e. the size of the soil domain explored by roots, by modulating root architecture (i.e. axial root growth angle, growth rate, number of axial roots, later root branching) [65–67]. At field scale, this can be measured as differences in the distribution of root length density over depth and its change over time. Another trait primarily related to exploration is the degree of mycorrhizal colonisation, supposed to reflect the abundance of extra-radical mycelium. Soil exploration can be distinguished from soil exploitation, i.e. how thoroughly resources are acquired within a given soil domain without further soil exploration [65]. Root hairs improve soil exploitation similarly to other rhizosphere modifications, like the release of exudates, increased activity or number of mineral nutrient transporters, and enhanced root-soil contact (root diameter, mucilage, rhizosphere porosity) [67]. The root length density within a given volume has an impact on exploitation as well. Exploitation strategies make a difference in environments with patchy, heterogeneous distribution of resources or a large proportion of nutrients with low mobility [68]. In turn, exploration is expected to be more successful if resources are only available in low amounts throughout the soil profile or if resources are only available at larger depths (distance to the seed). Hence, soil conditions like resource availability and distribution are expected to shape the plastic response to the lack of root hairs and the genotype specific integration of different root traits. For the latter, metabolic costs for different traits might be additional driving factors [69]. Experiments and *in silico* studies have shown that maintenance respiration comprises a significant part of plant carbon (C) budget; it can be lowered by aerenchyma formation, and it is also affected by root diameter and root hair formation [57,70,71] . At the field scale, apart from morphological and anatomical root traits, root to shoot ratio is a good indicator for plant C budget [72].

Here, we present the results of a field experiment comparing a maize wild-type (WT) to a corresponding root hair mutant (*rth3 – inhibited in root hair elongation*) grown in two soil textures (loam, sand) to introduce variability in nutrient mobility. With this we expand a previous twin laboratory based experiment [47] with the same treatments to the field scale following the challenge of upscaling laboratory based results [3]. As in the twin laboratory experiment nutrient supply was low, but the whole growing season under rain fed water supply was investigated instead of three weeks under optimal water supply. We tested the following hypotheses and expectations:
H1: Hairs matter at field scale for biomass production and nutrient uptake, The effect is larger in loam where nutrient mobility is lower than in sand.

H2: Root hairs contribute to plant water acquisition, in particular under drought stress. This results in a later onset of drought stress under water limiting conditions. As the mechanisms discussed are supposed to decrease water potential gradients in the rhizosphere, the effect will to be more relevant in sand compared to loam.

H3: The root hair mutant will show plasticity in other root traits to compensate for the lower surface area. This is reflected in greater root to shoot ratio, increase in root length densities, larger share of fine roots and more intense mycorrhizal colonization. All of these will impact rhizodeposition and, as a consequence, microbial composition and activity.

H4: As initial differences in nutrient availability between textures are levelled by fertilisation, no specific texture related differences in root traits are expected.

Note that for some specific aspects related to the above listed hypotheses and expectations there are individual publications referring to the same field experiment and providing an in-depth discussion of the methods used and the results obtained. Here we will only refer to the results when appropriate. We refer to Jorda et al.[73] for plant water relations, Ganther et al.[74] for root gene expression, Santangeli et al. [75]for root exudation and Rosskopf et al.[76] for soil mechanical properties.

2.2 Materials and Methods

2.2.1 Experimental design

The soil plot experiment was carried out in 2019 and 2020 at the Bad Lauchstädt research station in Germany (51°23’36.10’’ N; 11°52’30.29 E). Experimental design, maize genotypes, substrates, fertilization, agronomic measures and growth stages selected for sampling as well as monitoring devices for plant water relations are all described in detail in Vetterlein et al. [3] along with the motivation of conducting twin experiments at laboratory and field scale in order to extrapolate results. Therefore, these topics are only briefly described here. The basic design is a two factorial, randomised block design with six replications. Factor one is substrate (texture) with two levels (loam (L), sand (S)). Factor two is the *Zea mays* genotype with two levels comprising wild-type (WT), and a root hair mutant (*rth3*).

The monogenic mutant *rth3* is transposon induced and shows normal root hair initiation but disturbed hair elongation. The mutant shows no apparent aberrant shoot phenotype, but yield is reduced by 20 to 40% compared to the wildtype under field conditions [36]. The mutated gene encodes a GPI-anchored COBRA-like cell wall protein RTH3 that is involved in the organization of the synthesized cellulose [37]. The *rth3* mutants used in these experiments are genetically highly homozygous because they have been backcrossed to the inbred line B73 for more than eight generations.

The substrate loam was obtained by excavating 700 t of a haplic Phaeozem soil (from 0 to 50 cm depth) in Schladebach, Germany (51°18’31.41” N; 12°6’16.31” E). The substrate sand was obtained by repeated mixing and sieving of the loam with quartz sand (550 t, WF 33, Quarzwerke Weferlingen, Germany). Setting up the field plots started right after the sieving operation in October 2018. Individual field plots (11 x 3.1 m) were excavated to a depth of 1 m. Vertical side walls were covered with a root barrier. The bottom of the plots was filled with a 25 cm gravel layer (0/32) and a drainage textile was then placed on top of the gravel. Substrates were then filled up to the original soil surface with a thickness of 75 cm. The loam was gradually placed in layers of 15 cm by a wheel loader, evened out with wheel loader bucket and compacted with a vibrating plate. This procedure proved to be suitable in a pilot experiment, as X-ray CT scans of extracted undisturbed soil cylinders showed no layering (Figure 3 in Vetterlein et al. 2021 [3]). For treatment (S), sand was packed similarly; however, no vibrating plate was used.

The aim of fertilisation was to achieve a nutrient level in the range between slightly nutrient deficient to adequate nutrition for the wild-type genotype, in order for any investment into resource acquisition to pay-off. Initial differences in nutrient availability between substrates (Table AF1) should ideally be compensated by fertilisation. As a result of pre-trials N, P, K, and Mg were added at a dose twice as high in sand compared to loam, and Ca as well as micronutrients were only applied to sand (Table AF2). Fertilisers were surface applied, 50% prior to seeding, and the remaining 50% after first sampling. Fertilisation was the same in 2019 and 2020. Maize was sown to a depth of 5 cm. Distance within row was 20 cm; between rows 45 cm. This resulted in six rows with 54 plants each and a planting density of 9.5 plants m^{-2}; corresponding to a soil volume per plant of 78.935 dm^3 down to a depth of 75 cm. No pesticides were applied and weeding was done by hand. No heavy machinery was allowed to pass over the plots to avoid modification of soil structure. Soil cultivation in 2020 was only done by hand-hoeing during weed control. Temperature and precipitation for the research station Bad Lauchstädt for 2019 and 2020 are provided in Figure AF1. Note that irrigation was required to allow germination in 2019 and to avoid damaging crop losses in 2019 and 2020.

For shoot and root sampling events specific growth stages according to BBCH-scale were selected [77]. BBCH-scale is a system for a uniform coding of phenologically similar growth stages of all mono- and dicotyledonous plant species. The BBCH 14 growth stage (four leaves unfolded) was selected as the first sampling point as this corresponds to the developmental stage achieved after 21 days in the twin laboratory experiment [47] – in 2019 BBCH 14 was reached 42 days after planting (DAP). The BBCH 19 growth stage (nine or more leaves unfolded) was selected as second time point representing exponential growth (DAP 63 in 2019). The BBCH59 growth stage (end of tassel emergence) was selected as time point during the transition from vegetative to generative growth (DAP 98 in 2019) and the BBCH 83 growth stage (early dough) as a growth stage representing ripening phase (DAP154 in 2019).

Soil water status was monitored throughout 2019 and 2020 with soil water content (TEROS 10; Meter Group AG) and soil water potential (TEROS 21 and

TEROS 31; Meter Group AG) sensors installed in four depths (10, 20, 40 and 60 cm) in one representative plot per treatments [3,73].

2.2.2 Shoot biomass sampling

At BBCH 14, 19 and 59 three representative plants per plot were sampled. The youngest unfolded leaves were separated and tissue was dried at 65°C until constant weight. Youngest unfolded leaves and the remainder of the shoot were analysed separately. Nutrient concentrations in youngest unfolded leaves were used to derive plant nutrient status, analyses of remainder shoot and youngest leaves were used to calculate shoot nutrient content. Nutrient uptake was defined as shoot nutrient content divided by root surface area. For nutrient analyses tissue was chopped (Retsch SM2000) and subsamples were milled (30-50 min at 28/s with a Retsch mill MM400). C and N were analysed by combustion with a CNS analyser (vario EL cube, Elementar, Germany). Approx. 50 mg plant material was weighed and used for determining P, K and Ca concentrations using an inductively coupled plasma optical emission spectrometry (ICP-OES, iCAP 6000, Thermo Fisher Scientific, Dreieich, Germany) after pressure digestion with nitric acid and hydrogen peroxide (ultraCLAVE V, MLS, Germany).

2.2.3 Root sampling

Three root cores per plot were taken at several depths between rows in 10 cm distance from the sampled plant foot. The motorized root corer (Humax Bohrsonden, Martin Burch AG, Switzerland) was equipped with a 20 cm long and 5 cm in diameter cartridge and samples were taken at 0-20, 20-40 and 40-60 cm depth, resulting in nine samples per plot which were washed over 0.65 mm sieves. Hereby, the sample was cleared of small stones and litter and the obtained roots were stored in a 50% alcohol solution (i.e. diluted Rotisol®). Subsequently, roots were scanned at 720 dpi with a 35 µm resolution using a flatbed scanner (EPSON perfection V700). Root traits were analysed using the software WinRhizo 2019 (Regent Instruments, Canada).

Sampling the remaining depth down to the drainage layer at 75 cm was omitted in order to avoid damage of the drainage fleece. For BBCH 14 only 0-20 cm depth was sampled. For BBCH 19 all depths were sampled in 2020, but in 2019 40-60 cm depth was not yet sampled. In 2020 dead roots from 2019 were detected in sand treatments. Sorting out the dead roots by colour and appearance would have been too tedious and subjective. Hence, root degradation rate was estimated by a modelling approach assuming that most of the roots detected at BBCH 14 in 2020 were dead roots. In addition, it was assumed that degradation rate is temperature dependent and follows a first order kinetic. The model is described in detail in Jorda *et al.* [73]. Root length densities without correction are shown in Figure AF2.

2.2.4 Mycorrhization

After scanning with WinRhizo, the degree of mycorrhizal colonization was determined for subsamples consisting of ten fine root (Ø < 1 mm) segments. Fine roots selected were stained with ink (4001 Pelikan) after clearing roots in KOH (10%) [78]. For each sample, 100 fields of view were evaluated under light microscope. Following McGonigle et al. [79], the presence of arbuscules, hyphae and vesicles was scored separately. Since the extent of hyphal colonisation correlated highly with the level of arbuscule formation ($p<0.001$ according to ANOVA), and vesicle formation was rare in maize roots (<8% of the roots), only the percentage of arbuscule formation is presented.

2.2.5 Rating of root hairs

The presence of root hairs was scored for the roots used to determine mycorrhizal colonisation, in order to confirm the presence and sum up the numbers of elongated hairs in wild-type and to assess if the *rth3* root hair elongation defect [80] was consistently expressed under field conditions.

2.2.6 Ratio of root cortex: vascular bundle

Root axes were randomly selected from the field samples used for WinRhizo scanning. Ten segments per plot were analysed for root diameter, for each segment ten free-hand cross sections were cut and analysed by light microscopy for root diameter and the diameter of the vascular bundle. The ratio of cortex to vascular bundle diameter was then calculated. For the cross sections evaluated the share of aerenchyma was scored. The scale used is provided with the respective figure.

2.2.7 Root to shoot ratio

The ratio of root fresh weight to dry weight and the ratio of root volume to fresh weight were determined by Oburger for the same field experiment (Oburger et al. personal communication). From these ratios a conversion factor for root volume (RV) (determined with WinRhizo) to root dry weight (RDW) was derived: $RDW= RV*0.117\ g\ cm^3$. Root dry weights from different depths were multiplied by the respective volume corresponding to an individual plant (derived from planting density) to calculate the root dry weight per plant. Shoot dry weight per plant was measured directly (see shoot biomass sampling).

2.2.8 Water use efficiency (WUE)

WUE was calculated using mean values of shoot (and root) dry weight divided by cumulative water flux from the soil. The data on cumulative water flux from the soil were taken from Jorda et al. [73]. Briefly, cumulative water losses from soil were estimated from volumetric water content measurements. The cumulative water loss was calculated using a soil water balance from the soil water storage change, and the precipitation and irrigation. As data for cumulative water flux from the soil are only available for one replicate per treatment, no statistics could be provided for WUE.

2.2.9 Statistics

For all figures, standard errors and mean values of six replicates (plots) are provided. Technical replicates within plots are not considered for statistics. A log-transformation was used prior to statistical analyses when normal Q-Q plots and Shapiro test indicated that the normal distribution criterion was not met. The software R version 3.53 (R Core Team 2018) and the libraries lme4, car, multcomp, ggplot and emmeans were used. A two-factorial ANOVA for the fixed factors substrate, genotype and their interaction was conducted in conjunction with Tukey's HSD test. The fixed factor depth was additionally used for some root trait data. Significant differences ($p < 0.05$) between treatments are displayed with different letters in the figures.

2.3 Results

2.3.1 Environmental conditions

Both years (2019, 2020) were characterized by low temperatures in May (BBCH 0 - BBCH 14) and exceptionally high temperatures and low precipitation during June, July and beginning of August (Figure AF1). Weather conditions were slightly more extreme in 2019 compared to 2020. Soil matric potentials declined drastically between BBCH 19 (9 leave stage) and BBCH 59 (flowering), reducing plant available water to close to zero (pF 4.2) at flowering over the whole soil profile for all treatments, except S_*rth3* (Figure 2.1). In 2019, plants showed severe drought stress symptoms (leaf rolling) and deviation of actual from potential transpiration in the following temporal sequence: L_WT (DAP 82) < L_*rth3* (DAP 91) < S_WT (DAP 94) < S_*rth3* (DAP 106)[73]. In 2020, deviation of actual from potential transpiration was observed slightly later in the season and in general earlier for the wild-type as compared to *rth3* (L_WT (DAP 92) < S_WT (DAP 94) < L_*rth3* (DAP114) < S_*rth3* (DAP 138).

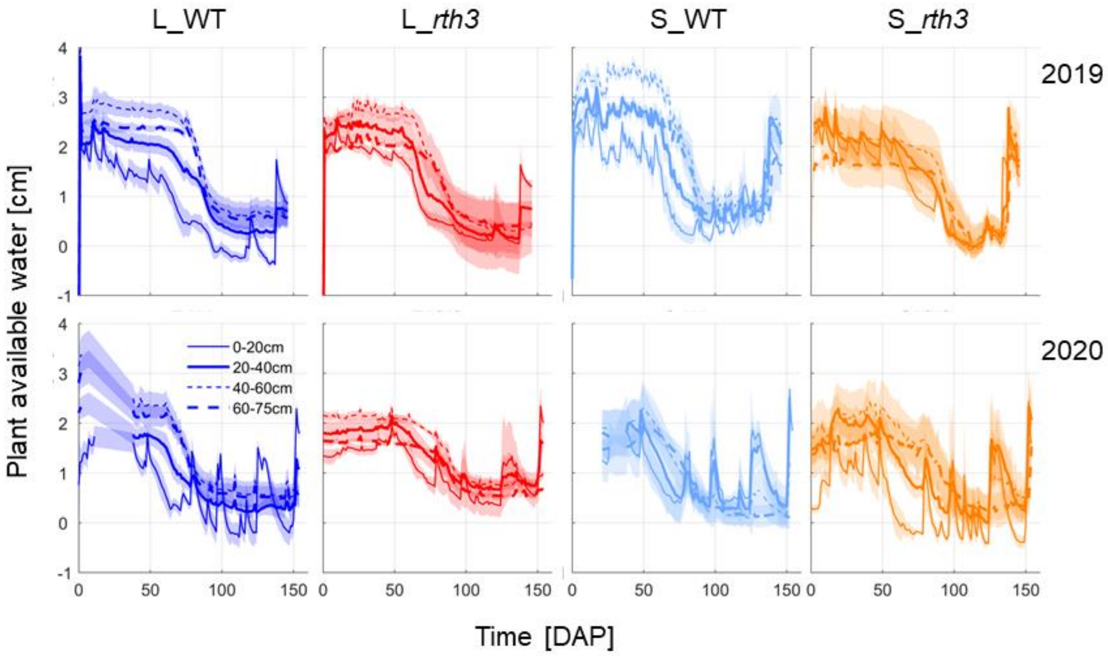

Figure 2.1: Time course of plant available water during the growing season in 2019 and 2020 for loam and sand planted with wild-type and root hair mutant, respectively. Data are based on measurement in the respective soil depths. Note that growth stage BBCH 14 corresponds to 42 days after planting (DAP), BBCH 19 to DAP 63 ; BBCH 59 to DAP 98 and BBCH 83 to DAP154 in 2019. The semi-transparent band shows standard deviation, referring to n=3 sensors within the same depth in an individual plot.

2.3.2 Shoot growth, shoot nutrient concentrations, content and nutrient uptake

During the early growth phase from germination to four leaves stage (BBCH 14) it was possible to compensate for the initial differences in nutrient supply through differential fertilisation of the two substrates. By this approach, the tissue concentration in the young unfolded leaves was not influenced (P, N) or only slightly influenced (K) by the substrate (Figure 2.2). As intended, the plant nutrient status was below adequate supply, especially of P and K. During further plant development (BBCH 19, BBCH 59), however, nutrient deficiency increased more in the sand treatments compared to the loam treatments. For tissue concentrations, no significant influence of genotype was observed for any of the elements at any time during plant development, except for N at BBCH 14 and BBCH 59. In contrast to the tissue concentrations, the production of shoot biomass was significantly influenced by the genotype (Figure 2.3). In both years and at all growth stages, the wild-type had a higher shoot dry weight than the mutant with defective root hairs. The substrate had a significant influence on shoot growth at BBCH 19 and 59, with the differences decreasing towards maturity (BBCH 83). In agreement with the dry weight of the shoots, the P content of the shoots (product of dry weight and concentration of shoot tissue) was significantly influenced by the genotype at all growth stages (Figure 2.4a).

Especially in loam, the wild-type showed a higher P content than *rth3*, which was reflected in a significant influence of substrate and a significant interaction term at BBCH 19 and BBCH 59. P uptake per unit root surface area was also higher in the wild-type compared to *rth3* in loam, but not in sand (Figure 2.4b). In general, the P uptake was higher in loam than in sand.

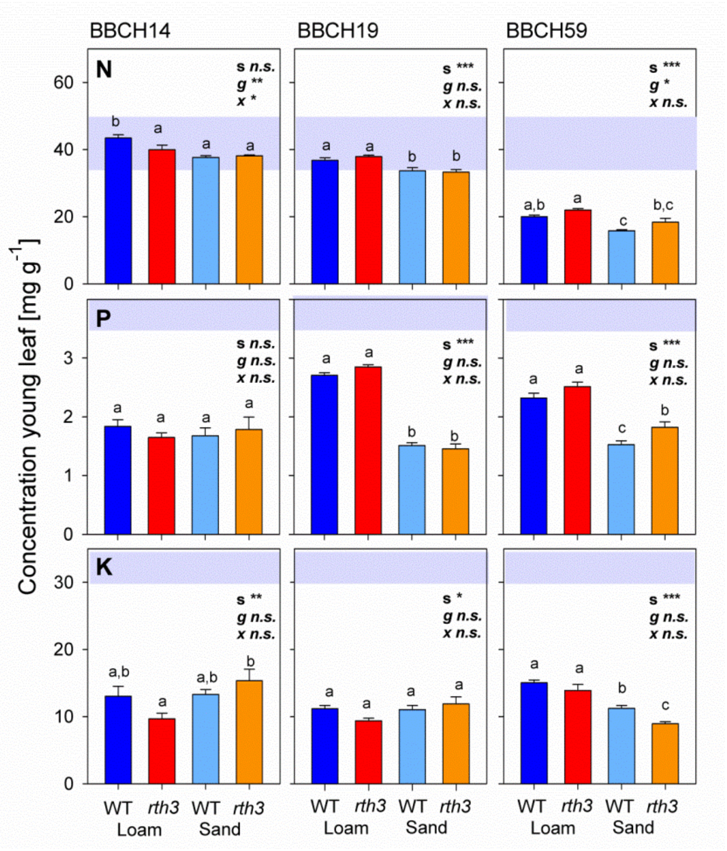

Figure 2.2: Impact of substrate (loam, sand) and maize genotype (wild-type—WT, root hair mutant rth3–rth3) on plant nutrient status at different stages of plant development (BBCH 14, BBCH 19, BBCH 59) in the first year of soil plot experiment (2019) indicated by N, P, K concentration in youngest unfolded leaves. Statistics: two-factorial ANOVA in conjunction with Tukey's HSD test was conducted for each growth stage. Significant effect of factor is denoted by s for substrate, g for genotype and x for interaction. Differences between treatments ($p < 0.05$) are indicated by different lower case letters. Whiskers indicate standard error, n=6. The grey shaded areas show the ranges for adequate supply according to Bergmann [81].

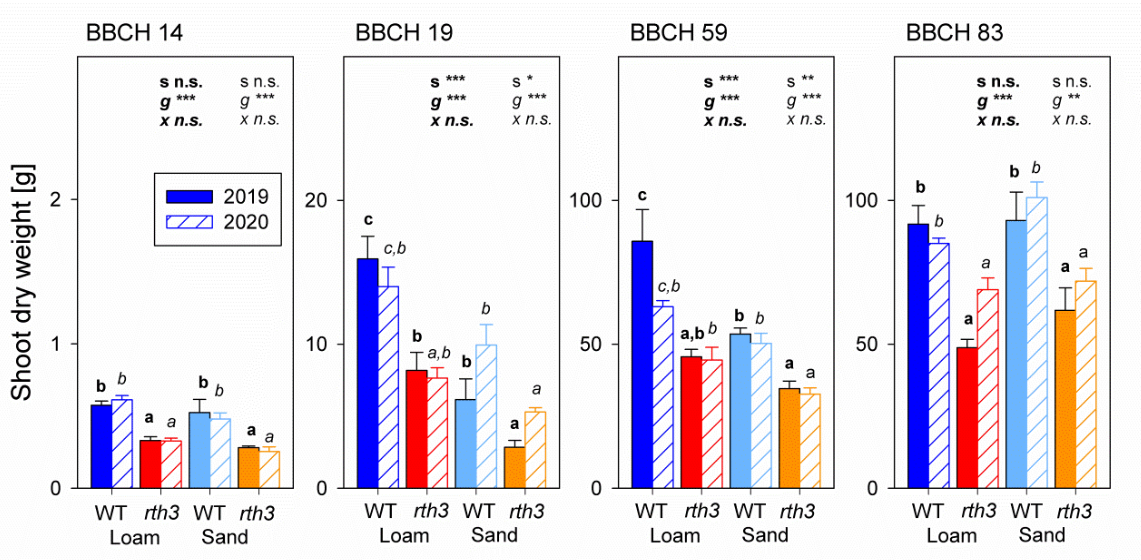

Figure 2.3: Impact of substrate (loam, sand) and maize genotype (wild-type—WT, root hair mutant rth3–rth3) on shoot dry weight at different stages of plant development (BBCH 14, BBCH 19, BBCH 59, BBCH 83) in the first (2019) and second (2020) year of soil plot experiment. Note the different scales for the different growth stages. Statistics: two-factorial ANOVA in conjunction with Tukey's HSD test was conducted for each growth stage. Significant effect of factor is denoted by s for substrate, g for genotype and x for interaction. Differences between treatments (p < 0.05) are indicated by different lower case letters. Whiskers indicate standard error, n=6. Bold letters refer to 2019, italic letters to 2020.

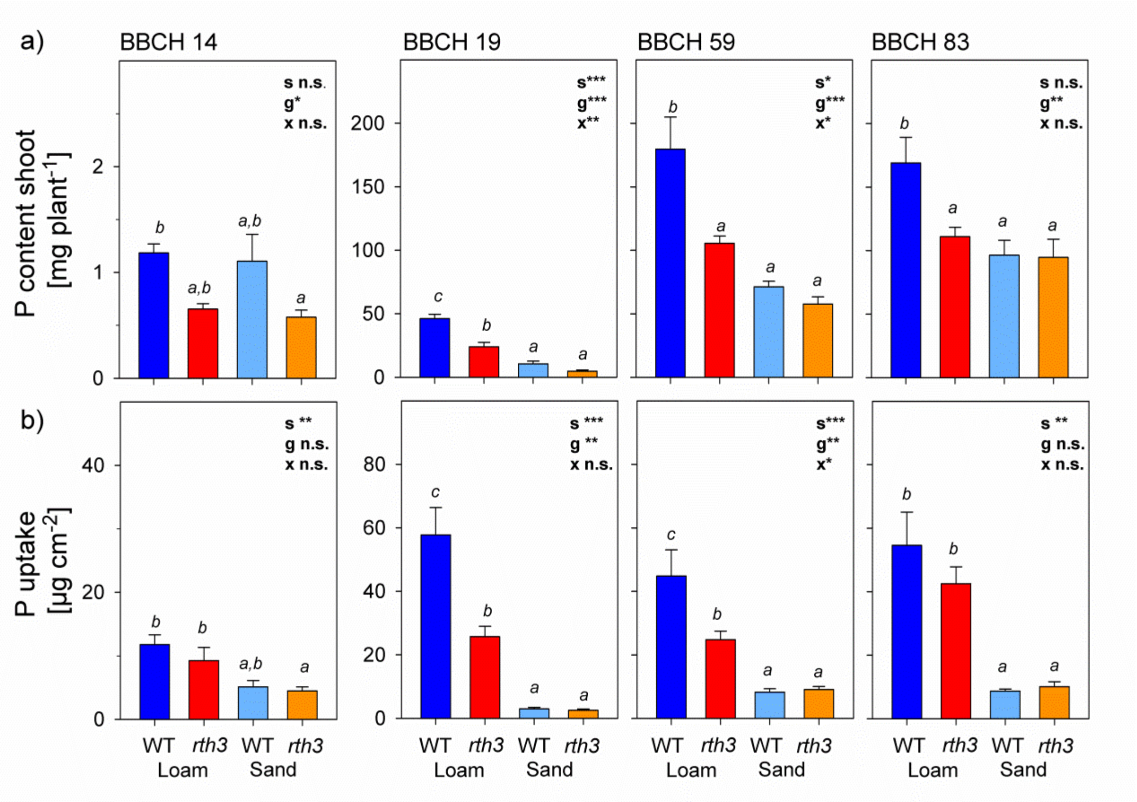

Figure 2.4: Impact of substrate (loam, sand) and maize genotype (wild-type—WT, root hair mutant rth3–rth3) on shoot P content and P uptake per unit root surface at different stages of plant development (BBCH 14, BBCH 19, BBCH 59, BBCH 83) in the first year (2019) of soil plot experiment. Note the different scales for the different growth stages. Statistics: two-factorial ANOVA in conjunction with Tukey's HSD test was conducted for growth stage. Significant effect of factor is denoted by s for substrate, g for genotype and x for interaction. Differences between treatments (p < 0.05) are indicated by different lower case letters. Whiskers indicate standard error, n=6.

2.3.3 Root traits

Unlike shoot dry mass, root length density across all depths was significantly higher in sand than in loam at all growth stages except for BBCH 14 (Figure 2.5). At BBCH 14 there was only a tendency for higher values for sand compared to loam; the values were generally low and the variability between the samples high. Genotype also had a significant effect on root length density: In the three depths, wild-type root length density was higher than that of *rth3* at BBCH 59 and BBCH 83 in sand. The differences between genotypes were smaller than those caused by substrate. In general, root length densities were higher in the top 20 cm in 2020 at BBCH 59 and 83. In 2020, it should be noted that the root length densities for sand were higher than for loam, despite the correction for dead roots. This correction was not necessary for loam as roots decomposed quicker in this substrate (see Figure AF2 for original values).

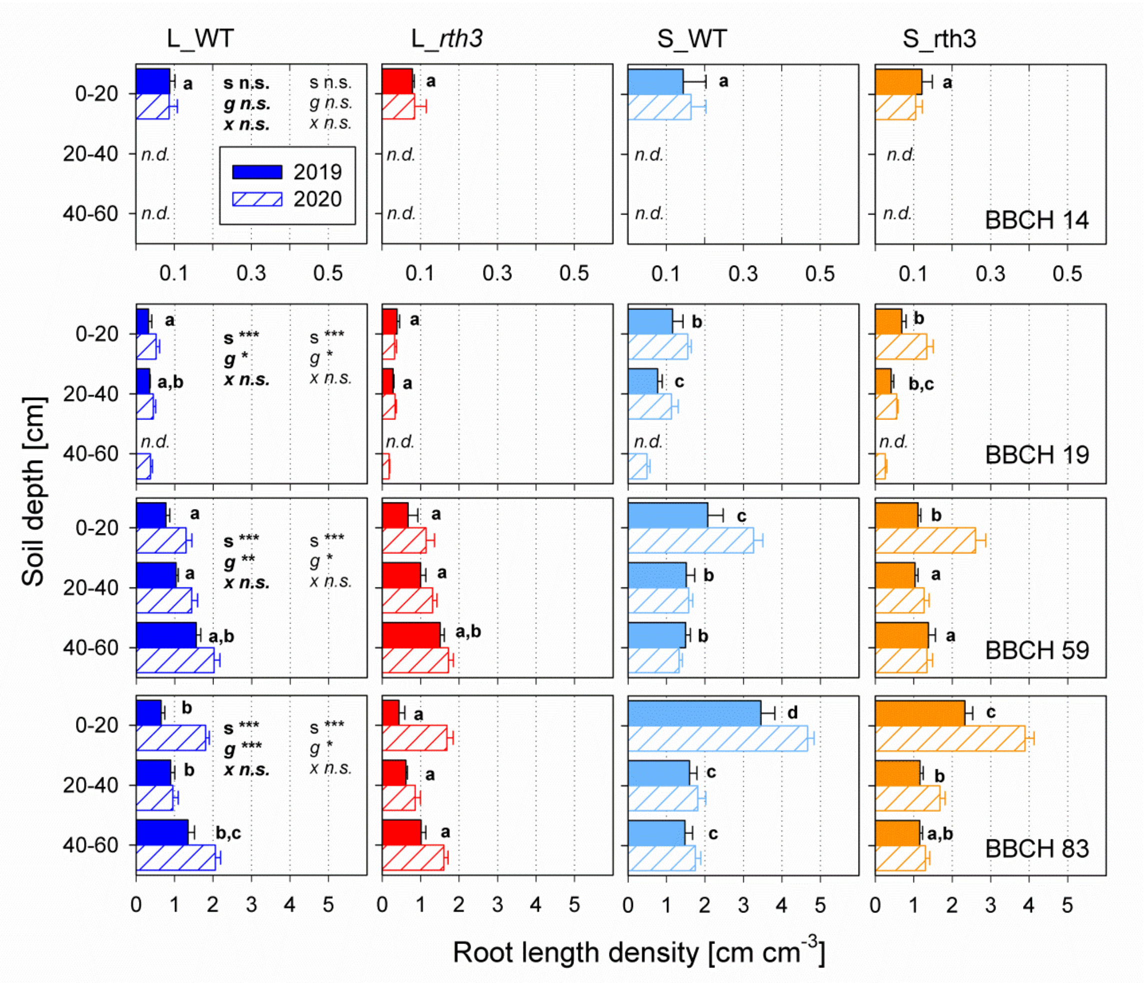

Figure 2.5: Impact of substrate (loam, sand) and maize genotype (wild-type—WT, root hair mutant rth3–rth3) on root length density distribution with depth at different stages of plant development (BBCH 14, BBCH 19, BBCH 59, BBCH 83) in the first (2019) and second (2020) year of soil plot experiment. Note the different scales for the different growth stages; n.d. indicates that no values were determined. Statistics: two-factorial ANOVA in conjunction with Tukey's HSD test was conducted for growth stage, for each depth. Significant effect of factor across depth is denoted by s for substrate, g for genotype and x for interaction. Differences between treatments ($p < 0.05$) are indicated by different lower case letters. Whiskers indicate standard error, n=6. Bold letters refer to 2019, italic letters to 2020.

In 2019, the first year of plant growth on the newly established, homogenized plots, substrate had a significant impact on mean root diameter, with larger diameters observed for sand treatments as compared to loam treatments (Figure 2.6). Genotype had a smaller impact on diameter, resulting in slightly larger values for *rth3* as compared to the wild-type. Significantly higher values for *rth3* than wild-type were observed e.g. in 0-20 cm depth at BBCH19 and BBCH59 in sand during 2019, but in both substrates in 2020. Similar effects by genotype were observed at all depths.

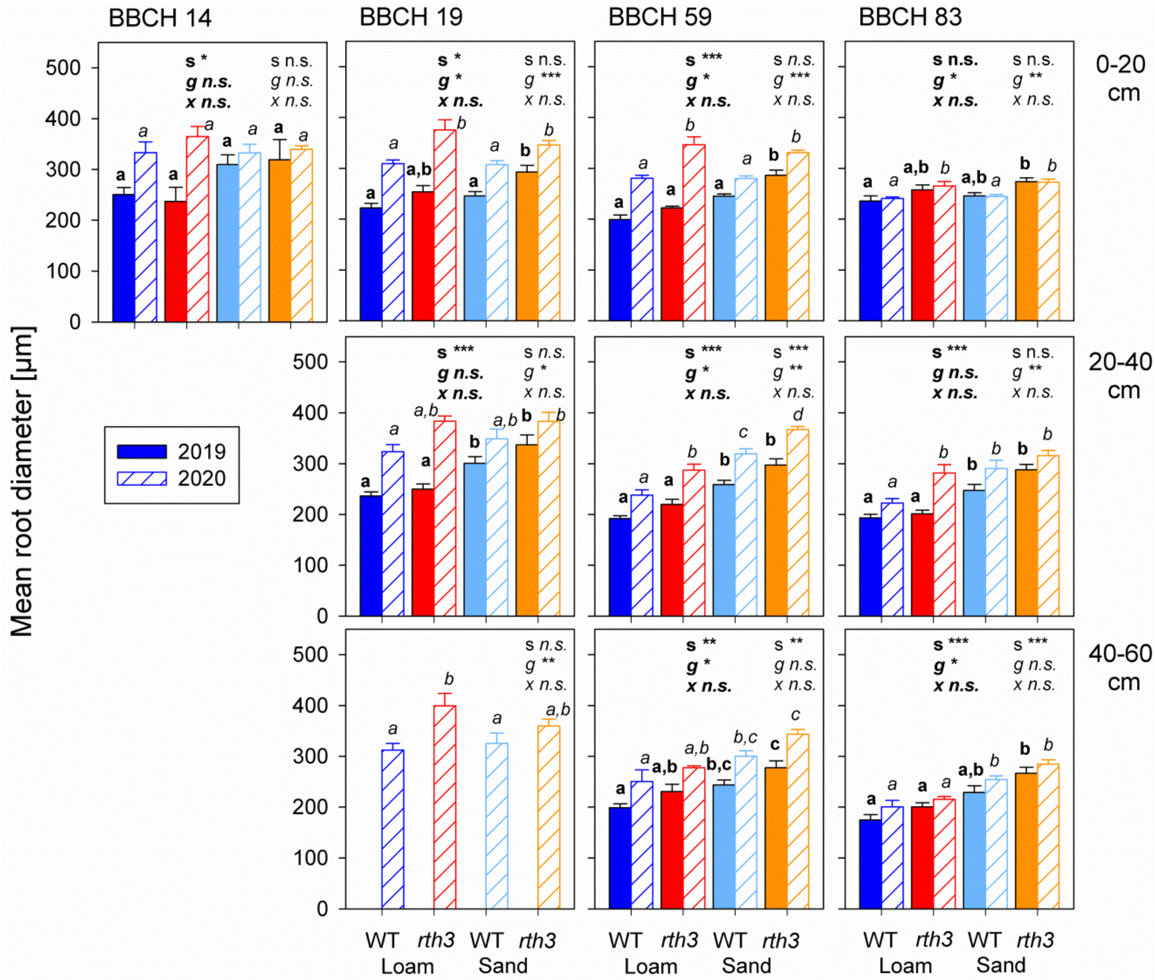

Figure 2.6: Impact of substrate (loam, sand) and maize genotype (wild-type—WT, root hair mutant rth3–rth3) on mean root diameter in different depths, at different stages of plant development (BBCH 14, BBCH 19, BBCH 59, BBCH 83) in the first (2019) and second (2020) year of soil plot experiment. Statistics: two-factorial ANOVA in conjunction with Tukey's HSD test was conducted for growth stage, for each depth. Significant effect of factor is denoted by s for substrate, g for genotype and x for interaction. Differences between treatments for each depth ($p < 0.05$) are indicated by different lower case letters. Whiskers indicate standard error, n=6. Bold letters refer to 2019, italic letters to 2020.

In 2020, mean root diameters across all treatments were larger compared to 2019 (313 ± 17 µm versus 248 ± 3µm). For 0-20 cm depth and partly for the lower depths the marked impact of substrate had vanished, whereas differences between genotypes became stronger in 0-20 and 20-40 cm depths. Differences in mean root diameter between treatments were reflected in a shift in the ratio of cortex width in relation to the width of the vascular bundle (Figure 2.7). Sand treatments had a higher ratio than loam in the 20-40 cm depth at BBCH 19 and 59 for both years. Interestingly, root segments investigated likewise showed differences in aerenchyma formation, the latter being more marked for the loam treatment as compared to the sand treatments.

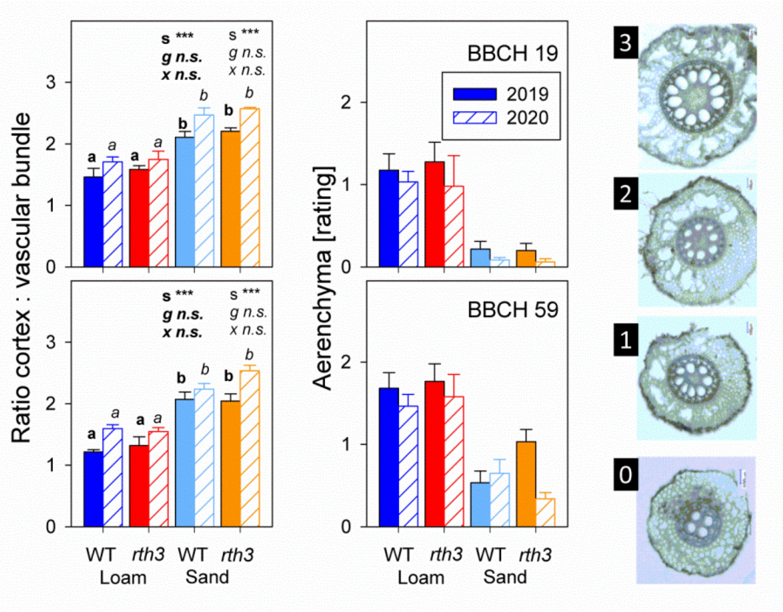

Figure 2.7: Impact of substrate (loam, sand) and maize genotype (wild-type—WT, root hair mutant rth3–rth3) on the ratio of cortex width to width of the vascular bundle (left) and the degree of aerenchyma formation (centre) in 20-40 cm depth at two growth stages (BBCH 19, BBCH 59) in the first (2019) and second (2020) year of soil plot experiment. Scale used for aerenchyma scoring is indicated on the right. Statistics: two-factorial ANOVA in conjunction with Tukey's HSD test was conducted for growth stage. Significant effect of factor is denoted by s for substrate, g for genotype and x for interaction. Differences between treatments ($p < 0.05$) are indicated by different lower case letters. Whiskers indicate standard error, n=6. Bold letters refer to 2019, italic letters to 2020.

Mycorrhizal colonisation was observed as early as at BBCH 14 and it reached values in the range of 40 to 60% at BBCH 59 in 0-20 cm depth (Figure 2.8). Colonisation rate increased by maize age and reduced by soil depth (p<0.05). After no differences between substrates at BBCH 14, higher level of colonisation in loam than sand at BBCH 19 changed to a reversed pattern at BBCH 59 (Figure 2.8). The impact of genotype was not significant.

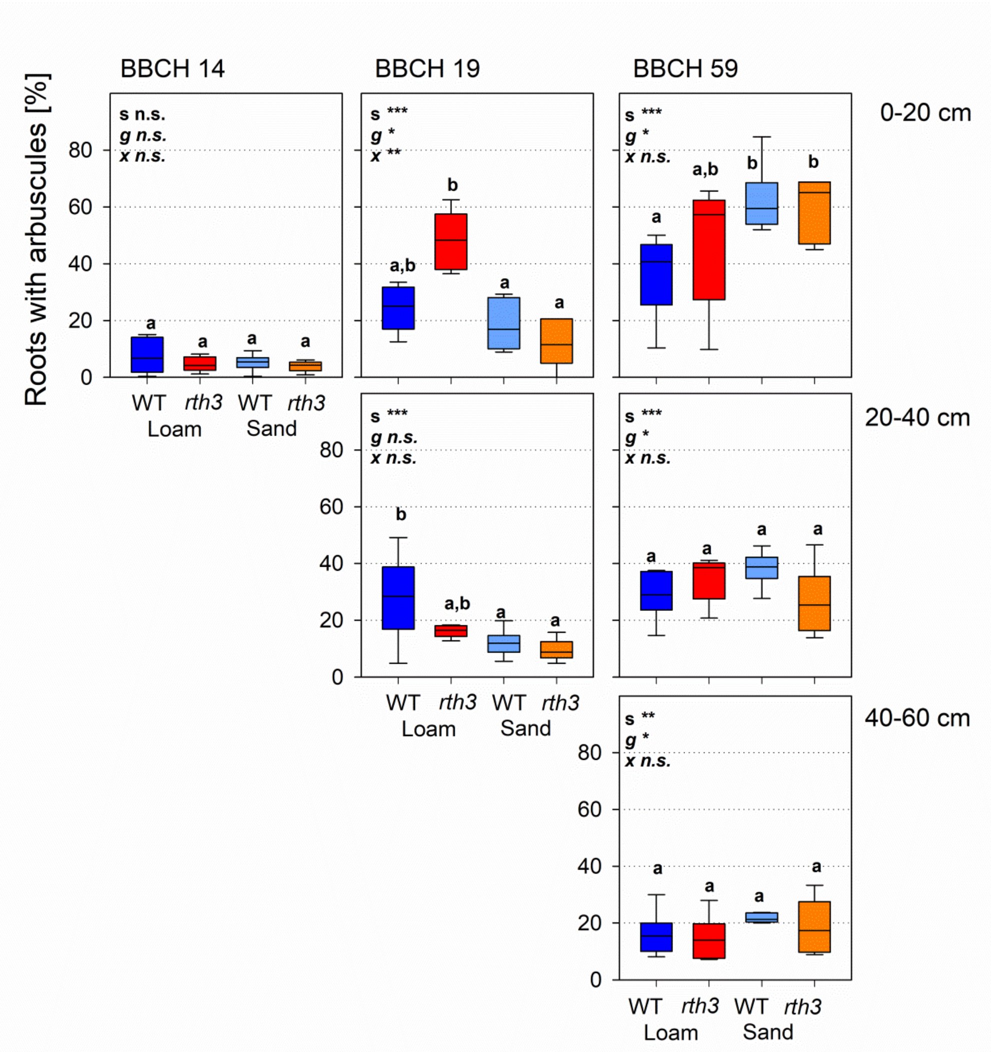

Figure 2.8: Impact of substrate (loam, sand) and maize genotype (wild-type—WT, root hair mutant rth3–rth3) on the colonisation of roots by arbuscular mycorrhiza for different depths at different growth stages (BBCH 14, BBCH 19, BBCH 59) in the first year (2019) of soil plot experiment. Statistics: two-factorial ANOVA in conjunction with Tukey's HSD test was conducted for growth stage and depths. Significant effect of factor is denoted by s for substrate, g for genotype and x for interaction. Differences between treatments ($p < 0.05$) are indicated by different lower case letters; n=6.

The root hair mutant *rth3* consistently showed only few roots segments (<20%) with some up to 50 µm extended hair like structures, but mostly only bulged epidermal cells, while 50-90% of wild-type root segments showed dense populations of elongated root hairs (Figure AF3).

2.3.4 Root to shoot ratio and water use efficiency

The different relevance of the factors substrate and genotype for shoot and root growth is reflected in the root to shoot ratio (Figure 2.9). Substrate as well as genotype showed a significant impact on root to shoot ratio, with higher values for sand than loam and higher values for the root hair mutant *rth3* than the wild-type. In line with what is expected during maize ontogeny, root to shoot ratios decreased with plant age. On average values in 2020 were 30 % higher compared to 2019.

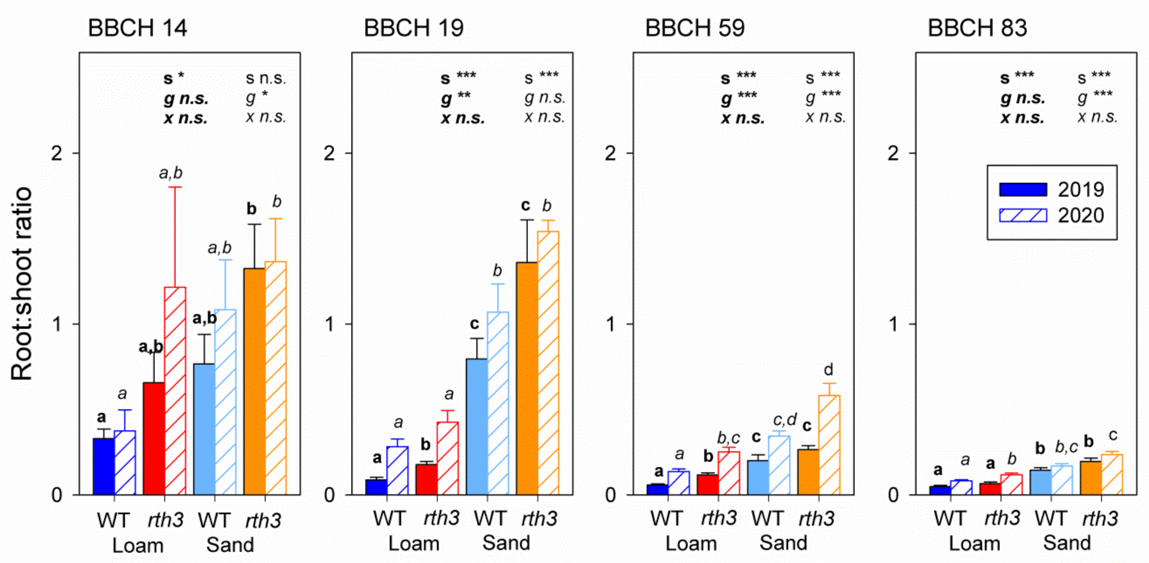

Figure 2.9: Impact of substrate (loam, sand) and maize genotype (wild-type—WT, root hair mutant rth3–rth3) on root to shoot dry weight ratio at different stages of plant development (BBCH 14, BBCH 19, BBCH 59, BBCH 83) in the first (2019) and second (2020) year of soil plot experiment. Statistics: two-factorial ANOVA in conjunction with Tukey's HSD test was conducted for growth stage. Significant effect of factor is denoted by s for substrate, g for genotype and x for interaction. Differences between treatments ($p < 0.05$) are indicated by different lower case letters. Whiskers indicate standard error, n=6. Bold letters refer to 2019, italic letters to 2020.

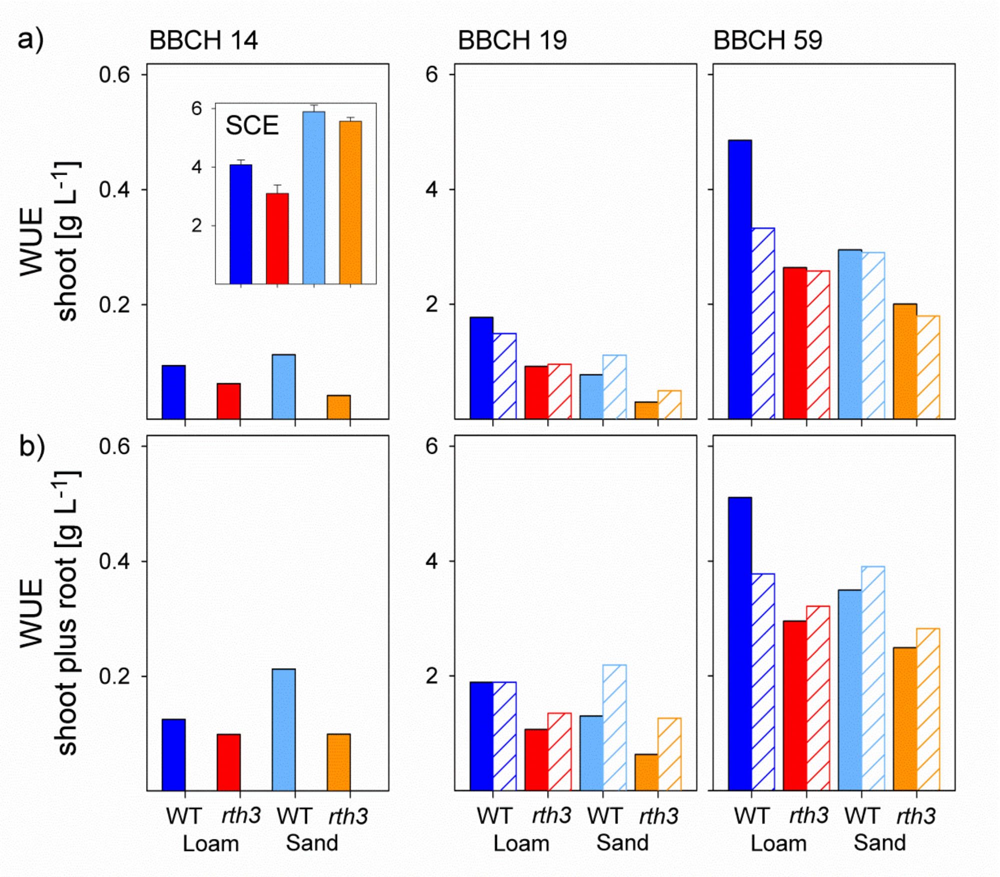

Figure 2.10: Impact of substrate (loam, sand) and maize genotype (wild-type—WT, root hair mutant rth3–rth3) on water use efficiency at different stages of plant development (BBCH 14, BBCH 19, BBCH 59) in the first (2019) and second (2020) year of soil plot experiment. Note that soil water extraction data are based on field measurement summed up across the soil profile (Jorda et al. [73]) for one replicate of each treatment. For comparison inset provides data for the same treatments in the twin laboratory experiment (SCE) for growth stage BBCH 14 under well-watered conditions[47]. WUE is provided with (shoot plus root) and without (shoot) including root dry weight.

Water use efficiency, expressing water loss from the soil profile (transpiration plus evaporation) in relation to biomass produced during the respective period, increased with time. This is because the share of unproductive evaporation in relation to total water consumption decreased (Figure 2.10, [73]). Water use efficiency was always higher for the wild-type as compared to the root hair mutant *rth3*. This was observed irrespective of substrate and year and is in line with observations in column experiments under well-watered conditions (Figure 2.10, inset).

2.4 Discussion

For the discussion part of our study, we will attempt to answer our original hypotheses and expectations stated in the introduction. The overall pattern emerging is conceptualized in Figure 2.11.

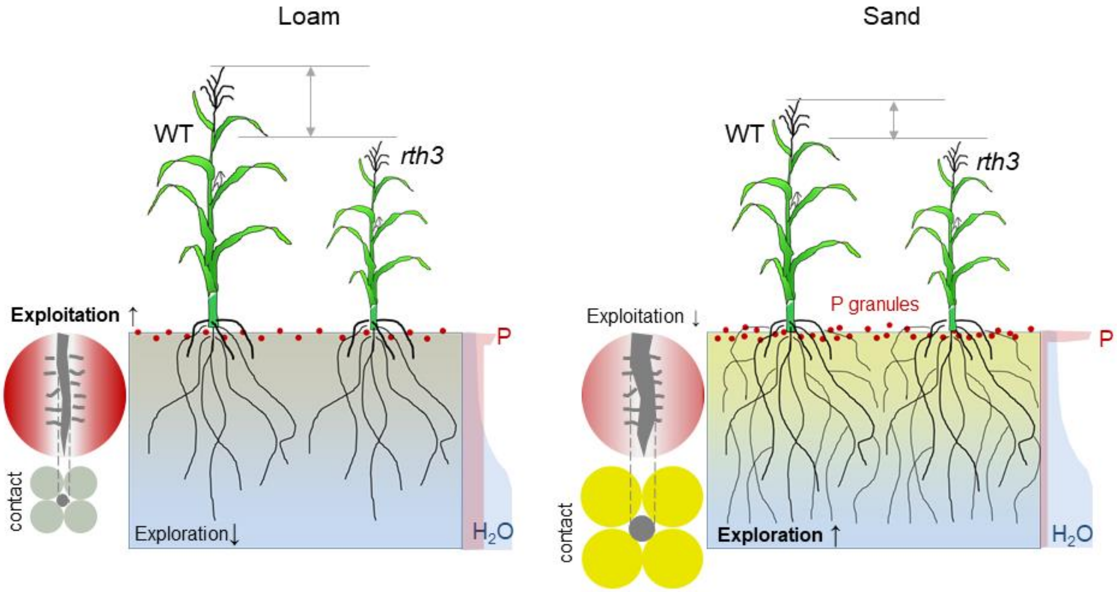

Figure 2.11: Graphical summary with schematic representation of the response of shoot and root growth of maize wild-type and root hair mutant rth3 to texture (loam and sand). The genotypes differed in shoot growth, with greater differences in loam than in sand. For root traits, especially root length density and root diameter, the differences between genotypes were small, but texture resulted in a large plasticity. The higher investment in root length density in sand is related to the lower concentration of plant-available nutrients in sand than in loam, which favours exploration over exploitation. Larger root diameters in sand than in loam are more likely explained by the need for soil contact of the roots.

2.4.1 Do hairs matter at field scale for biomass production and nutrient uptake, in particular for loam as mobility of nutrients is low?

The relevance of root hairs for plant nutrient acquisition has been reviewed in depth by Jungk [30] and was recently revisited by Bienert et al.[50] providing an overview on the location of respective transporters for all essential plant nutrients. In line with literature, the observed differences in shoot biomass development between the wild-type and the root hair mutant corresponded to differences in shoot P content, and for the substrate loam that was accompanied by higher P uptake per unit root surface. Such higher normalized P uptake could reflect the expected upregulation of P transporters in the hairs under P deficiency [50]. However, they could also simply be explained by increased surface area for uptake provided by the hairs, or the decrease in path length required for P diffusion across the rhizosphere [82]. The latter is of particular relevance for soils with low P mobility and would explain why differences in uptake rates were not observed in sand, not even for the early growth stages. In sand neither P uptake nor P content differed between genotypes. The differences in shoot biomass are potentially explained by the higher investment of the root hair mutant into root growth (reflected in root to shoot ratio), which might have enabled similar P uptake. The P concentration in young leaves indicate that P availability was lower for sand during the later growth stages (BBCH 19, BBCH 59). For sand, unlike loam, initial plant available P concentration and total P concentration [3,83] have been very low (8.3 and 53 mg kg^{-1} respectively). Thus, plants in the sand plots relied to a larger extent on surface-applied fertiliser, and when this was depleted or no longer available due to drying of the topsoil, the only viable adaptation strategy was to tap into a larger soil volume (Figure 2.11). In loam, initial plant available P concentration was four times higher than in sand (32.7 mg kg^{-1}), so it was expected that investments in exploitation strategies such as hairs and alteration of rhizosphere chemistry by release of organic acid anions or acid phosphatases would return more P to the plants. This was actually the case, as both genotypes extracted more P (and K, Figure AF4) from the loam plots then was applied as fertiliser (Table AF3). Our initial hypothesis 'hairs matter at field scale for biomass production and nutrient uptake, in particular for loam as mobility of nutrients is low' was confirmed. For sand the results are explained by higher mobility of fertiliser P during the initial growth stages as compared to loam. For the later growth stages, the results are explained by the required shift to an exploration strategy which altered the C budget (root to shoot ratio) more than the return in P. Differences in root hair development between substrates for the wild-type could provide an alternative explanation for the observed differences between sand and loam. Marin et al. [55] report longer root hairs for clay loam compared to sandy loam across all barley genotypes investigated. Note that root hair length was not measured in our field experiment, but in the twin laboratory experiment with the same treatments no differences in root hair length between the two substrates were observed [47].

2.4.2 Do root hairs contribute to water acquisition by plants, especially under drought stress, and is this effect more important in sandy substrates?

In both years precipitation was exceptionally low compared to the long-term average for the region and hence drought stress developed as the growing season advanced. As described above, up to growth stages BBCH 14 and BBCH 19, differences in shoot growth between genotypes can be explained by the availability of N, P and K. The strong decline in plant available water between BBCH 19 and 59, in particular in the topsoil (Figure 2.1), did not only render fertiliser less available in the topsoil, but resulted in visible symptoms of drought stress (leaf rolling) and in an increase of mechanical impedance from 0.5 MPa to >2.2 MPa [84]. We observed an earlier onset of drought stress for the wild-type in both years, which was related to larger shoot size and hence water requirement (potential transpiration) at that specific time point. Wild-type in loam suffered particularly strongly from drought stress and did not show any biomass increase past BBCH 59 in 2019. Hence, despite significant differences in shoot biomass development between genotypes the cumulative soil water extraction for the whole growing season, normalized to soil surface area was similar between the wild-type and *rth3* [73]. However, when cumulative water extraction is normalised to shoot dry weight, we observed higher water use efficiency of wild-type as compared to the root hair mutant. Higher water use efficiency could be explained by a more sensitive regulation of stomata in response to drought [85] or by a more inefficient use of the assimilated carbon by the root hair mutant. The latter could be related to higher maintenance respiration [86] or root exudation (Santangeli et al. personal communication) paired with an already larger investment into roots relative to shoot size. Even when the root biomass itself is accounted for in the calculation of water use efficiency (Figure 2.10b) the discrepancy between genotypes remained and was observed in both years. Based on the literature [87], hairs were expected to improve root-soil contact and increase the apparent root radius. Both mechanisms would help avoid or delay steep water potential gradients around the roots, thus allowing a longer maintenance of soil water extraction and thus a more thorough utilisation of plant-available soil water. These mechanisms would not be expected to alter water use efficiency *per se*, because they would increase water uptake and biomass production at the same time. More importantly, the relevance of this bridging effect has only been experimentally proven for barley, but has not been confirmed for maize in dedicated laboratory studies with the same substrates and genotypes [51]. Simulation of plant water relations for the present field study with Hydrus 1D matched measured results for soil water extraction, transpiration flux and plant water potential without requiring a genotype specific parametrisation of root hydraulic conductivity. The model runs showed that root length density never limited water extraction from the soil at the rate required by the evapotranspiration demand. In relation to shoot size and their transpiration needs, there were always enough roots to exploit soil water down to permanent wilting point [73]. Note that the model used for the simulations does not explicitly account for the conductivity/resistance of the rhizosphere.

Currently it cannot be ruled out that the observed differences in water use efficiency between genotypes might be the result of a pleiotropic effect of the *rth3* mutation. Differences in water use efficiency are systematic, as they were not only observed in the field or upon water limitation, but are likewise reported for laboratory experiments under well-watered conditions (Figure 2.10). Further studies addressing constitutive or inducible differences in stomata number and photosynthetic water use efficiency are currently conducted. Plasma membrane aquaporin expression in roots is not affected by maize genotype, and the changes in transcript abundancies due to substrate and drought stress at BBCH59 are conserved between the wild-type and *rth3* roots [74]. Alternatively, if root hairs function as sensors for drought stress as recently suggested by Kwasniewski et al. [53], this could also explain the observed differences.

2.4.3 Is the root hair mutant rth3 showing plasticity in other root traits to compensate for the lower surface? What is the relevance for rhizodeposition /carbon partitioning?

2.4.4 Root traits

Root dry weight and related root to shoot ratio development over time as well as absolute values were well within the range of values reported by Amos and Walters [88] and Ordóñez et al. [72] reviewing published data for maize (n= 45 and 125, respectively). Maximum root biomass production is expected at tassel emergence (BBCH 59) or shortly thereafter and root to shoot ratio decreases as plants grow and remains nearly constant during the reproductive growth stages (Amos and Walters 2006). This was the case for our root growth data (Figure 2.5) and root to shoot ratios (Figure 2.9) in both years. The selection of constant distance of 10 cm to the base of the plant for all sampling time points was a suitable compromise between overestimation of early root growth when sampling under the plant and overestimation for the later growth stages when sampling at mid-distance between the rows [89]. It proved important that sampling was conducted in three depth intervals down to 60 cm as the general assumption of root mass or length decreasing with depth, with the majority of roots located in the top 20 to 30 cm ([88] and citations therein) did not hold true under the encountered environmental conditions (drought, homogeneous substrate).

2.4.5 Root to shoot ratio

Our values at BBCH 59 and 83 are within the data range of 0.02 to 0.4 for maize derived from a meta-analysis of 125 datasets provided by Ordóñez et al. [72]. This paper indicates that maize as compared to soybean has a very high plasticity in root to shoot ratio and that shoot biomass cannot be used to estimate root biomass. This applies even more to the estimation of root length. This plasticity is reflected in significant differences in root to shoot ratios between our treatments and the different impact of drivers (substrate, genotype) on shoot biomass (Figure 2.3) versus root biomass (not shown) or root length density (Figure 2.5). The higher root to shoot ratio for the root hair mutant can be regarded as a compensation mechanism as stated in hypotheses 3.

2.4.6 Root length density

The mean values for root length density (n=17) reported for the reproductive phase of 1.8 (± 0.15) cm cm^{-3} [72,88] is higher than the values we observed for loam, but lower than those measured for sand. Root length density depth profiles serve as a proxy for root architecture at field scale. For the field, as in the corresponding laboratory experiments [47], no change in root length density profiles in response to the lack of root hairs could be found. This is in contrast to what has been suggested for other root hairless maize (rth2, [64]) or barley mutants (brb, [63]). The substrate, in turn, caused a pronounced and unexpected difference in root length density, which was accompanied by a shift in root length density across root diameter classes (Figure AF5). The larger root length densities for sand can in part be explained by the lower content in plant available nutrients. This is valid except for the surface where fertiliser has been applied. Progressive soil drying shifted root growth to larger soil depths. The fact that this shift was more pronounced for loam than sand might again be related to the more uneven nutrient distribution in sand. Higher root lengths in the coarser substrate were also observed by Marin et al. [55] for barley comparing sandy loam and clay loam.

2.4.7 Root diameter

The higher share of root length in the smallest root diameter class (0-100 µm) for loam as compared to sand is reflected in the lower root mean diameters (Figure 2.6). Larger share of fine roots is typically reported for nutrient rich patches in heterogeneous soils or for substrates with low availability of nutrients in general [24,90,91]. However, in the present experiment nutrients were homogeneously distributed except for the top centimetres affected by surface applied fertiliser. Plant available nutrient concentrations below the fertiliser affected surface were higher in loam than in sand. Similar differences in root diameters between the substrates have also been observed for the twin laboratory experiment for which fertiliser was homogeneously mixed into the substrate and similar amounts of plant available nutrients were present [47]. Doubling the amount of fertiliser in the laboratory experiments had no impact on root diameters (data not shown). Hence it is unlikely that nutrients are responsible for the observed differences in diameter. Increases in root diameters have most frequently been observed in response to increases in soil penetration resistance [92,93]. For the laboratory experiment penetration resistance was in the range of 0.1 to 0.5 MPa for sand and loam respectively [94]. For samples collected from the field values ranged from 0.5 to 2.2 MPa with water potential decreasing from -3 to -50 kPa with no significant differences between sand and loam in neither of the two depths investigated [84]. Not only there was no difference in penetration resistance between the substrates within the measured range of soil matric potential, below which the values only fell after BBCH 19 in 2019, but there was also no associated decrease in root growth (root length), which is typically observed when soil penetration resistance affects roots [93].

2.4.8 Arbuscular mycorrhiza (AM) formation

We expected that the *rth3* plants would show higher colonisation levels, especially as mycorrhiza formation can actually compensate for the loss of root hairs in the *rth3* mutant. By implementing an AMF inoculation experiment, Ma et al. [95] showed that the positive effects of mycorrhiza formation on plant growth and P acquisition in *rth3* were 1.5- to 3.9-fold greater than in the wild-type, and AMF colonisation complemented growth and P acquisition defects of the mutant. Interestingly, mycorrhizas also effectively substituted root hairs in P uptake in barley [96]. Our data suggest that either the *rth3* maize was not P limited but instead limited in mineral nutrients whose uptake is not dependent on mycorrhizal fungi [97,98], or it was not able to allocate enough carbon to the mycorrhizal fungi to support a higher colonisation of the roots than observed [99], and support the mycorrhiza dependent nutrient uptake. In general, availability of P in the soil in part determines how maize is colonised and how it responds to mycorrhiza colonization under field conditions. In this field experiment, the low levels of available P should support AM colonisation of maize roots.

In summary, we cannot confirm our hypothesis that *rth3* shows plasticity to compensate for the lower surface induced by the lack of root hairs, apart from a higher investment in root growth relative to shoot growth (Figure 2.11). However, both genotypes did show strong plasticity of root traits in response to substrate. While higher root length density in sand as compared to loam is probably brought about by the lower content of plant available nutrients [68,100], this does not explain the increase in mean root diameter observed for sand. Higher root length density combined with an increase in diameter and a smaller share of aerenchyma added up to a substantially larger input of carbon for sand as compared to loam which is expected to impact carbon sequestration over the years. Interestingly the observation of slower root degradation in sand is in line with observations from a laboratory experiment on biopore recycling for which X-ray CT revealed likewise that roots in loam were completely degraded after 78 days while still present in sand after 216 days [101].

2.4.9 What explains the texture related differences in root traits beyond differences in nutrient supply?

It is a unique feature of our experiment based on artificially established soil profiles, that we can compare the effect of texture on root growth in the field under identical environmental conditions. Other studies comparing different soil types or texture had to do so by establishing experiments at different sites or at least different areas within large sites [102–106].

There is a number of studies which investigated root traits for soils differing in texture, however, most of these studies did either (i) not report information on root diameter, (ii) could explain observed increases in root diameter by increasing mechanical resistance/compaction, or (iii) could not separate the effect of texture from differences in environmental conditions and management (precipitation, temperature, nutrient availability, soil cultivation) (Table AT4 and citations therein). Surprisingly few studies have addressed explicitly the impact of particle size distribution [107–109] or the shape of particles [110] on root diameter. Rogers et al. [108] found no consistent pattern among different rice genotypes; some did show an increase in root diameter with coarser substrate texture. Warnaars and Eavis [109] found a decrease in specific root length, used as a surrogate for root diameter, with increasing particle sizes and likewise Anderson et al. [107] reported the share of fine roots to decrease with increase in soil sand fraction. Larger root diameters in sand as compared to loam were observed throughout all growth stages and depths in 2019 when plants grew into the homogenized soil structure for the first time. For this reason it is unlikely that differences in root diameters can be explained by substrate specific shifts between root types (brace, crown, seminal root axis and respective laterals). In addition, the differences in diameter corresponded to different ratios or cortex width to vascular bundle width measured for main root axis. This would not be expected if the differences would be due to a larger share of fine lateral roots. Coarser particles or aggregates will show a lower contact area with a smooth surface such as the root surface as compared to fine particles. This was demonstrated by Schmidt et al. [111] for maize roots growing in aggregate fractions of 4-2, 2-1, 1-0.5 and $<$ 0.5 mm. Reduced root-soil contact is potentially unfavourable for nutrient and water uptake and might trigger adaption mechanisms to compensate for this. Increasing root diameter could be such an adaption mechanism but one associated with high carbon costs [57]. Currently the mechano-sensing of roots is poorly understood [112,113]. Roots can show responses to touch or impermeable mechanical barriers by changes in cell division patterns, growth direction, cell differentiation and gene expression. Changes in pressure at the plant cell surface are signalled by mechanosensitive ion channels and kinases to the microtubule cytoskeleton, and lead to altered cytoskeletal architecture and reinforcement of the cell wall [114,115].

Dupuy et al. [112] recently suggested re-visiting micromechanics of rooting development in soil by considering recent advances in granular matter physics. They pointed out that the ‘classical mechanics of continua’ is ill-equipped to explain the links between soil heterogeneity and stochasticity of plant development. They argue that this is of particular relevance for medium grained soils; here roots can displace individual particles from the soil, but the forces exerted by each of the particles can also influence the course of root development. The latter is not reflected in the measurement of mechanical impedance [94]. Crucial for this type of concept is the size aspect ratio between root’s diameter and typical length scale of soil heterogeneity (particle size) [116]. The increase of root diameter observed in sand can be interpreted as an attempt to maintain an optimal size aspect ratio.

The root phene ‘increased root diameter’ can be induced by ethylene as such, i.e. even in systems without soil or pressure [117]. Pandey et al. [118] recently concluded from their study that ethylene acts as an early warning signal for roots to avoid compacted soil and that the mechanism is related to altered gas diffusion in the rhizosphere. Hence the questions arise whether ethylene is also the signalling substance in our systems, and which mechanisms may result in increased ethylene concentrations in the rhizosphere. Root-soil contact [111], bulk density gradients in the rhizosphere [101] as well as gas diffusion per se differ between sand and loam due to differences in porosity and soil water content. Sensing of contact has been demonstrated for root tips [119], and is very likely related to root cap-dependent ethylene emission [120]. Sensing of contact points along the root surface could thus also be related to ethylene production and or distribution and release. Hence, as an alternative to differences in ethylene diffusion between substrates, we suggest that ethylene production might be triggered specifically in sand related to sensing of contact. The role of hairs in this respect is unclear. They might be involved in sensing contact, but they have also been reported to respond to increased ethylene concentrations, i.e. increased root hair length and numbers [121].

2.5 Conclusion and Outlook

Genotypes differed in shoot growth with differences being larger in loam than sand in line with hypothesis 1 (Figure 2.11). For the early growth stages, as long as topsoil was moist, exploitation strategy related to the presence of hairs might have been successful to tap the applied fertiliser. For later growth stages, as drought developed, roots had to explore the entire soil volume in particular for sand, being overall low in plant available nutrients. Root architecture was shaped primarily by the need to access nutrients with increasing drought progressively altering the volume which could be successfully explored for nutrients. Obviously exploitation strategy related to hairs ranked second under these conditions, in particular in sand. This explains the high root length density in sand associated with high root to shoot ratio. The larger root diameter in sand than in loam, which was also observed in twin laboratory experiments under well-water conditions for early growth stages was not related to the differences in mechanical resistance between substrates. We hypothesize that this is a general phenomenon in coarse textured substrates related to the need of optimising root-soil contact. The underlying mechanisms should be explored in future dedicated experiments. Higher root length density along with larger root diameters resulted in higher carbon input in sand than in loam. The impact of altered carbon budgets on microbial community composition and microbial activity as well as soil structure formation and stability is under investigation.

3 In soil measurement of radiation dose caused by X-ray computed tomography

3.1 Abstract

Radiation damage to plants through X-ray exposure has been reported to impair root growth. The literature on the critical dose for growth impairment is inconclusive, partly as dose measurements in soil are scarce. Here we fill this gap and show that the dose in a typical single pot scan amounts to 1.2 Gy. In addition, we demonstrate the shortcomings of estimating the dose from scan settings using the RadPro calculator and highlight the efficient reduction of X-ray exposure by a lead shield.

Lippold, E., Kleinau, P., Blaser, S.R.G.A., Schlüter, S., Phalempin, M., Vetterlein, D. (2021): In soil measurement of radiation dose caused by X-ray computed tomography
J. Plant Nutr. Soil Sci. 184 (3), 343 – 345, DOI: 10.1002/jpln.202000276

3.2 Introduction

X-ray computed tomography (CT) is increasingly used to study root growth in soil. While X-ray doses of typical industrial CT scanners have hardly any effect on physical and chemical properties of soil and water [122], studies showed the potential negative effect on living organisms. The effect of X-ray irradiation on microbial activity seems to be minor [123–125]. In contrast, the impact of X-ray irradiation on higher organisms such as plants is more apparent [126,127]. High doses of X-rays have been used routinely to deliberately induce mutations for plant breeding. However, when CT is used as an imaging technique to study root growth in soil, a potential effect of the radiation itself on the plant can be detrimental. Studies that investigated the effect of prolonged and repeated exposure of plants to X-rays during CT scanning reported varying results. The extent of the influence covers a spectrum, from no measurable effect [128] to a significant reduction in root growth depending on the plant species [126,129]. Hence it is essential to report the dose used in plant growth experiments and to keep it to a minimum.

In most studies the applied dose has not been measured but approximated from the settings of the X-ray device, using the RadPro Calculator. It was our goal to employ the RadPro calculator in line with the aforementioned studies and scrutinize those estimates by direct measurements for realistic settings of a plant growth experiment. We did so by taking into account the potential impact of the chosen substrate, including bulk density and water content, as well as the position within the pot, all of which are known to affect X-ray attenuation. This additional attenuation within soil cannot be accounted for in the RadPro calculator as the software can only evaluate the attenuation in air. As a consequence those estimates are only applicable to the incoming dose at the pot wall.

3.3 Materials and methods

Acrylic pots with a height of 25 cm, inner diameter of 7.0 cm and a wall thickness of 0.5 cm were filled either with a loamy soil (loam) or with a mix of 16.7% loam and 83.3% quartz sand to a bulk density of 1.26 and 1.47 g/cm^3 respectively according to a protocol by Vetterlein et al. [3]. Both substrates were sieved to <1 mm prior to filling. 24h before the X-ray CT measurements, pots were watered to 22% volumetric water content.

X-ray tomography was performed with an industrial µCT (X-TEK XTH 225, Nikon Metrology) at 160 kV, 296 µA, 500 ms exposure time and a 0.5 mm copper filter. Radiophotoluminescence (RPL) dosimeters (Glass OD FGD-10&SC-2, Asahi Techno Glass Corporation, Japan) were used to measure the dose at specific locations in the pots. As this type of dosimeter has an optimum angle of incidence and the dose for a specific location in the pot was of interest, static radiography instead of a computed tomography was conducted. Each static scan took 20 minutes. Radiation doses were measured at the pot wall, 1.5, 3.5 and 5 cm into the substrate for air and loam (Figure 3.1a). For sand only two positions

(3.5 and 5 cm) were measured. Additional dosimeters were suspended by threads into the field of view (FOV) to measure the dose in air without the shielding effect of soil and the pot.

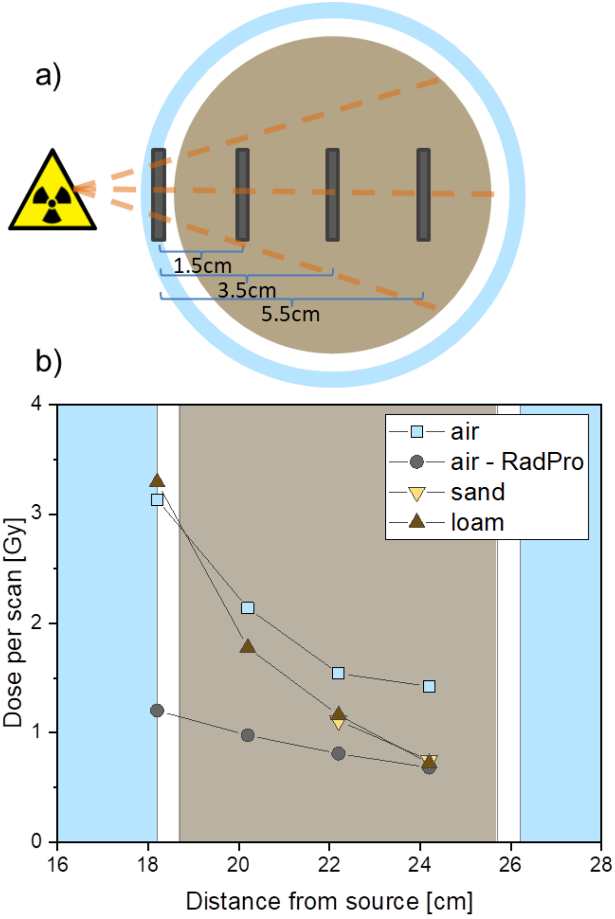

Figure 3.1: (a) Schematic top view of the pot setup with positioning of the dosimeters to investigate the influence of substrate and position on the measured dose. (b) X-ray dose in Gray per scan (22.9 min) measured with RPL dosimeters at different positions in a pot filled with sand (yellow) or loam (brown), or in air without shielding effect of the soil (blue). Air-RadPro is calculated using the RadPro software (grey).

Additionally we tested the effect of a lead-frame (0.5 mm thickness) with a window (2.5*2.5 cm) in 5 cm distance to the X-ray source. This frame lets X-ray photons pass into the field of view but minimizes the effect of the diverging beam outside the field of view, e.g. to the plant shoot and to the soil outside the field of view (Figure 3.2a). For this measurement, one dosimeter was placed 5 cm above the pot, one in the middle of the FOV and one 5 cm below the FOV. The pot was filled with Loam. The background dose was measured with an additional dosimeter and subtracted from the results. In addition to the direct measurements, doses in air were also calculated with the RadPro Calculator for Desktop PCs Version 3.26

(http://www.radprocalculator.com/RadProDownloads.aspx) neglecting the shielding effect of soil or scattering in the CT, as Rad Pro Calculator only considers air exposure. All radiation doses were calculated for an exposure time of 22.9 min corresponding to the scan time required for a typical CT scan for that pot geometry [125,130].

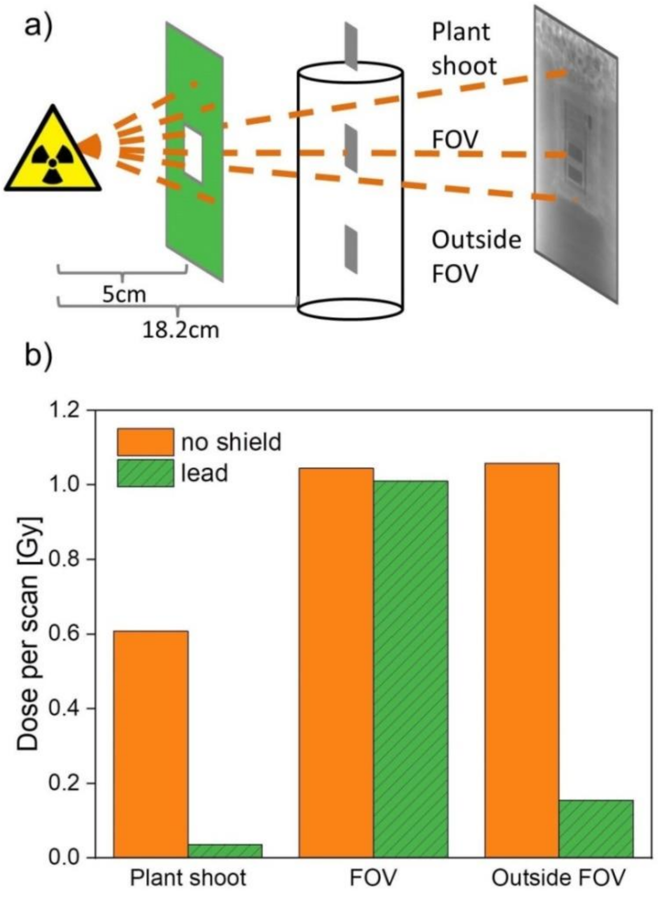

Figure 3.2: (a) Schematic representation of the experimental setup for dose measurement inside and outside the FOV and the use of the lead shield. (b) X-ray dose measured with a RPL dosimeter in the center of a pot filled with loam with (green) or without the use of the lead shield (orange).

3.4 Results and discussion

3.4.1 The effect of absorbing material on the measured dose

In soil a stronger reduction with distance was measured than in air, due to stronger absorption and scattering (Figure 3.1b). Due to backscattering of photons the dose value is slightly higher at the front of the acrylic pot filled with soil, than in air at the same position. There was no difference in dose between the sand and loam substrate despite the one that was expected due to the different bulk densities. The expected dose of a real tomogram in the center of the pot amounted to 1.2 Gy, which is a threefold decrease as compared to the pot wall. At the pot wall, the estimated dose with RadPro only amounts to one third of the measured dose and remains smaller throughout the air-filled pot. By coincidence and for the wrong reasons the RadPro dose estimate at the wall matches the real dose in the center of the soil pot for the combination of pot geometry and scan settings.

In the supporting information we identify previous mistakes in the dose calculation that went unnoticed in former publications [128,129,131]. These mistakes previously led to higher dose estimates. According to manufacturer information the response of RPL dosimeters depends on photon energy and varies between 0.9-1.2 in the expected polychromatic energy spectrum within the range of 20-160kV with an expected overall dose overestimation by approx. 10%. Real doses at the pot wall are therefore somewhat lower than shown here, but still substantially higher than the estimated dose. The reasons for the underestimation by RadPro calculator are elusive to us. They might be caused by a combination of inadequate assumptions on the X-ray tube configurations as pointed out in the RadPro manual.

3.4.2 The effect of shielding on the measured dose

Image resolution depends on CT settings and the distance between sample and X-ray source. Considering the distance from the X-ray source to the pot and in order to have a complete image of a 23 cm tall pot it is necessary to do 2 to 3 consecutive and overlapping scans [129,131]. Pot parts outside the actual field of view may still receive considerable radiation because of the uncollimated beam (Figure 3.2a). In fact, the dose in soil below the FOV was the same as within. The shoot of a plant outside the FOV would still receive 73% of the dose if no lead shield was used (Figure 3.2b). By using the lead shield we could reduce the dose to the shoot by 94% and for the area in soil outside the FOV by 85%.

3.5 Conclusions

The comparison of X-ray dose measurements in soil with the commonly used dose estimation from the settings of the X-ray device showed that RadPro Calculator underestimates the measured dose substantially, even in air. This discrepancy also applies to previous studies that employed those dose estimates using RadPro. A lead shield efficiently reduced the X-ray exposure outside the field of view; hence we strongly recommend using such a shield to reduce plant damage to a minimum.

4 Macroaggregates of loam in sandy soil show little influence on maize growth, due to local adaptations of root architecture to soil heterogeneity

4.1 Abstract

Aims: Root hairs and lateral growth are root traits among many which enable plants to adapt to environmental conditions. How different traits are coordinated under local heterogeneity, especially when two or more environmental factors vary in space, is currently poorly understood. We investigated the effect of heterogeneity on root system architecture of maize in response to the presence of loamy macroaggregates, which come along with both, increased penetration resistance and nutrient availability, i.e., two important environmental factors shaping root system architecture. The comparison between a mutant with defective root hairs and the corresponding wild-type made it possible to investigate the importance of root hairs in the adaptation strategies of plant roots to these factors.

Methods: Changes in root growth and root distribution with respect to macroaggregates were investigated using X-ray computed tomography. The wild-type of *Zea mays* L. was compared with the root hair defective mutant (*rth3*) to investigate the importance of root hairs in addition to adaption of root architecture.

Results: The presence of aggregates lead to increased root length and branch densities around aggregates, while only a few roots were able to grow into them. Thereby, wildtype and *rth3* were influenced in the same way. Aboveground biomass, however, was not affected by the presence of macroaggregates, as compared to controls with homogenously distributed loam.

Conclusions: Macroaggregation of loam in sandy soil shows little influence on maize growth, due to local adaptations of root architecture to the heterogeneity in nutrient availability and penetration resistance caused by the aggregates.

Lippold, E., Lucas, M., Fahrenkampf, T., Schlüter, S., Vetterlein, D. (2022): Macroaggregates of loam in sandy soil show little influence on maize growth, due to local adaptations of root architecture to soil heterogeneity, Plant Soil 478 (1-2), 163 – 175, DOI: 10.1007/s11104-022-05413-5

4.2 Introduction

Soils are heterogeneous and complex mixtures of organic matter, mineral particles, and pore space. Their functionality is determined by the spatial arrangement of these components on different scales, i.e. by the soil structure [38–41]. Roots interact with the soil and its structure. This interaction is governed by several environmental factors, which influence the development of roots and shape the root system architecture, making roots highly adaptive to the local environment [25,132]. Well known examples of these factors are water stress and mechanical impedance [93,133,134].

Root elongation decreases drastically in response to increasing penetration resistance and decreasing matric potential [133,135,136]. Hence, root penetration into aggregates, with their increased resistance to penetration[137], is likely to be impaired compared to their growth into the surrounding soil matrix. It was shown, that increasing aggregate size, density, and strength lead to reduced root growth and thus reduced aggregate size may be beneficial for root growth[138,139]. However, not just physical properties can change the growth of roots and resulting root system architecture. To assimilate nutrients efficiently, plants have developed a range of adaptive responses [24], e.g. plant roots may respond to localised phosphor sources with locally increased root elongation and increased branch density [131,140,141].

In addition, root hairs are assumed to be an important feature for roots to respond to soil heterogeneity in terms of penetration resistance and nutrient availability. For example, root hairs can be used to anchor during root establishment and thus overcome soil penetration resistance [31,32], while they also increase the availability of nutrients like phosphorus [3,133]. X-ray µCT has proven to be a useful tool to analyse such root morphological responses to local changes in soil structure as well as to the amount and distribution of nutrients [17,131,140,142–144].

In this study, we analysed the combined effect of heterogeneity in soil penetration resistance and nutrient availability on root system architecture. This is achieved by examining plant growth in columns with two sandy substrates with X-ray µCT. Though the average soil texture is identical, one of these substrates contains large sized loamy aggregates, while the other corresponds to a standardized, homogenized laboratory soil, in which the loam is sieved and evenly distributed. These loamy aggregates induce areas of larger penetration resistance due to their stability and thus may reduce root elongation. On the other hand, due to the higher cation exchange capacity and the higher content of Fe-(hydr)oxides in these loamy aggregates, there are higher concentrations of potentially available P. Plant roots therefore may prefer to grow towards larger loamy aggregates, which contain higher concentrations of P [131,141].

In addition, we investigated the importance of root hairs for the adaption in root system architecture. This is addressed by using two genotypes of *Zea mays* L. The first is the wild-type (WT) and the second is a corresponding mutant defective in root hair elongation (*rth3)* [36].

We hypothesized that 1) maize roots grow towards loamy aggregates to maintain sufficient nutrient uptake for plant growth, but 2) show reduced root growth into them because of higher penetration resistance. Thus, 3) total plant growth in aggregated substrates will be reduced, which is 4) especially true for hairless mutants, as they may not be able to overcome the penetration resistance of the aggregates.

4.3 Materials and Methods

4.3.1 Experimental design

The experiment was set up as a two factorial, randomized design with three replicates. The term replicates refers to individual soil columns. Factor one was substrate with two levels i.e. aggregated and sieved. Factor two was *Zea mays* L. genotype with two levels namely B73 wild-type (WT), and the corresponding root hair defective mutant (*rth3*).

4.3.2 Substrates varying in aggregation

Both substrates are a mixture of 83.3% quartz sand and 16.7% loam taken from a Haplic Phaeozem. The major difference between the two substrates is the soil structure. As described in Vetterlein et al. (2020), the aggregated substrate was created by mixing quartz sand and unsieved loam for a field experiment using a heavy double deck vibrating screen and used as such. For technical reasons, stable large sized loam aggregates (approx. 10 vol%) are created in the otherwise homogenous sandy substrate. The sieved substrate for laboratory experiments was generated by sieving the aggregated loam down to 1 mm using a cylindrical handhold sieve before mixing with the quartz sand. This was done to achieve an as homogenous mixture in column experiments as possible. The two substrates will be referred to as Aggregated and Sieved. The penetration resistance in the sieved substrate was measured in parallel experiments under identical conditions and amounted to 0.08 MPa [94]. The penetration resistance of individual macroaggregates embedded in the aggregated substrate was not measured. Unsorted, unmixed loam packed at a bulk density of 1.27 g cm^{-3} had a penetration resistance of 0.15 MPa in the moisture range of the experiment [94]. The macroaggregates are supposed to have a much higher penetration resistance due to higher bulk density and particularly high stability as they endured the vigorous mechanical agitation of the vibration screen.

Both substrates were fertilized with fertiliser solutions according to Vetterlein et al. [3]. To achieve a homogeneous distribution of nutrients the material was sieved again after drying with a handheld sieve after fertilization. As the loam aggregates in the aggregated treatment would have been partly destroyed in this manner, they were removed with a sieve from the mixture prior to fertilization and then added again after sieving. Following the packing protocol described in Lippold et al. [47], acrylic glass cylinders with an inner diameter of 7 cm and a total height of 25 cm were filled up to 23 cm height with the investigated substrates to a bulk density of 1.47 g cm^{-3}. Surface sterilized maize seeds were placed at 1 cm depth. Surface was covered with quartz gravel to reduce evaporation. The columns were irrigated from top and bottom in the night before day 2, 5, 9, 13, 15, 17, 19, and 21 after sowing to an average volumetric water content of 18%. Watering intervals were shortened with increasing plant size to avoid drought stress. All plants were grown in a climate chamber for 21 days with 12 h light per day and a light intensity of 350 $\mu M/m^2 * s$ of photosynthetic active radiation. Temperature was set to 22°C during the day and 18°C at night with constant relative humidity of 65%.

4.3.3 Shoot biomass sampling and nutrient analysis

On day 22, shoots were cut off and dried at 65°C for 72 hours. After determination of shoot dry weight the material was ground down to fine powder. C/N was analysed by combustion with a CN elemental analyzer (vario EL cube, Elementar, Germany). Phosphorus (P), Potassium (K) and Calcium (Ca) were determined by ICP-OES (ARCOS, Spectro AMETEC, Germany) after pressure digestion with HNO_3 in a microwave (Mars 6, CEM Corporation, USA). To compare the uptake of a highly mobile nutrient with one of low mobility without the confounding impact of plant growth, the Ca:P ratio in the shoot biomass was assessed for each replicate [47].

4.3.4 Destructive sampling of roots and substrate

After cutting the shoots, the soil was pushed out of the acrylic column. The soil was sliced into layers to separate areas scanned with X-ray CT from unscanned areas (0-23 cm depth). The layers were placed on a 0.63 mm sieve and roots were washed out carefully with deionised water after taking 30 g of each layer for substrate analysis. Roots were stored in 50% ethanol solution (Rotisol). Subsequent, roots were scanned on a flatbed scanner at 720 dpi (EPSON perfection V700). Thereafter, root traits were analysed using the software WinRhizo 2019 (Regent Instruments, Canada). The material from each layer for substrate analysis was pooled again to have one sample per biological replicate. However, former aggregates and fine material was bulked separately. Samples were air dried for 72 hours and sieved to 1 mm. Plant available P was determined by the CAL-method [145].

4.3.5 Leaf area

Effects of the different treatments on plant growth over time were investigated by measuring leaf area each time watering was done. Width and length of every leaf was recorded. All leaves were scanned on a flatbed scanner at day of harvest and then measured in colour classification mode in WinRhizo. To estimate the leaf area during the experiment and correct for the typical shape of a leaf, these results were then used to create a linear model using R. The best model fit was achieved with the following Model (adjusted $R^2 = 0.991$):

$$Area_{leaf} = 0.723 * Width_{leaf} * Length_{leaf}$$

4.3.6 X-ray µCT

X-ray tomography was performed with an industrial µCT (X-TEK XTH 225, Nikon Metrology) at 160 kV and 296 µA. A total of 2748 projections with an exposure time of 500 ms each were acquired during a full rotation of the columns. Samples were placed 18.2 cm away from the X-ray source during image acquisition. A 0.5 mm thick copper filter was used between the source and the column in order to reduce beam artefacts. A lead shield with a window (2.5*2.5 cm) was placed to minimize diverging photons outside the field of view, i.e. to the plant shoot and in the soil outside the field of view. With this setup, the dose per scan measured with a RPL dosimeter in the center of the column amounts to 1.2 Gy [48]. X-ray CT scanning was performed at day 21 after planting (DAP) during night time so as to not interfere with plant photosynthesis. Columns were scanned at two depths interval making sure that an overlapping region was present. Each depth interval scan took 23 min to complete. The obtained images were reconstructed into a 3D tomogram having a voxel size of 45 µm and an 8-bit greyscale via a filtered back projection algorithm with the CT Pro 3D software (Nikon metrology). During the 8-bit conversion, the greyscale range was normalized with a percentile method which sets the darkest and brightest 0.2% voxels to 0 and 255, respectively.

4.3.7 Segmentation of roots

The images were processed and roots were segmented with the Rootine workflow of Gao et al. [130]. The basis of this workflow is the use of the ‘Tubeness’ plugin (https://imagej.net/Tubeness) in Fiji [146,147]. This allows the use of the most common feature of all sized roots, which is their cylindrical shape. Prior to the feature extraction, image processing steps are performed, which 1) normalise the grey values with the ‘Attenuation correction’ plugin in Fiji and 2) reduce the noise by using a fast, unbiased 3D Non-Local Means filter [148] in ITK.

4.3.8 Segmentation of Aggregates

A new protocol was developed to segment loamy aggregates in the sandy substrate. This starts using the normalized and filtered image from the Rootine script. This offers already a good contrast between aggregates and sand particles (Figure 4.1). Afterwards a “White Top Hat” filter of the plugin MorphoLibJ (V1.4.1) in Fiji [149] is used. The result is subtracted from the filtered image and a threshold is applied to this difference image using Otsu’s method [150]. As some of the aggregates contained some macropores, 3D closing with a radius with a cube of 5x5x5 is used to close these holes. A 3D watershed transform of the binary image is used finally to split touching aggregates. These two functions are also implemented in the MorphoLibJ plugin.

4.3.9 Analysis of local changes in root growth

The "Skeletonize" and "Local Thickness" functions were used to compute the root length, root branching points (junctions) and root diameters from the resulting root image of Rootine. To describe the local changes in root growth in response to aggregates in a holistic way (Figure 4.1), we analysed 1) root length as well as root branch density, root diameter and root volume as a function of aggregate distance, 2) the distribution of aggregates and roots with respect to the column wall and 3) root length density within aggregates and in the surrounding sand substrate. To achieve 1) and 2) the Euclidean distances maps of the aggregates and the column wall was computed and combined with the root images as described in Lucas et al. [17]. The 3D ROI Manger was used to compute 3) [151].

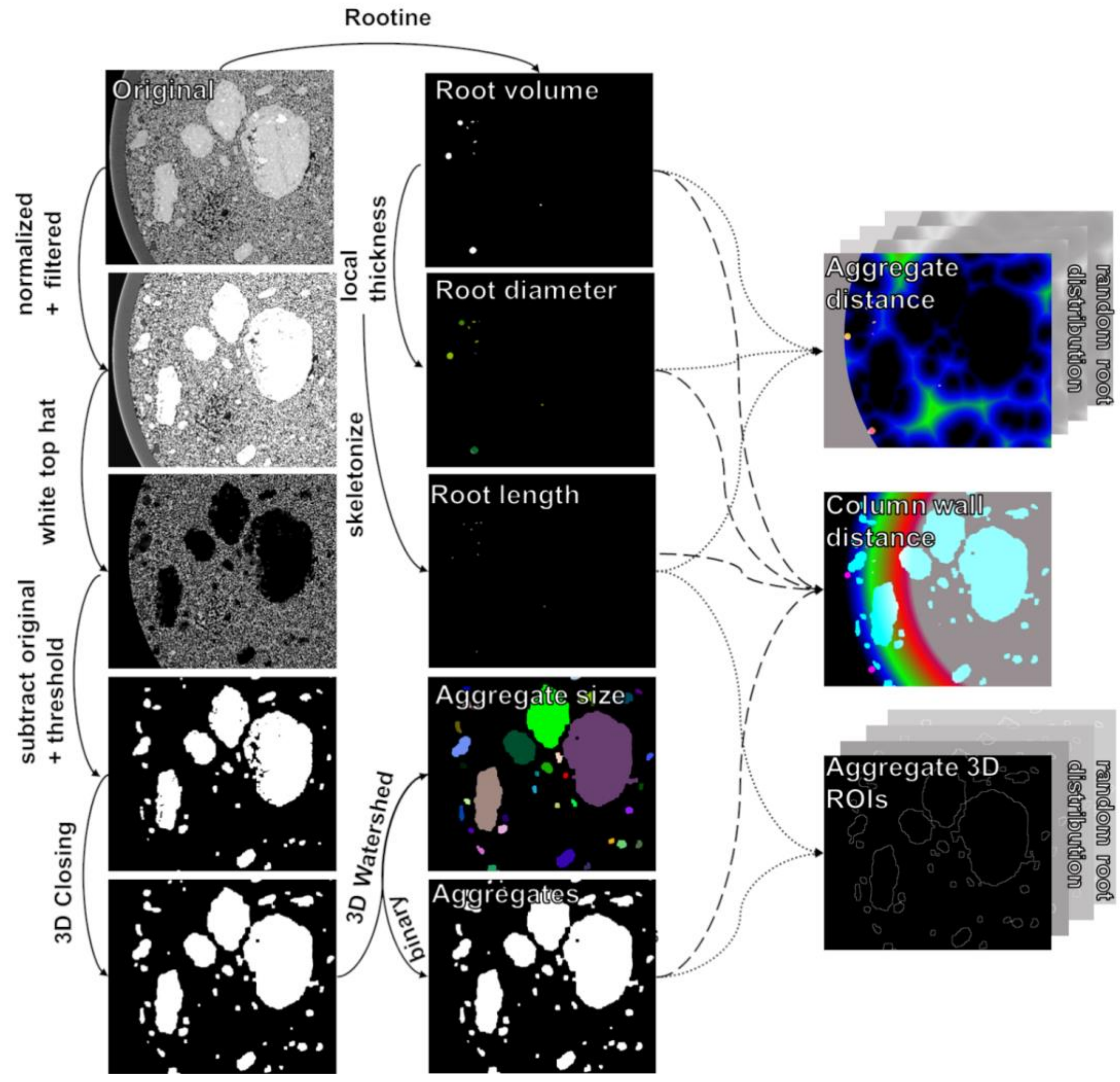
Rootine
Original
normalized + filtered
white top hat
subtract original + threshold
3D Closing
local thickness
skeletonize
3D Watershed
binary
Root volume
Root diameter
Root length
Aggregate size
Aggregates
Aggregate distance
random root distribution
Column wall distance
Aggregate 3D ROIs
random root distribution

Figure 4.1: Workflow for the segmentation of aggregates and analysis of root distribution in relation to aggregates. Aggregate distance refers to the distance from any soil voxel outside an aggregate to the nearest aggregate, likewise column wall distance refers to the distance from any soil voxel to the nearest voxel of the column wall.

4.3.10 Random root distribution

A response of root growth to certain soil features can be gauged in several ways. A common approach is compare measured root traits against a benchmark with identical average properties in which either the location of roots [152] or the location of soil features [153] are randomized. Here we adopt and modify the approach of Colombi et al. [153]. To compare the resulting root distributions with a root system not influenced by aggregates we generated random, but realistic root distributions from root images of the same data set. For this, the root images of the sieved treatments were used, by rotating the images stepwise three times by 90°. Thus, twelve root systems per column were generated for which the relative positions of roots and aggregates were randomized and corresponding root distributions were calculated.

The whole workflow of aggregate segmentation and image analysis can be found as ImageJ macro file in the Supplementary Material.

4.3.11 Statistics

Standard errors and mean values of the three replicates for each combination of maize genotype (WT and *rth3*) and soil substrate (Sieved and Aggregated) are provided. The influence of the two factors on leaf area and root length density at different locations (matrix, aggregates of different sizes) at the end of the experiment were additionally evaluated by two-factorial ANOVA's in conjunction with Tukey's HSD test. The assumptions of the different models were visually assed by evaluating plots of residuals (residuals vs residuals, QQ plot of standardized residuals). For all statistical analyses the software R 4.02 and the package agricolae [154] were used.

4.4 Results

4.4.1 Influence on total plant and root growth

The first set of analysis aimed to reveal changes in total plant and root growth affected by plant genotype and aggregation. On average WT plants developed larger leaf area than *rth3* plants in both substrates beginning from day 10 after planting until the day of harvest (Figure 4.2b). However, significant differences between the sieved soil and the aggregated field soil could not be detected for neither of the genotypes (Figure 4.2b, $p = 0.28$), although leaf growth after day 17 seem to be higher for plants growing in the aggregated substrate. The same is true for the observed root length densities (Figure 4.2c), which were more than twice as high for WT compared to *rth3* but independent of substrate ($p = 0.41$). In addition, significant differences between substrates (p =

$8.19 * 10^{-6}$) and between genotypes ($p < 2 * 10^{-16}$) were found for root diameters with *rth3* having thicker roots than WT and both genotypes having thicker roots in aggregated substrate (Figure AF6). The ratio between Calcium and Phosphorus in the shoot material was calculated as this is expected to be independent from any dilution by growth in contrast to individual tissue concentrations. The Ca:P ratio showed higher values for *rth3* as compared to WT ($p= 5.46 * 10^{-5}$). The substrate, however, had only a tendency to significant differences (p=0.054), which can be mainly related to difference in *rth3*, showing a tendency to higher Ca:P ratios in the aggregated substrate (Figure 4.2D).

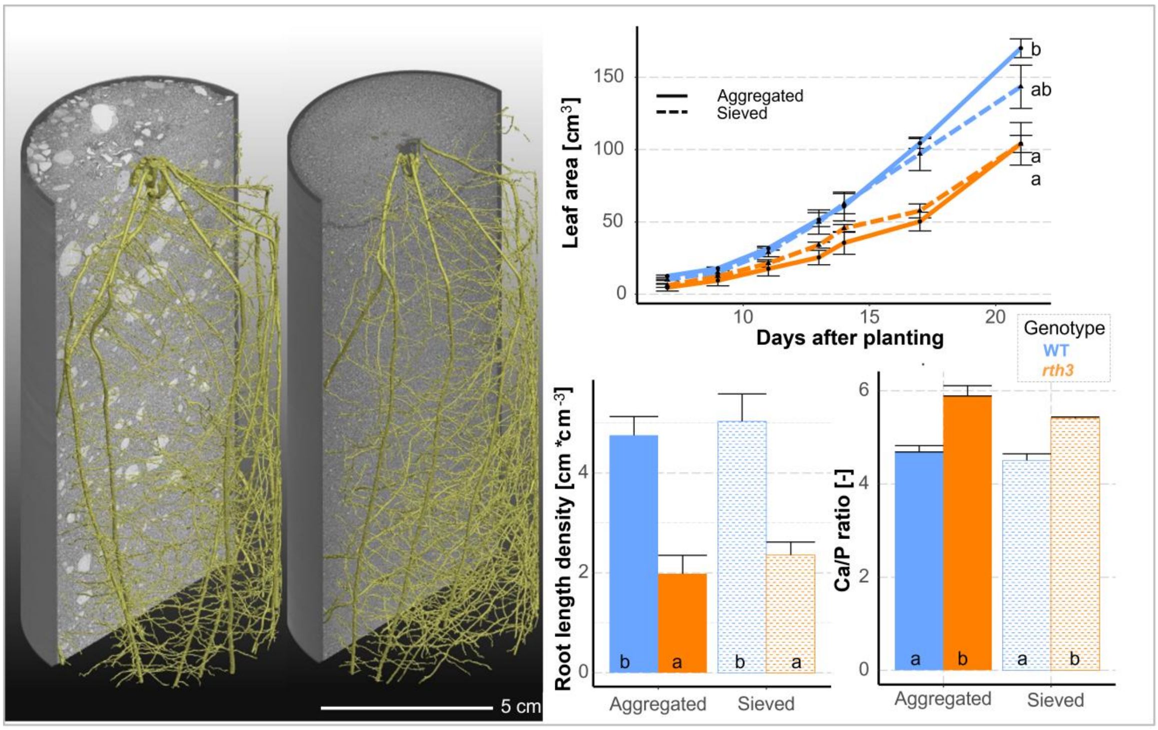

Figure 4.2: Rendered 3D images of root system in aggregated and sieved substrate (A). Plant growth (leaf area) over time (B). In addition, root length density (C) and Ca/P-ratio (D) at the end of the experiment. Different letters indicate significant differences (p-value < 0.05). Compared are the genotypes of maize (WT = wildtype, rth3 = root hairless variety) in the two substrates at the end of the experiment. Error bars show standard errors of the mean.

4.4.2 Local adaption of root traits in aggregated soil

The root length densities derived from X-ray CT data were in a good agreement with the WinRhizo data ($R^2 = 0.99$), although approx. 14% of the maize roots could not be recovered by the 3D imaging technique (Figure AF7). Especially roots of the WT showed lower recovery rate within the CT images compared to the results from destructive sampling. This can be attributed to differences in root diameters between the two genotypes. In both substrates the average root diameter was significantly lower for the WT ($p < 1 * 10^{-5}$) and hence its recovery in X-ray CT images was more challenging. Especially in the diameter class <0.1 mm root diameter was close to the resolution (2 voxels). In this diameter class root length of the WT was approx. doubled compared to *rth*3, when measured destructively.

There was a significant decrease of root length density within aggregates (Figure 4.3, p = 0.015 for *rth3* and p = 0.002 for WT). While the root length density in aggregates increased monotonously with increasing aggregate size for the WT, this was not true for *rth3*. Consequently, significantly lower root length densities could be found in aggregates >1 mm^3 in columns of *rth3* compared to columns of the WT (p = 0.01).

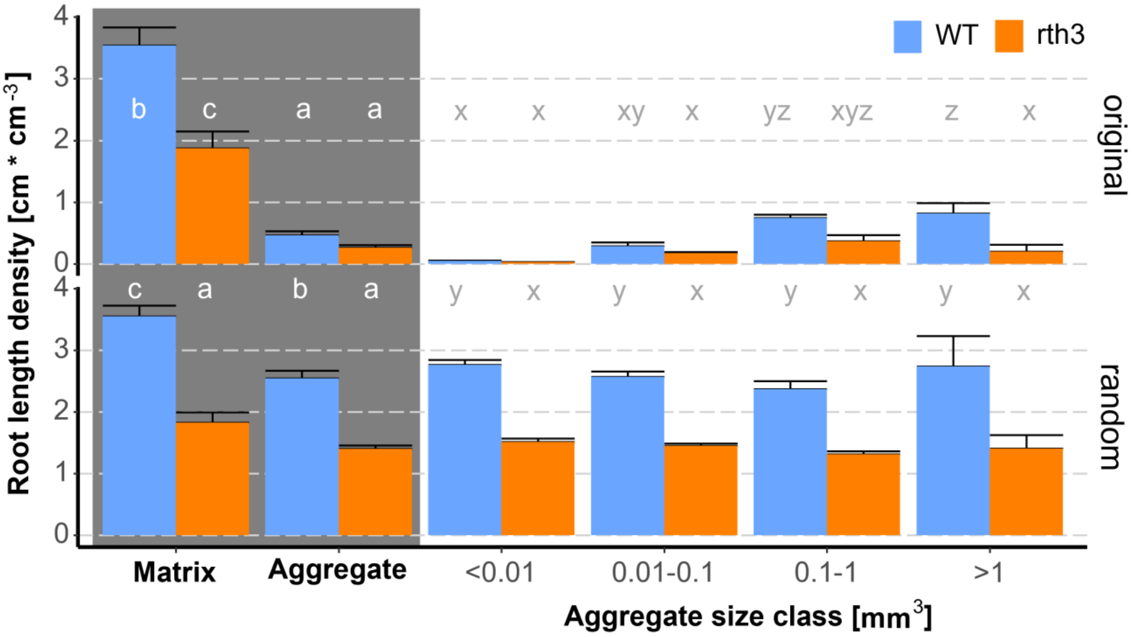

Figure 4.3: Roots in different locations. Different letters indicate significant differences (p-value < 0.05). Differences in root length density between genotypes (WT = wildtype, rth3 = root hair defective genotype) and spatial domains. Matrix vs aggregate and aggregates of different sizes were tested separately, which is indicated by different letters used (a, b, c compared to x, y, z). Error bars show standard errors of the mean.

From that data alone, it is not clear whether these differences were a response of adaptive root growth or simply arose from different volume fractions of aggregate sizes in different columns. Random root distributions were simulated to address this. For these, the differences in root length densities due to aggregate size vanished, and only significant difference between the genotypes occurred that are proportional to the differences in total root length density (Figure 4.2c). Surprisingly, also for the randomized root distributions of WT higher root length density could be found in the sand matrix compared to the loamy aggregates. These differences, however, were small compared to the differences that occurred with the original root system architecture.

The reason for the higher root length density within the sand matrix than within aggregates of the randomized root distributions is the heterogeneous distribution of roots and aggregates within such a column experiment. The pattern revealed by the analysis of root length density and aggregate volume fraction with distance to the column wall (Figure AF8) shows 1) increasing aggregate volumes with increasing wall distance to a plateau after roughly 1.5 mm as these convexly shaped objects cannot fit perfectly to the column wall, whereas 2) roots have the highest root length densities, root volumes and lowest root diameter at a distance of approx. 0.2 mm to the wall as there are on average much smaller than aggregates.

The highest root length densities in the sandy matrix were found in close proximity to aggregates (Figure 4.4). Combining all root information from the aggregate distance analysis two root morphological changes became apparent: 1) at a distance of approx. 0.6 mm to the aggregate boundaries there was a local increase in branching point density. The laterals that emerged from it and grew towards the aggregates caused a reduction in average root diameters at distances <0.6 mm. 2) at a distance of approx. 0.2 mm to aggregates boundaries another peak in branch densities occurred. This led to the aforementioned peak in root length densities but was not associated with a high root volume density, as mean root diameters decreased further towards aggregates. The random root distribution showed almost no trend as a function of aggregate distance. When pooling the continuous distance into distinctive distance classes (Table 4.1), the aggregates and their vicinity (<0.6mm) make up 30% of the total volume, which also roughly corresponds to 30% of all roots for both genotypes.

In addition to penetration resistance, nutrient availability could also have had an impact on root growth. Despite being removed prior to matrix fertilization, P concentrations in aggregates were significantly higher than in the sandy matrix at harvest (Figure AF9). The difference in the P concentration of matrix and aggregates was significantly higher for WT (56.3 mg kg^{-3}) than for rth3 (45.47 mg kg^{-3}, $p = 0.016$).

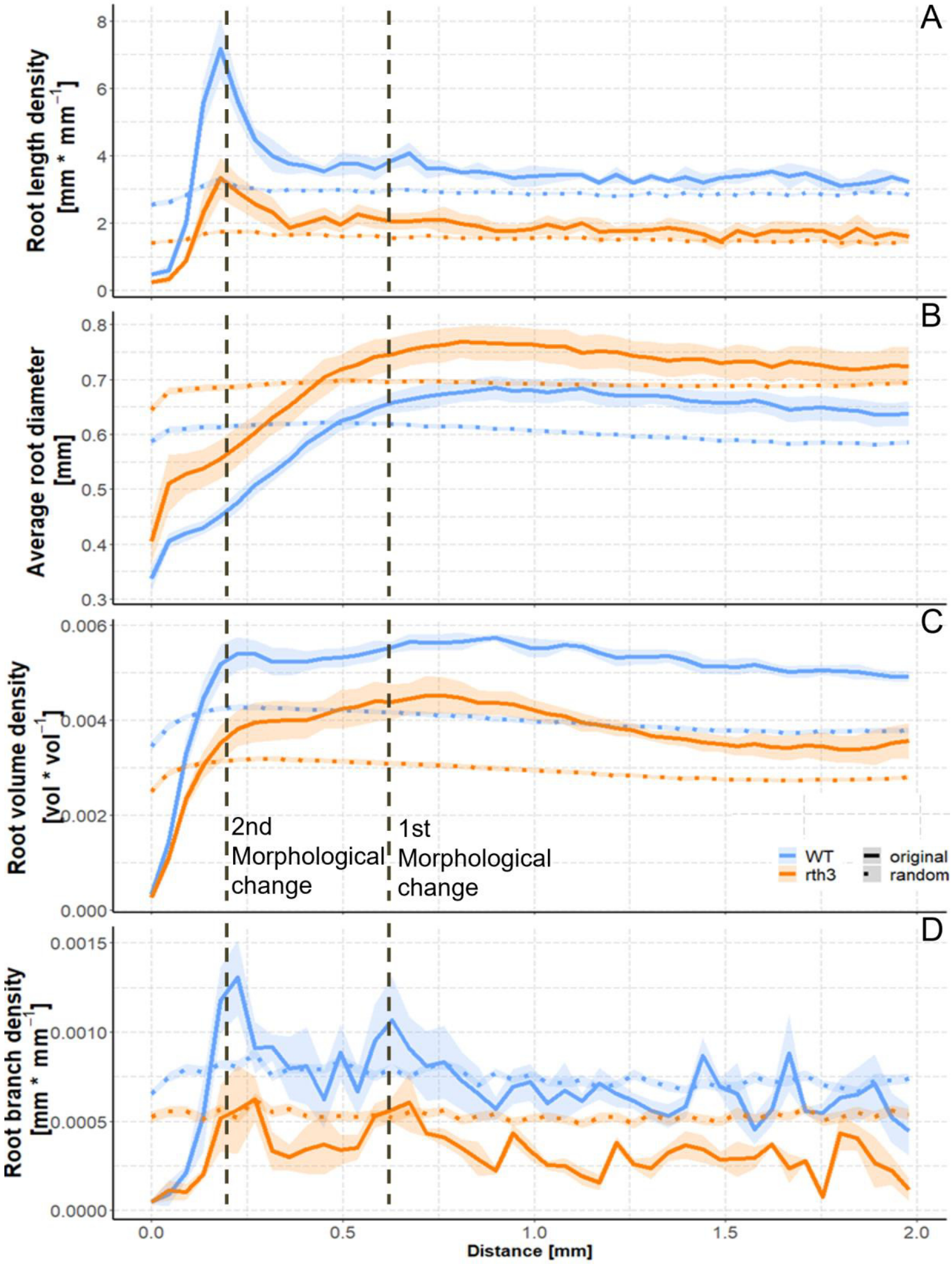
A
B
C
D
Root length density [mm * mm^{-1}]
0
2
4
6
8
Average root diameter [mm]
0.3
0.4
0.5
0.6
0.7
0.8
Root volume density [vol * vol^{-1}]
0.000
0.002
0.004
0.006
Root branch density [mm * mm^{-1}]
0.0000
0.0005
0.0010
0.0015
2nd Morphological change
1st Morphological change
WT
rth3
original
random
0.0
0.5
1.0
1.5
2.0
Distance [mm]

Figure 4.4: Root distribution around aggregates. Compared are the genotypes of maize (WT = wildtype, rth3 = root hairless variety) and randomized root distributions of these. Dashed lines point to distances at which morphological changes became apparent. These points of morphological changes a mainly declared based on the peaks in root branch density, which come along with changes in the other measures.

Table 4.1: Pooled continuous distance in distinctive distance classes for both genotypes (WT = wildtype, rth3 = root hair defective genotype). Numbers in brackets despict the standard error.

	within Aggregates		Aggregate vicinity (<0.6mm distance)		Aggregate + vicinity		Bulk soil (>0.6mm distance)	
	WT	*rth3*	WT	*rth3*	WT	*rth3*	WT	*rth3*
Relative root length [%]	1.51 (± 0.26)	1.63 (± 0.21)	25.50 (± 2.47)	26.44 (± 0.30)	27.0 (± 2.69)	28.07 (± 0.2)	73.00 (± 2.69)	71.93 (± 0.2)
Relative Volume [%]	10.5 (± 0.96)	11.12 (± 0.49)	20.78 (± 1.59)	21.26 (± 1.03)	31.28 (± 2.54)	32.43 (± 1.25)	68.72 (± 2.54)	67.57 (± 1.25)
Root length density [cm cm^{-3}]	0.46 (± 0.06)	0.24 (± 0.04)	3.97 (± 0.35)	2.11 (± 0.35)	2.79 (± 0.23)	1.47 (± 0.24)	3.44 (± 0.25)	1.79 (± 0.25)

4.5 Discussion

4.5.1 Local adaption of root growth to overcome soil heterogeneity

This study was set up with the aim to assess the change of root system architecture of maize due to presence of aggregates - which induce heterogeneity in both, penetration resistance and nutrient availability - in comparison to a sieved control in which the same amount of loam is homogeneously mixed into the sand. Penetration resistance information was only available for the sieved substrate (0.08 MPa). However, it can be inferred from complementary information that the penetration resistance of macroaggregates was much higher. In addition, the penetration resistance that the root tip experiences is particularly important for root plasticity, but different from what a rigid penetrometer tip is detecting. The presence of aggregates did not induce significant root or shoot growth differences between the two substrates (Figure 4.2). Based on that finding we conclude that maize plants were able to adapt to the heterogeneity in nutrient availability and penetration resistance caused by the aggregates. However, root length densities were much lower within aggregates compared to the sand substrate (Figure 4.3), even after taking into account the lower root recovery rate of 86% inside aggregates they were still less abundant indicating that root ingression into these dense aggregates was impaired. This is in agreement with the exponential decrease of root growth with increasing penetration resistance found in the literature [133,136] and findings of Montagu et al. [155] who showed that shoot growth in partially compacted soil is maintained, if reduced growth in compacted soil layers is compensated by enhanced root elongation in more loose areas.

Previous studies suggested root thickening as a plasticity trait to achieve greater penetration depth in compacted soil [133,156]. However, this study did find decreased root diameters at the transition towards the zones of higher penetration resistance (Figure 4.4b), i.e. only the smallest roots grew into them (Figure 4.4b). The increase in lateral root growth towards aggregates lead to a peak of root length densities in the direct vicinity of aggregates and simultaneously explains the smaller mean root diameters (Figure 4.4a, d). Freitas et al. [139] showed that once maize roots encounter a pathway between aggregates, they continue growing along the outside of the aggregate unless they find an intra-aggregate pore they can enter. Thus, during the growth around aggregates, roots may also preliminary have followed the existing macropore space, present in the sandy substrate. This would lead to localised radial compression and thus additionally to smaller mean root diameters, compared to roots responding to axial pressure by radial expansion [157].

However, the increased root length density was probably only a result of branching and the corresponding accumulation of roots around aggregates, as the pooled length densities of aggregates and the surrounding area was even slightly lower than in the rest of the soil. There are two main reasons for these different root length densities: 1) a pot experiment bias as most roots can be found at the column wall, where no aggregates are found (Figure AF8). Thus, even the random root distributions showed lower root length densities in aggregates compared to the matrix for WT. 2) An imaging bias as WT had a lower root recovery rate compared to *rth3*, because of thinner roots, and thus may also have had a lower recovery within aggregates. However, the general trend of the root diameters, which already started to decrease at a distance of 0.5 cm from the aggregate surface to the lowest values within the aggregates, revealed a general morphological change, i.e. increased root growth of laterals towards aggregates (Figure 4.5). This is in good agreement with the findings of Burr-Hersey et al. [143], which showed that radish responded to compacted soil by morphological changes, with the single thick taproot branching out into several finer roots that penetrated the denser soil. The increase of root length density around aggregates as a consequence of increased branching (Figure 4.4d) could also be an important factor to maintain sufficient nutrient uptake from the P rich aggregates. Nutrient analysis confirmed that there was an incentive for roots to grow towards the aggregates to acquire P. In addition, 3 days before harvest, the aggregated treatments seem to maintain an even higher growth of leaf area for both genotypes compared to their sieved equivalents, i.e., at a time point at which aggregates are already covered by roots. The accumulation of roots on the aggregate surface thus seems to be triggered mainly by the increased penetration resistance, while the increased branching simultaneously ensures sufficient P uptake.

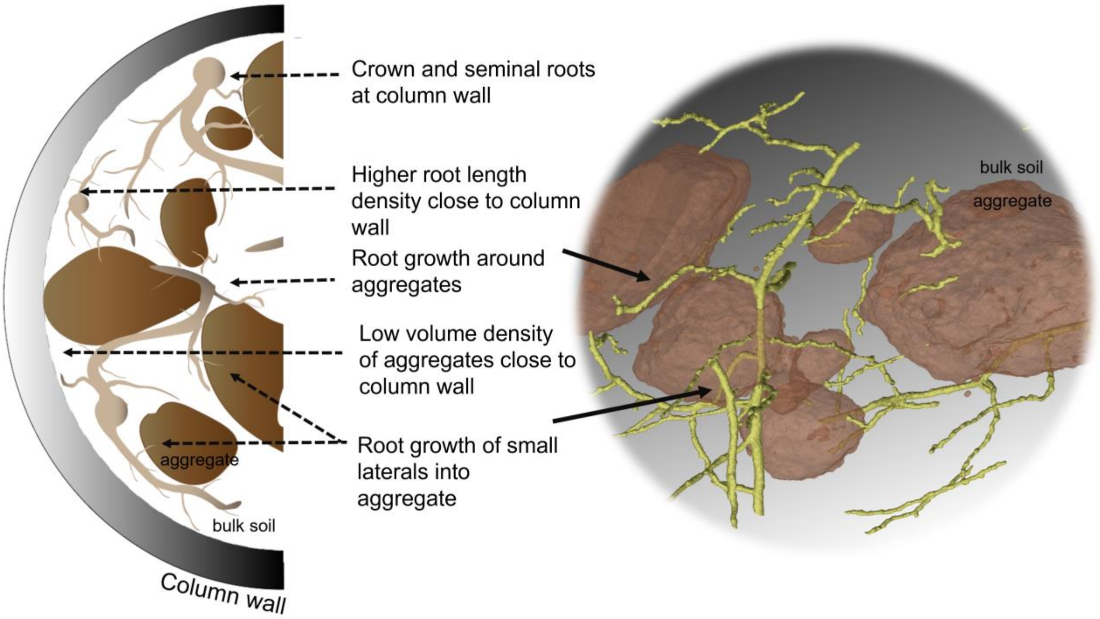
Crown and seminal roots at column wall
Higher root length density close to column wall
Root growth around aggregates
Low volume density of aggregates close to column wall
Root growth of small laterals into aggregate
aggregate
bulk soil
Column wall
bulk soil
aggregate

Figure 4.5: Scheme of root and aggregate distribution within columns (left) and CT image of small roots enclosing aggregates.

4.5.2 The importance of root hairs

For both substrates, the growth of the *rth3* mutant was significantly lower as compared to the wild-type. It developed less than half of the total root length density. These results are in line with results obtained in experiments under similar conditions with the sieved substrate [47,158]. Root growth into the aggregates is clearly hindered, i.e. the relative root length within aggregates is smaller than the relative volume. This applies equally to both genotypes, which show equal distribution of relative root length (Tab 4.1). The differences in the absolute root length (density) are therefore not due to the fact that *rth3* can penetrate less easily, but rather to a general poorer root and shoot growth of *rth3.* Despite poorer growth of rth3, the mutant developed significantly higher root diameters than the wild-type. One reason for root thickening could be the compensation for the lack of root anchorage as root thickening decreases penetration stress and stabilizes roots [156]. Another reason for developing thicker roots could be the lower root surface for *rth3*, as the uptake of nutrients strongly depends on a good root to soil contact [159] which suffers from the absence of hairs. This may lead to thicker roots in a substrate with bigger pores and gaps i.e. in the sandy matrix, to increase the root surface for a given unit of root length [32]. In contrast to our findings, Hill et al. [160] found a decreased root diameter and increased specific root length in response to P deficiency. Strock et al. [90] concluded reduced root secondary growth is a response to low P availability. Although the shoot P concentration in this experiment does not differ between the two genotypes, the Ca:P ratio revealed less efficient P uptake for the hairless mutant. This is in line with results obtained in a similar experiment [47] with both genotypes and the fine sieved substrate in combination with a loamy substrate. Since root length as well as branching density and root diameter of both genotypes behave the same in and around aggregates, it can be concluded that root hairs did not provide a major advantage for the WT compared to *rth3* for the growth into the dense aggregates. However, *rth3* was less well supplied with P, and thus root hairs or the smaller root diameters were beneficial for the P uptake of the WT. Another explanation for increased average diameters could be that in the absence of root hairs, the average diameter of fine roots increased to facilitate arbuscular mycorrhizal fungi colonization [161]. In a similar experiment with the fine sieved sandy substrate [47] first signs of mycorrhizal colonization were found, despite the early growth stage.

4.6 Conclusions

The analyses of root traits in a holistic way, i.e. by describing them with respect to their appearance (abundance and morphology) around aggregates and the column wall, enabled us to assess the change of root system architecture of maize induced by heterogeneity in penetration resistance and nutrient uptake into the shoot (Figure 4.5). A substrate containing larger sized loam aggregates mixed into the sand did not induce significant root or shoot growth differences in comparison to a sieved control in which the same amount of loam was homogeneously mixed. Thus, we conclude macroaggregation of loam in sandy soil shows little influence on maize growth, due to local adaptations of root architecture to the heterogeneity in nutrient availability and penetration resistance caused by the aggregates.

The conditions of this experiment may be only expected in anthropogenic soils to the same degree, within mixed substrates. However, macroaggregates formed by e.g. tillage or by earthworms can induce similar heterogeneity under field conditions. Due to the shown mechanisms of root adaptions, roots are able to compensate fully for these local heterogeneities.

5 Does the lack of root hairs alter root system architecture of Zea mays?

5.1 Abstract

Aims: Root hairs are one root trait among many which enables plants to adapt to environmental conditions. How different traits are coordinated and whether some are mutually exclusive is currently poorly understood. Comparing a root hair defective mutant with its corresponding wild-type, we explored if and how the mutant exhibited root growth adaptation strategies and how dependent this was on substrate.

Methods: Zea mays root hair defective mutant (*rth3*) and the corresponding wild-type siblings were grown under well-watered conditions on two substrates with contrasting texture and hence nutrient mobility. Root system architecture was investigated over time using repeated X-ray computed tomography.

Results: There was no plastic adaptation of root system architecture to the lack of root hairs, which resulted in lower uptake of nutrients especially in the substrate with high sorption capacity. The function of the root hairs for anchoring did not result in different root length density profiles between genotypes. Both maize genotypes showed a marked response to substrate. This was well reflected in the spatiotemporal development of rhizosphere volume fraction but especially in the highly significant response of root diameter to substrate, irrespective of genotype.

Conclusions: The most salient root plasticity trait was root diameter in response to substrate. Coping mechanisms for missing root hairs were limited to a shift in root-shoot ratio in loam. Further experiments are required, to elucidate whether observed differences can be explained by mechanical properties beyond mechanical impedance, root or microbiome ethylene production or differences in diffusion processes within the root or the rhizosphere.

Lippold, E., Phalempin, M., Schlüter, S., Vetterlein, D. (2021): Does the lack of root hairs alter root system architecture of Zea mays?, Plant Soil 467 (1-2), 267 – 286, DOI: 10.1007/s11104-021-05084-8

5.2 Introduction

Root hairs are important for nutrient uptake, in particular for those with low mobility like phosphorus (P) [29,30]. In addition, root hairs are thought to be important for anchorage during establishment and root tip penetration into the soil [31,32]. Their role for water uptake is discussed controversially [55,87]. Root hair formation as an anatomical feature is just one root trait among many which enables plants to adapt to environmental conditions such as low nutrient availability, limited water supply or unfavourable physical conditions [33]. Other plastic root morphological traits include changes in root diameter (diameter distribution, specific root length) or an overall change in root distribution in space. In summary, alterations in root system architecture enable an extremely flexible response to soil physical factors and limited or heterogeneous distribution of resources in time and space [25,34]. Furthermore, physiological traits can be altered, like activities of nutrient transporters and water channels, release of specific root exudates, and investment in mycorrhizal symbioses [2,27,33,68]. Such alterations would be reflected in higher normalized uptake rates [33]. As all these root traits come at different carbon costs for establishment and maintenance, the extent to which they are exploited is potentially reflected in the root:shoot ratio [57,64]. How the different traits are coordinated and whether some are mutually exclusive is currently poorly understood [27]. The relative importance of root traits is probably modulated by the soil and its physical and chemical properties. On the one hand nutrient availability depends on the sorption capacity and the forms of binding for the nutrients in question, for instance Phosphorus (P) [162]. On the other hand texture related properties such as mechanical impedance, macroporosity, water holding capacity and aeration strongly impact root system architecture [17,133] and specifically root hair length [163]. Hairs favour contact in low strength soils, and improve penetration of high strength soils, hence their relevance for P uptake is expected to depend on soil physical conditions [32].

To address the plasticity of root traits in response to the lack of hairs under different soil physical conditions we compared a root hair defective mutant to the corresponding wild-type in two substrates. Specifically, we investigated the following hypotheses:

(1) Under nutrient limited conditions, the lack of root hairs will be compensated by an increased investment in root growth in general and more specifically in the growth of fine roots to maintain sufficient root surface area;
(2) The role of root hairs for anchorage will cause an adaptation in root system architecture, more specifically soil depth exploration with time, which could partly mask their expected response to low nutrient availability;
(3) The differences between wild-type and mutant will be larger in a substrate with a high sorption capacity, i.e. low mobility of the limiting nutrients, as this increases the need for enhanced soil exploration;

(4) Substrate itself will alter root system architecture, irrespective of genotype and nutrient supply, due to differences in mechanical properties and aeration.

In this study *Zea mays* root hair defective mutant (*rth3*) and the corresponding wild-type siblings (WT) were grown for three weeks under well-watered conditions on two substrates with contrasting texture and hence nutrient mobility; loam and sand. Root system architecture was investigated non-invasively by repeated X-ray computed tomography (CT) over time. This enabled not only to derive spatial distribution of roots over time, but likewise to address the changes in root demography and hence the spatial distribution of 'active' roots. The latter is important, since we assumed that roots and in particular root hairs are only functional in uptake for a few days [16,164]. The potential and limitations of X-ray CT as a non-invasive tool to study root system architecture in 4D is explored in detail. From this data we were able to observe changes over time and to derive rhizosphere volume fractions (RVF); traits that cannot be achieved by destructive sampling. We also used conventional destructive root sampling to provide independent validations for root lengths and root diameters.

5.3 Materials and Methods

Experimental design

The main experiment was set up as a two factorial, randomised design with six replicates. The term replicates here refers to individual soil columns. Factor one was substrate with two levels (loam (L), sand (S)). Factor two was *Zea mays* genotype with two levels comprising B73 wild-type (WT), and a root hair defective mutant (*rth3*). The experiment was set up in duplicate; one set consisting of six columns for each of the four treatments (L_WT, L_*rth3*, S_WT, S_*rth3*) was used for X-ray CT scanning. The other set, likewise with six columns per treatment, served as a control to check whether the X-ray dose associated with CT scanning had an impact on the parameters of interest (Control). The results presented refer to the six scanned replicates per treatment. For shoot dry weight and root length, the comparison between scanned columns and control is shown in the supplement.

Genotypes

For the experiments, the *Zea mays* root hair defective mutant *rth3* and the corresponding wild-type siblings were selected [165]. The monogenic mutant *rth3* is transposon induced and shows normal root hair initiation but disturbed elongation. The mutant shows no apparent aberrant shoot phenotype, but grain yield in field experiments is reduced by 19 to 42% compared to the wild-type [36]. The mutated gene encodes a GPI-anchored COBRA-like cell wall protein RTH3 that is involved in the organization of the synthesized [37]. The *rth3* mutants used in these experiments are genetically highly homozygous because they have been backcrossed to the inbred line B73 for more than 8 generations.

Substrates, sieving and packing

The loam substrate was obtained from the upper 50 cm of a haplic Phaeozem soil profile, dried to 10% gravimetric water content and then sieved down to <1 mm. The sand substrate constitutes a mix of 83.3% quartz sand (WF 33, Quarzwerke Weferlingen, Germany) and 16.7% of the sieved loam. Details on chemical and physical properties are provided in [3]. A brief summary is provided in Table 5.1.

Columns were packed carefully in order to avoid particle sorting and hence the presence of layers. This was achieved by placing a coarse sieve (4 mm of mesh size) above a column during filling which was continuously moved laterally. The loam treatment was packed to a bulk density of 1.26 g cm^{-3}, while the sand treatment was packed to a bulk density of 1.47 g cm^{-3} to have comparable bulk densities found in field sites. Filling the columns to the target bulk density was achieved by “tapping” the entire column on a flat surface (Lippold and Ohmann 2019).

Table 5.1: Physico-chemical properties of the substrates ‘loam’, ‘sand’.

	BD [g cm^{-3}]	pH ($CaCl_2$)	$CaCO_3$ [g kg^{-1}]	Sand [%]	Silt [%]	Clay [%]	CEC [mmol$_c$ kg^{-1}]	C_{org} [%]	N_t [%]	P plant available [mg kg^{-1}]	K plant available [mg kg^{-1}]	Fe_{ox} [g kg^{-1}]
‘loam’	1.26	6.21	<1	33.2	47.7	19.1	76.1	0.84	0.084	33.41	26.67	1.32
‘sand’	1.47	6.25	<1	88.6	8.1	3.3	13.0	0.14	0.014	5.67	5.44	0.22

Table 5.2: Fertiliser application [mg nutrient kg^{-1}] to the substrates ‘loam’, ‘sand’.

Type	NH_4NO_3	$CaHPO_4$	K_2SO_4	$MgCl_2$ x $6H_2O$	$CaSO_4$ x $2H_2O$	MnSO4 x H_2O	$Zn(NO_3)_2$ x $4H_2O$	$CuSO_4$ x $5H_2O$	H_3BO_3	Fe-EDTA
Nutrient	N	P	K	Mg	Ca	Mn	Zn	Cu	B	Fe
‘loam’	50	40	50	25						
‘sand’	100	80	100	50	100	3.25	0.79	0.5	0.17	3.25

Soil column design

Individual soil columns consist of an acrylic glass tube (25 cm height, 7 cm inner diameter). A nylon mesh (30 µm mesh size) is placed at the bottom of the column in order to retain the soil. The columns were filled up to 23 cm height with the substrates (Figure 5.1). With such a set-up, the volume available for plant growth is 885 cm³.

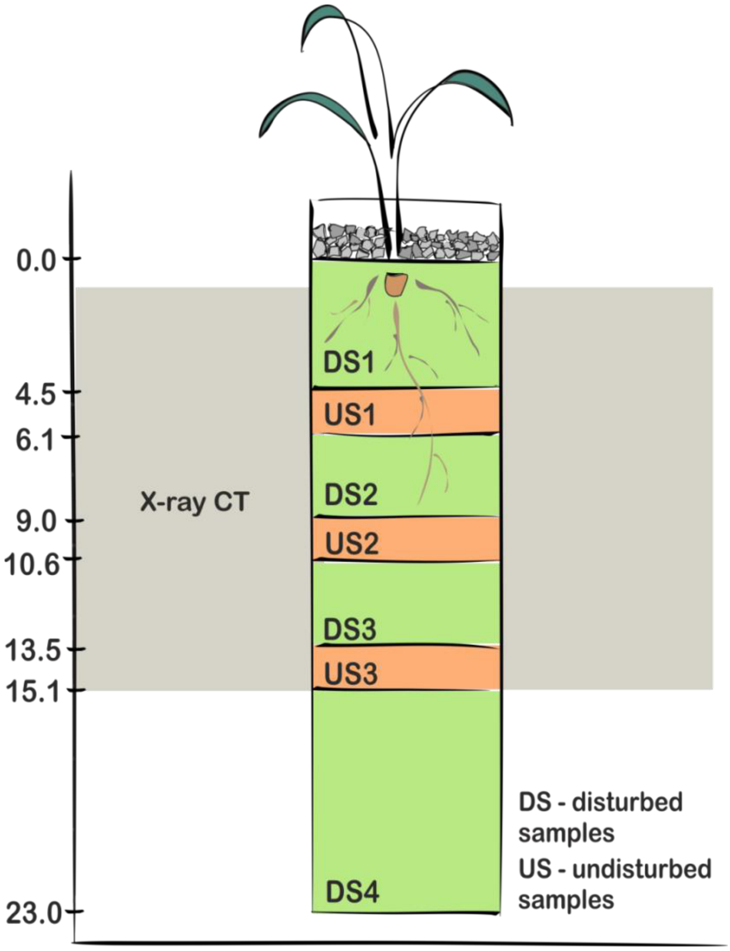

Figure 5.1: Sketch of a soil column indicating X-ray CT-scanned depth (grey, 1.0-15.1 cm), depth for destructive sampling (light green, DS1 0-4.5 cm, DS2 6.1-9.0 cm, DS3 10.6-13.5 cm, DS4 15.1-23.0 cm) as well as layers for subsamples providing higher resolution scans and material for microbiome and gene expression analyses addressed in Ganther et al. [125,158] *(orange; US1 4.5-6.1 cm, US2 9.0-10.6 cm, US3 13.5-15.1 cm)*

Soil fertilisation

Nitrogen (N), Phosphorus (P), Potassium (K), and Magnesium (Mg) were added at a dose twice as high in sand as compared to loam. Calcium (Ca) as well as micronutrients were only applied to sand (Table 5.2). This substrate-specific fertilisation was carried out to account for the initial substrate specific differences in nutrient availability. The aim was to achieve a phosphorus level per shoot dry weight which is below adequate supply for the WT genotype (< 3.5 mg g^{-1}; [81]) in order for root hairs to play a role in P acquisition under P limiting conditions.

The fertilisation dose used in this experiment was tested in pre-trials in order to achieve similar plant growth for WT, but still low plant P status [3].

Plant growth conditions

Maize seeds were surface sterilised for 5 min in 10% hydrogen peroxide and placed at a depth of 1 cm. The soil surface was covered with quartz gravel to reduce evaporation. Columns were carefully watered from top and bottom to an average volumetric water content of 22% for loam and 18% for sand. Fluctuation of water content was low as watering intervals were shortened as plant transpiration increased. Growth chamber was set to 22°C during the day and 18°C at night with a 12 h light-period, 350 µM m^{-2} s^{-1} photosynthetically active radiation and a constant relative humidity at 65%. Growth duration was 21 days, i.e. harvest was conducted on day 22 after planting.

Shoot biomass sampling and nutrient analysis

At day 22 after planting, shoots were cut and dried at 65°C for 72 hours. After the determination of shoot dry weight the material was ground down to fine powder. C and N was analysed by combustion with a CNS analyser (vario EL cube, Elementar, Germany). P, K, Ca were determined by ICP-OES (Inductively coupled plasma- optical emission spectroscopy, ARCOS, Spectro AMETEC, Germany) after pressure digestion with nitric acid and hydrogen peroxide in a microwave (Mars 6, CEM Corporation, USA). Shoot nutrient content was obtained by multiplying the measured tissue concentration and the shoot dry weight. In order to compare the uptake of a nutrient with high mobility to one with low mobility without confounding impact of plant growth, the Ca:P ratio in the shoot biomass was assessed for each replicate.

Destructive sampling of roots and WinRhizo

After the shoot was cut, the soil was pushed out of the acrylic column using a custom made subsampling device (UGT GmbH, Germany) and then sliced into seven layers. The second, fourth and sixth layer were used for further subsampling (for investigation of spatial gradients, gene expression, microbiome analyses which are presented elsewhere; [3,158,166]. The remaining layers were put on a 0.63 µm sieve and roots were washed off carefully with deionised water. Roots were stored in 50% alcohol solution (i.e. diluted Rotisol®). Subsequently, roots were scanned at 720 dpi with 35 µm resolution using a flatbed scanner (EPSON perfection V700). Root traits were analysed using the software WinRhizo 2019 (Regent Instruments, Canada).

The length of the root hairs was measured under a microscope on one cm long root segments of lateral roots one cm after the first emerging hairs above the root tip. Three segments per column were analysed. The mean root hair length was 0.24 mm with no significant difference between substrates but a tendency towards longer root hairs in sand.

Mycorrhizal colonization

After scanning with WinRhizo the degree of mycorrhizal colonization was determined. For the depth 6.1-9 cm (WR2) ten fine root (∅ < 1 mm) segments per column were selected for staining with ink (4001 Pelikan®) after clearing roots in KOH (10%) [78]. For each column, 100 fields of view were evaluated under the microscope. Following McGonigle et al. [79], presence of arbuscules, hyphae and vesicles was scored separately.

X-ray CT scanning

X-ray tomography was performed with an industrial Micro-computed tomograph - µCT (X-TEK XTH 225, Nikon Metrology) operated at 160 kV and 296 µA. A total of 2748 projections with an exposure time of 500 ms each were acquired during a full rotation of the columns. Samples were placed 18.2 cm away from the X-ray source during image acquisition. A 0.5 mm thick copper filter was used between the source and the column in order to reduce beam artefacts. A lead shield with a window (2.5*2.5 cm) was also placed between source and the column to minimize photons scatter outside the field of view, i.e. to the plant shoot and in the soil outside the field of view. With this setup, the dose per scan measured with a radiophotoluminescence dosimeter in the centre of the column amounts to 1.2 Gy [48]. The obtained images were reconstructed into a 3D tomogram having voxel side length of 45 µm and an 8-bit greyscale via a filtered back projection algorithm with the CT Pro 3D software (Nikon metrology). During the 8-bit conversion, the greyscale range was normalised with a percentile stretching method which sets the darkest and brightest 0.2% voxels to 0 and 255 respectively.

X-ray CT scanning was performed at 7, 14 and 21 days after planting (DAP) during night time to not interfere with plant photosynthesis. Columns were scanned at two depth intervals making sure that an overlapping region was present. Each depth interval scan took 23 min to complete. The bottom and top scans were then stitched together so that the analysed region had a vertical extent of -1.27 to -14.77 cm from the soil surface (Figure 5.1).

Root segmentation

Root segmentation of each column scan was performed with the algorithm Rootine v2 [152]Rootine v2 is a free macro for the image processing software ImageJ [146]. It combines a series of pre- and postprocessing filters with a shape based detection of cylindrical roots at various scales.

In order to assess the recovery of roots during segmentation, a comparison was made with the results from destructive sampling (DS). The investigated layers were located at the depth of 6.1-9.0 cm and 10.6-13.5 cm for DS2 and DS3 respectively (Figure 5.1). The obtained root length measurements were compared to the ones obtained with X-ray CT for the soil depths investigated with both methods. The root recovery and the error consistency (i.e. respectively the slope and the coefficient of determination of the line of best fit) were assessed by pooling genotypes and depths together.

X-ray CT derived analysis

The properties of the root systems obtained with X-ray CT data were systematically investigated in a depth-dependent fashion. To perform such analysis, the methods described below were applied sequentially after splitting the full 3D stacks in 20 depth intervals, yielding an equidistant spacing of 6.75 mm in the Z direction.

Root length density (RLD): The quantification of RLD was performed after a step of skeletonization with the “Analyse Skeleton” plugin available in the BoneJ plugin suite [167]. The skeletonization step conducts a medial axis transformation of the segmented root system, thereby reducing every root to a 1 pixel wide object. The RLD was then calculated by dividing the obtained root length by the analysed volume in the considered soil layer. With simple arithmetic operations on the RLD results obtained at different scanning events, the fraction of young roots (i.e. roots younger than 7 days old) was calculated for 14 and 21 DAP.

Mean root diameter: The quantification of the root diameter distribution was performed directly on the segmented root systems with the “Local Thickness” method available in the BoneJ plugin. This method assigns to every root voxel a value corresponding to the diameter of the largest sphere that fits into the root and contains it. In order to avoid that big roots contribute to more voxels than smaller roots in the obtained histogram, the results of this method were intersected with the skeletonized images. The resulting images are skeletonized root systems where each medial axis voxel contains the local root diameter information. The histogram of the obtained images is then computed to retrieve the root length corresponding to all diameter classes. Additionally, and in a more condensed fashion, the mean of the frequency distribution (referred here to as the mean root diameter) was assessed by computing the first central moment of the histogram.

Mean root distance: The quantification of the Euclidian distances to root in soil was performed by applying a so-called “Euclidian Distance Transform” on the segmented root systems. This method assigns to every soil voxel a value corresponding to its distance to the closest root in a 3D volume. Retrieving the root distance histogram (RDH) (i.e. the histogram of the results obtained from the Euclidian distance transformation) provides additional information with regard to how roots explore the available soil volume over time [168]. In a similar fashion as for the mean root diameter, the mean of the frequency distribution (referred to as the mean root distance) was assessed by computing the first central moment of the RDH.

Rhizosphere volume fraction (RVF): The RVF is here defined as the rhizosphere volume divided by the total soil volume analysed. The rhizosphere volume was computed by integrating the RDH over all distances smaller than a given rhizosphere extent. The rhizosphere extent was taken from literature and considered equal for both soil types. The value of 1.8 mm was deduced from the Figure 5.4 in [169] who measured the concentration profile of the isotopically exchangeable soil phosphate at the surface of 5 days old maize root segments grown in a sandy soil. For the WT treatment, the root hair effect on the rhizosphere extent was taken into account by simply adding the measured root hair length of 0.24 mm to the rhizosphere extent of 1.8 mm.

Statistics

For all figures, standard errors and mean values of six replicates are provided. A log-transformation was used prior to statistical analyses if normal Q-Q plots and Shapiro test indicated that the normal distribution criterion was not met. The software R version 3.53 [170] and the libraries lme4, car, multcomp, ggplot and emmeans were used. A two-factorial ANOVA for the fixed factors substrate, genotype and their interaction was conducted in conjunction with Tukey's HSD test. Significant differences between treatments are displayed with small letters for $p<0.05$ in the figures.

5.4 Results

Shoot and root growth, P acquisition

Plant P tissue concentration was low in both substrates as intended in order for root hairs to play a role in P acquisition under P limited conditions (in loam 2.4 mg g^{-1} for *rth3* and 2.6 mg g^{-1} for WT, in sand 2.7 mg g^{-1} for *rth3* and WT). Overall, there was a significant impact of substrate on shoot and root growth, with a shift in root:shoot ratio (Figure 52a, b, c). Lack of root hairs resulted in a reduction of shoot and root growth. These effects were larger for shoots than for roots, the latter being reflected in a shift in root:shoot ratio towards the roots for *rth3* (Figure 5.2c). Growth reduction (shoot and root) was larger for loam than for sand and the differences between genotypes were even more obvious for plant P content (Figure 5.2d). There was no significant difference between the genotypes with respect to P uptake per unit root surface, albeit there was a tendency for lower uptake for *rth3* as compared to WT for loam (Figure 5.2e). Likewise the Ca:P ratio showed higher values for *rth3* as compared to WT for loam. However, no difference between genotypes was found for sand (Figure 5.2f).

A higher investment in root growth to compensate for the lack of absorbing surface provided by root hairs was not found in absolute terms (Figure 5.2b) but in relative terms, at least for loam (Figure 5.2c).

The X-ray dose associated with X-ray CT scanning had no significant impact on shoot or root growth with the scan settings and scanning frequency chosen (Figure AF11).

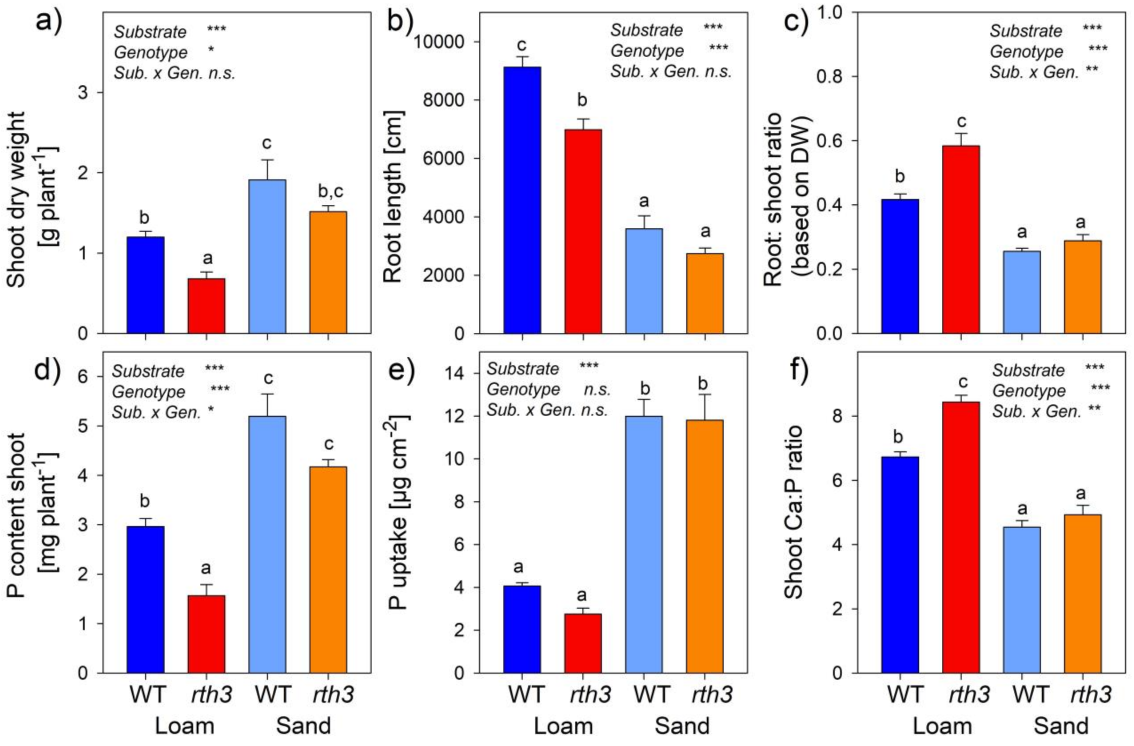

Figure 5.2: Impact of substrate (loam, sand) and maize genotype (wild-type - WT, root hair defective mutant rth3 – rth3) on shoot dry weight (a), root length (b), root:shoot ratio (c), shoot P content (d), P uptake per unit root surface (e) and the stoichiometric ratio of the mobile element Ca over the immobile nutrient P (f) in the shoot 22 days after planting.

Root system architecture in 4D

Time resolved X-ray CT scanning and superposition of scans from different time points provided insight into the 3D architecture of the root system and its temporal development including detailed information on root diameters (Figure 5.3). Comparison with the sketch of maize root development clearly shows that, with X-ray CT, the primary roots and seminal roots including their laterals can be identified (pink colour – 7 days). The roots captured additionally at day 14 (green) mainly represent the crown roots and their laterals, while those captured at day 21 represent the brace roots (blue). It should be noted that this simple assignment between scanning events and root type is only valid for the main root axis and differs in detail for the lateral roots. Note that the recovery of roots with X-ray CT was different for the loam and sand and that this difference should be kept in mind for the interpretation of the X-ray CT acquired results. The recovery of roots was equal to 99 % ($R^2 = 0.84$; n = 24) for the sand treatment whereas it amounted to 71 % ($R^2 = 0.61$; n = 19) for the loam treatment (Figure AF12).

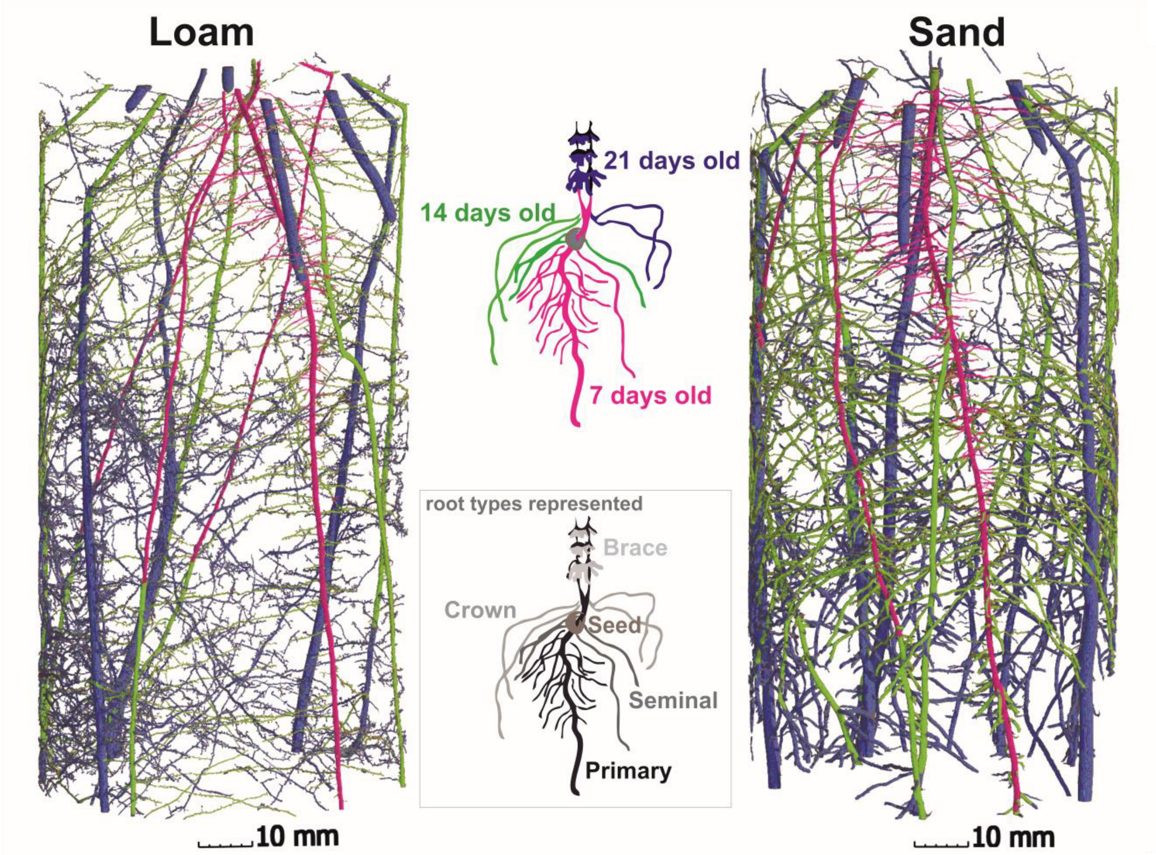

Figure 5.3: Root system architecture (from -1.27 to 14.77 cm depth) derived from X-ray CT scanning at 7, 14 and 21 days after planting (pink = 7 DAP; green = roots grown between 7 and 14 DAP; blue = root grown between 14 and 21 DAP). A representative example for WT (root length of the sample closest to the mean of the six biological replicates per treatment) is shown in both substrates. The sketch in black and grey illustrates the different root types of maize which can be found.

Root length density (RLD)

Root length density profiles (Figure 5.4, Figure AF13) showed significant differences between substrates for most depth intervals at 14 DAP and the lower ones at 21 DAP. Genotype only had a significant impact on depth exploration at 7 DAP, when overall RLD was still very low. For 21 DAP significant impact of genotype in the upper depth intervals is related to desiccation induced artefact described below. Hence, only the differences found for the lower depth intervals will be discussed further. The strong increase in root length density in the lower part of the columns observed for loam towards the end of the experiment was mostly outside the scanned region. This was quantified by destructive sampling and analysis with WinRhizo at harvest (Figure AF13).

It should be noted that, due to lower recovery of roots in loam than in sand, the root length densities for the loam treatments were underestimated relative to the sand treatments for X-ray CT derived data (Figure AF12, AF13). This was especially true for L_WT on day 21 with the highest proportion of roots <100 µm (Figure AF14). Very likely, a higher root length density at the top of the column for the L_WT treatment at 21 days was not recovered due to the stronger desiccation of the soil, which might have led to root shrinkage. The associated reduction of root diameter could be responsible for a lower recovery of laterals during root segmentation (Figure 5.4).

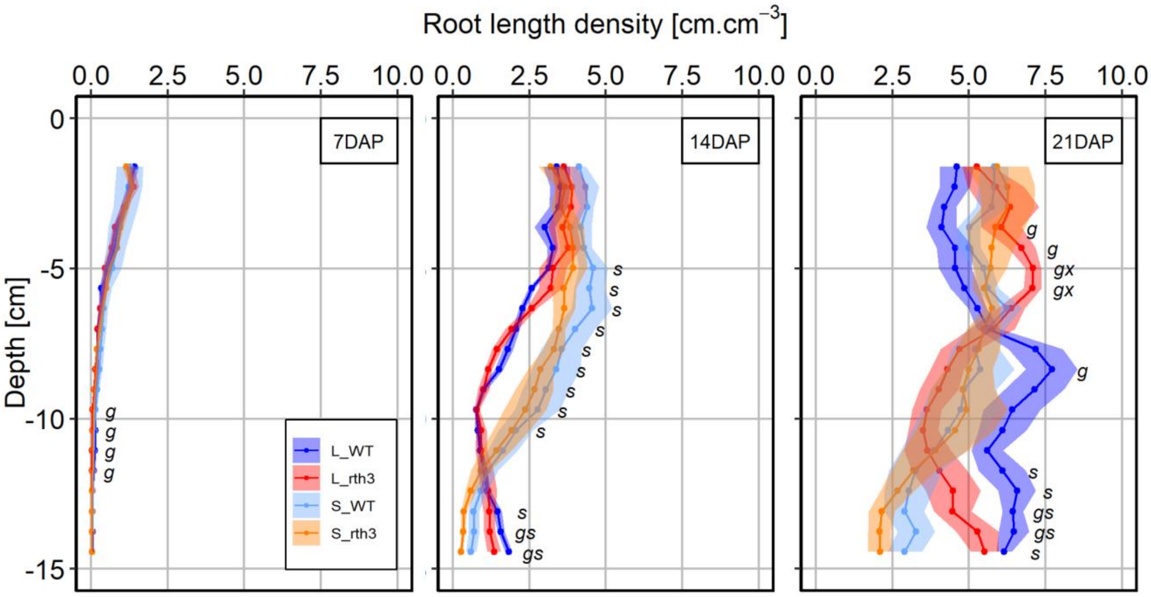

Figure 5.4: Change of root length density with depth for 7, 14 and 21 days after planting for two maize genotypes (wild-type - WT, root hair defective mutant rth3 – rth3) grown in loam (L) and sand (S). Data are derived from X-ray CT scanning; n=6, shaded areas represent standard error. Statistics: two-factorial ANOVA in conjunction with Tukey's HSD test was conducted for depth interval. Significant effect of factor is denoted by s for substrate, g for genotype and x for interaction, for p > 0.05 no letter is displayed.

Depth profiles of differences in RLD between two consecutive scans (Figure 5.5) show that the share of young roots (i.e. <7 days old) in the scanned region is significantly higher for sand than for loam at 14 DAP in most of the lower depth intervals. For loam, plants started to explore deeper unscanned soil layers earlier. At 21 DAP however, this is reversed; i.e. plants in loam showed significantly higher fraction of young roots in the scanned region.

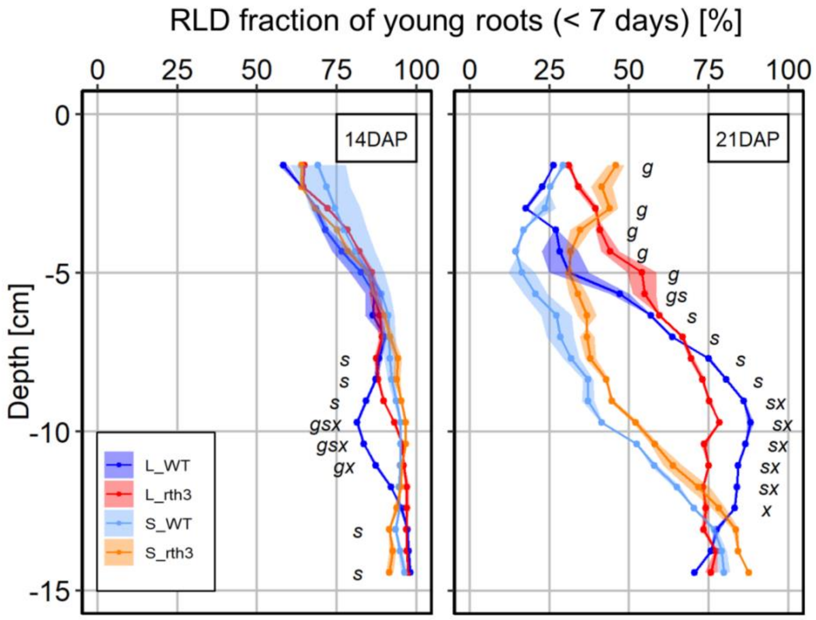

Figure 5.5: Depth distribution of roots younger than 7 days at 14 days and 21 days after planting for two maize genotypes (wild-type - WT, root hair defective mutant rth3 – rth3) grown in loam (L) and sand (S). Data are derived by simple arithmetic operations on the dataset shown in Figure 5.4; n=6, shaded areas represent standard error. Statistics: two-factorial ANOVA in conjunction with Tukey's HSD test was conducted for depth interval. Significant effect of factor is denoted by s for substrate, g for genotype and x for interaction, for $p > 0.05$ no letter is displayed.

Root diameter distribution – mean root diameter

Root diameter information is available from X-ray CT for all three scanning events (7, 14, 21 DAP) (Figure 5.6) and from destructive sampling after harvest (22 DAP) (Figure AF14). The comparison of root diameter distributions in selected depth layers shows a good agreement between the two measuring approaches (data not shown). The root diameter distribution from X-ray CT is summarized with mean root diameter profiles to simplify the comparison between treatments (Figure 5.6). Mean root diameter is consistently and for 14 and 21 DAP also significantly smaller for plants grown in loam as compared to those grown in sand, irrespective of soil depth or method used for the analysis of root diameter. For loam, a significantly larger share of roots falls into diameter classes < 200 µm (Figure AF14). Differences in root diameter between genotypes are not as obvious; however, for DAP 21 a significant impact of genotype is detected with coarser roots seen for *rth3* especially in sand in X-ray CT based data. For destructive sampling a similar tendency is seen. Mean root diameter based on destructive sampling was 360 µm for WT and 390 µm for *rth3* in sand, and 230 µm for WT and 240 µm for *rth3* in loam, respectively.

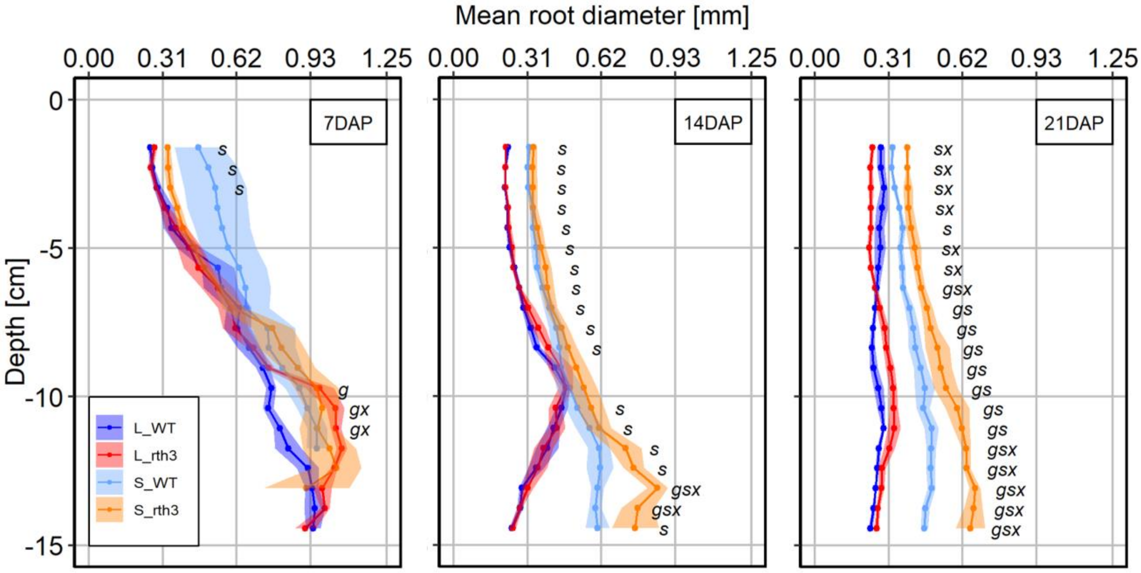

Figure 5.6: Change of mean root diameter with depth for 7, 14 and 21 days after planting for two maize genotypes (wild-type - WT, root hair defective mutant rth3 – rth3) grown in loam (L) and sand (S). Data are derived from X-ray CT scanning; n=6, shaded areas represent standard error. Statistics: two-factorial ANOVA in conjunction with Tukey's HSD test was conducted for depth interval. Significant effect of factor is denoted by s for substrate, g for genotype and x for interaction, for p > 0.05 no letter is displayed.

Root distance maps

The exploration of the soil by roots can be visualized with root distance maps (Figure 5.7a) and quantified with root distance histograms (RDH) (Fig 5.7b). The mean root distance in soil is derived from that RDH and differentiated according to soil depth (Figure 5.8). In general, the mean root distance reflects the root length density rather well (Figure 5.4). That is, an increase in root length density results in a higher frequency of short root distances making large distances less frequent (Figure 5.7b) and hence reducing mean root distance (Figure 5.8). Seven days after planting the root network is poorly developed at the bottom of the field of view and comprises only the primary root and a few seminal roots without laterals, which causes a marked increase of mean root distance with depth. At this early stage the same root length densities in sand and loam evoke different mean root distances across the entire column. This is due to two out of six replicates which had no laterals yet along the primary root at this time point for treatment S_WT (Figure AF15). Their absence has a huge impact on mean root distance in a sparsely populated soil (7 DAP) that is not reflected to the same degree in RLD. In addition, sand and loam treatments might differ in the spatial arrangement of seminal roots. The seminal roots and the primary root seemed to be more clustered in one semicircle of the column wall in loam as compared to more equidistant radial positions in sand (Figure AF15). At 14 DAP the root length density is higher in sand for almost the entire field of view except for the very bottom (below -12 cm). This difference in RLD was also reflected in the corresponding depth distribution of mean root distance, i.e. shorter mean root distance with a higher RLD and vice versa. At 21 DAP the field of view is already densely populated with roots in both substrates. There seems to be a universal limit at approx. 3 mm below which the mean root distances cannot fall despite different RLD in the range of 4-8 cm cm^{-3}. For all scanning events differences in mean root distance between genotypes are absent in both substrates, except for the lowest depth intervals at 7 DAP.

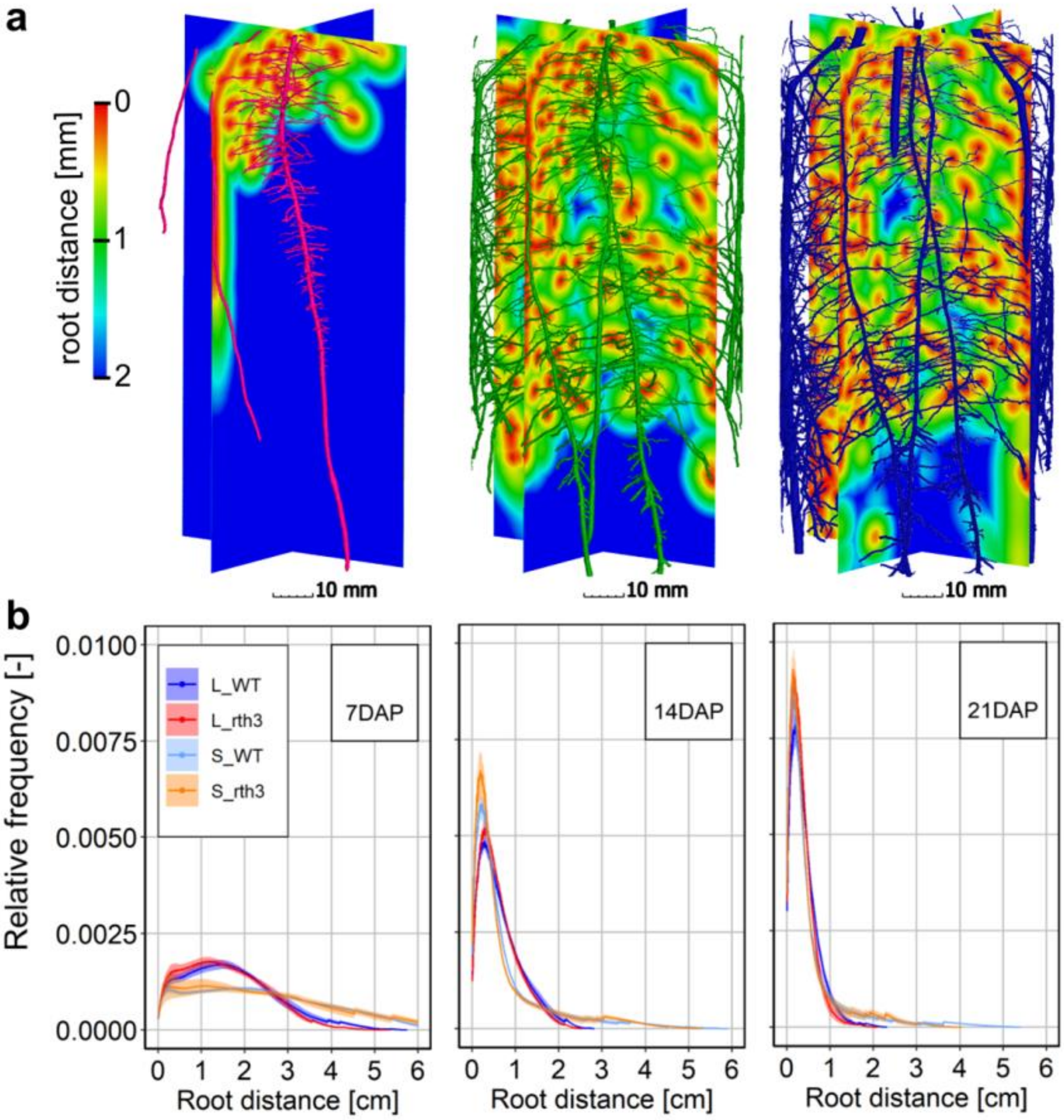

Figure 5.7 a) Root distance maps determined 7, 14 and 21 DAP for the S_ WT sample depicted in Figure 5.3. b) The root distance histograms are shifted towards shorter distance with increasing root length density over time.

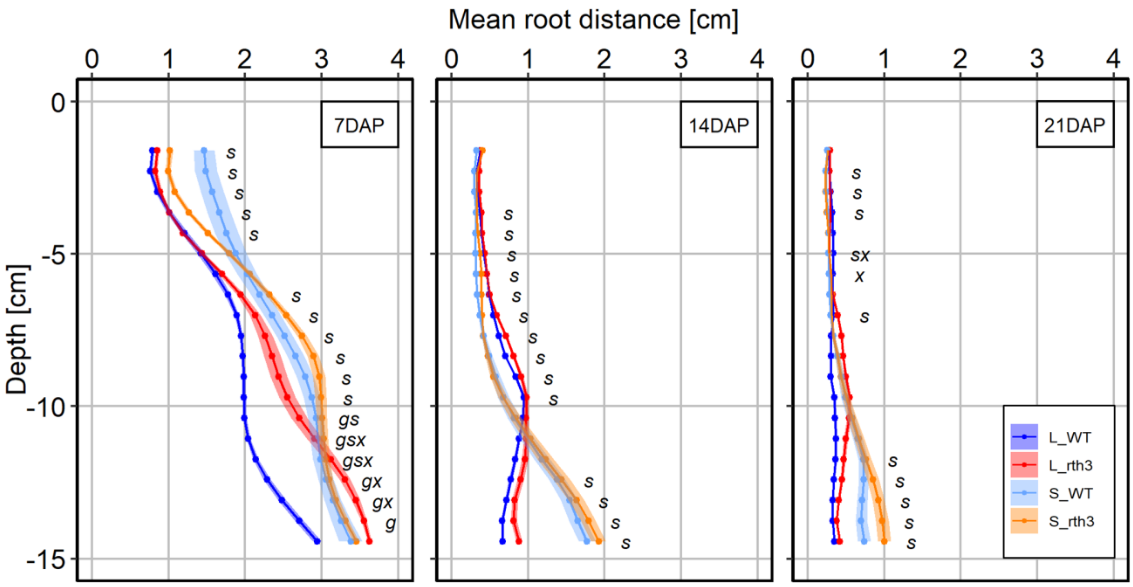

Figure 5.8: Depth profile of mean root distance for 7, 14 and 21 days after planting for two maize genotypes (wild-type - WT, root hair defective mutant rth3 – rth3) grown in loam (L) and sand (S). Data are derived from frequency 942 distribution of distances derived from distance maps calculated on 3D X-ray data;; n=6, shaded areas represent standard error. Statistics: two-factorial ANOVA in conjunction with Tukey's HSD test was conducted for depth interval. Significant effect of factor is denoted by s for substrate, g for genotype and x for interaction, for p > 0.05 no letter is displayed.

Rhizosphere volume fractions (RVF)

We recall that the hypothetical rhizosphere volume fractions (Figure 5.9) are directly derived from the root distance histograms by determining the frequency of soil voxels with root distances < 1.8 mm, which we considered to be a typical rhizosphere extent for P. In addition, for root hairs of the maize wild-type, the rhizosphere extent was increased by the measured root hair length of 0.24 mm. Again, the vertical distributions of rhizosphere volume fractions reflect root length density profiles for all time points very well. The only deviation from this congruence is a much higher RVF in the top 5 cm at 21 DAP in sand despite similar RLD values in that depth. This increase in RVF was not exclusively due to the larger root diameter in sand, as this would have led to more soil voxels in the direct vicinity of the root interface in the entire scanned region and not just the top. The insets at 21 DAP (Figure 5.9) show vastly different RVF (orange) for one loam (a) and one sand (b) column with identical RLD. Roots in loam had a preference for growing along the wall, supposedly in cracks that formed due to desiccation. The rhizosphere of roots growing along the wall was truncated to a semi-circle and contributed less to the RVF. Despite explicitly accounting for hair length, genotype had no significant effect on RVF.

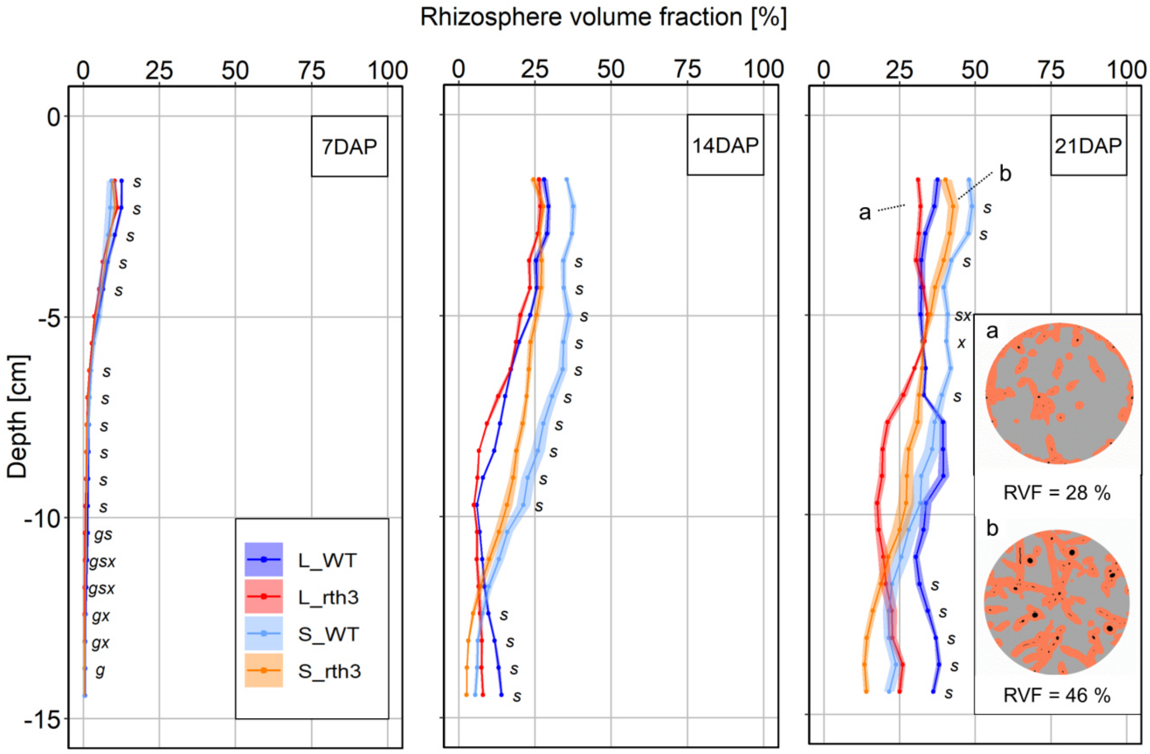

Figure 5.9: Depth profile of rhizosphere volume fraction for 7, 14 and 21 days after planting for two maize genotypes (wild-type - WT, root hair defective mutant rth3 – rth3) grown in loam (L) and sand (S). Data are derived from frequency distribution of distances derived from distance maps calculated on 3D X-ray data; Rhizosphere volume fraction is determined assuming a typical rhizosphere extent of < 1.8 mm for P depletion reported by Hendriks et al. [169] *for 5 day old root segments. For the wild-type 0.24 mm were added to account for hair length; n=6, shaded areas represent standard error. Statistics: two-factorial ANOVA in conjunction with Tukey's HSD test was conducted for depth interval. Significant effect of factor is denoted by s for substrate, g for genotype and x for interaction, for p > 0.05 no letter is displayed.*

5.5 Discussion

For the discussion part of our work, we will attempt to answer our original hypotheses stated in the introduction.

Is the lack of root hairs compensated by an increased investment in root growth in general and more specifically in the growth of fine roots?

Despite employing two complementary root system architecture measurements (µCT, destructive sampling), we did not observe an increase in fine root growth as a compensation for the lack of roots hairs. This is surprising, as the mutant exhibited a plastic response in root growth with respect to substrate. This finding is in contrast to the one by [64] who compared *Zea mays* WT to the root hair defective mutant *rth2*. They reported a shift towards finer roots for the mutant. However, in order to detect this shift, they had to compile data across treatments differing vastly in P and water supply. Their plants were growing in subsoil material and were non-mycorrhizal, while the plants in the present experiment showed first signs of mycorrhizal colonization (Table S1) despite the early growth stage. A more intense infection with mycorrhizal fungi as a compensation for the lack of hairs was suggested by [171] for barley and confirmed by [161] for maize, but only for later growth stages. The type of mutation is another potential explanation for the differences in compensation mechanism observed by [64] and the present experiment. In mutant *rth3* the mutated gene encodes a GPI-anchored COBRA like cell wall protein involved in the organization of the synthesized cellulose [36]. For the *rth2* gene the mechanism is not yet identified.

In general, a significantly higher investment in root growth by the root hair defective mutant as it is reported in literature [63,64] is also found in the present study, although only in relative but not in absolute terms and only for loam, i.e. the substrate with lower P mobility. The shift in root:shoot ratio was not sufficient to compensate for the lack of hairs as total P uptake was significantly lower for *rth3* as compared to WT in loam. With respect to physiological plasticity our results are inconsistent. While without morphological and physiological compensation lower uptake rates per unit root are expected, we found no significant differences in normalized P uptake between the genotypes, with only a tendency towards lower values for *rth3* in the substrate with the lower P mobility. In general, much lower P uptake rates per unit root surface were found for loam as compared to sand, despite the low plant P status in loam (leaf tissue P concentration of 2.4 mg g^{-1} for *rth3* and 2.6 mg g^{-1} for WT, which is expected to trigger expression of high affinity P transporters. This is in line with relative root gene expression data for the same experimental setup, reported by [158]. They did not find gene functions relating to phosphate uptake to be differentially expressed between WT and *rth3*. It is still possible that the activity of the transporters is regulated at the protein level, since apart from transcriptional regulation, post-translational modifications of phosphate transporters are widespread [172]. For soil based systems, uptake rate per unit root is strongly influenced by diffusion and root to soil contact. [32] found significantly lower P uptake rates per unit root length for the root hair defective mutant of barley compared to the wild-type, for high but more so for low P soils. Root hairs were relevant for maintaining contact in loose soils and for improved penetration in dense soils. The importance of hairs for P uptake in particular under conditions of restricted P transport is confirmed by observations in hydroponics, i.e. systems with no major limitations for transport. [173] found in hydroponic systems no differences in P uptake rates per unit root dry weight between rice genotypes differing in root hair development, irrespective of P supply. The differences between substrates observed here are related to their differences in P diffusion.

Is the role of root hairs for anchorage causing an adaptation in root system architecture? – How does this relate to soil exploration?

Bengough et al. [31] have demonstrated the importance of root hairs for anchorage using the same maize genotypes as in the present study. Peak anchorage forces were up to five times greater for the wild-type compared to the root hair defective mutant. As a consequence, wild-type primary roots penetrated deeper into the soil during a given time interval as compared to the mutant. The difference was 5 fold at low bulk density and decreased continuously with increasing bulk density/mechanical impedance. At the bulk density and water content investigated in the present experiment, penetration resistance in both substrates was well below 0.1 MPa (U. Rosskopf, S. Peth, D. Uteau personal communication). This value is an order of magnitude below the critical value for root elongation rate of 2 MPa suggested by Bengough et al. [133]. With two exceptions no differences were observed in depth exploration between the two genotypes within the same substrate. At 7 DAP, wild-type showed significantly higher values in the lower depth intervals, which is in line with the postulated role of hairs for anchorage, however in absolute values these differences were very small. A distinct exception occurred for the last time point in loam most likely due to a technical artefact. During the last four days of growth, plant water consumption for wild-type in loam was so high, that short-term desiccation of top soil occurred between the watering events. This likely caused root shrinkage which in turn reduced recovery with X-ray CT. The study of [31] focused on the very early growth stage, i.e. 3 days after germination with just the primary root (1-3 cm long) at the start of the experiment and a duration of the experiment of maximum 48 hours. At later growth stages, it can be expected that lateral root formation as well as seminal roots partly take over the function of anchorage from the hairs [174]. Lateral roots on the primary root are abundant at 7 days after planting (Figure AF15).

Root distance histograms were derived from X-ray CT data to quantify soil exploration in more detail, as they simultaneously take into account the actual 3D geometry, differences in length and diameter [168]. Root distance histograms or the mean root distance derived from these data (Figure 5.7, 5.8) are a very sensitive measure in particular at early growth when exploration is poor. This is indicated by the strong impact of delayed lateral root formation in two out of six replicates being reflected in mean root distance but not in RLD (Figure AF15). While the measure nicely reflects the progressive exploration of the soil columns from top to bottom and over time with distinct differences between substrates, no significant differences between genotypes were observed. At later growth stages, when root length densities were higher a limit in mean root distance of 3 mm was attained. Such a limit in the range of 3 mm was also reported by Lucas et al. [17] for root-induced biopores in undisturbed field samples. This suggests that an investment in more root growth may not pay off in terms of better root exploration but only increase competition between roots for the same resources. However, whether that is really the case would be better assessed with nutrient specific rhizosphere volume fractions, which are more sensitive to growth patterns at high RLD.

For the RVF, for which the measured root hair length (0.24 mm) was explicitly added to the assumed extension of the P depletion zone (1.8 mm derived from [169]) for the wild-type, no significant effect of genotype was detected at 14 and 21 days after planting at all depths. RVF reached 25 to 50% at day 21 (Figure 5.9), indicating that a large fraction was already explored for P at this early stage. Note that these results are hypothetical and depend on the assumed extension of rhizosphere. More accurate RVF estimates would require spatially resolved information about radial depletion patterns of plant available P on multiple, intact rhizosphere sections to capture them representatively.

It should be noted that the measured root hair length of 0.24 mm is rather short as compared to literature data. Frequently higher values in the range of 0.7 to 0.9 mm are reported for maize [169,175]. In general root hair lengths can vary with soil P status and bulk density [32,176]; there was a tendency towards longer root hairs in sandy substrate. Increasing hair length in our calculation of RVF would result in higher values (Figure AF16). This increase is linear for realistic root lengths. The relative importance of root diameter over root hair length for RVF would increase as the extension assumed for the rhizosphere process in question decreases.

Root length density is the dominant factor that governs differences in RVF. However, genotype (i.e. added hair length) and substrate had an additional impact (Figure AF17). For the latter one cannot disentangle the preferential growth along the wall in loam (fewer neighbouring soil voxels for roots at the wall) from the differences in root diameter (increasing the number of neighbouring soil voxels with circumference) between loam and sand. These results are valid irrespective of the exact value for the hypothetical spatial extent of P depletion, i.e. for the only variable that could not be measured in our study.

Is the difference between wild-type and mutant larger in a substrate with a high sorption capacity, i.e. low mobility of the limiting nutrients?

Nutrient mobility is expected to be lower in loam as compared to sand as loam has a higher number of sorption sites based on higher content of Fe-oxides, loam and organic matter [3]. Interpretation of biomass nutrient concentration *per se* is confounded by dilution through growth. Interpretation of shoot nutrient uptake is confounded by differences in shoot size and hence nutrient requirement. To evaluate differences in mobility we therefore used not only P uptake itself, but in addition the stoichiometric ratio of Ca (having a high mobility in soils) over P (having a low mobility in soils) [177]. For our substrates Ca:P ratio was well suited to show the differences between genotypes for loam. Differences between genotypes were significant for most of the measured growth and uptake parameters in loam, but not in sand. This is in line with our hypothesis and the observation of others [32,173], i.e. roots hairs only matter if transport to the root surface is limiting uptake.

Why do we see a high plasticity with respect to substrate, but only small compensation for the lack of root hairs?

While differences between genotypes in root traits were small in loam or absent in sand for most time points and soil depths, they were very prominent between substrates, irrespective of genotype. This is all the more remarkable as X-ray CT measurements systematically underestimated the root length (in particular fine roots) in loam. Differences between substrates were observed for root diameter, for depth distribution of RLD, share of young roots and the associated measurements such as mean root distance and RVF. While some literature suggests that intensive fine root development can increase P uptake [178,179], this is only true if P is non-uniformly distributed, e.g. greater in topsoil as found in most soils. In uniform low P, it is more common that exploratory behaviour is favoured, with increased branching only occurring when a patch of greater P is encountered As reviewed by Mollier at al. [180], a shift in root:shoot ratio is found in most studies, but results regarding root length or more specific root traits are inconsistent. In their own study with maize, they observed only a transient promotion of root growth 4 days after P starvation, which was related to carbon partitioning between shoot and root. Despite these findings, there is an agreement that local increase in P supply promotes lateral root formation in a P deficient system [131]. In the current experiment, we rule out P supply as a reason for shift in root traits between substrates. Indeed, P supply was homogenous and no differences between genotypes in loam were detected, despite their difference in P uptake.

Roots in loam showed a shift to smaller root diameter classes (Figure AF14) and smaller mean root diameters across all depth intervals and both genotypes (Figure 5.6). Differences in root diameters were detected early on and were very consistent at later time points. Changes were observed in all diameter classes. Careful inspection of segmented images (Figure 5.3) indicated that all root types were affected, i.e. it was not only due to a shift in the share of main axis (primary, seminal, crown, and brace roots) and lateral roots. It should be noted, that for 21 DAP an additional differentiation in root diameter between genotypes was observed. Especially in sand coarser roots were detected for *rth3* compared to the wild-type.

The most frequent cause for shifts in root diameter reported in literature is alterations in soil compaction, bulk density and mechanical impedance, which are tightly linked with changes in soil water content and gas diffusion [92,133,181–183]. Root diameter increase by up to 2-fold in case of mechanical impedance has been reported, as a result of cortical cells expanding radially due to microfibril reorientation in the primary cell wall [133]. Causal relationship is straight forward, if increasing bulk densities within the same soil/substrate are investigated [32,184]. An increase in root diameter upon compaction was also observed for our loam in a parallel experiment (Table AT6). When comparing different substrates causal relationships are more difficult to unravel. Kirby et al. [185] have nicely shown for the comparison of a sandy loam and a clay loam that penetration resistance alone is not sufficient to predict root thickening. They demonstrated that local values of axial and shear stresses experienced by the root near its tip may be as important as penetration resistance in constraining root growth. Ethylene is often associated with the morphological response of roots to mechanical impedance [120,181]. Increased levels of ethylene have been observed to induce increase in root diameter even for unimpeded roots [186]. An induced expression of genes related to phytohormone signalling was detected only in sand by [158] in an experimental setup like the one used here. Ethylene, but also gibberellic acid and jasmonate were affected, which indicates that processes related to development and growth are altered by the substrate. Further studies are required to evaluate whether observed differences can be explained by mechanical properties beyond mechanical impedance [185], root [118,187] or microbiome ethylene production [188] or differences in diffusion processes within the root or in the rhizosphere [189]. Anoxia as a trigger for ethylene production is ruled out for our system, at least not beyond occasional microsites. At the volumetric water content used in this experiment (22 % in loam, 18% in sand), air filled pore volume is well above 10% even at the bottom of the sand columns [3].

Increase in root diameter in sand as compared to loam did not result in an increased investment in root growth in general. Root:shoot ratio was lower in sand. This suggests that plant demands in terms of water and nutrients could be covered with a less intensive soil exploration. As differences in P uptake did not occur in sand it is difficult to assess whether compensation for the lack of root hairs did not occur in sand because there was no need for it or because fine root growth was hindered by other factors in this substrate. Unfortunately, no support for either possibility can be derived from the data of Klamer et al. [64] as they have evaluated changes in diameter across all treatments including two textures.

System limitations – relevance for field conditions

It should be noted that despite major advances in root segmentation in the past years [152,190], we still face the trade-off between image resolution and sample size resulting in fine roots being partly missed out. In the present case, this afflicts the differences between sand and loam as the share of fine roots was larger in loam. Smaller column diameters associated with a higher scanning resolution would have overcome this problem, but would have restricted our experiment to even shorter growth period. One could argue that already in the present setup results after 14 days are less confounded by the limited volume than the ones obtained 21 days after planting. This is also reflected in the higher standard errors observed for the later time point. Shorter growth durations would make it even more difficult to account for interaction of roots with the microbiome, in particular the mycorrhizal symbiosis, which is only starting to interact within the given time [172]. Moreover, we emphasize the limitation of pot trials for the study of exploration strategies. The limited soil volume of pot trials may induce feedback loops which would not be observed in the field at the same time point.

Comparison of present data with those from the field with the same treatments Vetterlein et al. [3] will not only show whether the findings are consistent but in particular how much we can learn under controlled conditions about the behaviour in the field.

5.6 Conclusions

Adaptations in root system architecture in response to lacking root hairs were investigated with a comprehensive experimental setup that combined nutrient uptake analysis, destructive root sampling and X-ray CT scanning that allows monitoring various root system architecture metrics over time. The CT derived metrics enable quantification of soil exploration and at the same time integrate the effect of various root traits, i.e. root diameter, 3D-distribution, depth distribution, hair length.

Experimental conditions were well suited to confirm the general consensus on root hairs being of particular relevance for uptake of low mobility nutrients such as P, especially in soils with a high sorption capacity. Root hair defective mutants showed low plasticity of root traits related to limited P availability, despite their general ability to express high root plasticity. The function of the root hairs for anchoring did not result in different depth profiles of the root length density. We suggest that, in more developed root systems, as in our experiment, part of the anchoring function can be taken over by lateral roots.

Both maize genotypes showed a marked response to substrates differing in soil texture mainly reflected in mean root diameter. Increase in root diameter is typically induced by higher penetration resistance. However, penetration resistance was low at the given water content in both substrates. Further experiments are required to elucidate whether observed differences can be explained by mechanical properties beyond mechanical impedance, root or microbiome ethylene production or differences in diffusion processes within the root or in the rhizosphere. A more systematic literature review including studies comparing textures at different levels of nutrient supply is needed. Results from field studies comparing different substrates under the same environmental conditions can also help to unravel the mechanisms involved.

6 Correlative Imaging of the Rhizosphere - A Multimethod Workflow for Targeted Mapping of Chemical Gradients

6.1 Abstract

Examining *in-situ* processes in the soil rhizosphere requires spatial information on physical and chemical properties under undisturbed conditions. We developed a correlative imaging workflow for targeted sampling of roots in their 3D context and assessing the imprint of roots on chemical properties of the root-soil contact zone at µm to mm scale. Maize (*Zea mays*) was grown in ^{15}N-labelled soil columns and pulse-labelled with $^{13}CO_2$ to visualize the spatial distribution of carbon inputs and nitrogen uptake together with the redistribution of other elements. Soil columns were scanned by X-ray computed tomography (X-ray CT) at low resolution (45 µm) to enable image-guided subsampling of specific root segments. Resin embedded subsamples were then analysed by X-ray CT at high resolution (10 µm) for their 3D structure and chemical gradients around roots using micro X-ray fluorescence spectroscopy (µXRF), nanoscale secondary ion mass spectrometry (NanoSIMS), and laser-ablation isotope ratio mass spectrometry (LA-IRMS). Concentration gradients, particularly of calcium and sulphur, with different spatial extents could be identified by µXRF. NanoSIMS and LA-IRMS detected the release of ^{13}C into soil up to a distance of 100 µm from the root surface, whereas ^{15}N accumulated preferentially in the root cells. We conclude that combining targeted sampling of the soil-root system and correlative microscopy opens new avenues for unravelling rhizosphere processes *in situ*.

6.2 Synopsis

Chemical mapping of the rhizosphere in three dimensions remains a methodological challenge. Our novel imaging workflow allows for targeted root sampling and chemical analysis, successfully studying rhizosphere processes *in situ*.

Lippold, E., Schlüter, S., Mueller, C.W., Höschen, C., Harrington, G., Kilian, R., Gocke, M.i., Lehndorff, E., Mikutta, R., Vetterlein, D. (2023): Correlative imaging of the rhizosphere ― A multimethod workflow for targeted mapping of chemical gradients, Environ. Sci. Technol. 57 (3), 1538 – 1549, DOI: 10.1021/acs.est.2c07340

6.3 Introduction

Roots as an essential part of plants perform essential functions such as anchoring the plant to the soil [191] and absorbing water [192] and nutrients [193]. The zone of soil affected by roots can be defined as the rhizosphere [3]. Most of our knowledge on rhizosphere properties is based on operationally defined ways of sampling the rhizosphere, such as brushing, shaking, or washing off soil adhering to the roots after extracting them from bulk soil. These approaches do not refer to a certain distance from the root surface, although nutrient gradients are reported to extend over less than one mm up to several cm [8–11]. Furthermore, destructive rhizosphere samples can be contaminated with root cells i.e. root hairs being also brushed off [194]. Current knowledge with respect to chemical gradients in rhizosphere soil has primarily been based on systems not considering the radial geometry of transport to and from roots such as rhizobox or split-compartment experiments. Not accounting for this geometry in planar experimental setups leads to an amplification of the extent and magnitude of gradients [5,12]. In addition, chemical gradients change with time of interaction [13] and depend on root type and age [14,15] as well as soil texture and mineral composition. Therefore, both factors (soil and roots properties) are supposed to be a crucial parameter for the extent of physical and chemical gradients [16]. Soil properties can be quantified *ex situ* whilst root age and root type can hardly be assessed by conventional methods in pot experiments due to opaque soil. Both properties are accessible by repeated non-invasive imaging [47,195] which can be combined with subsequent 2D-chemical imaging to acquire information in 3D context. Currently, most chemical and biological microscopy techniques in intact soil can only be performed on exposed soil surfaces within two-dimensional soil surfaces. This introduces severe biases since spatial information outside of the imaging plane is unavailable [18], including all roots that are out of plane. For this reason, there is a need for methods that combine 3D structural information with 2D biochemical information to integrate this spatial context. This so-called image registration or co-registration has been demonstrated for combinations of 3D X-ray computed tomography (X-ray CT) with several different techniques such as scanning electron microscopy (SEM) coupled with energy-dispersive X-ray spectroscopy to reveal elemental maps [19,20], fluorescence microscopy to assess bacterial distributions [18,21], zymography to unravel enzyme release patterns [22] or light and near infrared spectroscopy to account for the spatial distribution of organic matter [23]. All these microscopy techniques have in common that spatial resolution and mapped areas roughly match the spatial resolution and cross-sectional areas captured with X-ray CT. With other techniques a dimensional or scale discrepancy must first be overcome before the biochemical information can be registered into the 3D spatial context. This can occur because the method provides only point or line information, e.g. laser ablation isotope ratio mass spectroscopy (LA-IRMS) [196] and laser ablation inductively coupled plasma mass spectrometry [197]. It can also happen that 2D information is only available with a tiny field of view as is the case for electron microscopy with electron energy loss spectroscopy [198] or nanoscale secondary ion mass spectrometry (NanoSIMS) [199,200]. In these cases, a two-step registration approach with another microscopy technique that bridges both scales is beneficial [18,201]. A successful 2D-3D image registration routine inherently demands the structural integrity of a given sample during preparation and each subsequent analysis step. The mentioned spectromicroscopic techniques often have common prerequisites for sample preparation as samples need to be dehydrated and vacuum stable [202]. Likewise complex samples as for instance intact soil cores are oftentimes embedded and sectioned in a resin or agar matrix to preserve the structural integrity but the structural integrity before and after embedding is rarely checked [23]. Moreover, the unintentional modification of chemical gradients by colloid redistribution or solute leaching during sample preparation remains unclear [202].

The aim of the current study was to capture radial chemical gradients in the rhizosphere of well-characterized 3D root segments as a result of interacting processes at the interface between roots, microorganisms, and the soil matrix. To do so, we established a procedure for correlative image analysis of resin-embedded rhizosphere soil containing roots types of a specific age. This protocol was tested on a maize column experiment involving ^{13}C- and ^{15}N-isotope labelling to trace the release of plant-derived C into the soil and plant uptake of inorganic N within the rhizosphere. For the first time we used targeted sampling of specific root segments instead of sample extraction at pre-defined positions [101] in order to reveal the formation of chemical gradients upon root growth in a 3D context. X-ray CT was combined with a range of techniques (µXRF, NanoSIMS, LA-IRMS) probing different chemical features of the rhizosphere (Table 1). Several methodological improvements were combined to advance the information content and accuracy of correlative imaging. First, the spatial context of individual root segments within the root system, i.e. root type, root order, root age, and time of interaction with the soil, was revealed by repeated whole-column X-ray CT scans prior to subsample extraction. Second, the sequence of 2D imaging techniques, each providing complementary chemical information, were assigned such that co-registration is possible and adverse effects by sample preparation are minimal. Third, the obtained 2D radial gradients are registered with 3D root distance information retrieved from X-ray CT scans of subsamples to include knowledge about roots outside of the imaging plane.

Table 6.1: Sequence, required sample preparation steps and purpose of X-ray CT, light microscopy, µXRF, SEM, NanoSIMS, and LA-IRMS fulfilled within the correlative imaging workflow

technique	sample preparation	purpose
X-ray CT	targeted sampling	track changes after resin impregnation, determine root distances
light microscopy	targeted sampling, chemical fixation, dehydration, resin impregnation, thin sectioning	reference image for orientation and image registration of all image data
µXRF	targeted sampling, chemical fixation, dehydration, resin impregnation, thin sectioning	elemental mapping of nutrients, pore detection with Cl channel, particle detection with Si channel
SEM	targeted sampling, chemical fixation, dehydration, resin impregnation,thin sectioning, sputter coating with Au/Pd layer	reference image for orientation and image registration of NanoSIMS
NanoSIMS	targeted sampling, chemical fixation, dehydration, resin impregnation, thin sectioning, sputter coating with Au/Pd layer	isotope mapping of $^{16}O^-$, $^{12}C^{12}C^-$, $^{12}C^{13}C^-$ $^{12}C^{14}N^-$, $^{12}C^{15}N^-$, $^{27}Al^{16}O^-$, qualitative interpretation of LA-IRMS transects
LA-IRMS	targeted sampling, chemical fixation, dehydration, resin impregnation, thin sectioning	quantitative $\delta^{13}C$ transects

6.4 Materials and Methods

6.4.1 Growth system, X-ray CT scanning, localisation of subsamples, and sample extraction

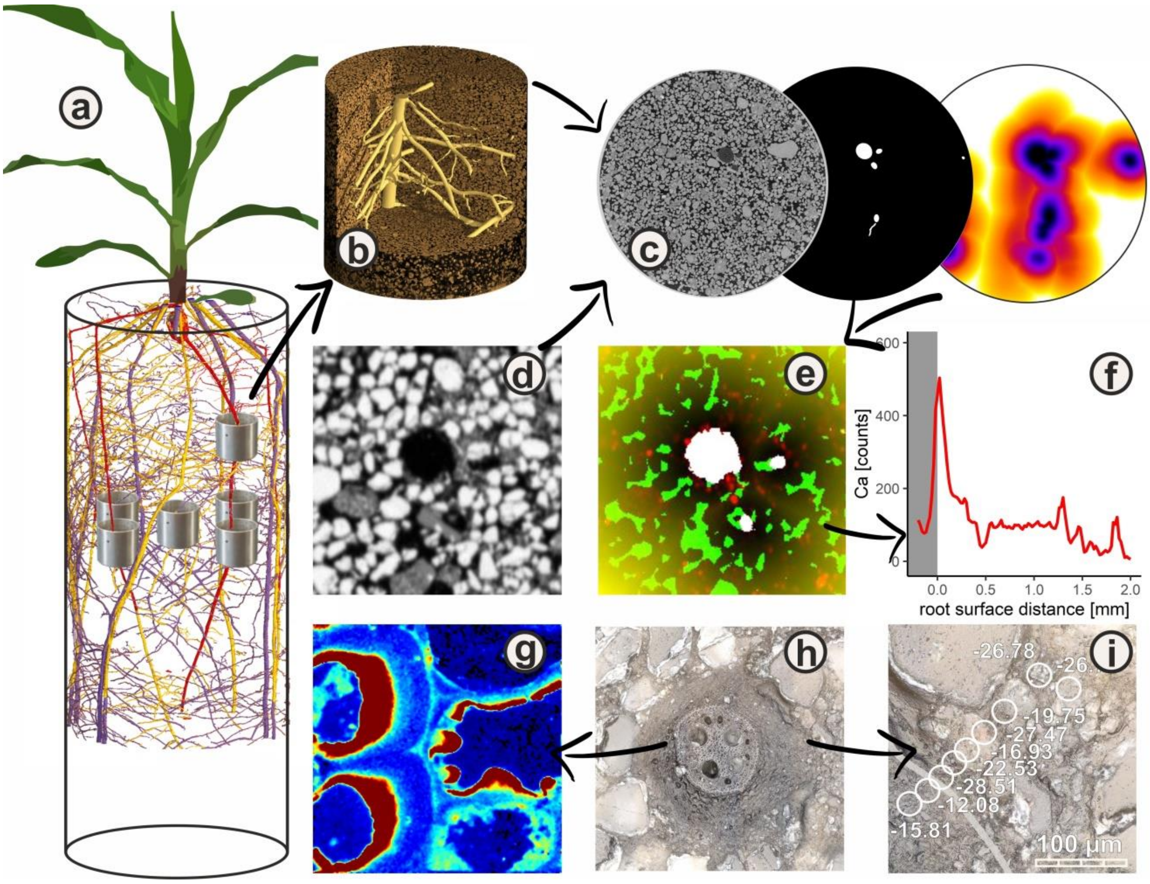

Figure 6.1: Workflow for imaging of radial 2D chemical rhizosphere gradients in a 3D structural context, all images show the same sample with sandy substrate: a) segmented root system, red: at least 14-day old roots, yellow: up to 14-day old roots, purple: up to 7-day old roots; cylinders in upper row show targeted position of a sample around the primary root; cylinders in the middle show untargeted sampling approach; b) targeted sample of primary root showing segmented root system; c) Image analysis of 2D imaging slice including raw image, root segmentation and root distance; d) µXRF Si channel which is registered into 3D context; e) image stack of µXRF images showing Ca channel (red) and Cl channel (green, representing resin filled pores excluded from following image analysis), root mask (white), Euclidean distances to the root surface (yellow); f) Ca counts as a function of root distance; g) NanoSIMS image of root tissue (focusing on the endodermis with casparian band) showing ^{13}C ratio ($^{12}C^{13}C$-:$^{12}C^{2-}$), natural abundance (blue) up to high enriched areas (red); h) brightfield microscope image of primary root, and i) LA-IRMS transect registered onto brightfield image, circles indicate ablation spots, numbers refer to δ ^{13}C at ablated spots.

Samples were taken from a soil column planting experiment described elsewhere [47]. Briefly, acrylic glass tubes (250 mm height, 70 mm inner diameter) were filled with a sandy substrate which consists of a mix of 83.3% quartz sand

(WF 33, Quarzwerke Weferlingen, Germany) and 16.7% of sieved loam obtained from the upper 50 cm of a haplic Phaeozem soil profile [3]. Fertilisation with a combination of unlabelled and isotope-labelled fertiliser was done prior to filling the columns. To trace the fate of inorganic N, ^{15}N was applied as $NH_4{}^{15}NO_3$ (98 atom%, Euriso-Top GmbH, Germany) at a dose of 50 mg N kg^{-1} together with the basal fertilisation of all other essential nutrients. Growth of *Zea mays* took place over a time period of 21 days under controlled conditions in a climate chamber, which was set to 22°C during the day and 18°C at night with a 12 h light period, 350 µM m^{-2} s^{-1} photosynthetically active radiation, and a relative humidity of 65%. At day 21, plants were pulse labelled in ^{13}C-enriched atmosphere to trace the fate of assimilated C. Gas tight chambers covering eight plants were set up and $^{13}CO_2$ ($Na_2{}^{13}CO_3$, 99 atom%, Euriso-Top, Germany) was released by adding sulfuric acid to the initial solution of sodium carbonate and 200 ml water following a protocol adapted from Heinrich et al. [203]. The second $^{13}CO_2$ pulse was performed 2 hours after the first pulse without opening the chambers in between. Each pulse added 2030 ppmv CO_2 to the atmosphere; chambers were removed after the full light period of 12 h.

In order to follow root development, X-ray CT scanning was performed at day 7, 14, and 21 after planting during the night to not interfere with plant photosynthesis in the same way as described by Lippold et al. [47]. A lead shield was also placed between X-ray source and the soil column to shield the plant shoot and the soil outside the field of view. With this setup, the dose per scan in the centre of the column amounts to 1.2 Gy [48]. The obtained whole-column images with a resolution of 45 µm [47] were used during sampling to allow for a targeted sampling of specific root types and root ages (Figure 6.1a). In this study, a sample was selected that featured a primary root which was at least 14 days old and which included several laterals of the same age.

Aluminium rings with a wall thickness of 0.25 mm and 16 mm inner diameter and height were used for sampling, further on referred to as 'subsamples' (Figure 6.2c). The subsample dimensions have been chosen according to the following criteria: (i) sufficient resolution with X-ray CT (10 µm), (ii) optimum resin infiltration, minimum wall thickness to avoid compaction of the sample during insertion and, at the same time, (iii) sufficient stiffness to avoid wall deformation by touching and transport, and (iv) covering a size adjusted to usual sample holders during 2D imaging. A small hole (1 mm diameter) was drilled into the aluminium cylinder before sampling which always pointed into the same direction in all the following steps. The hole is visible in X-ray CT scans and provides orientation during subsequent sample analyses.

Sampling was done with a custom-made sampling device (UGT GmbH, Germany) potentially allowing for extraction of up to five subsamples from one layer of the soil column (Figure 6.2a). The aluminium rings were pushed into soil by moving the specimen mount down or pushing the rings into the soil surface by hand. The entire soil column was then pushed 20 mm upwards with a piston from below (Figure 6.2a). This kept the internal structure of the subsample intact, as soil compaction through mechanical stress by the piston was only exerted on the opposite site of the soil core and fractures along the cylinder wall were generally small. Aluminium rings can be mounted such that they are pushed into the soil at predefined locations with equidistant spacing (Figure 6.2b). Sampling a predefined position (Figure 6.2b) allows for capturing the spatial heterogeneity in root and soil properties in a systematic way [101]. However, it requires a rather large number of samples for subsequent chemical fixation and X-ray CT, as every sample has to be checked for roots and their position within the sample. Alternatively, the rings can be placed freely such that the sampling point on the surface of the soil column can be selected for targeted sampling of individual root segments which were previously identified by whole-column X-ray CT scans (Figure 6.2e). This targeted sampling reduces sample numbers, the time between sampling and embedding, and therefore improves the quality of each individual sample.

After removing the subsamples by hand with a razor blade, small cavities were filled up with pure quartz sand to prevent any dislocation of small particles during fixation, CT scanning, and resin impregnation. Then, top and bottom of the subsamples were closed with 30-µm nylon mesh and cable tie (Figure 6.2c).

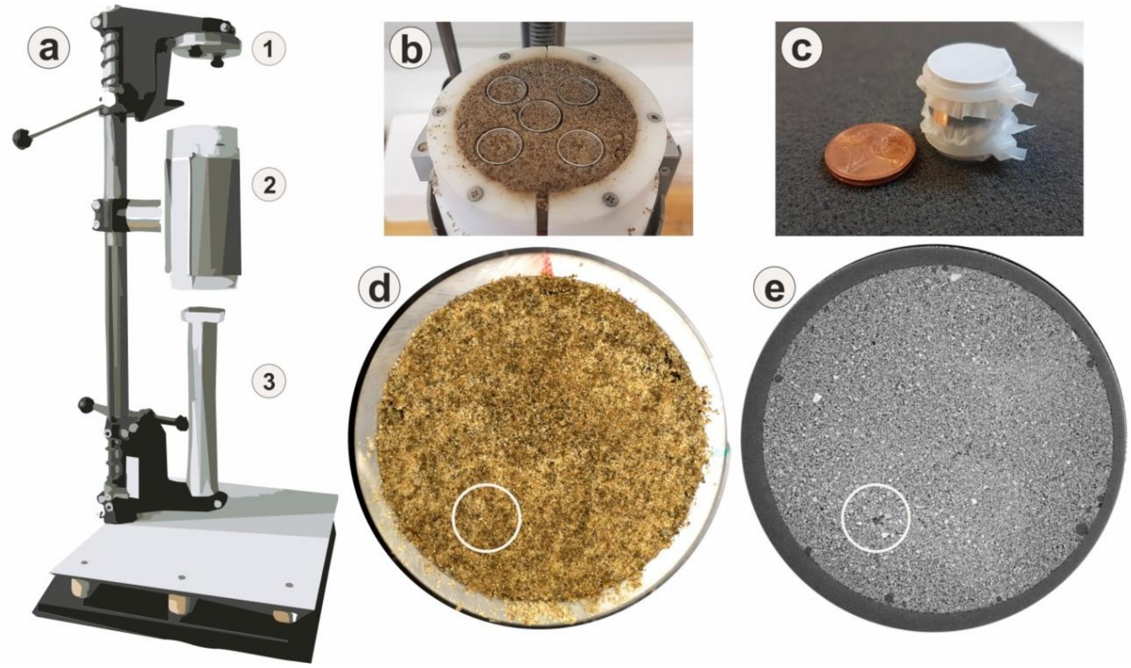

Figure 6.2: a) Device for extraction of subsamples with 1) specimen mount for non-targeted sampling of subsamples from soil columns, 2) specimen mount for soil column, and 3) moveable punch to push the soil out of the column; b) non-targeted soil sampling; c) sample with mesh and cable tie; d) top-view on the soil surface of the whole soil column with selection for targeted sampling in the sandy substrate; e) X-ray CT image of the same soil slice as shown in (d) with selection for targeted sampling showing the primary root.

6.4.2 Chemical fixation and embedding

To stop metabolic processes in the roots and soil microorganisms as well as to sustain biological cell integrity, subsamples were chemically fixated using Karnovsky fixative [204]. The fixative was applied through capillary rise by placing the sample in five drops of fixative from below and three onto the top of the sample. This approach guaranteed sufficient fixation and at the same time caused less structural damage, bubble formation, and particle relocation than full immersion into the fixative at ambient pressure or even under mild vacuum (Figure 6.3) [205,206]. The redistribution of particles or soluble compounds by liquid movement during fixation is discussed below. Fixated samples were stored at 4°C until X-ray CT analysis with a resolution of 10 µm as described by Phalempin et al. [101] to have a 3D image with optimal contrast of the root and the surrounding soil matrix for correlative imaging.

After a maximum storage time of 7 days between sampling and X-ray CT analysis at 7°C in the dark, samples were dehydrated in graded acetone according to the adapted method of Herrmann et al. [206]. This approach was chosen as alternative to freeze-drying. In samples with these dimensions, moisture from inside did not escape fast enough during drying and therefore caused structural damage upon freezing. Likewise, air drying leads to a loss of root-soil contact caused by shrinkage of roots and/or soil (images not shown). However, root-soil contact ought to be maintained for a correct determination of the extent of chemical gradients within the rhizosphere. Dehydration with a series of acetone additions, however, bears the risk of washing out easily soluble compounds, which might also occur to some degree during subsequent resin embedding as discussed below. The dehydrated samples were embedded in Araldite 502 as described by Mueller et al. [205] and cured at 60°C for 48 h until complete polymerization. A vacuum (~200 mbar below atmospheric pressure, varying between samples was applied during the embedding procedure to enhance capillary saturation and at the same time reduce dislocation of particles, as repacked, unconsolidated soils have very low structural stability (Figure 6.3). To keep track of any particle displacement all samples were scanned again with X-ray CT, using the same scanner settings as before the embedding. Note that in X-ray CT scans of embedded samples roots are barely visible anymore as the electron density of resin and organic material are very similar. Their position can be determined by their relative position to the soil matrix known from previous scans (Figure 6.3).

It was also possible to use epifluorescence microscopy to identify the roots in some cases (images not shown) [207].

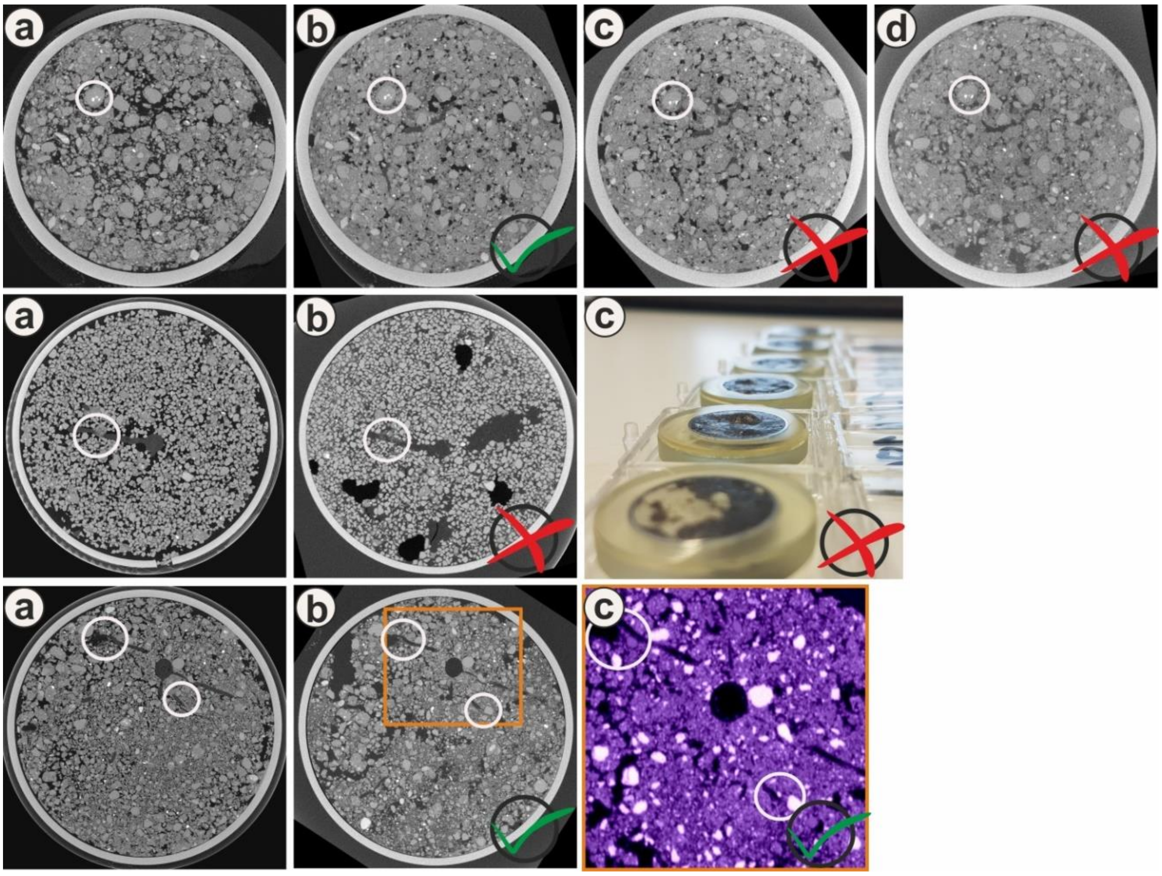

Figure 6.3: Examples of best practise and failures during sample fixation, embedding, slicing, and polishing. White circles show landmarks for orientation within X-ray CT images unless otherwise stated. Upper row: a) undisturbed soil structure; b) soil after partial saturation through capillary rise after partial immersion into fixative; c) soil after almost full immersion into fixative (only top 1 mm reaches out of fixative); d) soil exposed to strong vacuum under boiling of fixative at 30 mbar for 5 min. Middle row: a) undisturbed soil sample with primary root and lateral root in sand; b) same soil after resin impregnation; c) photo of visible deformation because of outgassing during hardening and too strong vacuum during resin impregnation. Last row: a) undisturbed soil sample with primary root and lateral root; b) same soil sample after resin impregnation with almost no relocation of particles; c) co-registered µXRF image of the Si channel.

6.4.3 Thin section preparation for chemical imaging

There were several criteria for selecting the cutting plane of the embedded soil cores. Despite the careful treatment of the subsamples, small air entrapments were still present in the embedded samples causing small areas of displaced particles. Such areas were identified by X-ray CT and disregarded for correlative microscopy. In addition, some of the big roots showed some shrinkage in their cortex cells due to desiccation between sampling and embedding. This shrinkage could have been reduced by applying more fixative. However, this would have posed the risk that chemical gradients would have been deteriorated even stronger. Based on those observations and the comparison of X-ray CT images before and after embedding, subsamples with minimal disturbances and a good root to soil contact were cut at a targeted plane using an automatic precision saw with a diamond blade (Minitom, Struers, Germany). The criteria for selecting a target plane were to cut roots perpendicularly and select for roots with a sufficient wall distance surrounded by intact soil.

The cut and resin-embedded subsample was cured again for 24 hours at 65°C after gently removing the remaining aluminium cylinder. This drying step is very important to remove water being pressed into the sample during cutting. Otherwise, the sample would lose vacuum stability during subsequent imaging. Removing the aluminium cylinder avoids artefacts during elemental mapping and dents and scratches on the sample surface during polishing. During the whole procedure the orientation of the original sample was kept to ensure the subsequent registration of the different imaging approaches. After drying, the soil section was glued with a two-component epoxy resin onto a glass disc of 25.4 mm diameter and cured again for 24 h at 65°C. Soil sections were thinned and subsequently polished manually using a manual grinding and polishing machine (EcoMet30, Buehler, Germany) with diamond sanding plates with increasing fineness (MD-Piano 80, 500, 1200, 2000, and 4000; Struers, Germany). The sample surface was checked repeatedly under a microscope to ensure whether the targeted cross section identified with X-ray CT was already reached. This way it was possible to reach the targeted cross section with very high precision of ± 30 µm. There is a rather narrow range of optimal soil section thickness for correlative imaging. A sufficient thickness of the sample was especially required for µXRF analysis to ensure to not underestimate the photon counts of heavier elements with greater excitation depth, as the maxima of excitation may exceed the sample thickness. The final section thickness should thus not be thinner than 25 µm. For high-quality µXRF imaging it was also vital to obtain samples being perfectly parallel over the full range of the thin section. Sections thicker than 100 µm also compromise imaging techniques like electron microscopy and NanoSIMS due to more intense outgassing under vacuum conditions. After the last step of polishing, samples were cleaned in an ultrasonic bath in demineralised water for 30 s and then dried again at 65°C for 24 h. A brightfield reflected light microscopy image (AxioImager Z2, Carl Zeiss, Germany) of the whole soil section was then acquired, being later used as reference image for the registration of images derived from the various chemical mapping techniques.

6.4.4 Sequence of imaging

An appropriate sequence of imaging techniques has to fulfil at least two criteria: First, the workflow should begin with larger scale and higher-dimensional imaging modality to identify the rhizosphere and interesting transects or sites. Second, interference of one imaging technique with another, e.g. by sputtering or material ablation via laser shots should be minimized [202]. Based on the prerequisites of individual imaging techniques (Table 6.1) in the current study this resulted in the following sequence: X-ray CT, light microscopy, µXRF, SEM, NanoSIMS, and LA-IRMS (Figure 6.1). The thinner the soil section, the more reflection from the sample holder was visible in the epifluorescence images (images not shown). This impaired visual root detection, which was prerequisite for further measurements and the subsequent image analysis steps. Alternatively, the position of roots and regions of interest for correlative chemical imaging were identified in this study by jointly screening the two X-ray CT images of the samples (before and after embedding) and the following µXRF images, whenever roots were not directly visible.

6.4.5 Micro X-ray fluorescence spectroscopy

Elemental mapping was carried out with µXRF (Micro-XRF Spectrometer M4 TORNADO, Bruker). From a suite of elements that could potentially be analysed only results for calcium (Ca), phosphorus (P), and sulphur are interpreted here, but other elements like chlorine (Cl) and silicon (Si) provide valuable auxiliary information for correlative microscopy. The size of the 2D region of interest was chosen such that the root was in the centre and surrounded by 2.5-4 mm of soil to cover the anticipated gradients based on literature [11,22,208]. Whenever exact root interfaces could not be identified clearly with X-ray CT or light microscopy, a map with a short scan time of the whole sample was done and the combined image of Si and Ca as well as sulphur was used to identify soil particles and roots, respectively. The settings for µXRF were chosen as follows: Ag anode at 50 kV with 599 µA and 20 µm spot size, stage speed of 667 µm s^{-1} equivalent to an acquisition time of 30 ms $pixel^{-1}$. To reduce sample damage by excessive X-ray exposure, an area of interest was mapped ten times at low acquisition times at higher stage speeds and these ten frames were accumulated to improve count statistics. Depending on the size of the region of interest and the minimum stage speed, one scan took 4 to 6 hours.

6.4.6 Nanoscale secondary ion mass spectrometry

To study the polished thin sections a scanning electron microscope (SEM; Jeol JSM 5900LV, Tokyo, Japan) equipped with a back-scattered electron detector (LVBED-C) was used at 10 keV. Based on the SEM image, a transect from the root into the surrounding soil was mapped using nanoscale secondary ion mass spectrometry (NanoSIMS). The NanoSIMS images were recorded with a Cameca NanoSIMS 50L (Gennevilliers, France). Prior to the NanoSIMS measurements, an Au/Pd layer (~30 nm) was sputter coated to avoid charging during the measurements. Additionally, the electron flood gun was used to compensate for any charging effects due to the nonconductive mineral particles (e.g., larger quartz grains). The Cs^+ primary ion beam was used with a primary ion impact energy of 16 keV. Prior to final analysis, contaminants and the Au/Pd coating layer were sputtered away at 50 × 50 µm using a high primary beam current of 270 pA for 5 min (pre-sputtering). During this pre-sputtering, the reactive Cs^+ ions were implanted into the sample to enhance the secondary ion yields until steady state for the secondary ions is reached. The primary beam (ca. 2 pA) was focused at a lateral resolution of about 150 nm and was scanned over the sample, with $^{16}O^-$, $^{12}C^{12}C^-$, $^{12}C^{13}C^-$ $^{12}C^{14}N^-$, $^{12}C^{15}N^-$, $^{27}Al^{16}O^-$, and $^{56}Fe^{16}O^-$ secondary ions collected on electron multipliers with an electronic dead time fixed at 44 ns. The mass resolution was set to accurately detect the secondary ions affected by mass interferences with their isobars. All measurements were done in imaging mode with a field of view of 30 × 30 µm, 40 planes were acquired using a dwell time of 1 ms/pixel, with 256 × 256 pixels. Images were corrected for electron multiplier dead time and the measurements stacks were accumulated using the openMIMS plugin in ImageJ [209]. The combination of all seven channels into one image stack and further calculations such as image ratios and Hue-Saturation-Intensity maps of any combination of isotopes were done in Fiji/ImageJ [146].

6.4.7 Laser-ablation isotope ratio mass spectrometry

Laser-ablation isotope ratio mass spectrometry was performed for probing $\delta^{13}C$ transects using a custom-made system equipped with a cold Nd:YAG laser (LSX-213G2+, Teledyne-CETAC, Omaha, NE, USA) attached to a combustion system, GC-column, ConFlo, and a Delta V isotope ratio mass spectrometer as detection system [196]. Two transects across the primary root were measured over a distance of 200 µm extending away from the root surface as well as from the root surface into the centre of the root. Each laser ablation site was set to 30 µm in diameter corresponding to one single NanoSIMS image to compare and cross validate both methods (Figure 6.4b). The $\delta^{13}C$ of the ablated material was corrected daily for the $\delta^{13}C$ of the CO_2 background and an acryl standard was used as reference material [196].

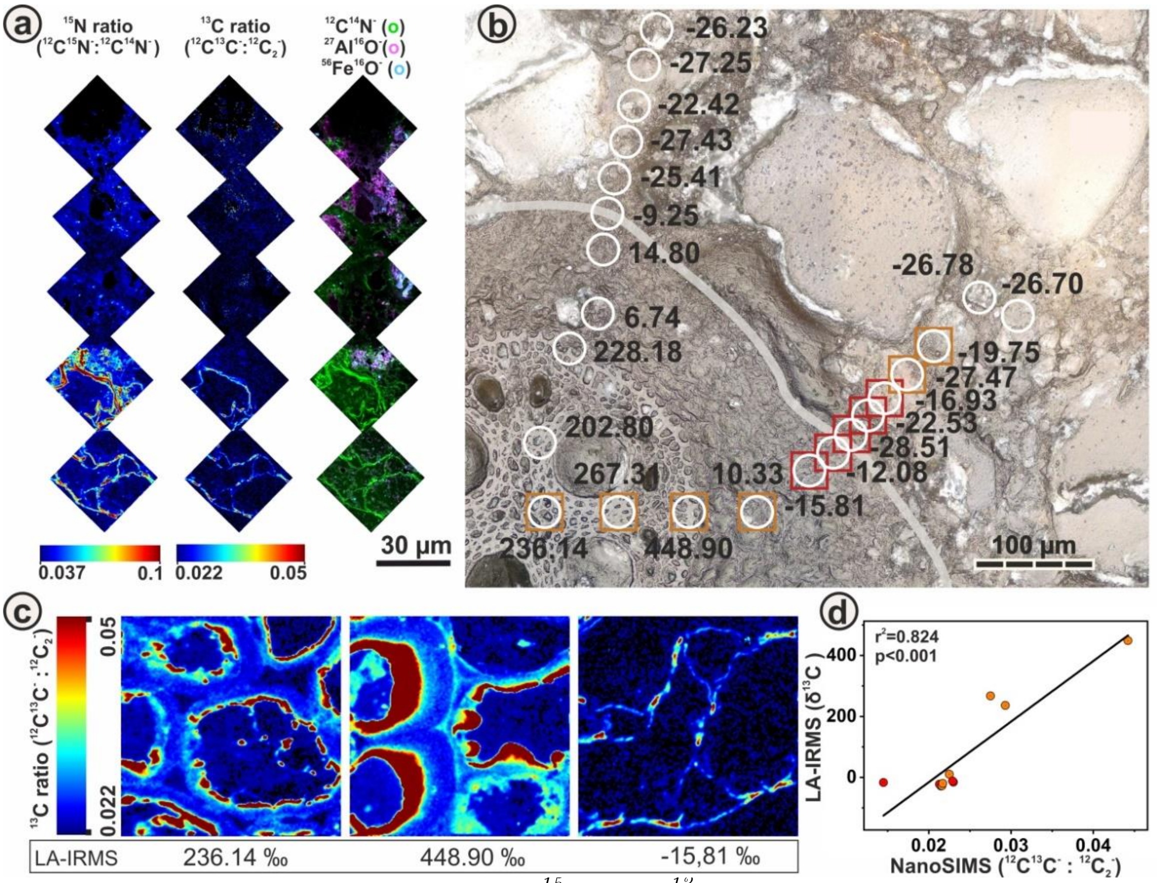

Figure 6.4: a) NanoSIMS results of ^{15}N *and* ^{13}C *isotopic ratios of the transect marked by red rectangles in (b) and composite images of* $^{12}C^{14}N^{-}$ *(green),* $^{27}Al^{16}O^{-}$ *(magenta), and* $^{65}Fe^{16}O^{-}$ *(cyan) secondary ions showing root tissue of primary root (bottom), rhizosphere, and mineral matrix of sandy substrate (top); b) light microscopy image with the root-soil interface indicated by the white line. White circles show LA-IRMS spots registered on brightfield microscopy image with corresponding* $\delta^{13}C$ *values and red and orange rectangles indicate the NanoSIMS spots, red rectangles show the position of the NanoSIMS transect presented in (a); c) NanoSIMS images of root tissue and corresponding values of LA-IRMS measurements done at the same location show that* ^{13}C *enrichment barely varied because of locally different* ^{13}C *enrichment in cell walls, but because of randomly varying cell wall area fractions covered in each LA-IRMS spot; d) correspondence between average* ^{13}C *enrichment in a NanoSIMS map (arithmetic mean of all 256 x 256 pixels) and the* ^{13}C *enrichment in a co-localized LA-IRMS spot (*$r^2=0.82$*,* $p<0.001$*), red circles depict red rectangles in (b), the same accounts for orange circles.*

6.4.8 Image registration

To merge information from various imaging techniques a registration of all images onto each other is necessary. Image registration of all 2D imaging techniques was carried out with the ImageJ plug-in Correlia [201]. As NanoSIMS provides spatial information of a very small field of view, all NanoSIMS images were first registered onto SEM images (images not shown) based on electron backscattering as described above. This approach provides very good contrast between mineral particles, organic soil constituents, and embedding resin, thus capturing the overall soil pore structure well. Thus, the largest SEM image was used to register all NanoSIMS onto the reflected light microscopy image (Figure 6.4b). The LA-IRMS measurements were automatically combined with a camera image acquired during the ablation process. This auxiliary image was used to align LA-IRMS with the light microscopy images and thereby also with SEM and NanoSIMS maps. This bridging via the light microscopy reference image was essential because a direct registration of NanoSIMS maps and LA-IRMS spots would have been impossible. Dark patches visible in the auxiliary light microscopy image before LA-IRMS (image not shown) were caused by prior NanoSIMS imaging, which slightly changed the material contrast. This effect was harnessed to locate target spots for LA-IRMS measurements. All elemental maps retrieved with µXRF were registered with the light microscopy image by means of the Si channel with very good contrast between mineral particles and air-filled pores. Likewise, X-ray CT images were registered into the µXRF Si channel by aligning the pore structure (Fig 6.1d, c). For registration of the 3D X-ray CT image into a 2D reference image we used the elastix software [210]. Image registration with different dimensionality is not implemented in elastix but the 2D image can be converted into a 3D image with a thickness of one slice beforehand. The exact co-registration of the 2D microscopy plane with the 3D CT image can be substituted by simply selecting the best matching horizontal slice, when the microscopy plane was not tilted by more than three times the voxel resolution during gluing, cutting, and polishing.

6.4.9 Image analysis

A prerequisite for quantitative image analysis is image segmentation of grayscale data into material classes. Root segmentation of the whole-column and subsample X-ray CT scans was carried out with a modified version of the root segmentation algorithm “Rootine v.2” [101]. Elastix was also used to register root images after 7, 14 and 21 days with each other in order to generate composite images of root age (Figure 6.1a). Resin and root segmentation in X-ray CT or µXRF data was carried out with the default thresholding method in ImageJ. By using the µXRF image of the chlorine channel, pores filled with resin were segmented as the resin contains traces of chlorine. Roots and resin-filled pore space were separated using supervised segmentation in ImageJ. Root distances in soil were retrieved with the Euclidean distance transform of binary root images in ImageJ. This was either done directly in the 2D microscopy image or in 3D CT images, and the resulting 3D distance maps were subsequently registered into the microscopy plane, thus accounting for potentially shorter distances to roots outside of the microscopy plane (Figure 6.5c). Finally, average element counts of various µXRF element maps in none-pore pixels (retrieved from segmented µXRF chlorine maps (Figure 6.1e) were calculated as a function of root distance (retrieved from registered 3D distance maps) with ImageJ (Figure 6.6). R version

3.53 (Team 2013) and the libraries readxl, stringr, and ggplot were used to create Figure 6.1f and Figure 6.6b. All figures are compiled with CorelDraw 2018 (Corel Corporation).

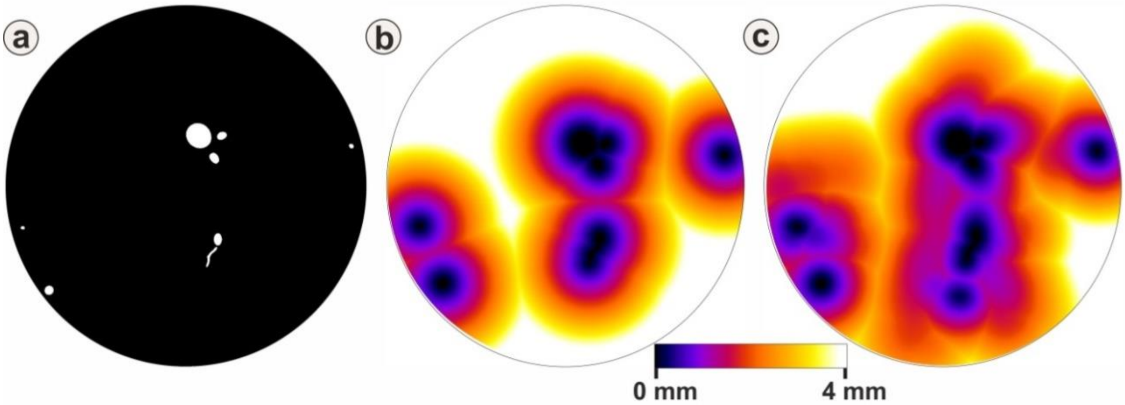

Figure 6.5: a) Slice of segmented co-registered root system; b) Euclidean distance map (EDT) done on 2D image ignoring hidden roots outside of microscopy plane; c) EDT calculated on 3D image so that roots outside the microscopy plane are accounted for.

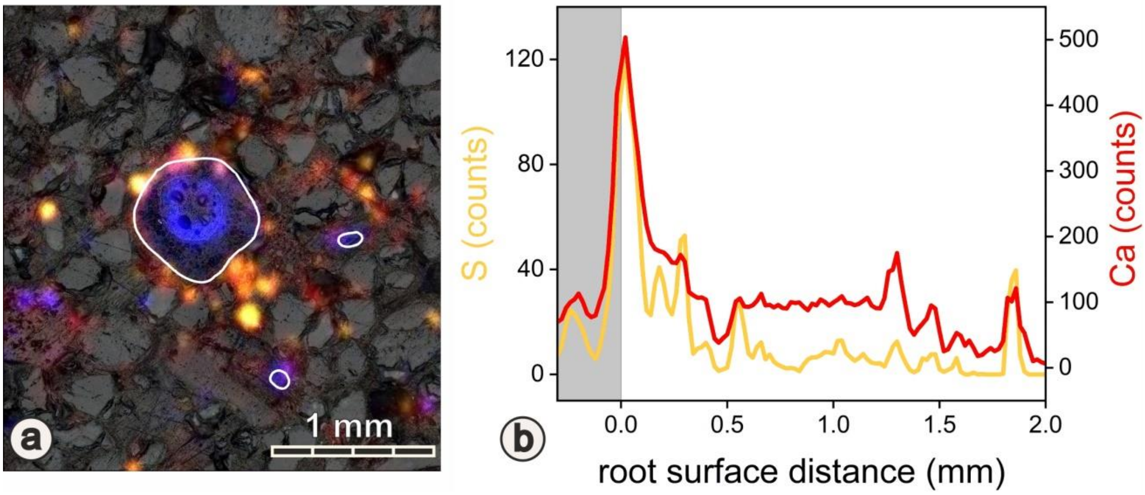

Figure 6.6 a) Light microscopy image with co-registered µXRF image of phosphor (blue), sulphur (yellow), and calcium (red). White lines in µXRF image represent the root-soil interface of primary root and laterals of the primary root. Note, the bright blue circle indicating high phosphorus concentrations is spatially associated with the endodermis and not with the root-soil interface; b) Calcium (Ca) and sulphur (S) counts with increasing distance from the root surface are shown as well as Ca counts from the root surface into the centre of the root (grey).

6.5 Results and Discussion

6.5.1 Imaging of 2D radial gradients

The outlined correlative imaging approach was applied to planted soil columns repeatedly scanned by X-ray CT, which informed on the root development with weekly resolution and enabled targeted subsampling directly after harvest of the three weeks old plant (Figure 6.1a). The subsample for which correlative microscopy was demonstrated was centered on a primary root being at least 14 days old and including laterals of the same age (Figure 6.1b). The prolonged root-soil interaction around the investigated primary root resulted in a Ca accumulation gradient in the rhizosphere with a spatial extent of ~200 µm that was detected by µXRF (Figure 6.1f, Figure 6.6). A gradient of the same spatial extent was detected for S. Even though the speciation cannot be analysed with µXRF, the matching gradients suggest the precipitation of gypsum ($CaSO_4 \cdot 2H_2O$) around the primary root. A possible reason could be supply of Ca and sulphur by the soil was greater than the uptake by the roots with the consequence that mass flow was the primary mechanism for the supply of Ca and sulphur to the root surface, which would be consistent with experimental observations by Oliveira et al. [211]. As reported by Ahmed et al. [212] water uptake of *Zea mays* L. depends on root type. Therefore a different range of gradients can presumably be observed for younger roots and other root types. Precipitation of gypsum in the rhizosphere has also been reported for substrates with high concentrations of Ca and SO_4 in the soil solution [193]. Likewise Hinsinger et al. [10] observed an enrichment of water-extractable Ca in direct vicinity of roots when Ca-containing rock phosphate was added to alumina sand planted with clover or ryegrass. Using synchroton-based X-ray absorption near edge structure spectroscopy, Veelen et al. [213] found an increase of Fe oxides, such as FeO and Fe_2O_3 as well as a three-fold increase of inorganic sulfate (SO_4^{2-}) in the direct proximity of the root. With µXRF we could potentially detect all elements heavier than sodium, including the macronutrient phosphorus (P). Unlike for Ca and sulphur, there was no gradient formation visible for P when analysed by µXRF, despite of significant P uptake into maize plants [47]. This can be explained by matrix effects causing high background noise level [214] and small X-ray yield, thus leading to low P sensitivity. Nevertheless, some patches of larger P accumulation, potentially related to abundant P-bearing minerals or remnants of the fertiliser, could be observed (images not shown).

For the investigated rhizosphere transect we found by LA-IRMS that ^{13}C enrichment occurred even at distant soil locations up to 100 µm away from the direct root-soil interface (Figure 6.4b). This finding accords with recent observations of rhizosphere distances >100 µm that have been detected with LA-IRMS in resin embedded topsoil samples from a Miscanthus field [196]. The NanoSIMS maps (Figure 6.4) revealed that these deviations from the baseline $\delta^{13}C$ values of the bulk soil in LA-IRMS spots are caused by small areas of high enrichment that only comprise a small fraction of the laser spot, possibly reflecting ^{13}C bound to specific mineral surfaces or contained in soil microorganisms like bacteria (Figure 6.4a). Mycorrhiza are also known to transport ^{13}C to distant soil locations [199,215] but plants in our experiment showed only minor signs of mycorrhizal colonization [47]. Because of the patchy appearance of ^{13}C enrichment up to the penultimate spot of the transect, we conclude an even longer transect would have been necessary to completely capture the enrichment zone around the primary root. This would be in line with the predictions of a modeling approach by Landl et al. [216] suggesting elevated concentrations of exudates (mucilage and citrate) up to a distance of 250 µm for 10 and 15 day old *Vicia faba* roots. Therefore, further investigation of targeted samples of other root types and ages is necessary to picture ^{13}C release into the soil.

In addition to ^{13}C measurements it was also possible to map the spatial distribution of ^{15}N with NanoSIMS (Figure 6.4a). We observed ^{15}N in various distinct areas within the soil matrix, potentially reflecting individual ^{15}N-enriched microorganisms [200], but most pronounced ^{15}N enrichment occurred in the root tissue (Figure 6.4a). As there was no gradual transition between high and low ^{15}N enrichment areas, we speculate that some of the initial NO_3-N label was partially removed during the embedding procedure.

In summary, each 2D imaging technique used in the presented workflow has specific advantages and limitations and hence provides complementary information at different scales. Microscopic imaging methods generally determine only total element concentrations that are not necessarily related to concentration in soil solution or the empirically determined plant-available fractions obtained with specific extractants. This is of particular relevance for elements with only a small plant-available fraction in relation to total concentration as it is typically the case for P [217]. With µXRF only relative differences between samples of different parent materials can be investigated. A quantification of absolute element contents per area with µXRF would be possible but requires a large number of reference samples and standards or a complex calculation based on the assumption that all elements in the sample were detected. For quantification of element contents per soil weight other methods based on destructive sampling would have to be added into the sampling cascade. However, such measurements would be incompatible with the non-destructive assessment of 3D rhizosphere properties. While current approaches with rhizoboxes or root windows allow quantification of mass-based element contents [11], they generally lack the spatial 3D information which we can tackle with our targeted mapping approach.

We also showed that small-scale information on the fate of ^{13}C and ^{15}N at the single cell level can be derived from NanoSIMS measurements (field of view of 30 × 30 µm with a resolution of 0.12 µm) in order to provide a qualitative picture of C and N allocations patterns brought about by plant-microbe-soil interactions for a limited number of locations (Figure 6.4a) [199,200]. In contrast to NanoSIMS, LA-IRMS is able to map larger transects of δ^{13}C with lower costs at a spot size of 30 µm (Figure 6.4b). It is the only truly quantitative method in the presented workflow and as such can quantify C allocation patterns in the rhizosphere. Correlative imaging of NanoSIMS and LA-IRMS therefore provides some added benefits: First, NanoSIMS can inform why specific isotope enrichment was observed with LA-IRMS, e.g. small-scale variability can be related to varying area fractions of enriched cell wall residues or varying number of microorganisms per spot area (Figure 6.4c). Second, LA-IRMS can be harnessed to calibrate qualitative information on isotope ratios with quantitative $\delta^{13}C$ values. This is possible because the laser spot size roughly matches the spatial dimensions of the NanoSIMS images resulting in very good agreement between LA-IRMS readings and average ^{13}C enrichment (arithmetic mean of 256 × 256 pixels) in NanoSIMS images ($R^2=0.82$, $n=11$, $p<0.001$; Figure 6.4d).

In addition to our workflow Bandara et al [207] developed a workflow which is suitable to identify bacteria in undisturbed soil. On a similar set of samples Lohse et al. [218] presented a workflow using mass resolution laser desorption ionization Fourier-transform ion cyclotron resonance mass spectrometry for the direct analysis of the molecular gradients in the rhizosphere. Our workflow can be used with the mentioned approaches as they complement each other and result in a more holistic picture of rhizosphere processes.

6.5.2 Structural integrity

To the best of our knowledge, there is no study to date that systematically examines the structural changes during the fixation and embedding procedure. Here we could show that the combination of dehydration with acetone and resin embedding with araldite under mild vacuum leads to minimal structural deformation. Dehydration as a necessary condition for vacuum stability is a prerequisite for a lot of techniques like NanoSIMS or LA-IRMS. Preservation of original root-soil contact is essential to calculate correct distances from the soil to the root surface which could be only estimated in other studies [213]. A fixation of the root after sampling is a necessary step in this workflow, as root shrinkage can occur before sampling because of drought stress [159]; assuming a perfect root-soil contact in air-dried samples can therefore lead to misinterpretation of results. To preserve the structural integrity, we decided to dehydrate the samples in a series of acetone additions. The chemical gradients observed with correlative imaging might therefore represent conservative estimates of the true rhizosphere extent as easily soluble compounds might have been partially washed out. This wash-out effect was also reduced by only partially saturating the subsamples with fixative through capillary rise instead of full immersion (Figure 6.3). Furthermore, unsaturated subsamples showed a better structural stability during the second X-ray CT scan at 10 µm resolution as any movement of an unconsolidated soil fully saturated with liquid inevitably leads to settling of the subsample.

6.5.3 Registration of 2D radial gradients in 3D context

The combination of 3D structural and 2D chemical information is crucial to represent the radial geometry of accumulation and depletion zones around roots. Calculating root distance maps on a 2D plane can lead to a bias because information about roots outside of the microscopy plane is missing. The direct comparison of root distance maps which are based on the 2D microscopy (Figure 6.5b) to distance maps calculated for the whole 3D image stack (Figure 6.5c) show that for distances in the range of up to ~200 µm there were hardly any differences. That is, for the detected gradients (Ca and sulphur with µXRF, ^{13}C with NanoSIMS and LA-IRMS) in this study the discrepancy between apparent 2D and real 3D root distances are irrelevant for the findings. In other words, the risk of missing an even closer, hidden root is low in the direct vicinity of a visible root. However, in more distant areas considering true 3D distances can reduce any uncertainty related to roots that come close to the soil sections, but do not touch it. A direct comparison of 2D and 3D root distances shows that this is not the case for this particular subsample (Figure 6.5).

To sum up, targeted sampling enables to determine chemical rhizosphere gradients for root segments of known type and age. With this sampling method at hand the temporal development of gradients can be addressed in the future, i.e. it will be possible to investigate how quickly element gradients develop and how long they last after root activity fainted. Combination of 3D and 2D information overcomes a prominent artefact of rhizobox systems. Information on root activity above and below the analysed plane is available and can be used for data interpretation by ruling out the uncertainty brought about by hidden roots. Overcoming the second major artefact of rhizoboxes – growth along a solid plane with altered properties as compared to soil – comes at a prize. It is possible to perform chemical imaging for soil-grown roots and the root-soil contact can be maintained by a careful protocol of sample extraction, fixation, and embedding. However, smearing of original gradients by the infiltration of the fixative and embedding medium cannot be fully ruled out. The patchy appearance of small-scale gradients measured with our workflow, which is obviously related to the size of individual soil particles, expresses not only the necessity of systematic measurements done with a sufficient number of biological replicates but also that with the given resolution one has to move from the concept of continuum scale to pore scale processes.

7 Synthesis and conclusion

7.1 Summary and discussions

This work aimed to contribute to a better understanding of the complex interaction between roots and soil. In the course of this work, a scale transition was made from a larger scale level (the field) via the laboratory to the mm and µm scale in subsamples.

Various overarching questions were addressed, which were described in more detail in Chapter 1.2. The individual questions posed were addressed in the following chapters, which are based on individual scientific publications. This section of the thesis aims to examine the chapters presented in the light of the underlying, broader context of the project. In addition, the methods and scale levels used are briefly listed and the respective limitations are pointed out.

The strength of this work lies in the fact that work was carried out at different scale levels. The conclusions obtained from each scale can be checked both from the large to the small and vice versa; classical methods of rhizosphere research were extended by the approach of 3D imaging and correlative imaging.

Adaption to the lack of root hairs under field conditions; The field experiment presented in Chapter 2 [219] aimed to answer the first question posed in Chapter 1.2, i.e. how does an absence of root hairs, as well as different soil textures, influence plant growth over the duration of an entire growing season under field conditions? Is there a plastic adaptation to the absence of root hairs?

Shoot growth and P and K uptake of the plants were promoted by the presence of hairs at all growth stages. Differences between genotypes were greater on loam than on sand until tassel emergence, presumably as additional exploitation by hairs is more relevant in loam. Soil exploration can be distinguished from soil exploitation, i.e. how thoroughly resources are acquired within a given soil domain without further soil exploration [65]. Root hairs improve soil exploitation similarly to other rhizosphere modifications, like the release of exudates, increased activity or number of mineral nutrient transporters, and enhanced root-soil contact (root diameter, mucilage, rhizosphere porosity) [67]. The root length density within a given volume has an impact on exploitation as well. Exploitation strategies make a difference in environments with patchy, heterogeneous distribution of resources or a large proportion of nutrients with low mobility [68]. In turn, exploration is expected to be more successful if resources are only available in low amounts throughout the soil profile or if resources are only available at larger depths (distance to the seed). For the early growth stages, as long as topsoil was moist, exploitation strategy related to the presence of hairs might have been successful to tap the applied fertiliser. For later growth stages, as drought developed, roots had to explore the entire soil volume in particular for sand, being overall low in plant available nutrients. Root architecture was shaped primarily by the need to access nutrients with increasing drought progressively altering the volume which could be successfully explored for nutrients. Exploitation strategy related to hairs ranked second under these conditions, in particular in sand. This explains the high root length density in sand associated with high root to shoot ratio.

To briefly answer the question posed at the beginning, compensation for the absence of root hairs by increased root growth was not observed in absolute terms. Root traits showed high plasticity in response to texture, the most salient being a greater mean root diameter in sand, irrespective of genotype. Root length density was higher in sand, which can be explained by a greater need for exploration than exploitation in this substrate.

Local adaptations of root architecture to soil heterogeneity; In the pot experiment presented in Chapter 4[46], the aim was to answer the second question posed Chapter 1.2, i.e. how does an absence of root hairs, as well as different soil textures, influence plant growth in the laboratory in structured soil, and does root growth react to the existing heterogeneity? Roots system architecture was analysed over time by repeated X-ray CT. The difference between Chapter 2 [219] and 3 [46] lies in the exact composition of the respective substrates. While in Chapter 5[47] homogeneous substrates with different textures (loam and sand) and thus nutrient availability were used, Chapter 4 [46] focussed on the changes in root system architecture in relation to macroaggregates and thus local heterogeneity in penetration resistance and nutrient availability. The presence of aggregates led to increased root length and branch densities around aggregates, while only a few roots were able to grow into them (Table 4.1). Thereby, wild-type and *rth3* were influenced in the same way. Aboveground biomass, however, was not affected by the presence of macroaggregates (sand substrate equal to that in Chapter 2 [219]), as compared to controls with homogenously distributed loam (substrate equal to that in Chapter 5 [47]). Macroaggregation of loam in sandy soil shows little influence on maize growth, due to local adaptations of root architecture to the heterogeneity in nutrient availability and penetration resistance caused by the aggregates. An additional factor that could hinder the comparison between laboratory and field is the change in plant growth caused by the applied X-rays. Although a relatively high cumulative dose was used compared to other studies [129], the effect on plant growth was drastically reduced by methodolocical precautions in the studies presented here. In Chapter 5 [47], a control variant was used to investigate the influence of radiation. The X-ray dose associated with X-ray CT scanning had no significant impact on shoot or root growth with the scan settings and scanning frequency chosen. This was also shown for other parameters such as gene expression, which only showed a response to the radiation dose within the first 24 hours [125]. A reason for this small effect could be the lead shield, which was used for the first time in these experiments. This shield was able to effectively protect the unscanned areas from scattered radiation (Figure 3.2). The findings from this chapter allow the conclusion that the change in aggregate structure towards macroaggregates does not influence the treatment sand in such a way that the results from the field and laboratory are not comparable. For this reasons, the results of the project's laboratory experiments, such as the one in Chapter 5 [47], can be compared with their upscaled sister experiment in Chaper 2 [219] and *vice versa.*

Adaptation of root architecture in homogenised substrate and applicability of data from laboratory experiments; In Chapter 5 [47], the announced downscaling of the field experiment to laboratory scale for both substrates, sand and loam, takes place. The first sampling time in the field, at which four leaves were unfolded, corresponds approximately to the growth stage of the plants in the laboratory with the selected 21-day growth period. The aim was to answer the third question posed in the introduction of this paper, namely how the absence of root hairs and different soil textures influence plant growth under laboratory conditions with homogenised substrate, and how applicable are the rhizospheric processes observed in laboratory experiments to the data obtained under field conditions? In the laboratory experiment, as in the field, no plastic adaption of root system architecture due to the lack of root hairs was observed, which, in the pot experiment in well-watered conditions, resulted in lower P uptake per cm^2 root surface area in particular in the substrate L with low P mobility. The lack of hairs did not result in different depth profiles of the root length density between genotypes in the laboratory experiment. In the field, where weather-related drought stress in the first two years was recorded, P uptake was lower in sand than in loam, with a tendency towards lower uptake rates in the young growth stages for *rth3*, which is comparable to the laboratory experiment. As the plants were significantly smaller in the field at BBCH14 than the plants after 21 days of growth in the laboratory due to the drought, the BBCH19 stage can also be used for comparison. The poorer supply of P for the hairless mutant is visible here (Figure 2.4), as well as in the laboratory (Figure 5.2).

Notwithstanding, both maize genotypes showed a clear response to the homogensized substrate. This was reflected in the spatio-temporal development of the volume fraction of the rhizosphere, but above all in the strong reaction of the root diameter to the substrate, irrespective of the genotype (Figure 5.6, Figure 5.9). Thus, considering both approaches, field and laboratory, it can be concluded that the most prominent feature of root plasticity was root diameter in response to the substrate while coping mechanisms for missing root hairs were less obvious.

However, in contrast to the plants grown in sand in the field experiment, the plants in the laboratory showed a lower root growth in sand and a higher aboveground biomass at a comparable growth stage in the field. The lower root length density in sand can be partly explained by the higher and evenly distributed content of plant-available nutrients in the homogeneous substrate used in laboratory experiments. Due to the progressive drying of the soil in the field, additional root growth was shifted to greater soil depths, while the plants in the laboratory found a uniform water supply, making further soil exploration unnecessary. In addition, exploration as a factor is not very meaningful in a system with limited soil volume.

An increase in fine root growth as compensation for the lack of root hairs was not observed (Chapter 5 [47]). This is surprising, as the mutant exhibited a plastic response in root growth concerning the substrate. This finding is in contrast to the one by Klamer et al.[64] who compared *Zea mays* WT to the root hair defective mutant *rth2*. They reported a shift towards finer roots for the mutant. However, to detect this shift, they had to compile data across treatments differing vastly in P and water supply. Their plants were growing in subsoil material and were non-mycorrhizal, while the plants in the present experiment showed the first signs of mycorrhizal colonisation (see table AT.4) despite the early growth stage.

Mycorrhizal colonisation in the field was observed as early as at BBCH 14 (Figure 2.8). Colonisation rate increased by maize age and reduced by soil depth ($p < 0.05$). After no differences between substrates at BBCH 14, a higher level of colonisation in loam than sand at BBCH 19 changed to a reversed pattern at BBCH 59 (Figure 2.8). The impact of genotype was not significant. A more intense infection with mycorrhizal fungi as compensation for the lack of hairs was suggested by Li et al. [171] for barley and confirmed by Kumar et al. [161] for maize, but only for later growth stages, as shown in Figure 2.8.

In general, a significantly higher investment in root growth by the root hair defective mutant as it is reported in literature [63,64] is also found in the present study, although only in relative but not in absolute terms and only for loam, i.e. the substrate with lower P mobility. The shift in root:shoot ratio was not sufficient to compensate for the lack of hairs as the P content in shoot material was significantly lower for *rth3* as compared to WT in loam.

With respect to physiological plasticity, the presented results for the laboratory scale are inconsistent. While without morphological and physiological compensation lower uptake rates per unit root are expected, no significant differences in normalized P uptake between the genotypes were found, with only a tendency towards lower values for *rth3* in the substrate with the lower P mobility. In general, much lower P uptake rates per unit root surface were found for loam as compared to sand, despite the low plant P status in loam, which is expected to trigger expression of high-affinity P transporters. This is in line with relative root gene expression data for the same experimental setup, reported by Ganther et al. [158]. They did not find gene functions relating to phosphate uptake to be differentially expressed between WT and *rth3*.

For soil-based systems, the uptake rate per unit root is strongly influenced by diffusion and root-to-soil contact. The differences observes in shoot biomass development between the wild-type and the root hait mutan could simply be explained by increased surface area for uptake provided by the hairs, or the decrease in path length required for P diffusion across the rhizosphere [82]. The latter is of particular relevance for soils with low P mobility and would explain why differences in uptake rates were not observed in sand, the substrate with higher P mobility. In the sand, neither the P uptake nor the P content differed significantly between the genotypes in either the field or the laboratory.

Haling et al. [32] found significantly lower P uptake rates per unit root length for the root hair defective mutant of barley compared to the wild-type, for high but more so for low P soils. Root hairs were relevant for maintaining contact in loose soils and for improved penetration in dense soils. The importance of hairs for P uptake in particular under conditions of restricted P transport is confirmed by observations in hydroponics, i.e. systems with no major limitations for transport. Suzuki et al. [173] found no differences in P uptake rates per unit root dry weight between rice genotypes differing in root hair development in hydroponic systems, irrespective of P supply. The differences between substrates observed here are related to their differences in P diffusion.

In all experiments, a nutrient status just below the optimum supply for the WT genotype was selected [3]. One reason for the different root diameters measured could be this nutrient deficiency, to which the plants react by changing the proportion of individual root types in the total root length. On one hand, plant available nutrient concentrations below the fertiliser-affected soil surface were higher in loam than in sand in the field (Chapter 2 [45]). On the other hand, similar differences in root diameters between the substrates could also have been observed for the twin laboratory experiment for which fertiliser was homogeneously mixed into the substrate and similar amounts of plant available nutrients were present (Chapter 5.3 [47]). Doubling the amount of fertiliser in the laboratory experiments had no impact on root diameters. An exact analysis of the individual root types in an additional experiment also showed that almost all root types reacted with a change in diameter towards thicker diameters in the coarser textured substrate.

For this reason, it can be assumed that the change in root diameter in response to soil texture appears to have other causes. The most frequent cause for shifts in root diameter reported in literature is alterations in soil compaction, bulk density and mechanical impedance, which are tightly linked with changes in soil water content and gas diffusion [92,133,181–183]. In contrast to many of those classical studies reporting an increase in root diameter as a result of soil compaction, no co-occuring in root growth rate was observed. Under field conditions, roots were not only showing larger diameters in sand as compared to loam but also much higher root length densities throughout the soil profile. Dupuy et al. [112] suggested re-visiting micromechanics of rooting development in soil. They argue that this is of particular relevance for medium grained soils; here roots can displace individual particles from the soil, but the forces exerted by each of the particles can also influence the course of root development. The latter is not reflected in the measurement of mechanical impedance for the substrated used in this thesis [94]. Crucial for this type of concept is the size aspect ratio between root's diameter and the particle size [116]. The increase of root diameter observed in sand can be interpreted as an attempt to maintain an optimal size aspect ratio.

The root phene ‘increased root diameter’ can also be induced by ethylene, which is often associated with the morphological response of roots to mechanical impedance [120,181], but even in systems without soil or pressure [117]. In this context a publication by Pandey et al. [118] is of interest, questioning that ethylene induced root thickening is required to overcome soil resistance. It is suggested that ethylene rather acts an early warning signal for roots to avoid compacted soil and the mechanism is related to altered gas diffusion in the rhizosphere. Further experiments are required, to elucidate whether observed differences can be explained by mechanical properties beyond mechanical impedance, root or microbiome ethylene production or differences in diffusion processes within the root or the rhizosphere.

Two main findings can be derived from this part of the work: I) The relative higher investment in root growth for the root hair defective mutant, reflected in an increase of root:shoot ratio for *rth3* as compared to WT, observed at field and lab scale was in line with expectations. II) The consistent differences in root diameter between substrates (lab and field scale) but likewise between genotypes (more pronounced at field than at lab scale) were surprising.

Linking spatio-temporal gradients in the rhizosphere to root development; Root diameters have implications for the extent and magnitude of chemical gradients in radial systems. The same applies to the size of the root system and the above-ground biomass, which directly influence the uptake rate from the soil. Furthermore, it can be assumed that the spatial context of individual root segments also plays a role, as well as their age and thus interaction time with the soil. Bilyera et al. [11] used custom-designed root windows installed in the same field experiment to apply 2D-chemical imaging methods to visualise soil pH (via optodes), acid phosphatase activity (via zymography), and labile P and Mn fluxes (via diffusive gradients in thin films, DGT). Different rhizosphere expansions were found with this method, while once again root hairs seemed to have no influence. However, the age of the roots played a role, acidification was significantly stronger for young root tissue (<2 cm from the root cap) than for older root segments (>4 cm from the root cap) and stronger in WT than *rth3*. In contrast to the uptake of nutrients stands the release of root exudates as the main pathway of organic carbon into the soil. Lohse et al. [220] used six different analytical approaches to reveal the molecular diversity of maize root exudates in the field experiment described in Chapter 2 [219]. The *rth3* mutant genotypes showed a higher carbon and nitrogen exudation rate than their corresponding WT siblings despite the absence of root hairs. The same effect was observed by Santangeli et al. [75] who, in addition, found exudation rates were higher in loam, i.e. the substrate with lower nutrient mobility. Although these approaches have their justification, they work on different scales and neglect the radial geometry of chemical gradients [5,12].

Based on the aforementioned observations, a correlative imaging workflow for targeted sampling of roots in their three-dimensional (3D) context was developed as part of this thesis (Chapter 6 [49]). The influence of roots on the chemical properties of the root-soil contact zone in the micrometre to millimetre range was investigated.

The wild-type of *Zea mays* L. was grown in ^{15}N-labeled soil columns and pulse-labelled with $^{13}CO_2$ to visualize the spatial distribution of carbon inputs and nitrogen uptake together with the redistribution of other elements. Soil columns were scanned by X-ray computed tomography (X-ray CT) at low resolution (45 µm) to enable image-guided subsampling of specific root segments. After dehydration in a series of acetone and embedding in epoxy resin, subsamples were analysed by X-ray CT at high resolution (10 µm) for their 3D structure. Dehydration as a necessary condition for vacuum stability is a prerequisite for a lot of techniques like nano-scale secondary ion mass spectrometry (NanoSIMS) or laser ablation isotope ratio mass spectrometry (LA-IRMS). Preservation of original root-soil contact is essential to calculate correct distances from the soil to the root surface which could be only estimated in other studies [213]. Here it could be shown that the combination of dehydration with acetone and resin embedding with araldite under mild vacuum leads to minimal structural deformation.

Subsequently, after CT image-guided targeted preparation of thin sections, chemical gradients in the vicinity of roots could be measured using micro X-ray fluorescence spectroscopy (µXRF), NanoSIMS and LA-IRMS. Concentration gradients, particularly of calcium and sulphur, with different spatial extents could be identified by µXRF. NanoSIMS and LA-IRMS detected the release of ^{13}C into the soil up to a distance of 100 µm from the root surface, whereas ^{15}N accumulated preferentially in the root cells (see section 6.4.6).

Overcoming one of the major artifacts of rhizoboxes - growth along a solid plane with altered properties as compared to soil - comes at a prize. Smearing of original gradients by infiltration of the fixative and embedding medium cannot be fully ruled out. Furthermore, due to the complexity of the sample preparation and the time required for the measurements themselves, only a limited sample throughput is possible. For example, a sample area of 5 x 5 mm requires an average of around 10 hours of pure measurement time for a single µXRF measurement with the settings selected in this work. NanoSIMS and LA-IRMS are also very costly and time-consuming techniques that require expert knowledge for operation.

Other imaging approaches, which require different sample preparations, but similar sampling systems and the same sampling steps described in Chapter 6 [49] can be used to visualise plant metabolites in the rhizosphere using laser desorption ionization ultra-high resolution mass spectrometry [218] and perform microbial identification [207].

The combination of 3D and 2D information presented in Chapter 6 [49] overcomes a prominent artifact of rhizobox systems, i.e. not accounting for the radial geometry of chemical gradients in planar experimental setups [5,12]. Each 2D imaging technique used in the presented workflow has specific advantages and limitations and hence provides complementary information (Table 6.1) at different scales. Information on root activity above and below the analyzed plane is available and can be used for data interpretation by ruling out the uncertainty brought about by hidden roots. This way it is possible to perform chemical imaging for soil-grown roots and the root–soil contact can be maintained by a careful protocol of sample extraction, fixation, and embedding.

7.2 Upscaling and downscaling

The present work shifts the focus from the field perspective to the laboratory scale and back again, which considers individual plants in defined pot sizes under controlled growth conditions, to a small-scale analysis of chemical gradients at the pore scale. Probably everyone who works in the laboratory has already been confronted with the question of the transferability of their data to the field perspective. Apart from methodological challenges that arise when scaling up or down (see Chapter 4 [46], which examines the substrate differences in the field and laboratory as a result of methodological challenges during experiment setup), the time component alone is a major potential confounding factor. In field studies, which are dependent on the seasons, an experiment without prophetic foresight of the weather is at the mercy of it. For this reason alone, the knowledge gained in the laboratory cannot be transferred unconditionally to the field. Furthermore, an entire growing period is difficult to replicate in the laboratory, as the pot size will be a limitation at some point. In the case of this work, the experimental setup was adapted to the resolution limits of the X-ray CT used. Despite major advances in root segmentation in the past years [152,190] ,we still face the trade-off between image resolution and sample size resulting in fine roots being partly missed out. In the present case, this afflicts the differences between sand and loam as the share of fine roots was larger in loam. Smaller column diameters associated with a higher scanning resolution would have overcome this problem but would have restricted the experiment to an even shorter growth period (Chapter 5 [47]). Shorter growth durations would make it even more difficult to account for interaction of roots with the microbiome, in particular the mycorrhizal symbiosis, which is only starting to interact within the given time [172]. Moreover, the limitation of pot trials for the study of exploration strategies has to be emphasized. The limited soil volume of pot trials may induce feedback loops which would not be observed in the field at the same time point.

One scale level further down, in the range of a few µm resolution (for imaging methods such as µXRF or NanoSIMS), the question arises as to what extent the results can be transferred to the landscape level in a heterogeneous matrix such as soil. The 3D and 2D imaging techniques presented in the workflow are not applicable in the field, but can be applied to structurally intact field samples. In combination with the findings from the laboratory experiments, a deeper understanding of the processes at field level can be gained. However, in Chapter 6 [49] the patchy appearance of small-scale gradients measured with the workflow, which is related to the size of individual soil particles, expresses not only the necessity of systematic measurements done with a sufficient number of biological replicates but also that with the given resolution one has to move from the concept of continuum-scale to pore-scale processes. However, especially with cost- and time-intensive measurements such as NanoSIMS, a sample throughput of several hundred samples or even more cannot be achieved. Baveye et al. [221] wrote a review article in which they also addressed the topic of scale levels and heterogeneous soil microenvironments. They argue that conventional measurements do not sufficiently reflect the enormous complexity of soils at the microscopic scale to make accurate predictions at the macroscopic level. This problem is always a much-discussed one, for which there is still no conclusive solution due to the complexity of measurements at the small scale level [7]. Complexity here means factors such as the measurement with NanoSIMS, for example, where the selection of measurement surfaces alone results in enormous differences in the validity of the results due to the heterogeneity that already exists in the microcosm alone. A higher number of measurements is not realistically feasible due to the pure measurement time and the costs for a single measurement. Nevertheless, each of the methods presented can provide important new insights in plant-soil interaction. Despite the limitations and complexities involved, the combination of diverse methodological approaches on a single sample surface, as well as in a series of coordinated experiments, represents a promising avenue for elucidating hitherto poorly understood processes occurring in the rhizosphere.

8 Future work

To answer the question of why the roots of the maize genotypes considered in this work react with an altered diameter, further experiments are necessary to test subsequent hypotheses. The root phene ‘increased root diameter’ can be induced by ethylene as such, i.e. even in systems without soil or pressure [117]. Pandey et al. [118] concluded from their study that ethylene acts as an early warning signal for roots to avoid compacted soil and that the mechanism is related to altered gas diffusion in the rhizosphere. Hence the questions arise whether ethylene is also the signalling substance in the systems presented within this thesis, and which mechanisms may result in increased ethylene concentrations in the rhizosphere. As the larger root diameter in sand than in loam was not related to the differences in mechanical resistance between substrates, it can also be hypothesized that this is a general phenomenon in coarse textured substrates related to the need of optimising root-soil contact.

The workflow presented in Chapter 6 [49] can also be used to systematically determine the expansion of the rhizosphere for different elements (with µXRF) on a larger number of samples. Other publications [11,222] have already found differences in the formation of chemical gradients depending on root age working with 2D Systems, but these observations have yet to be verified on a laboratory scale and in 3D instead of 2D context.

In the field, consecutive measurement with X-ray CT is not possible. Nevertheless, based on observations in the laboratory, it may be possible to recognise root ages in the field in the future without sequential CT images. In this way, the results can be transferred from the laboratory to the field to extend the time period for the investigation of spatio-temporal patterns to an entire growth period to allow for the development of heterogeneities in parameter distribution over time.

In addition to gathering evidence, it is also important to develop theoretical and modelling frameworks that incorporate experimental information and allow predictions to be made. In each case, the experimental data should be used to refine the theories and models, which in turn can provide guidance (e.g. through sensitivity analyses) for obtaining additional data. The result of such an iterative approach will hopefully be a satisfactory description of the individual dynamics, which can then be integrated initially in a pairwise fashion and finally all together into a comprehensive model of soil processes at the microscale.

Appendices

8.1 Appendices for Chapter 2

AT.1: Selected characteristics of the substrates loam and sand from 5-10 cm depth after establishment of soil plot experiment in the field (modified from Vetterlein et al. 2021)

	Bulk density [g cm^{-3}]	pH ($CaCl_2$)	Carbonate [g kg^{-1}]	Sand [%]	Silt [%]	Clay [%]	CEC [mmol$_c$ kg^{-1}]	C_{org} [%]	N_t [%]	P plant available [mg kg^{-1}]	K plant available [mg kg^{-1}]	Fe_o [g kg^{-1}]
Loam	1.39 *(0.01)*	6.37	<1 *(0. 0)*	32.5 *(0.36)*	47.9 *(0.17)*	19.5 *(0.26)*	98.6 *(4.7)*	0.85 *(0.01)*	0.083 *(0.001)*	32.69 *(0.40)*	28.51 *(0.72)*	1.32 *(0.01)*
Sand	1.50 *(0.01)*	6.29	<1 *(0. 0)*	91.8 *(0.51)*	5.6 *(0.35)*	2.6 *(0.17)*	33.1 *(2.6)*	0.15 *(0.01)*	0.017 *(0.001)*	8.29 *(0.37)*	7.84 *(0.61)*	0.25 *(0.01)*

AT.2: Substrate specific fertilisation of soil plot experiments. Fertilization was conducted in the same way in 2019 and 2020. 50% of the fertiliser was applied prior to seeding, 50% after first sampling (BBCH 14); modified from Vetterlein et al.[3] (2021).

Substrate	Nutrient	Application rate [kg nutrient ha^{-1}]	Type
Loam	N	50	Calcium ammonium nitrate
	P	12	Triple superphosphate
	K	50	60s corn potash
	Mg	18	Epsom salt
	Ca	27	(applied with other fertilisers)
Sand	N	100	Calcium ammonium nitrate
	P	24	Triple superphosphate
	K	100	60s corn potash
	Mg	33	Epsom salt
	Ca	52	(applied with other fertilisers)
	Micron.	50	Excello

AT.3: Impact of substrate (loam, sand) and maize genotype (wild-type—WT, root hair mutant rth3–rth3) on nutrient removal by above ground biomass at different stages of plant development (BBCH 14, BBCH 19, BBCH 59, BBCH 83) in 2019. Standard errors of mean are provided in brackets, n=6. For comparison nutrient input via fertiliser application is shown.

Treatment	Fertiliser [kg ha^{-1}]	Removal by above ground biomass [kg ha^{-1}]			
	N	BBCH 14	BBCH 19	BBCH 59	BBCH 83
L_WT	50	1.9 (0.1)	47.0 (3.5)	136.4 (19.3)	127.1 (10.8)
L_rth3	50	1.3 (0.1)	25.6 (3.4)	81.9 (4.3)	80.1 (4.8)
S_WT	100	1.6 (0.3)	16.2 (3.3)	57.1 (2.4)	75.6 (7.4)
S_rth3	100	0.7 (0.1)	7.8 (1.3)	45.1 (4.3)	65.8 (9.9)
	P				
L_WT	12	0.11 (0.01)	4.4 (0.3)	17.1 (2.4)	16.1 (1.9)
L_rth3	12	0.06 (0.01)	2.4 (0.3)	10.0 (0.6)	10.3 (0.7)
S_WT	24	0.11 (0.02)	1.0 (0.2)	6.8 (0.4)	9.2 (1.1)
S_rth3	24	0.06 (0.01)	0.4 (0.1)	5.5 (0.5)	9.0 (1.4)
	K				
L_WT	50	0.9 (0.1)	27.6 (3.0)	107.1 (12.0)	77.5 (8.0)
L_rth3	50	0.4 (0.1)	12.4 (2.0)	53.4 (4.3)	42.0 (4.4)
S_WT	100	1.0 (0.2)	10.4 (2.5)	42.6 (2.6)	46.4 (6.1)
S_rth3	100	0.4 (0.1)	4.4 (0.6)	24.2 (1.1)	32.2 (4.6)

AT.4: Studies relating root diameter (RD) to soil texture. + denotes an increase of RD with increasing particle size, or a negative correlation of root diameter with root length, respectively.

Reference	**Scale**	**Textures/soil type**	**Plant species**	**Research focus**	**Methods, remarks**	**RD ↑with coarse texture**	**Trade-off RD and length**
Warnaars and Eavis (1972)	lab	five types of sand	*Pisum sativum, Zea mays*, grass	particle size distribution		+	+
Veen (1982)	lab	glass beads; pressure	*Zea mays*	mech. resis.			+
Sene *et al.* (1985)	field	sand, sandy loam, loamy sand, silt loam	*Zea mays*	tillage system	root properties are discussed, only yield data		
Dwyer *et al.* (1988)	field	sandy, clay, loam, till	*Zea mays*	water, rooting depth	root length: sandy> loam, clay		
Atwell (1990)	field	loamy sand	*Triticum aestivum*	compaction	Microscopy; 47 d after sowing		+
Materechera *et al.* (1991)	lab	siliceous sandy soil, vermiculite	22 plant species	mech. resis.	microscopy		+
Materechera *et al.* (1992)	lab	sandy loam	8 species	compaction	penetration ability relates to RD		
Chassot *et al.* (2001)	field,	silt loam, loam soil	*Zea mays*	tillage system	median root diameter 317 to 447; increases with depth;		±

part two of the table can be found on the following page

Reference	**Scale**	**Textures/soil type**	**Plant species**	**Research focus**	**Methods, remarks**	**RD ↑with coarse texture**	**Trade-off RD and length**
Qin *et al.* (2005)	field	loamy silt, sandy loam	*Zea mays*	Tillage system	Root diameter differed between years	+	
Anderson *et al.* (2007)	lab	sandy loam, loam, loamy sand	*Digitaria spec.*, *Themeda spec.*	Adaptation	smaller proportion of fine roots if share of sand increases	+	
Lipiec *et al.* (2012)	lab	silt loam	*Zea mays* and 4 other species	compaction	observed root deformation		±
Tracy *et al.* (2012a)	lab	sandy loam, bulk densities	*Triticum aestivum*	bulk density	X-ray CT		+
Tracy *et al.* (2012b)	lab	loamy sand, clay loam	*Solanum lycopersicum*	bulk density		-	+
Xie *et al.* (2012)	lab	sand, clay	*Gossypium spec.*	allometry	specific root length	-	
Chimungu *et al.* (2014)	lab, field		Zea mays, diff. genotypes	drought	root cortical cell file number – reduces metabolic costs		
Dal Ferro *et al.* (2014)	field	sandy loam	*Zea mays*	Tillage system	root diameters decreased with increasing bulk denstiy;		
Lipiec *et al.* (2016)	lab	sand (shape of grains)	*Triticum aestivum*	mech. resis.	microscopy	+	+
Rogers *et al.* (2016)	lab	granular substrates sieved; silica beads	*Oryza sativa*	particle size	X-ray CT, 7-day old plants	±	
Marin *et al.* (2020)	field	sandy loam, clay loam	*Zea mays*	root hairs	shorter root length in clay loam		

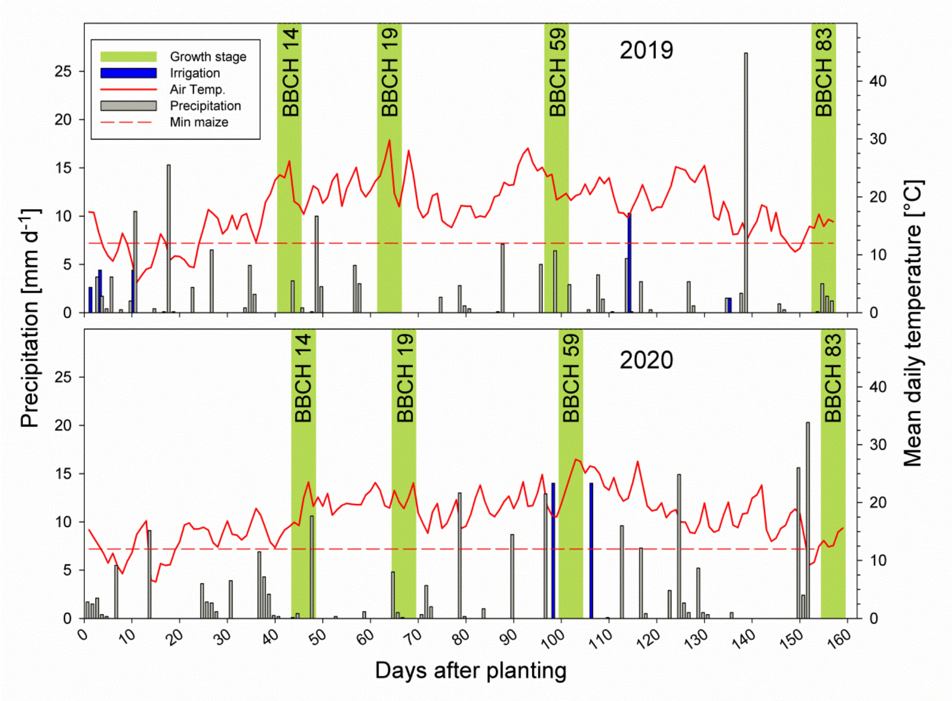

AF.1: Daily precipitation and mean daily temperature during the 2019 and 2020 growing seasons at the Bad Lauchstädt research station. The growth stages for sampling shoot and root growth are indicated by green bars. The minimum temperature for maize growth of 12°C is shown by the red dashed line. Irrigation events required to allow germination and avoid damaging crop losses are shown in blue.

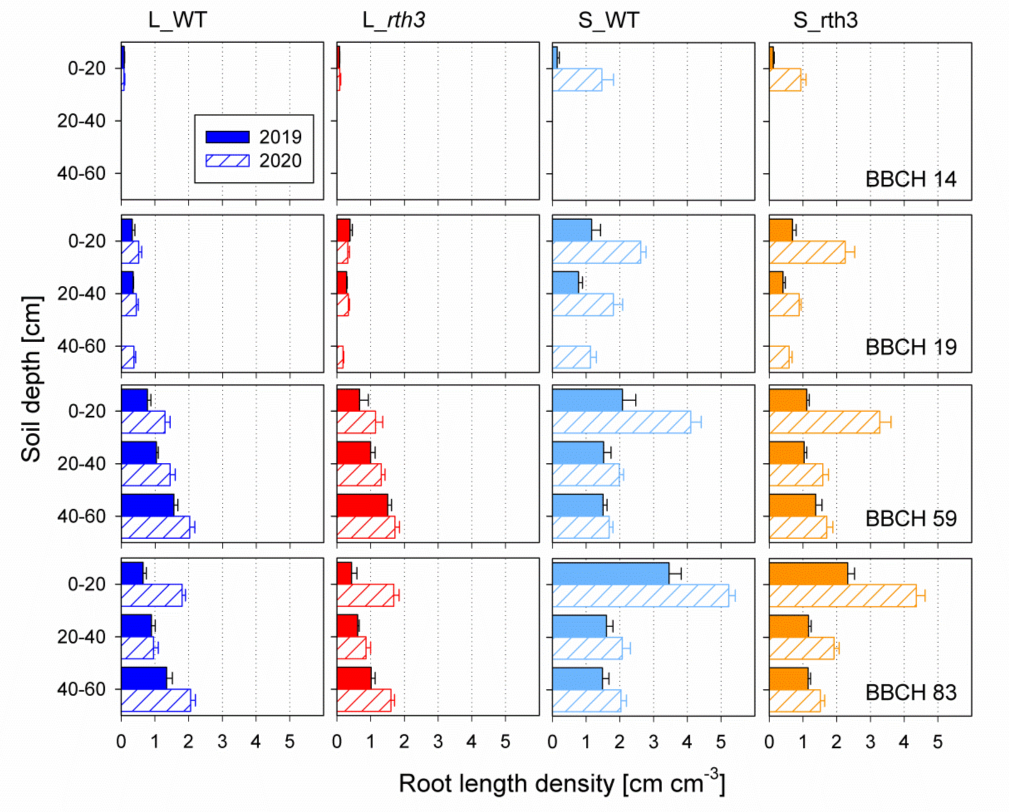

AF.2: Impact of substrate (loam, sand) and maize genotype (wild-type—WT, root hair mutant rth3–rth3) on root length density distribution with depth at different stages of

plant development (BBCH 14, BBCH 19, BBCH 59, BBCH 83) in the first (2019) and second (2020) year of soil plot experiment. Data for 2020 without correction for dead roots.

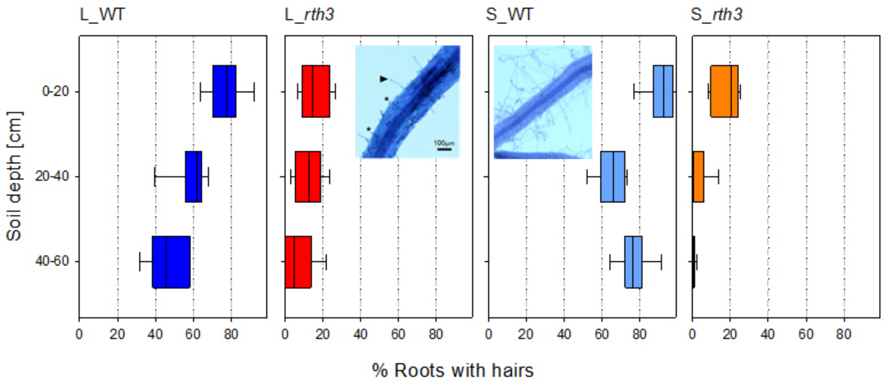

AF.3: Impact of substrate (loam, sand) and maize genotype (wild-type—WT, root hair mutant rth3–rth3) on the fraction of roots showing root hairs at BBCH 59 in 2019. Note that the insets provide representative examples for the observed root hair phenotype. Triangle indicates an elongated hair in rth3, asterisk the more bulge shape in rth3.

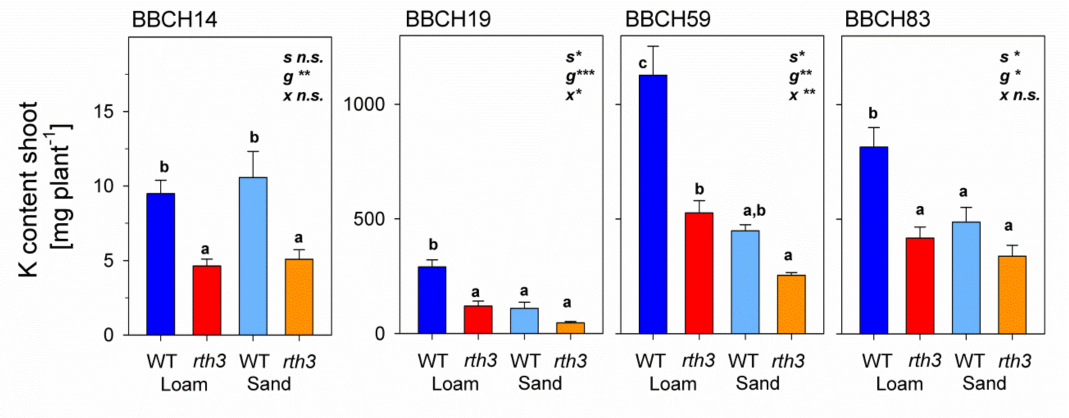

AF.4: Impact of substrate (loam, sand) and maize genotype (wild-type—WT, root hair mutant rth3–rth3) on shoot K content at different stages of plant development (BBCH 14, BBCH 19, BBCH 59, BBCH 83) in the first year (2019) of soil plot experiment. Note the different scales for the different growth stages. Statistics: two-factorial ANOVA in conjunction with Tukey's HSD test was conducted for growth stage. Significant effect of factor is denoted by s for substrate, g for genotype and x for interaction. Differences between treatments (p < 0.05) are indicated by different lower case letters. Whiskers indicate standard error, n=6.

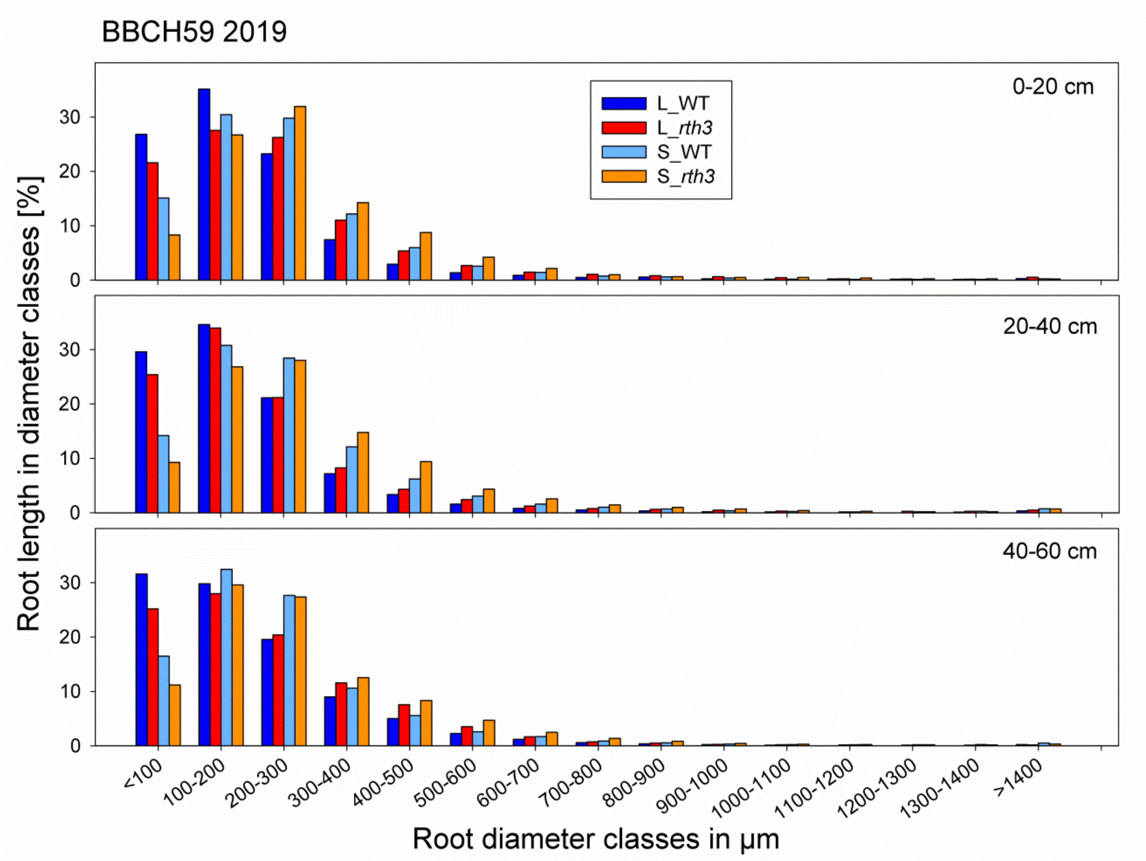

AF.5: Root length in different root diameter classes (class width 100 µm) at BBCH 59 in 2019 for two maize genotypes (wild-type - WT, root hair mutant rth3 – rth3) grown on either loam (L) or sand (S). Mean values of six replicates are shown.

8.2 Appendices for Chapter 3

At this point we want to take the opportunity to reveal a mistake which was done when the dose was calculated in former studies. The actual dose at the pot wall, as it is given in Blaser et al. [129] or Gao et al. [131] can be assumed to be a twofold lower.

	value given in the paper	recalculated value
Blaser et al. 2018	4.2 Gy/h at pot wall	2.2 Gy/h at the pot wall
	4.2 Gy 'moderate scanning'	2.2 Gy 'moderate scanning'
	7.8 Gy 'frequent scanning'	4.2 Gy 'frequent scanning'
Gao et al. 2019	0.45 Gy	0.2 Gy

Recalculating the values of different papers also revealed an internal mistake in RadPro. Some authors used the program output given in Sv and converted them directly into Gy, as the weighting factor for X-ray is 1(*ICRP*, 2003) and therefore Sv is equal to Gy. Apparently RadPro calculations are performed in Roentgen and then converted to Sv, using a conversion factor. As 1 Roentgen = 0.876 rad (air) *(Stupian,* 2007) and 100 rad is 1Gy it should multiply Sv with 0.00876 (which is also written in the RadPro FAQ online). But what it actually does is multiplying by 0.0114 (because dividing by 0.876 instead of multiplying).

correct equation	equation used by RadPro
$1R * 0.876 = 1rad$	$\frac{1R}{0.876} = 1rad$
$\frac{1rad}{100} = 1Sv$	$\frac{1rad}{100} = 1Sv$

As there is no support for the desktop version of RadPro anymore, we strongly recommend using the value given in Roentgen and converting it whenever it is not possible to measure the dose in soil.

8.3 Appendices for Chapter 4

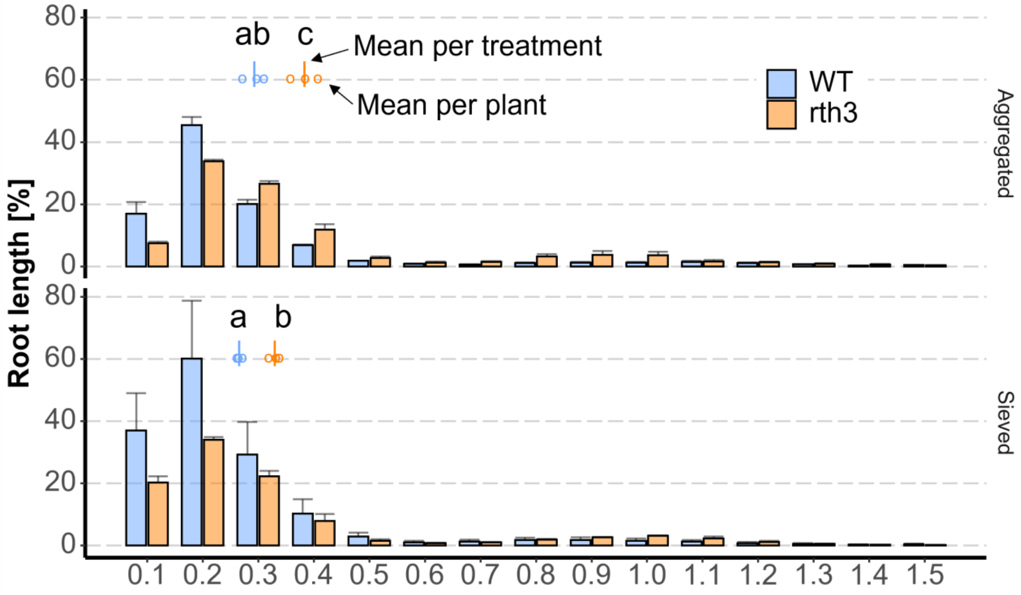

AF.6: Root size distribution of the two genotypes within the two substrates (sieved and aggregated). Whiskers show the standard error of n=3 replicated plants. In addition, mean root diameter per plant (circles) and per treatment (dash).

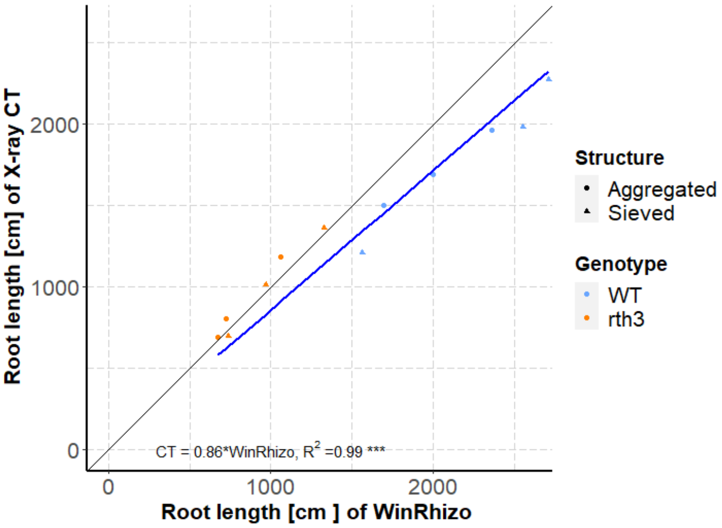

AF.7: Correlation of root length derived using WinRhizo and root length derived using X-ray CT.

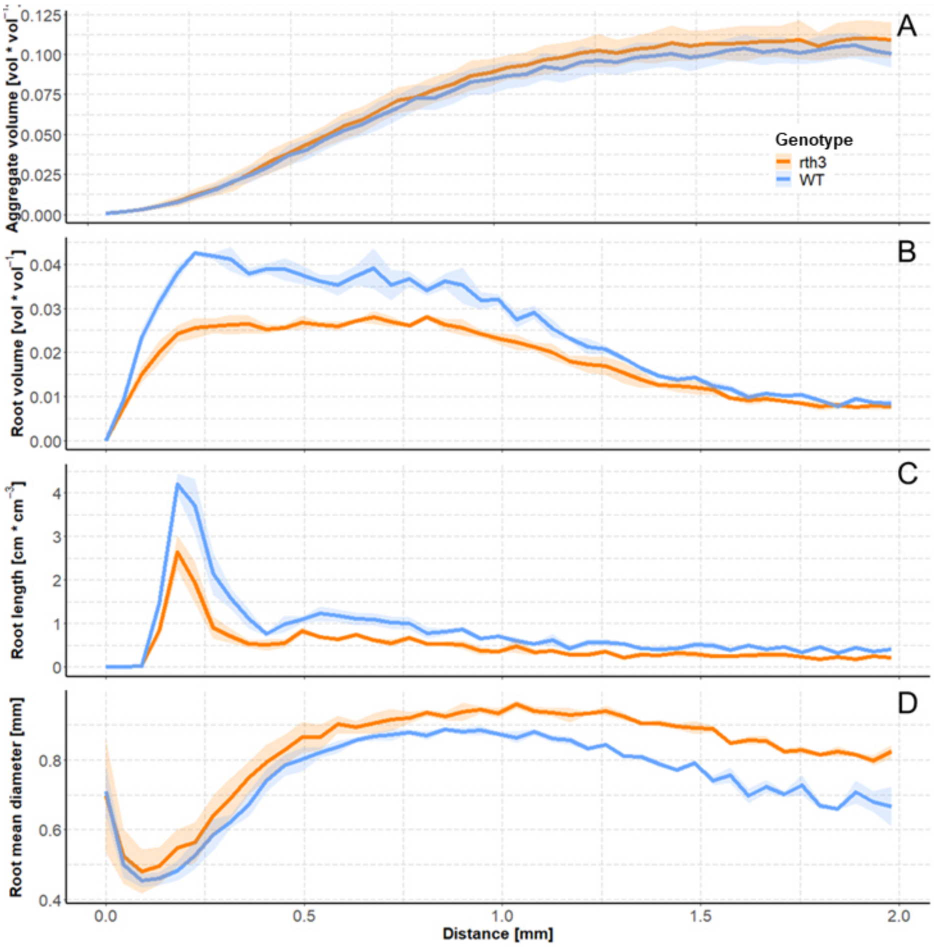

AF.8: Distribution of root traits and aggregate volume with respect to the column wall. Shadows show the standard error of n=3 replicated plants.

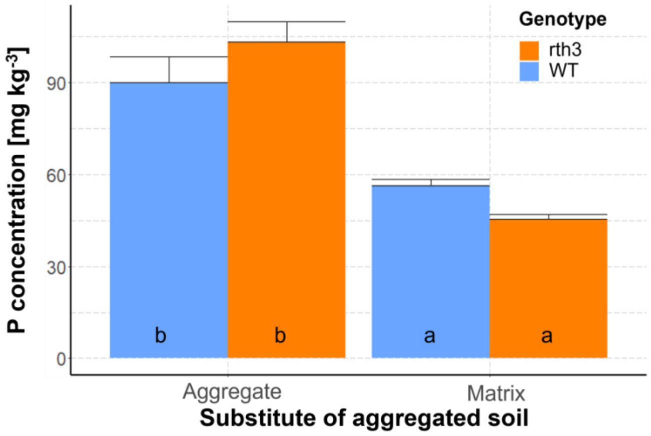

AF.9: Concentration of phosphorous in large macroaggregates and the sandy soil matrix after the experiment. Whiskers show the standard error of n=3 replicated plants.

The following are screenshots of the Image-J script, which was published as an ijm file with the publication in chapter 4.

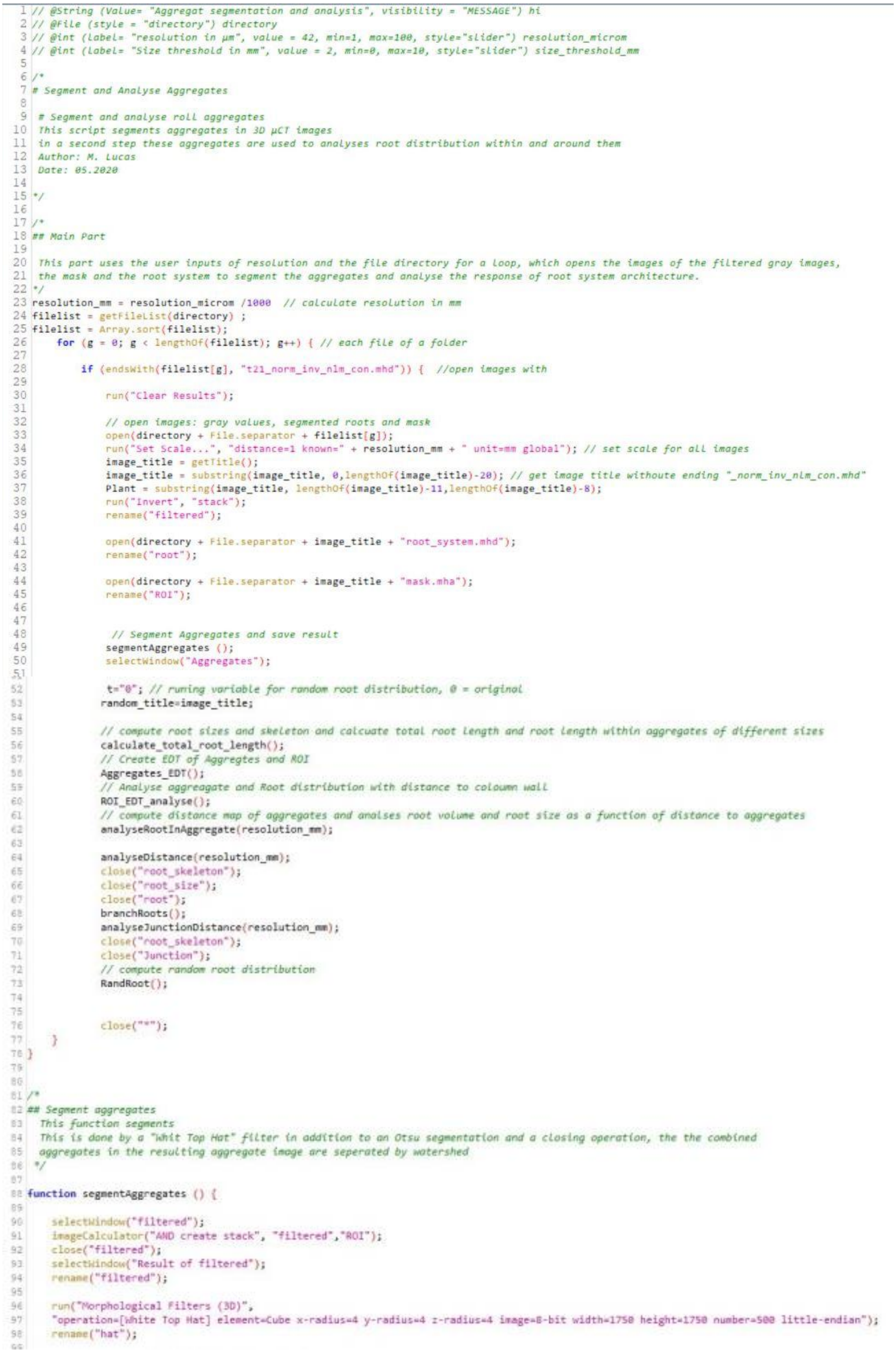

```
// @String (Value= "Aggregat segmentation and analysis", visibility = "MESSAGE") hi
// @File (style = "directory") directory
// @int (label= "resolution in µm", value = 42, min=1, max=100, style="slider") resolution_microm
// @int (label= "Size threshold in mm", value = 2, min=0, max=10, style="slider") size_threshold_mm

/*
# Segment and Analyse Aggregates

 # Segment and analyse roll aggregates
 This script segments aggregates in 3D µCT images
 in a second step these aggregates are used to analyses root distribution within and around them
 Author: M. Lucas
 Date: 05.2020

*/


/*
## Main Part

 This part uses the user inputs of resolution and the file directory for a loop, which opens the images of the filtered gray images,
 the mask and the root system to segment the aggregates and analyse the response of root system architecture.
*/
resolution_mm = resolution_microm /1000  // calculate resolution in mm
filelist = getFileList(directory) ;
filelist = Array.sort(filelist);
    for (g = 0; g < lengthOf(filelist); g++) { // each file of a folder

        if (endsWith(filelist[g], "t21_norm_inv_nlm_con.mhd")) {  //open images with

            run("Clear Results");

            // open images: gray values, segmented roots and mask
            open(directory + File.separator + filelist[g]);
            run("Set Scale...", "distance=1 known=" + resolution_mm + " unit=mm global"); // set scale for all images
            image_title = getTitle();
            image_title = substring(image_title, 0,lengthOf(image_title)-20); // get image title withoute ending "_norm_inv_nlm_con.mhd"
            Plant = substring(image_title, lengthOf(image_title)-11,lengthOf(image_title)-8);
            run("Invert", "stack");
            rename("filtered");

            open(directory + File.separator + image_title + "root_system.mhd");
            rename("root");

            open(directory + File.separator + image_title + "mask.mha");
            rename("ROI");


             // Segment Aggregates and save result
            segmentAggregates ();
            selectWindow("Aggregates");

             t="0"; // runing variable for random root distribution, 0 = original
            random_title=image_title;

            // compute root sizes and skeleton and calcuate total root length and root length within aggregates of different sizes
            calculate_total_root_length();
            // Create EDT of Aggregtes and ROI
            Aggregates_EDT();
            // Analyse aggreagate and Root distribution with distance to coloumn wall
            ROI_EDT_analyse();
            // compute distance map of aggregates and analses root volume and root size as a function of distance to aggregates
            analyseRootInAggregate(resolution_mm);

            analyseDistance(resolution_mm);
            close("root_skeleton");
            close("root_size");
            close("root");
            branchRoots();
            analyseJunctionDistance(resolution_mm);
            close("root_skeleton");
            close("Junction");
            // compute random root distribution
            RandRoot();


            close("*");
    }
}


/*
## Segment aggregates
  This function segments
  This is done by a "Whit Top Hat" filter in addition to an Otsu segmentation and a closing operation, the the combined
  aggregates in the resulting aggregate image are seperated by watershed
 */

function segmentAggregates () {

    selectWindow("filtered");
    imageCalculator("AND create stack", "filtered","ROI");
    close("filtered");
    selectWindow("Result of filtered");
    rename("filtered");

    run("Morphological Filters (3D)",
    "operation=[White Top Hat] element=Cube x-radius=4 y-radius=4 z-radius=4 image=8-bit width=1750 height=1750 number=500 little-endian");
    rename("hat");
```

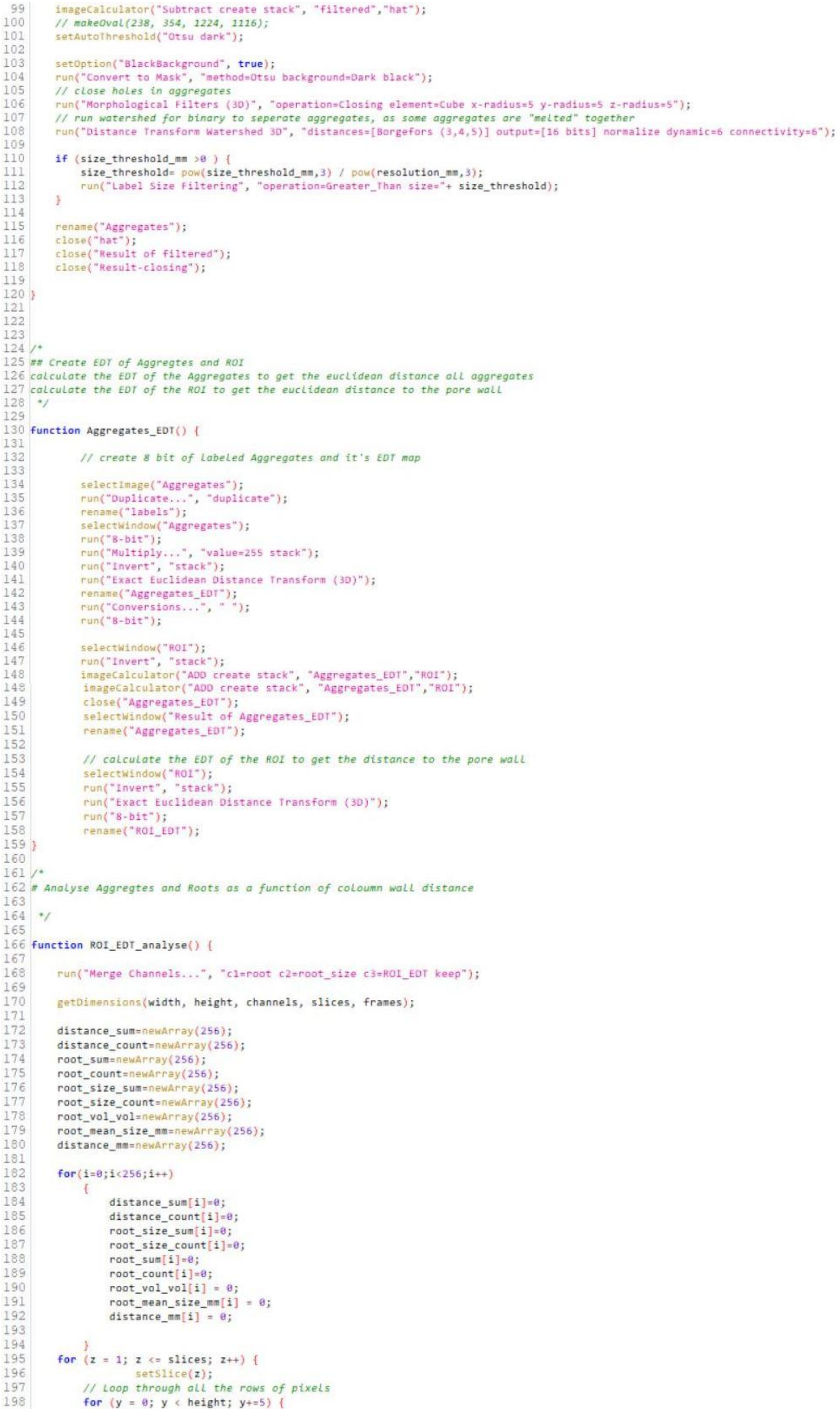

```
    imageCalculator("Subtract create stack", "filtered","hat");
    // makeOval(238, 354, 1224, 1116);
    setAutoThreshold("Otsu dark");

    setOption("BlackBackground", true);
    run("Convert to Mask", "method=Otsu background=Dark black");
    // close holes in aggregates
    run("Morphological Filters (3D)", "operation=Closing element=Cube x-radius=5 y-radius=5 z-radius=5");
    // run watershed for binary to seperate aggregates, as some aggregates are "melted" together
    run("Distance Transform Watershed 3D", "distances=[Borgefors (3,4,5)] output=[16 bits] normalize dynamic=6 connectivity=6");

    if (size_threshold_mm >0 ) {
        size_threshold= pow(size_threshold_mm,3) / pow(resolution_mm,3);
        run("Label Size Filtering", "operation=Greater_Than size="+ size_threshold);
    }

    rename("Aggregates");
    close("hat");
    close("Result of filtered");
    close("Result-closing");

}



/*
## Create EDT of Aggregtes and ROI
calculate the EDT of the Aggregates to get the euclidean distance all aggregates
calculate the EDT of the ROI to get the euclidean distance to the pore wall
 */

function Aggregates_EDT() {

        // create 8 bit of labeled Aggregates and it's EDT map

        selectImage("Aggregates");
        run("Duplicate...", "duplicate");
        rename("labels");
        selectWindow("Aggregates");
        run("8-bit");
        run("Multiply...", "value=255 stack");
        run("Invert", "stack");
        run("Exact Euclidean Distance Transform (3D)");
        rename("Aggregates_EDT");
        run("Conversions...", " ");
        run("8-bit");

        selectWindow("ROI");
        run("Invert", "stack");
        imageCalculator("ADD create stack", "Aggregates_EDT","ROI");
        imageCalculator("ADD create stack", "Aggregates_EDT","ROI");
        close("Aggregates_EDT");
        selectWindow("Result of Aggregates_EDT");
        rename("Aggregates_EDT");

        // calculate the EDT of the ROI to get the distance to the pore wall
        selectWindow("ROI");
        run("Invert", "stack");
        run("Exact Euclidean Distance Transform (3D)");
        run("8-bit");
        rename("ROI_EDT");
}

/*
# Analyse Aggregtes and Roots as a function of coloumn wall distance

 */

function ROI_EDT_analyse() {

    run("Merge Channels...", "c1=root c2=root_size c3=ROI_EDT keep");

    getDimensions(width, height, channels, slices, frames);

    distance_sum=newArray(256);
    distance_count=newArray(256);
    root_sum=newArray(256);
    root_count=newArray(256);
    root_size_sum=newArray(256);
    root_size_count=newArray(256);
    root_vol_vol=newArray(256);
    root_mean_size_mm=newArray(256);
    distance_mm=newArray(256);

    for(i=0;i<256;i++)
        {
            distance_sum[i]=0;
            distance_count[i]=0;
            root_size_sum[i]=0;
            root_size_count[i]=0;
            root_sum[i]=0;
            root_count[i]=0;
            root_vol_vol[i] = 0;
            root_mean_size_mm[i] = 0;
            distance_mm[i] = 0;

        }
    for (z = 1; z <= slices; z++) {
                setSlice(z);
        // Loop through all the rows of pixels
        for (y = 0; y < height; y+=5) {
```

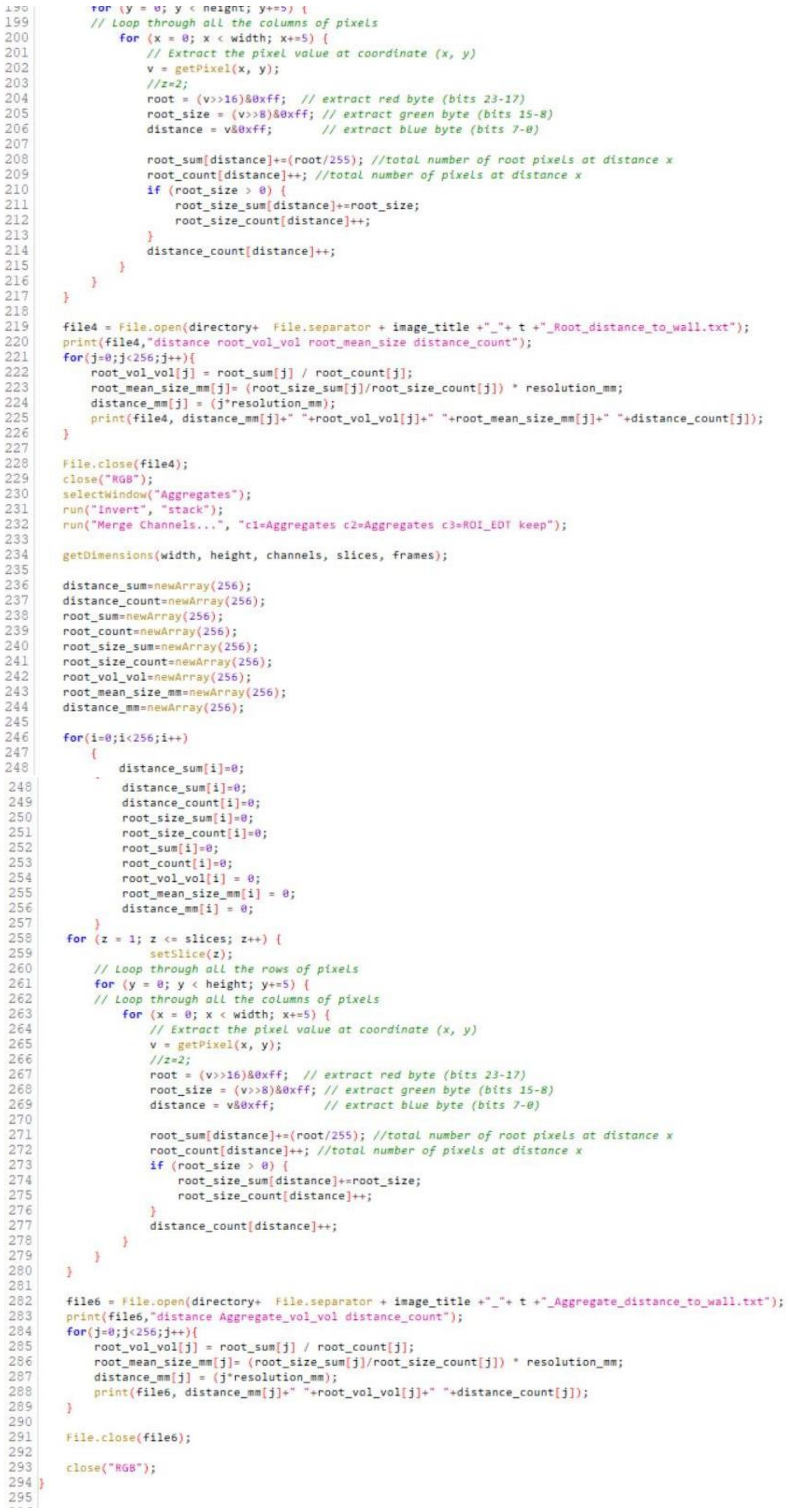

```
        for (y = 0; y < height; y+=5) {
        // Loop through all the columns of pixels
            for (x = 0; x < width; x+=5) {
                // Extract the pixel value at coordinate (x, y)
                v = getPixel(x, y);
                //z=2;
                root = (v>>16)&0xff;  // extract red byte (bits 23-17)
                root_size = (v>>8)&0xff; // extract green byte (bits 15-8)
                distance = v&0xff;       // extract blue byte (bits 7-0)

                root_sum[distance]+=(root/255); //total number of root pixels at distance x
                root_count[distance]++; //total number of pixels at distance x
                if (root_size > 0) {
                    root_size_sum[distance]+=root_size;
                    root_size_count[distance]++;
                }
                distance_count[distance]++;
            }
        }
    }

    file4 = File.open(directory+  File.separator + image_title +"_"+ t +"_Root_distance_to_wall.txt");
    print(file4,"distance root_vol_vol root_mean_size distance_count");
    for(j=0;j<256;j++){
        root_vol_vol[j] = root_sum[j] / root_count[j];
        root_mean_size_mm[j]= (root_size_sum[j]/root_size_count[j]) * resolution_mm;
        distance_mm[j] = (j*resolution_mm);
        print(file4, distance_mm[j]+" "+root_vol_vol[j]+" "+root_mean_size_mm[j]+" "+distance_count[j]);
    }

    File.close(file4);
    close("RGB");
    selectWindow("Aggregates");
    run("Invert", "stack");
    run("Merge Channels...", "c1=Aggregates c2=Aggregates c3=ROI_EDT keep");

    getDimensions(width, height, channels, slices, frames);

    distance_sum=newArray(256);
    distance_count=newArray(256);
    root_sum=newArray(256);
    root_count=newArray(256);
    root_size_sum=newArray(256);
    root_size_count=newArray(256);
    root_vol_vol=newArray(256);
    root_mean_size_mm=newArray(256);
    distance_mm=newArray(256);

    for(i=0;i<256;i++)
        {
            distance_sum[i]=0;
            distance_sum[i]=0;
            distance_count[i]=0;
            root_size_sum[i]=0;
            root_size_count[i]=0;
            root_sum[i]=0;
            root_count[i]=0;
            root_vol_vol[i] = 0;
            root_mean_size_mm[i] = 0;
            distance_mm[i] = 0;
        }
    for (z = 1; z <= slices; z++) {
                setSlice(z);
        // Loop through all the rows of pixels
        for (y = 0; y < height; y+=5) {
        // Loop through all the columns of pixels
            for (x = 0; x < width; x+=5) {
                // Extract the pixel value at coordinate (x, y)
                v = getPixel(x, y);
                //z=2;
                root = (v>>16)&0xff;  // extract red byte (bits 23-17)
                root_size = (v>>8)&0xff; // extract green byte (bits 15-8)
                distance = v&0xff;       // extract blue byte (bits 7-0)

                root_sum[distance]+=(root/255); //total number of root pixels at distance x
                root_count[distance]++; //total number of pixels at distance x
                if (root_size > 0) {
                    root_size_sum[distance]+=root_size;
                    root_size_count[distance]++;
                }
                distance_count[distance]++;
            }
        }
    }

    file6 = File.open(directory+  File.separator + image_title +"_"+ t +"_Aggregate_distance_to_wall.txt");
    print(file6,"distance Aggregate_vol_vol distance_count");
    for(j=0;j<256;j++){
        root_vol_vol[j] = root_sum[j] / root_count[j];
        root_mean_size_mm[j]= (root_size_sum[j]/root_size_count[j]) * resolution_mm;
        distance_mm[j] = (j*resolution_mm);
        print(file6, distance_mm[j]+" "+root_vol_vol[j]+" "+distance_count[j]);
    }

    File.close(file6);

    close("RGB");
}
```

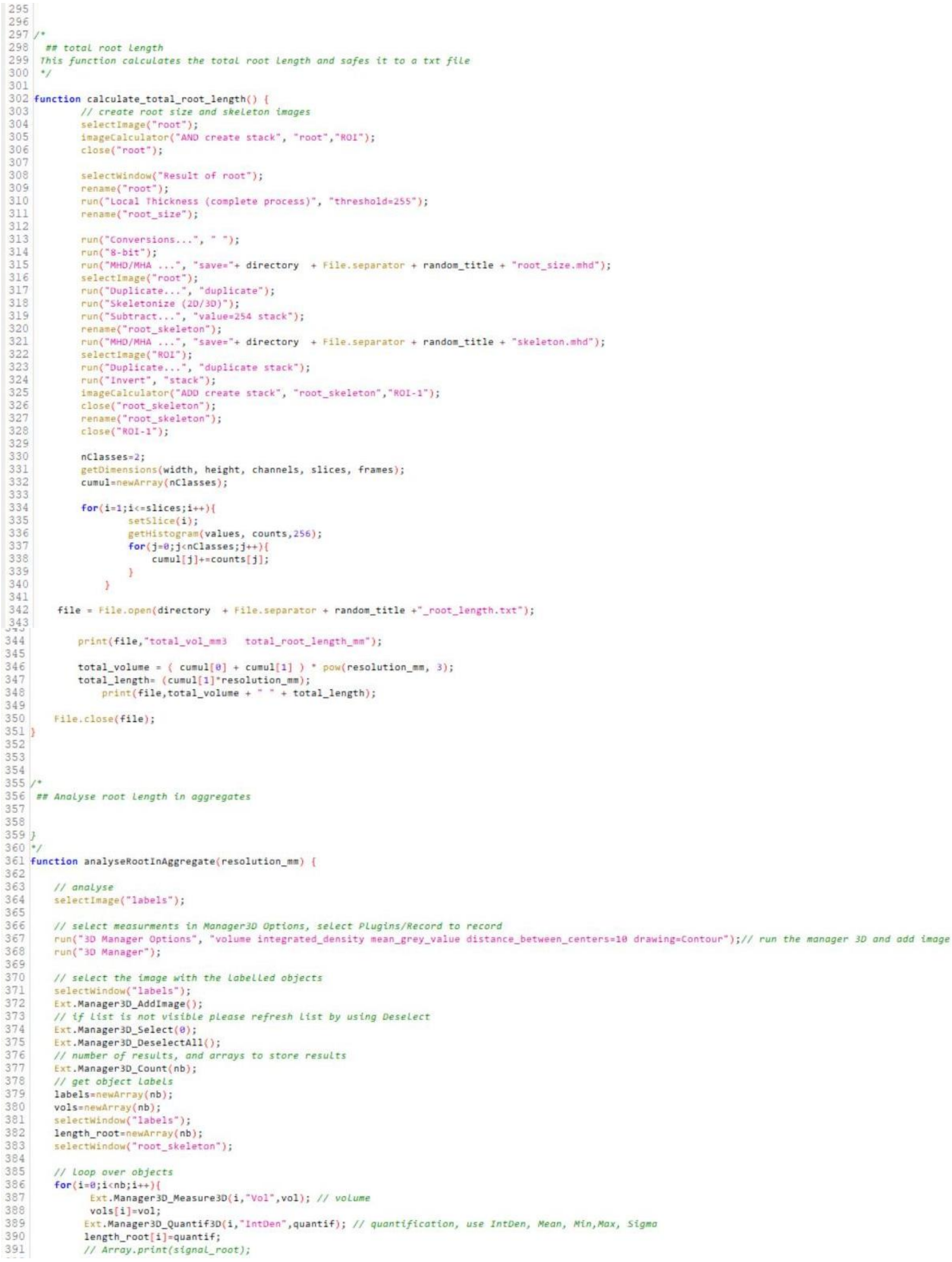

```


/*
  ## total root length
 This function calculates the total root length and safes it to a txt file
 */

function calculate_total_root_length() {
        // create root size and skeleton images
        selectImage("root");
        imageCalculator("AND create stack", "root","ROI");
        close("root");

        selectWindow("Result of root");
        rename("root");
        run("Local Thickness (complete process)", "threshold=255");
        rename("root_size");

        run("Conversions...", " ");
        run("8-bit");
        run("MHD/MHA ...", "save="+ directory  + File.separator + random_title + "root_size.mhd");
        selectImage("root");
        run("Duplicate...", "duplicate");
        run("Skeletonize (2D/3D)");
        run("Subtract...", "value=254 stack");
        rename("root_skeleton");
        run("MHD/MHA ...", "save="+ directory  + File.separator + random_title + "skeleton.mhd");
        selectImage("ROI");
        run("Duplicate...", "duplicate stack");
        run("Invert", "stack");
        imageCalculator("ADD create stack", "root_skeleton","ROI-1");
        close("root_skeleton");
        rename("root_skeleton");
        close("ROI-1");

        nClasses=2;
        getDimensions(width, height, channels, slices, frames);
        cumul=newArray(nClasses);

        for(i=1;i<=slices;i++){
                setSlice(i);
                getHistogram(values, counts,256);
                for(j=0;j<nClasses;j++){
                    cumul[j]+=counts[j];
                }
            }

    file = File.open(directory  + File.separator + random_title +"_root_length.txt");

       print(file,"total_vol_mm3   total_root_length_mm");

       total_volume = ( cumul[0] + cumul[1] ) * pow(resolution_mm, 3);
       total_length= (cumul[1]*resolution_mm);
           print(file,total_volume + " " + total_length);

    File.close(file);
}




/*
 ## Analyse root length in aggregates


}
*/
function analyseRootInAggregate(resolution_mm) {

    // analyse
    selectImage("labels");

    // select measurments in Manager3D Options, select Plugins/Record to record
    run("3D Manager Options", "volume integrated_density mean_grey_value distance_between_centers=10 drawing=Contour");// run the manager 3D and add image
    run("3D Manager");

    // select the image with the labelled objects
    selectWindow("labels");
    Ext.Manager3D_AddImage();
    // if list is not visible please refresh list by using Deselect
    Ext.Manager3D_Select(0);
    Ext.Manager3D_DeselectAll();
    // number of results, and arrays to store results
    Ext.Manager3D_Count(nb);
    // get object labels
    labels=newArray(nb);
    vols=newArray(nb);
    selectWindow("labels");
    length_root=newArray(nb);
    selectWindow("root_skeleton");

    // loop over objects
    for(i=0;i<nb;i++){
          Ext.Manager3D_Measure3D(i,"Vol",vol); // volume
          vols[i]=vol;
         Ext.Manager3D_Quantif3D(i,"IntDen",quantif); // quantification, use IntDen, Mean, Min,Max, Sigma
         length_root[i]=quantif;
         // Array.print(signal_root);
```

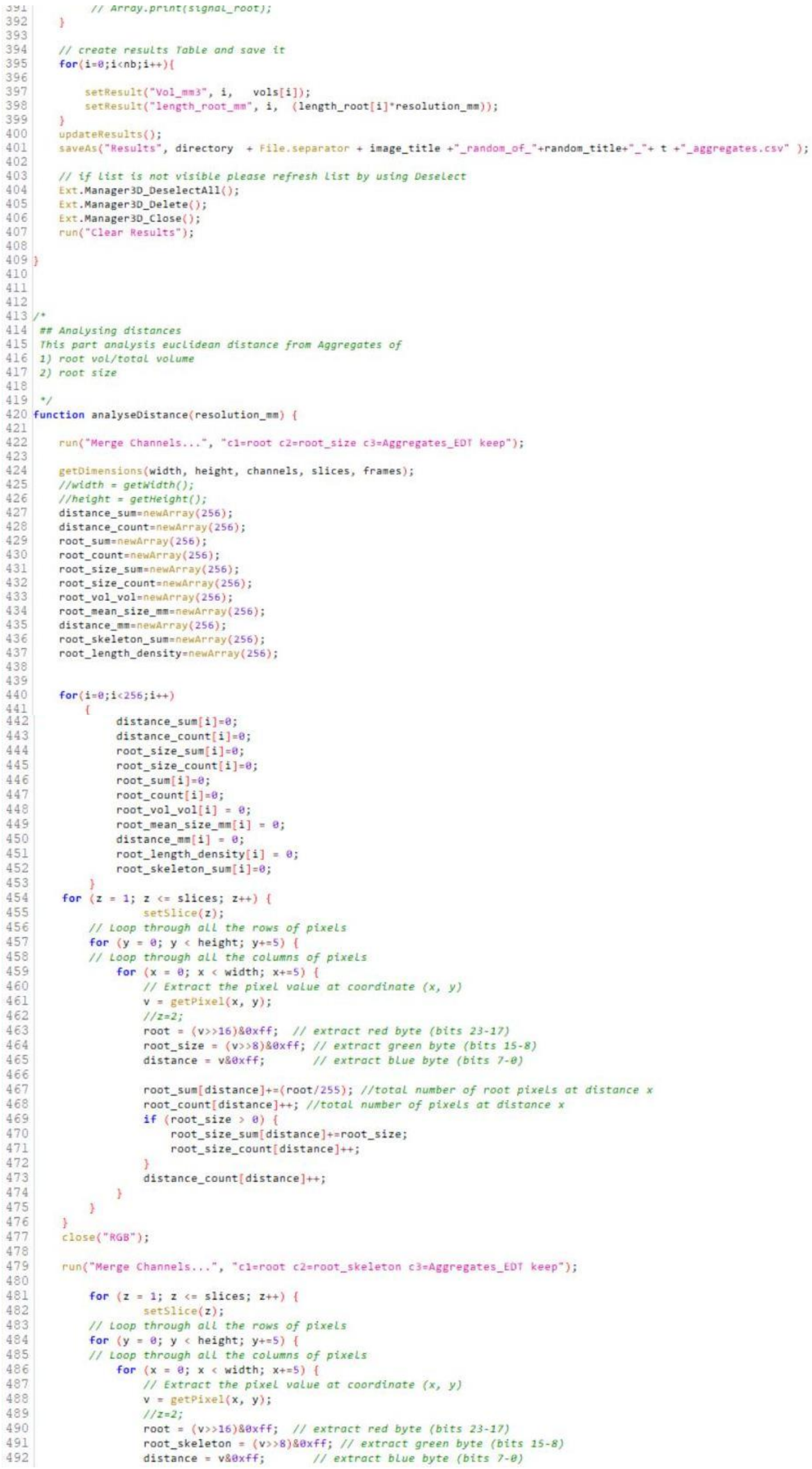

```
        // Array.print(signal_root);
    }

    // create results Table and save it
    for(i=0;i<nb;i++){

        setResult("Vol_mm3", i,   vols[i]);
        setResult("length_root_mm", i,  (length_root[i]*resolution_mm));
    }
    updateResults();
    saveAs("Results", directory  + File.separator + image_title +"_random_of_"+random_title+"_"+ t +"_aggregates.csv" );

    // if list is not visible please refresh list by using Deselect
    Ext.Manager3D_DeselectAll();
    Ext.Manager3D_Delete();
    Ext.Manager3D_Close();
    run("Clear Results");

}



/*
 ## Analysing distances
 This part analysis euclidean distance from Aggregates of
 1) root vol/total volume
 2) root size

 */
function analyseDistance(resolution_mm) {

    run("Merge Channels...", "c1=root c2=root_size c3=Aggregates_EDT keep");

    getDimensions(width, height, channels, slices, frames);
    //width = getWidth();
    //height = getHeight();
    distance_sum=newArray(256);
    distance_count=newArray(256);
    root_sum=newArray(256);
    root_count=newArray(256);
    root_size_sum=newArray(256);
    root_size_count=newArray(256);
    root_vol_vol=newArray(256);
    root_mean_size_mm=newArray(256);
    distance_mm=newArray(256);
    root_skeleton_sum=newArray(256);
    root_length_density=newArray(256);


    for(i=0;i<256;i++)
        {
            distance_sum[i]=0;
            distance_count[i]=0;
            root_size_sum[i]=0;
            root_size_count[i]=0;
            root_sum[i]=0;
            root_count[i]=0;
            root_vol_vol[i] = 0;
            root_mean_size_mm[i] = 0;
            distance_mm[i] = 0;
            root_length_density[i] = 0;
            root_skeleton_sum[i]=0;
        }
     for (z = 1; z <= slices; z++) {
                setSlice(z);
        // Loop through all the rows of pixels
        for (y = 0; y < height; y+=5) {
        // Loop through all the columns of pixels
            for (x = 0; x < width; x+=5) {
                // Extract the pixel value at coordinate (x, y)
                v = getPixel(x, y);
                //z=2;
                root = (v>>16)&0xff;  // extract red byte (bits 23-17)
                root_size = (v>>8)&0xff; // extract green byte (bits 15-8)
                distance = v&0xff;       // extract blue byte (bits 7-0)

                root_sum[distance]+=(root/255); //total number of root pixels at distance x
                root_count[distance]++; //total number of pixels at distance x
                if (root_size > 0) {
                    root_size_sum[distance]+=root_size;
                    root_size_count[distance]++;
                }
                distance_count[distance]++;
            }
        }
    }
    close("RGB");

    run("Merge Channels...", "c1=root c2=root_skeleton c3=Aggregates_EDT keep");

        for (z = 1; z <= slices; z++) {
                setSlice(z);
        // Loop through all the rows of pixels
        for (y = 0; y < height; y+=5) {
        // Loop through all the columns of pixels
            for (x = 0; x < width; x+=5) {
                // Extract the pixel value at coordinate (x, y)
                v = getPixel(x, y);
                //z=2;
                root = (v>>16)&0xff;  // extract red byte (bits 23-17)
                root_skeleton = (v>>8)&0xff; // extract green byte (bits 15-8)
                distance = v&0xff;       // extract blue byte (bits 7-0)
```

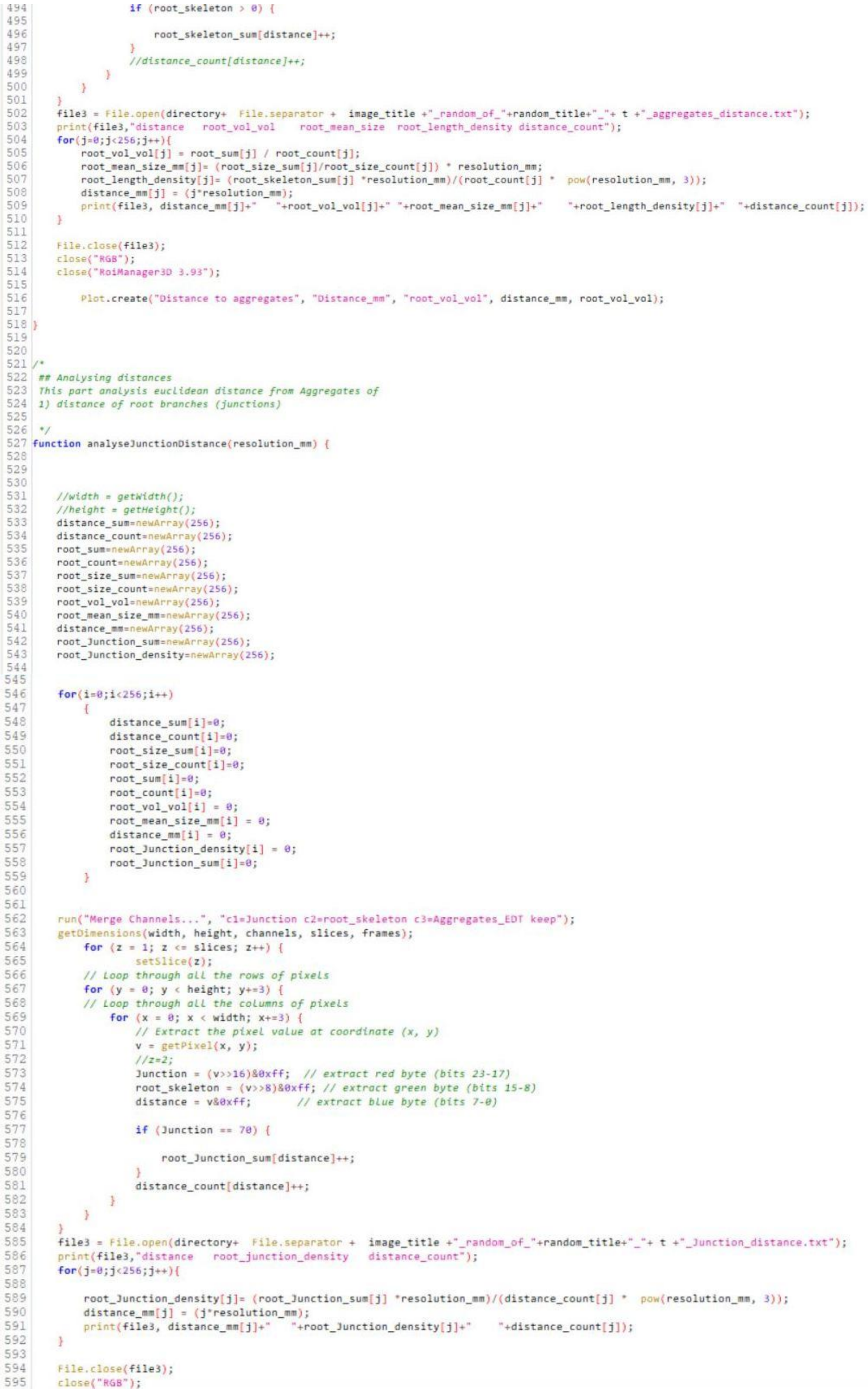

```
                if (root_skeleton > 0) {

                    root_skeleton_sum[distance]++;
                }
                //distance_count[distance]++;
            }
        }
    }
    file3 = File.open(directory+  File.separator +  image_title +"_random_of_"+random_title+"_"+ t +"_aggregates_distance.txt");
    print(file3,"distance   root_vol_vol    root_mean_size  root_length_density distance_count");
    for(j=0;j<256;j++){
        root_vol_vol[j] = root_sum[j] / root_count[j];
        root_mean_size_mm[j]= (root_size_sum[j]/root_size_count[j]) * resolution_mm;
        root_length_density[j]= (root_skeleton_sum[j] *resolution_mm)/(root_count[j] *  pow(resolution_mm, 3));
        distance_mm[j] = (j*resolution_mm);
        print(file3, distance_mm[j]+"   "+root_vol_vol[j]+" "+root_mean_size_mm[j]+"    "+root_length_density[j]+"  "+distance_count[j]);
    }

    File.close(file3);
    close("RGB");
    close("RoiManager3D 3.93");

        Plot.create("Distance to aggregates", "Distance_mm", "root_vol_vol", distance_mm, root_vol_vol);

}


/*
 ## Analysing distances
 This part analysis euclidean distance from Aggregates of
 1) distance of root branches (junctions)

 */
function analyseJunctionDistance(resolution_mm) {



    //width = getWidth();
    //height = getHeight();
    distance_sum=newArray(256);
    distance_count=newArray(256);
    root_sum=newArray(256);
    root_count=newArray(256);
    root_size_sum=newArray(256);
    root_size_count=newArray(256);
    root_vol_vol=newArray(256);
    root_mean_size_mm=newArray(256);
    distance_mm=newArray(256);
    root_Junction_sum=newArray(256);
    root_Junction_density=newArray(256);


    for(i=0;i<256;i++)
        {
            distance_sum[i]=0;
            distance_count[i]=0;
            root_size_sum[i]=0;
            root_size_count[i]=0;
            root_sum[i]=0;
            root_count[i]=0;
            root_vol_vol[i] = 0;
            root_mean_size_mm[i] = 0;
            distance_mm[i] = 0;
            root_Junction_density[i] = 0;
            root_Junction_sum[i]=0;
        }


    run("Merge Channels...", "c1=Junction c2=root_skeleton c3=Aggregates_EDT keep");
    getDimensions(width, height, channels, slices, frames);
        for (z = 1; z <= slices; z++) {
                setSlice(z);
        // Loop through all the rows of pixels
        for (y = 0; y < height; y+=3) {
        // Loop through all the columns of pixels
            for (x = 0; x < width; x+=3) {
                // Extract the pixel value at coordinate (x, y)
                v = getPixel(x, y);
                //z=2;
                Junction = (v>>16)&0xff;  // extract red byte (bits 23-17)
                root_skeleton = (v>>8)&0xff; // extract green byte (bits 15-8)
                distance = v&0xff;        // extract blue byte (bits 7-0)

                if (Junction == 70) {

                    root_Junction_sum[distance]++;
                }
                distance_count[distance]++;
            }
        }
    }
    file3 = File.open(directory+  File.separator +  image_title +"_random_of_"+random_title+"_"+ t +"_Junction_distance.txt");
    print(file3,"distance   root_junction_density   distance_count");
    for(j=0;j<256;j++){

        root_Junction_density[j]= (root_Junction_sum[j] *resolution_mm)/(distance_count[j] *  pow(resolution_mm, 3));
        distance_mm[j] = (j*resolution_mm);
        print(file3, distance_mm[j]+"   "+root_Junction_density[j]+"    "+distance_count[j]);
    }

    File.close(file3);
    close("RGB");
```

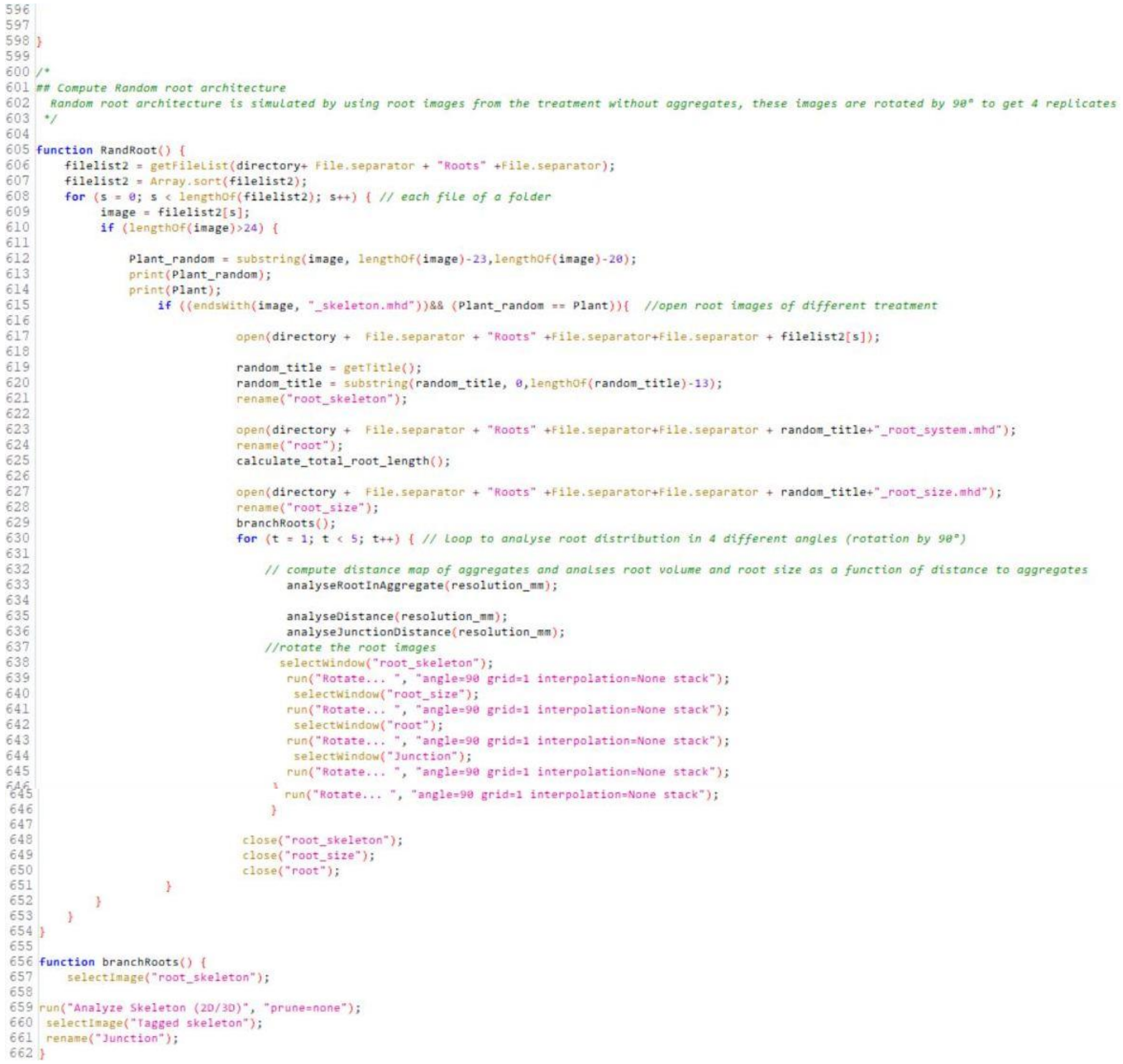

```
}

/*
## Compute Random root architecture
  Random root architecture is simulated by using root images from the treatment without aggregates, these images are rotated by 90° to get 4 replicates
 */

function RandRoot() {
    filelist2 = getFileList(directory+ File.separator + "Roots" +File.separator);
    filelist2 = Array.sort(filelist2);
    for (s = 0; s < lengthOf(filelist2); s++) { // each file of a folder
         image = filelist2[s];
         if (lengthOf(image)>24) {

             Plant_random = substring(image, lengthOf(image)-23,lengthOf(image)-20);
             print(Plant_random);
             print(Plant);
                 if ((endsWith(image, "_skeleton.mhd"))&& (Plant_random == Plant)){  //open root images of different treatment

                             open(directory +  File.separator + "Roots" +File.separator+File.separator + filelist2[s]);

                             random_title = getTitle();
                             random_title = substring(random_title, 0,lengthOf(random_title)-13);
                             rename("root_skeleton");

                             open(directory +  File.separator + "Roots" +File.separator+File.separator + random_title+"_root_system.mhd");
                             rename("root");
                             calculate_total_root_length();

                             open(directory +  File.separator + "Roots" +File.separator+File.separator + random_title+"_root_size.mhd");
                             rename("root_size");
                             branchRoots();
                             for (t = 1; t < 5; t++) { // loop to analyse root distribution in 4 different angles (rotation by 90°)

                                 // compute distance map of aggregates and analses root volume and root size as a function of distance to aggregates
                                    analyseRootInAggregate(resolution_mm);

                                    analyseDistance(resolution_mm);
                                    analyseJunctionDistance(resolution_mm);
                                 //rotate the root images
                                   selectWindow("root_skeleton");
                                    run("Rotate... ", "angle=90 grid=1 interpolation=None stack");
                                     selectWindow("root_size");
                                    run("Rotate... ", "angle=90 grid=1 interpolation=None stack");
                                     selectWindow("root");
                                    run("Rotate... ", "angle=90 grid=1 interpolation=None stack");
                                     selectWindow("Junction");
                                    run("Rotate... ", "angle=90 grid=1 interpolation=None stack");
                                    run("Rotate... ", "angle=90 grid=1 interpolation=None stack");
                                 }

                              close("root_skeleton");
                              close("root_size");
                              close("root");
                 }
         }
    }
}

function branchRoots() {
    selectImage("root_skeleton");

run("Analyze Skeleton (2D/3D)", "prune=none");
 selectImage("Tagged skeleton");
 rename("Junction");
}
```

AF.10: Image-J script, which was published as an ijm file together with the publication in chapter 4.

8.4 Appendices for Chapter 5

AT.4: Impact of substrate (loam, sand) and maize genotype (wild-type - WT, root hair defective mutant rth3 – rth3) on mycorrhizal colonisation of roots 22 days after planting; numbers in brackets refer to standard error.

	L_WT	L_*rth3*	S_WT	S_*rth3*
Arbuscules%	1.0 (0.5)	3.3 (0.9)	3.5 (1.5)	3.02 (0.6)
Hyphae%	9.3 (2.06)	27.3 (1.5)	21.2 (3.6)	26.8 (3.2)
Vesicles%	0 (0)	0.5 (0.5)	0 (0)	0 (0)

AT.5: Share or root length in diameter classes > 0.5 mm for two different bulk densities in loam for root hair defective mutant rth3 and its corresponding wild-type. Results refer to an additional experiment set up like the main experiment of this MS, for loam only with n=5.

	L_WT		L_*rth3*	
Bulk density cm cm^{-3}	1.3	1.45	1.3	1.45
Root length in diameter classes >0.5 mm in %	3	45	7	58

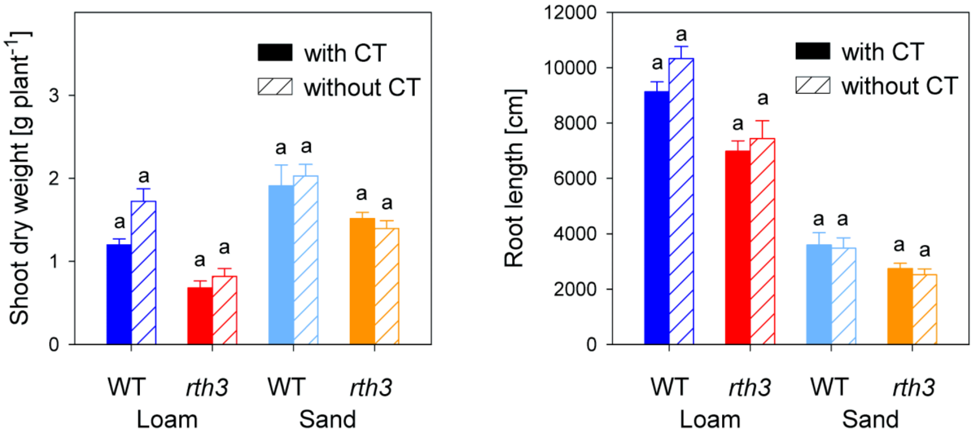

AF.11: Impact of X-ray CT scanning on shoot and root growth of two maize genotypes (wild-type - WT, root hair defective mutant rth3 – rth3) in loam (L) and sand (S) 22 days after planting. Plants were either scanned 7, 14 and 21 days after planting or were

not exposed to X-ray CT at all. Mean values of six replicates are shown, error bars denote the standard error. Statistics: three-factorial ANOVA in conjunction with Tukey's HSD test. Significant differences between treatments are displayed with small letters for $p < 0.05$.

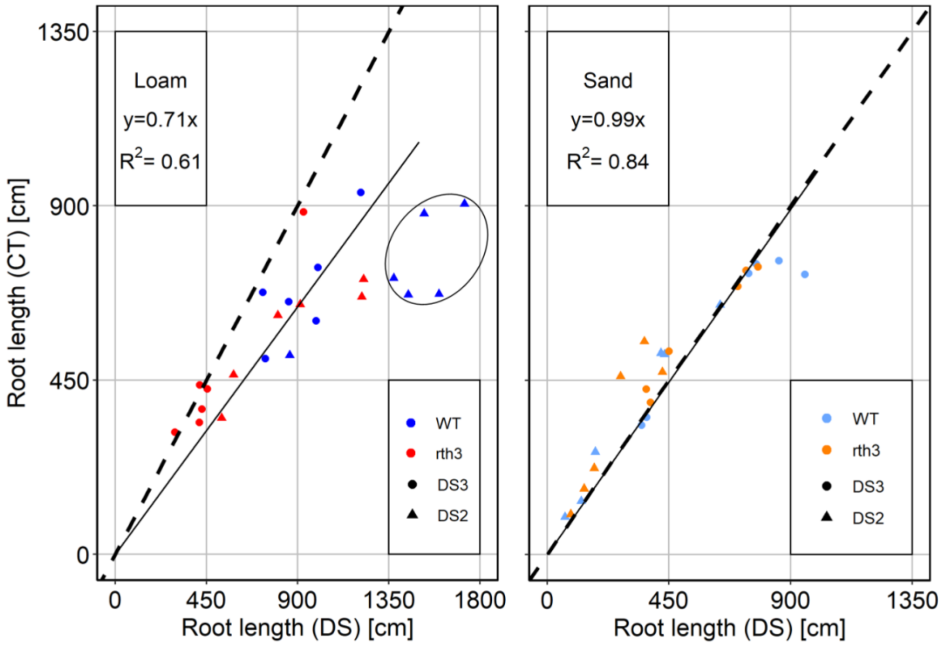

AF.12: Root recovery with destructive sampling as compared to root recovery with non-invasive X-ray CT scanning and subsequent segmentation of roots with the algorithm Rootine 2.0. For the correlation only layers WR2 and WR3 were used (Figure 5.1). The encircled values from the layer WR2 from treatment L_WT at 21 days after planting were not included in the calculation..

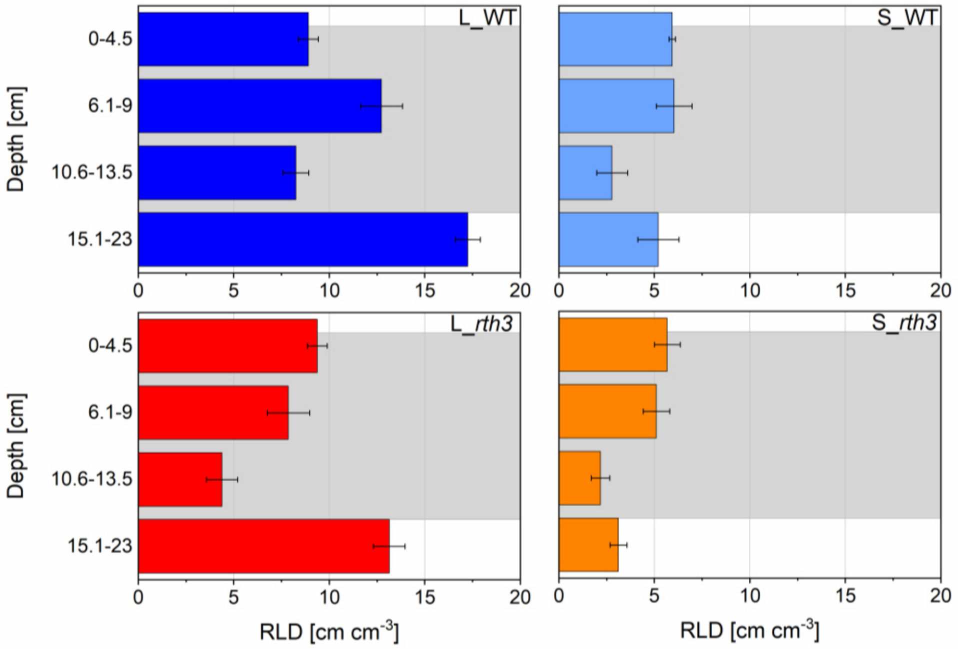

AF.13: Change of root length density with depth for 22 days after planting for two maize genotypes (wild-type - WT, root hair defective mutant rth3 – rth3) grown in loam (L)

and sand (S). Data are derived from destructive sampling of soil columns in layers; n=6, bars represent standard error. The layers which correspond to the depth analysed by X-ray CT are shaded in grey. Significant differences between depths within treatments are displayed next to the bars with small letters for p < 0.05. Significant effects of factor between treatments within the same depth is denoted by s for substrate, g for genotype and x for interaction next to the graphs for p < 0.05.

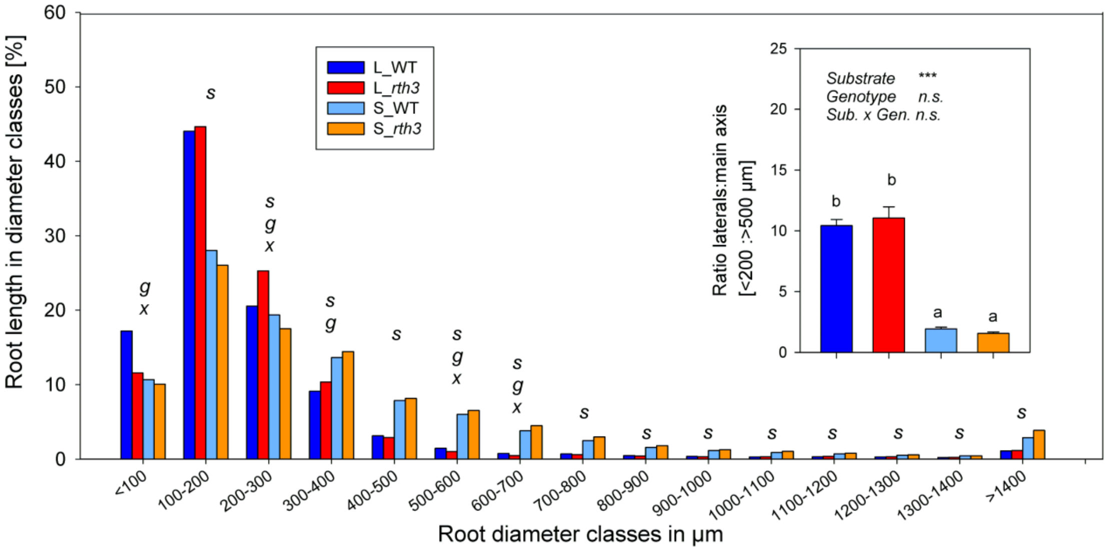

AF.14: Root length in different root diameter classes (class width 100 µm) 22 days after planting for two maize genotypes (wild-type - WT, root hair defective mutant rth3 – rth3) grown on either loam (L) or sand (S). Data are derived from WinRhizo after destructive sampling of soil columns; n=6. Statistics: two-factorial ANOVA in conjunction with Tukey's HSD test was conducted for each diameter class. Significant effect of factor is denoted by s for substrate, g for genotype and x for interaction, for p > 0.05 no letter is displayed. The inset shows proportion of laterals roots versus thick axial roots, i.e. assuming that roots diameter classes < 200 µm comprise laterals only; root diameter classes > 500 µm comprise thick axial roots only. Mean values of six replicates are shown, error bars denote the standard error. Statistics: three-factorial ANOVA in conjunction with Tukey's HSD test. Significant differences between treatments are displayed with small letters for p < 0.05.

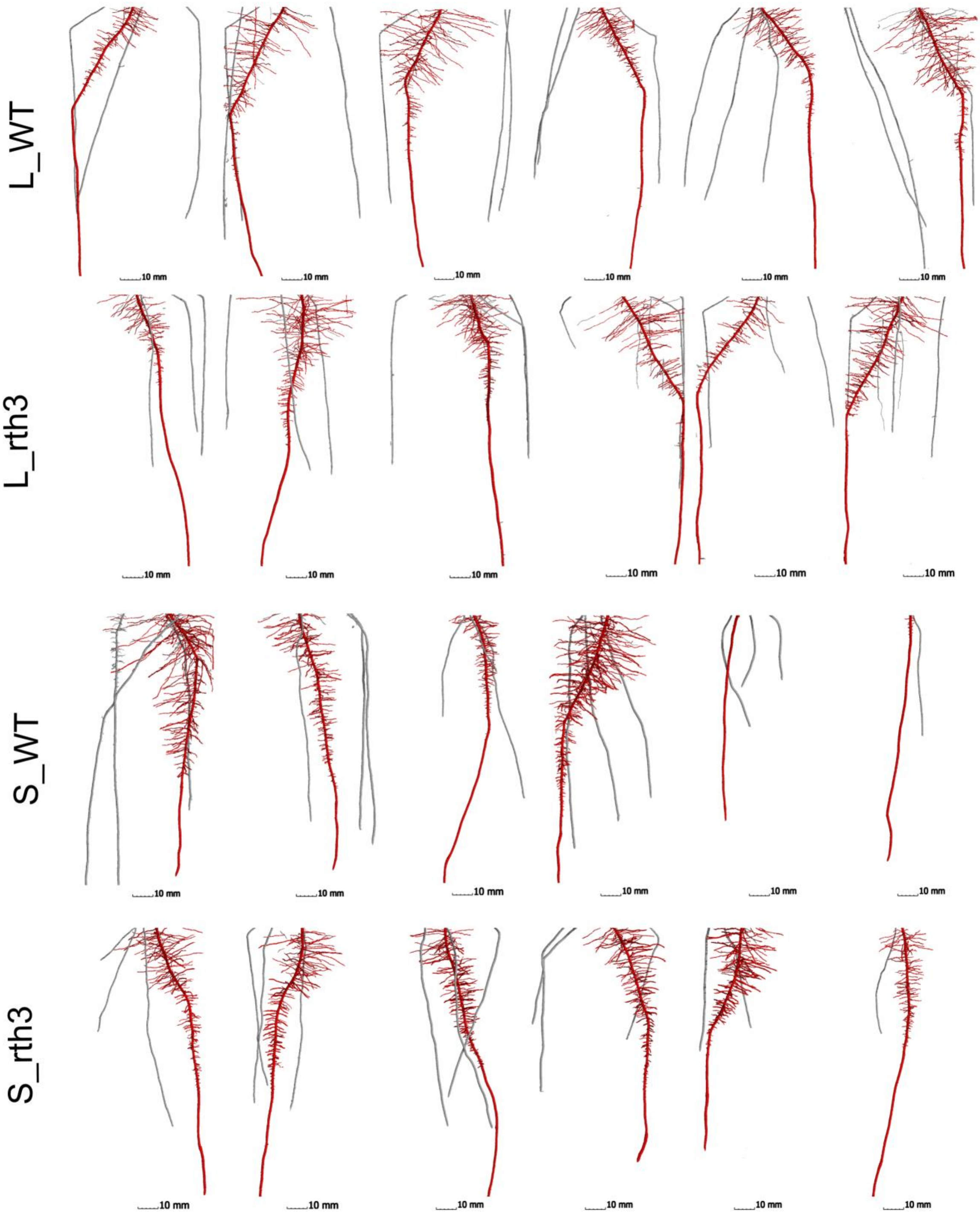
L_WT
L_rth3
S_WT
S_rth3
10 mm

AF.15: 3D rendering of root networks 7 days after planting for all replicates of each treatment. The primary root and all laterals connected to it are depicted in red; seminal roots in grey.

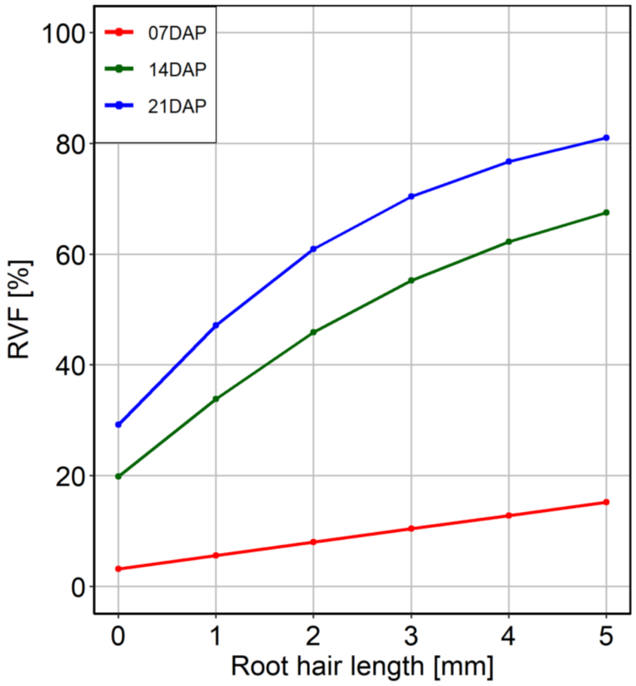

AF.16: Change of RVF with time for different root length scenarios. Scenarios were calculated based on root system architecture of the treatment S_WT. Values for root hair length = 0 correspond to extent of P depletion zone of 1.8 mm (see Figure 5.9).

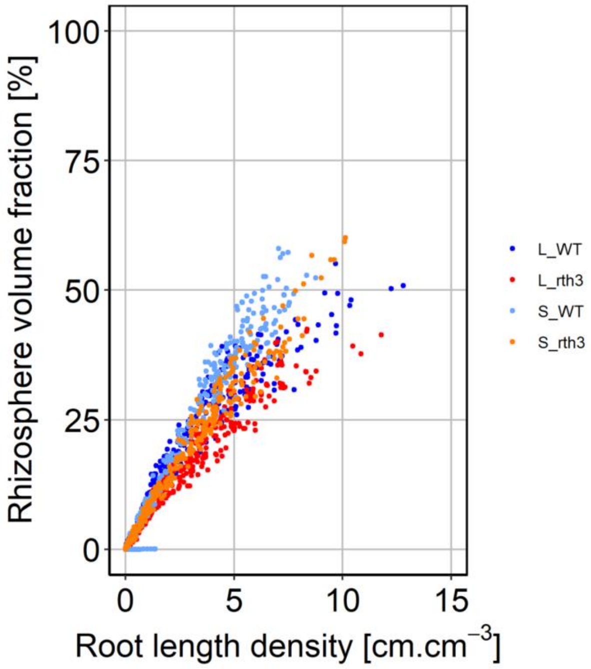

AF.17: Scatter plot of RVF versus RLD for all time points and treatments across all depths. Different colours indicate the different treatments. Rhizosphere volume fraction is determined assuming a typical rhizosphere extent for P depletion of < 1.8 mm, plus 0.24 mm for hair length in WT.

Bibliography

(1) Philippot, L.; Raaijmakers, J. M.; Lemanceau, P.; Van Der Putten, W. H. Going Back to the Roots: The Microbial Ecology of the Rhizosphere. *Nat. Rev. Microbiol.* 2013, *11* (11), 789–799. https://doi.org/10.1038/nrmicro3109.

(2) Pierret, A.; Doussan, C.; Capowiez, Y.; Bastardie, F.; Pagès, L. Root Functional Architecture: A Framework for Modeling the Interplay between Roots and Soil. *Vadose Zo. J.* 2007, *6* (2), 269–281. https://doi.org/10.2136/vzj2006.0067.

(3) Vetterlein, D.; Lippold, E.; Schreiter, S.; Phalempin, M.; Fahrenkampf, T.; Hochholdinger, F.; Marcon, C.; Tarkka, M.; Oburger, E.; Ahmed, M.; Javaux, M.; Schlüter, S. Experimental Platforms for the Investigation of Spatiotemporal Patterns in the Rhizosphere—Laboratory and Field Scale. *J. Plant Nutr. Soil Sci.* 2021, *184* (1), 35–50. https://doi.org/10.1002/jpln.202000079.

(4) Hinsinger, P.; Bengough, A. G.; Vetterlein, D.; Young, I. M. Rhizosphere: Biophysics, Biogeochemistry and Ecological Relevance. *Plant Soil* 2009, *321* (1–2), 117–152. https://doi.org/10.1007/s11104-008-9885-9.

(5) Vetterlein, D.; Carminati, A.; Kögel-Knabner, I.; Bienert, G. P.; Smalla, K.; Oburger, E.; Schnepf, A.; Banitz, T.; Tarkka, M. T.; Schlüter, S. Rhizosphere Spatiotemporal Organization–A Key to Rhizosphere Functions. *Front. Agron.* 2020, *2* (July), 1–22. https://doi.org/10.3389/fagro.2020.00008.

(6) Schnepf, A.; Carminati, A.; Ahmed, M. A.; Ani, M.; Benard, P.; Bentz, J.; Bonkowski, M.; Knott, M.; Diehl, D.; Duddek, P.; Kröner, E.; Javaux, M.; Landl, M.; Lehndorff, E.; Lippold, E.; Lieu, A.; Mueller, C. W.; Oburger, E.; Otten, W.; Portell, X.; Phalempin, M.; Prechtel, A.; Schulz, R.; Vanderborght, J.; Vetterlein, D. *Linking Rhizosphere Processes across Scales: Opinion*; 2022; Vol. 478. https://doi.org/10.1007/s11104-022-05306-7.

(7) Oburger, E.; Schmidt, H. New Methods To Unravel Rhizosphere Processes. *Trends Plant Sci.* 2016, *21* (3), 243–255. https://doi.org/10.1016/j.tplants.2015.12.005.

(8) Kuzyakov, Y.; Razavi, B. S. Rhizosphere Size and Shape: Temporal Dynamics and Spatial Stationarity. *Soil Biol. Biochem.* 2019, *135* (May),

343–360. https://doi.org/10.1016/j.soilbio.2019.05.011.

(9) Darrah, P. R. The Rhizosphere and Plant Nutrition: A Quantitative Approach. *Plant Soil* 1993, *155–156* (1), 1–20. https://doi.org/10.1007/BF00024980.

(10) Hinsinger, P.; Gilkes, R. J. Mobilization of Phosphate from Phosphate Rock and Alumina-Sorbed Phosphate by the Roots of Ryegrass and Clover as Related to Rhizosphere PH. *Eur. J. Soil Sci.* 1996, *47* (4), 533–544. https://doi.org/10.1111/j.1365-2389.1996.tb01853.x.

(11) Bilyera, N.; Hummel, C.; Daudin, G.; Santangeli, M.; Zhang, X.; Santner, J.; Lippold, E.; Schlüter, S.; Bertrand, I.; Wenzel, W.; Spielvogel, S.; Vetterlein, D.; Razavi, B. S.; Oburger, E. Co-Localised Phosphorus Mobilization Processes in the Rhizosphere of Field-Grown Maize Jointly Contribute to Plant Nutrition. *Soil Biol. Biochem.* 2022, *165*, 108497. https://doi.org/10.1016/j.soilbio.2021.108497.

(12) Roose, T.; Keyes, S. D.; Daly, K. R.; Carminati, A.; Otten, W.; Vetterlein, D.; Peth, S. Challenges in Imaging and Predictive Modeling of Rhizosphere Processes. *Plant Soil* 2016, *407* (1–2), 9–38. https://doi.org/10.1007/s11104-016-2872-7.

(13) Göttlein, A.; Heim, A.; Matzner, E. Mobilization of Aluminium in the Rhizosphere Soil Solution of Growing Tree Roots in an Acidic Soil. *Plant Soil* 1999, *211* (1), 41–49. https://doi.org/10.1023/A:1004332916188.

(14) Dessureault-Rompré, J.; Nowack, B.; Schulin, R.; Luster, J. Modified Micro Suction Cup/Rhizobox Approach for the in-Situ Detection of Organic Acids in Rhizosphere Soil Solution. *Plant Soil* 2006, *286* (1–2), 99–107. https://doi.org/10.1007/s11104-006-9029-z.

(15) Werner, L. M.; Knott, M.; Diehl, D.; Ahmed, M. A.; Banfield, C.; Dippold, M.; Vetterlein, D.; Wimmer, M. A. Physico-Chemical Properties of Maize (Zea Mays L.) Mucilage Differ with the Collection System and Corresponding Root Type and Developmental Stage of the Plant. *Plant Soil* 2022, No. 0123456789. https://doi.org/10.1007/s11104-022-05633-9.

(16) Vetterlein, D.; Doussan, C. Root Age Distribution: How Does It Matter in Plant Processes? A Focus on Water Uptake. *Plant Soil* 2016, *407* (1–2), 145–160. https://doi.org/10.1007/s11104-016-2849-6.

(17) Lucas, M.; Schlüter, S.; Vogel, H.; Vetterlein, D. Soil Structure Formation along an Agricultural Chronosequence. *Geoderma* 2019, *350* (November 2018), 61–72. https://doi.org/10.1016/j.geoderma.2019.04.041.

(18) Schlüter, S.; Eickhorst, T.; Mueller, C. W. Correlative Imaging Reveals

Holistic View of Soil Microenvironments. *Environ. Sci. Technol.* 2019, *53* (2), 829–837. https://doi.org/10.1021/acs.est.8b05245.

(19) Hapca, S.; Baveye, P. C.; Wilson, C.; Lark, R. M.; Otten, W. Three-Dimensional Mapping of Soil Chemical Characteristics at Micrometric Scale by Combining 2D SEM-EDX Data and 3D X-Ray CT Images. *PLoS One* 2015, *10* (9). https://doi.org/10.1371/journal.pone.0137205.

(20) Keyes, S.; van Veelen, A.; McKay Fletcher, D.; Scotson, C.; Koebernick, N.; Petroselli, C.; Williams, K.; Ruiz, S.; Cooper, L.; Mayon, R.; Duncan, S.; Dumont, M.; Jakobsen, I.; Oldroyd, G.; Tkacz, A.; Poole, P.; Mosselmans, F.; Borca, C.; Huthwelker, T.; Jones, D. L.; Roose, T. Multimodal Correlative Imaging and Modelling of Phosphorus Uptake from Soil by Hyphae of Mycorrhizal Fungi. *New Phytol.* 2022, *234* (2), 688–703. https://doi.org/10.1111/nph.17980.

(21) Juyal, A.; Otten, W.; Falconer, R.; Hapca, S.; Schmidt, H.; Baveye, P. C.; Eickhorst, T. Combination of Techniques to Quantify the Distribution of Bacteria in Their Soil Microhabitats at Different Spatial Scales. *Geoderma* 2019, *334* (February 2018), 165–174. https://doi.org/10.1016/j.geoderma.2018.07.031.

(22) Kravchenko, A. N.; Guber, A. K.; Razavi, B. S.; Koestel, J.; Blagodatskaya, E. V.; Kuzyakov, Y. Spatial Patterns of Extracellular Enzymes: Combining X-Ray Computed Micro-Tomography and 2D Zymography. *Soil Biol. Biochem.* 2019, *135* (June), 411–419. https://doi.org/10.1016/j.soilbio.2019.06.002.

(23) Lucas, M.; Pihlap, E.; Steffens, M.; Vetterlein, D.; Kögel-Knabner, I. Combination of Imaging Infrared Spectroscopy and X-Ray Computed Microtomography for the Investigation of Bio- and Physicochemical Processes in Structured Soils. *Front. Environ. Sci.* 2020, *8* (April), 1–12. https://doi.org/10.3389/fenvs.2020.00042.

(24) Hodge, A. The Plastic Plant: Root Responses to Heterogeneous Supplies of Nutrients. *New Phytol.* 2004, *162* (1), 9–24. https://doi.org/10.1111/j.1469-8137.2004.01015.x.

(25) Morris, E. C.; Griffiths, M.; Golebiowska, A.; Mairhofer, S.; Burr-Hersey, J.; Goh, T.; von Wangenheim, D.; Atkinson, B.; Sturrock, C. J.; Lynch, J. P.; Vissenberg, K.; Ritz, K.; Wells, D. M.; Mooney, S. J.; Bennett, M. J. Shaping 3D Root System Architecture. *Curr. Biol.* 2017, *27* (17), R919–R930. https://doi.org/10.1016/j.cub.2017.06.043.

(26) Miguel, M. A.; Postma, J. A.; Lynch, J. P. Phene Synergism between Root Hair Length and Basal Root Growth Angle for Phosphorus Acquisition. *Plant Physiol.* 2015, *167* (4), 1430–1439.

https://doi.org/10.1104/pp.15.00145.

(27) Wen, Z.; Li, H.; Shen, Q.; Tang, X.; Xiong, C.; Li, H.; Pang, J.; Ryan, M. H.; Lambers, H.; Shen, J. Tradeoffs among Root Morphology, Exudation and Mycorrhizal Symbioses for Phosphorus-Acquisition Strategies of 16 Crop Species. *New Phytol.* 2019, *223* (2), 882–895. https://doi.org/10.1111/nph.15833.

(28) York, L. M.; Carminati, A.; Mooney, S. J.; Ritz, K.; Bennett, M. J. The Holistic Rhizosphere: Integrating Zones, Processes, and Semantics in the Soil Influenced by Roots. *J. Exp. Bot.* 2016, *67* (12), 3629–3643. https://doi.org/10.1093/jxb/erw108.

(29) Bates, T. R.; Lynch, J. P. Root Hairs Confer a Competitive Advantage under Low Phosphorus Availability. *Plant Soil* 2001, *236* (2), 243–250. https://doi.org/10.1023/A:1012791706800.

(30) Jungk, A. Root Hairs and the Acquisition of Plant Nutrientsfrom Soil. *J. Plant Nutr. Soil Sci.* 2001, *164*, 121–129.

(31) Bengough, A. G.; Loades, K.; McKenzie, B. M.; Bengough Glyn, A.; Loades, K.; McKenzie, B. M.; Bengough, A. G.; Loades, K.; McKenzie, B. M.; Bengough Glyn, A.; Loades, K.; McKenzie, B. M.; Bengough, A. G.; Loades, K.; McKenzie, B. M. Root Hairs Aid Soil Penetration by Anchoring the Root Surface to Pore Walls. *J. Exp. Bot.* 2016, *67* (4), 1071–1078. https://doi.org/10.1093/jxb/erv560.

(32) Haling, R. E.; Brown, L. K.; Bengough, A. G.; Young, I. M.; Hallett, P. D.; White, P. J.; George, T. S. Root Hairs Improve Root Penetration, Root-Soil Contact, and Phosphorus Acquisition in Soils of Different Strength. *J. Exp. Bot.* 2013, *64* (12), 3711–3721. https://doi.org/10.1093/jxb/ert200.

(33) Schmidt, J. E.; Gaudin, A. C. M. Toward an Integrated Root Ideotype for Irrigated Systems. *Trends Plant Sci.* 2017, *22* (5), 433–443. https://doi.org/10.1016/j.tplants.2017.02.001.

(34) Hodge, A. Root Decisions. *Plant, Cell Environ.* 2009, *32* (6), 628–640. https://doi.org/10.1111/j.1365-3040.2008.01891.x.

(35) Nestler, J.; Liu, S.; Wen, T. J.; Paschold, A.; Marcon, C.; Tang, H. M.; Li, D.; Li, L.; Meeley, R. B.; Sakai, H.; Bruce, W.; Schnable, P. S.; Hochholdinger, F. Roothairless5, Which Functions in Maize (Zea Mays L.) Root Hair Initiation and Elongation Encodes a Monocot-Specific NADPH Oxidase. *Plant J.* 2014, *79* (5), 729–740. https://doi.org/10.1111/tpj.12578.

(36) Hochholdinger, F.; Wen, T.; Zimmermann, R.; Chimot-Marolle, P.; da Costa e Silva, O.; Bruce, W.; Lamkey, K. R.; Wienand, U.; Schnable, P. S.

The Maize (Zea Mays L.) Roothairless3 Gene Encodes a Putative GPI-Anchored, Monocot-Specific, COBRA-like Protein That Significantly Affects Grain Yield. *Plant J.* 2008, *54* (5), 888–898. https://doi.org/10.1111/j.1365-313X.2008.03459.x.

(37) Hochholdinger, F.; Yu, P.; Marcon, C. Genetic Control of Root System Development in Maize. *Trends Plant Sci.* 2018, *23* (1), 79–88. https://doi.org/10.1016/j.tplants.2017.10.004.

(38) Ritz, K.; McNicol, J. W.; Nunan, N.; Grayston, S.; Millard, P.; Atkinson, D.; Gollotte, A.; Habeshaw, D.; Boag, B.; Clegg, C. D.; Griffiths, B. S.; Wheatley, R. E.; Glover, L. A.; McCaig, A. E.; Prosser, J. I. Spatial Structure in Soil Chemical and Microbiological Properties in an Upland Grassland. *FEMS Microbiol. Ecol.* 2004, *49* (2), 191–205. https://doi.org/10.1016/j.femsec.2004.03.005.

(39) Portell, X.; Pot, V.; Garnier, P.; Otten, W.; Baveye, P. C. Microscale Heterogeneity of the Spatial Distribution of Organic Matter Can Promote Bacterial Biodiversity in Soils: Insights From Computer Simulations. *Front. Microbiol.* 2018, *9* (July), 1–16. https://doi.org/10.3389/fmicb.2018.01583.

(40) Rabot, E.; Wiesmeier, M.; Schlüter, S.; Vogel, H.-J. J. Soil Structure as an Indicator of Soil Functions: A Review. *Geoderma* 2018, *314* (June 2017), 122–137. https://doi.org/10.1016/j.geoderma.2017.11.009.

(41) Kravchenko, A.; Guber, A. Imaging Soil Structure to Measure Soil Functions and Soil Health with X-Ray Computed Micro-Tomography; 2021; pp 111–138. https://doi.org/10.19103/AS.2020.0079.11.

(42) Jarvis, N. J. A Review of Non-Equilibrium Water Flow and Solute Transport in Soil Macropores: Principles, Controlling Factors and Consequences for Water Quality. *Eur. J. Soil Sci.* 2007, *58* (3), 523–546. https://doi.org/10.1111/j.1365-2389.2007.00915.x.

(43) Tinker, P. B.; Nye, P. *Solute Movement in the Rhizosphere*; Oxford University Press, 2000. https://doi.org/10.1093/oso/9780195124927.001.0001.

(44) Passioura, J. B. Viewpoint: The Perils of Pot Experiments. *Funct. Plant Biol.* 2006, *33* (12), 1075–1079. https://doi.org/10.1071/FP06223.

(45) Vetterlein, D.; Phalempin, M.; Lippold, E.; Schlüter, S.; Schreiter, S.; Ahmed, M. A.; Carminati, A.; Duddek, P.; Jorda, H.; Bienert, G. P.; Bienert, M. D.; Tarkka, M.; Ganther, M.; Oburger, E.; Santangeli, M.; Javaux, M.; Vanderborght, J. Root Hairs Matter at Field Scale for Maize Shoot Growth and Nutrient Uptake, but Root Trait Plasticity Is Primarily Triggered by Texture and Drought. *Plant Soil* 2022, *478* (1–2), 119–141.

https://doi.org/10.1007/s11104-022-05434-0.

(46) Lippold, E.; Lucas, M.; Fahrenkampf, T.; Schlüter, S.; Vetterlein, D. Macroaggregates of Loam in Sandy Soil Show Little Influence on Maize Growth, Due to Local Adaptations of Root Architecture to Soil Heterogeneity. *Plant Soil* 2022, No. 0123456789. https://doi.org/10.1007/s11104-022-05413-5.

(47) Lippold, E.; Phalempin, M.; Schlüter, S.; Vetterlein, D. Does the Lack of Root Hairs Alter Root System Architecture of Zea Mays? *Plant Soil* 2021, *467* (1–2), 267–286. https://doi.org/10.1007/s11104-021-05084-8.

(48) Lippold, E.; Kleinau, P.; Blaser, S. R. G. A.; Schlüter, S.; Phalempin, M.; Vetterlein, D. In Soil Measurement of Radiation Dose Caused by X-Ray Computed Tomography. *J. Plant Nutr. Soil Sci.* 2021, 1–3. https://doi.org/10.1002/jpln.202000276.

(49) Lippold, E.; Schlüter, S.; Mueller, C. W.; Höschen, C.; Harrington, G.; Kilian, R.; Gocke, M. I.; Lehndorff, E.; Mikutta, R.; Vetterlein, D. Correlative Imaging of the Rhizosphere─A Multimethod Workflow for Targeted Mapping of Chemical Gradients. *Environ. Sci. Technol.* 2023, *57* (3), 1538–1549. https://doi.org/10.1021/acs.est.2c07340.

(50) Bienert, M. D.; Werner, L. M.; Wimmer, M. A.; Bienert, G. P. Root Hairs: The Villi of Plants. *Biochem. Soc. Trans.* 2021, *49* (3), 1133–1146. https://doi.org/10.1042/BST20200716.

(51) Cai, G.; Carminati, A.; Abdalla, M.; Ahmed, M. A. Soil Textures Rather than Root Hairs Dominate Water Uptake and Soil-Plant Hydraulics under Drought. *Plant Physiol.* 2021, *187* (2), 858–872. https://doi.org/10.1093/plphys/kiab271.

(52) Carminati, A.; Benard, P.; Ahmed, M. A.; Zarebanadkouki, M. Liquid Bridges at the Root-Soil Interface. *Plant Soil* 2017, *417* (1–2), 1–15. https://doi.org/10.1007/s11104-017-3227-8.

(53) Kwasniewski, M.; Daszkowska-Golec, A.; Janiak, A.; Chwialkowska, K.; Nowakowska, U.; Sablok, G.; Szarejko, I. Transcriptome Analysis Reveals the Role of the Root Hairs as Environmental Sensors to Maintain Plant Functions under Water-Deficiency Conditions. *J. Exp. Bot.* 2016, *67* (4), 1079–1094. https://doi.org/10.1093/jxb/erv498.

(54) Segal, E.; Kushnir, T.; Mualem, Y.; Shani, U. Water Uptake and Hydraulics of the Root Hair Rhizosphere. *Vadose Zo. J.* 2008, *7* (3), 1027–1034. https://doi.org/10.2136/vzj2007.0122.

(55) Marin, M.; Feeney, D. S.; Brown, L. K.; Naveed, M.; Ruiz, S.; Koebernick,

N.; Bengough, A. G.; Hallett, P. D.; Roose, T.; Puértolas, J.; Dodd, I. C.; George, T. S. Significance of Root Hairs for Plant Performance under Contrasting Field Conditions and Water Deficit. *Ann. Bot.* 2021, *128* (1), 1–16. https://doi.org/10.1093/aob/mcaa181.

(56) Singh Gahoonia, T.; Nielsen, N. E. Root Traits as Tools for Creating Phosphorus Efficient Crop Varieties. *Plant Soil* 2004, *260* (1–2), 47–57. https://doi.org/10.1023/B:PLSO.0000030168.53340.bc.

(57) Lynch, J. P.; Ho, M. D. Rhizoeconomics: Carbon Costs of Phosphorus Acquisition. *Plant Soil* 2005, *269* (1–2), 45–56. https://doi.org/10.1007/s11104-004-1096-4.

(58) Gebauer, L.; Bouffaud, M. L.; Ganther, M.; Yim, B.; Vetterlein, D.; Smalla, K.; Buscot, F.; Heintz-Buschart, A.; Tarkka, M. T. Soil Texture, Sampling Depth and Root Hairs Shape the Structure of ACC Deaminase Bacterial Community Composition in Maize Rhizosphere. *Front. Microbiol.* 2021, *12* (February), 1–12. https://doi.org/10.3389/fmicb.2021.616828.

(59) George, T. S.; Brown, L. K.; Ramsay, L.; White, P. J.; Newton, A. C.; Bengough, A. G.; Russell, J.; Thomas, W. T. B. Understanding the Genetic Control and Physiological Traits Associated with Rhizosheath Production by Barley (Hordeum Vulgare). *New Phytol.* 2014, *203* (1), 195–205. https://doi.org/10.1111/nph.12786.

(60) Nestler, J.; Keyes, S. D.; Wissuwa, M. Root Hair Formation in Rice (Oryza Sativa L.) Differs between Root Types and Is Altered in Artificial Growth Conditions. *J. Exp. Bot.* 2016, *67* (12), 3699–3708. https://doi.org/10.1093/jxb/erw115.

(61) Nestler, J.; Wissuwa, M. Superior Root Hair Formation Confers Root Efficiency in Some, but Not All, Rice Genotypes upon P Deficiency. *Front. Plant Sci.* 2016, *7* (DECEMBER2016), 1–13. https://doi.org/10.3389/fpls.2016.01935.

(62) Ruiz, S.; Koebernick, N.; Duncan, S.; Fletcher, D. M. K.; Scotson, C.; Boghi, A.; Marin, M.; Bengough, A. G.; George, T. S.; Brown, L. K.; Hallett, P. D.; Roose, T. Significance of Root Hairs at the Field Scale – Modelling Root Water and Phosphorus Uptake under Different Field Conditions. *Plant Soil* 2020, *447* (1–2), 281–304. https://doi.org/10.1007/s11104-019-04308-2.

(63) Dodd, I. C.; Diatloff, E. Enhanced Root Growth of the Brb (Bald Root Barley) Mutant in Drying Soil Allows Similar Shoot Physiological Responses to Soil Water Deficit as Wild-Type Plants. *Funct. Plant Biol.* 2016, *43* (2), 199–206. https://doi.org/10.1071/FP15303.

(64) Klamer, F.; Vogel, F.; Li, X.; Bremer, H.; Neumann, G.; Neuhäuser, B.; Hochholdinger, F.; Ludewig, U. Estimating the Importance of Maize Root Hairs in Low Phosphorus Conditions and under Drought. 2019, 1–8. https://doi.org/10.1093/aob/mcz011.

(65) Fitter, A. H. AN ARCHITECTURAL APPROACH TO THE COMPARATIVE ECOLOGY OF PLANT ROOT SYSTEMS. *New Phytol.* 1987, *106* (s1), 61–77. https://doi.org/10.1111/j.1469-8137.1987.tb04683.x.

(66) Lynch, J. P. Steep, Cheap and Deep: An Ideotype to Optimize Water and N Acquisition by Maize Root Systems. *Ann. Bot.* 2013, *112* (2), 347–357. https://doi.org/10.1093/aob/mcs293.

(67) York, L. M.; Nord, E. A.; Lynch, J. P. Integration of Root Phenes for Soil Resource Acquisition. *Front. Plant Sci.* 2013, *4* (SEP). https://doi.org/10.3389/fpls.2013.00355.

(68) Hodge, A. Plastic Plants and Patchy Soils. *J. Exp. Bot.* 2006, *57* (2 SPEC. ISS.), 401–411. https://doi.org/10.1093/jxb/eri280.

(69) Lynch, J. P.; Strock, C. F.; Schneider, H. M.; Sidhu, J. S.; Ajmera, I.; Galindo-Castañeda, T.; Klein, S. P.; Hanlon, M. T. *Root Anatomy and Soil Resource Capture*; Springer International Publishing, 2021; Vol. 466. https://doi.org/10.1007/s11104-021-05010-y.

(70) Jaramillo, R. E.; Nord, E. A.; Chimungu, J. G.; Brown, K. M.; Lynch, J. P. Root Cortical Burden Influences Drought Tolerance in Maize. *Ann. Bot.* 2013, *112* (2), 429–437. https://doi.org/10.1093/aob/mct069.

(71) Postma, J. A.; Lynch, J. P. Theoretical Evidence for the Functional Benefit of Root Cortical Aerenchyma in Soils with Low Phosphorus Availability. *Ann. Bot.* 2011, *107* (5), 829–841. https://doi.org/10.1093/aob/mcq199.

(72) Ordóñez, R. A.; Archontoulis, S. V.; Martinez-Feria, R.; Hatfield, J. L.; Wright, E. E.; Castellano, M. J. Root to Shoot and Carbon to Nitrogen Ratios of Maize and Soybean Crops in the US Midwest. *Eur. J. Agron.* 2020, *120* (February), 126130. https://doi.org/10.1016/j.eja.2020.126130.

(73) Jorda, H.; Ahmed, M. A.; Javaux, M.; Carminati, A.; Duddek, P.; Vetterlein, D. Field Scale Plant Water Relation of Maize (Zea Mays) under Drought – Impact of Root Hairs and Soil Texture. *Plant Soil* 2022, 59–84. https://doi.org/10.1007/s11104-022-05685-x.

(74) Ganther, M.; Lippold, E.; Bienert, M. D.; Bouffaud, M. L.; Bauer, M.; Baumann, L.; Bienert, G. P.; Vetterlein, D.; Heintz-Buschart, A.; Tarkka, M. T. Plant Age and Soil Texture Rather Than the Presence of Root Hairs Cause Differences in Maize Resource Allocation and Root Gene Expression

in the Field. *Plants* 2022, *11* (21). https://doi.org/10.3390/plants11212883.

(75) Santangeli, M.; Steininger-Mairinger, T.; Vetterlein, D.; Hann, S.; Oburger, E. Maize (Zea Mays L.) Root Exudation Profiles Change in Quality and Quantity during Plant Development – A Field Study. *Plant Sci.* 2024, *338* (October), 111896. https://doi.org/10.1016/j.plantsci.2023.111896.

(76) Rosskopf, U. Development of Mechanical Soil Stability In An Initial Homogeneous Loam And Sand Under In-Situ Field Conditions. 2021, 1–25. https://doi.org/10.21203/rs.3.rs-1181463/v1.

(77) Hack, H.; Bleiholder, H.; Buhr, L.; Klose, R.; Meier, U.; Weber, E. Einheitliche Codierung Der Phänologischen Entwicklungsstadien von Kultur- Und Schadpflanzen - Erweiterte BBCH-Skala. *Nachrichtenblatt des Dtsch. Pflanzenschutzdienstes* 1992, *44* (12), 265–270.

(78) Vierheilig, H.; Coughlan, A. P.; Wyss, U.; Piché, Y. Ink and Vinegar, a Simple Staining Technique for Arbuscular-Mycorrhizal Fungi. *Appl. Environ. Microbiol.* 1998, *64* (12), 5004–5007. https://doi.org/10.1128/aem.64.12.5004-5007.1998.

(79) McGonigle, T. P.; Miller, M. H.; Evans, D. G.; Fairchild, G. L.; Swan, J. A. A New Method Which Gives an Objective Measure of Colonization of Roots by Vesicular—Arbuscular Mycorrhizal Fungi. *New Phytol.* 1990, *115* (3), 495–501. https://doi.org/10.1111/j.1469-8137.1990.tb00476.x.

(80) Hochholdinger, F.; Wen, T.; Zimmermann, R.; Chimot-marolle, P. The Maize (Zea Mays L .) Roothairless3 Gene Encodes A. *Plant J.* 2008, No. February 2018. https://doi.org/10.1111/j.1365-313X.2008.03459.x.

(81) Bergmann, W. *Ernährungsstörungen Bei Kulturpflanzen: Entstehung, Visuelle Und Analytische Diagnose*, 2., erweit.; VEB Gustav Fischer Verlag Jena, 1986.

(82) Leitner, D.; Klepsch, S.; Ptashnyk, M.; Marchant, A.; Kirk, G. J. D.; Schnepf, A.; Roose, T. A Dynamic Model of Nutrient Uptake by Root Hairs. *New Phytol.* 2010, *185* (3), 792–802. https://doi.org/10.1111/j.1469-8137.2009.03128.x.

(83) Bilyera, N.; Zhang, X.; Duddek, P.; Fan, L.; Banfield, C. C.; Schlüter, S.; Carminati, A.; Kaestner, A.; Ahmed, M. A.; Kuzyakov, Y.; Dippold, M. A.; Spielvogel, S.; Razavi, B. S. Maize Genotype-Specific Exudation Strategies: An Adaptive Mechanism to Increase Microbial Activity in the Rhizosphere. *Soil Biol. Biochem.* 2021, *162* (July), 108426. https://doi.org/10.1016/j.soilbio.2021.108426.

(84) Rosskopf, U.; Uteau, D.; Peth, S. Development of Mechanical Soil Stability

in an Initial Homogeneous Loam and Sand Planted with Two Maize (Zea Mays L.) Genotypes with Contrasting Root Hair Attributes under in-Situ Field Conditions. *Plant Soil* 2022, *478* (1–2), 143–162. https://doi.org/10.1007/s11104-022-05572-5.

(85) Benešová, M.; Holá, D.; Fischer, L.; Jedelský, P. L.; Hnilička, F.; Wilhelmová, N.; Rothová, O.; Kočová, M.; Procházková, D.; Honnerová, J.; Fridrichová, L.; Hniličková, H. The Physiology and Proteomics of Drought Tolerance in Maize: Early Stomatal Closure as a Cause of Lower Tolerance to Short-Term Dehydration? *PLoS One* 2012, *7* (6). https://doi.org/10.1371/journal.pone.0038017.

(86) Earl, H. J.; Liu, W.; Bowley, S. R.; Tollenaar, A. Effects of Abiotic Stress on Respiratory Carbon Loss of Two Maize (Zea Mays L.) Inbred Lines and Their Hybrid during Silking and Grain-Filling. *Crop Sci.* 2012, *52* (4), 1795–1802. https://doi.org/10.2135/cropsci2011.11.0615.

(87) Carminati, A.; Passioura, J. B.; Zarebanadkouki, M.; Ahmed, M. A.; Ryan, P. R.; Watt, M.; Delhaize, E. Root Hairs Enable High Transpiration Rates in Drying Soils. *New Phytol.* 2017, *216* (3), 771–781. https://doi.org/10.1111/nph.14715.

(88) Amos, B.; Walters, D. T. Maize Root Biomass and Net Rhizodeposited Carbon. *Soil Sci. Soc. Am. J.* 2006, *70* (5), 1489–1503. https://doi.org/10.2136/sssaj2005.0216.

(89) Gajri, P. R.; Arora, V. K.; Kumar, K. A Procedure for Determining Average Root Length Density in Row Crops by Single-Site Augering. *Plant Soil* 1994, *160* (1), 41–47. https://doi.org/10.1007/BF00150344.

(90) Strock, C. F.; Morrow de la Riva, L.; Lynch, J. P.; De La Riva, L. M.; Lynch, J. P.; Morrow de la Riva, L.; Lynch, J. P.; De La Riva, L. M.; Lynch, J. P. Reduction in Root Secondary Growth as a Strategy for Phosphorus Acquisition. *Plant Physiol.* 2018, *176* (1), 691–703. https://doi.org/10.1104/pp.17.01583.

(91) Vejchasarn, P.; Lynch, J. P.; Brown, K. M. Genetic Variability in Phosphorus Responses of Rice Root Phenotypes. *Rice* 2016, *9* (1). https://doi.org/10.1186/s12284-016-0102-9.

(92) Bengough, A. G.; Bransby, M. F.; Hans, J.; McKenna, S. J.; Roberts, T. J.; Valentine, T. A. Root Responses to Soil Physical Conditions; Growth Dynamics from Field to Cell. *J. Exp. Bot.* 2006, *57* (2 SPEC. ISS.), 437–447. https://doi.org/10.1093/jxb/erj003.

(93) Correa, J.; Postma, J. A.; Watt, M.; Wojciechowski, T. Soil Compaction and the Architectural Plasticity of Root Systems. *J. Exp. Bot.* 2019, *70*

(21), 6019–6034. https://doi.org/10.1093/jxb/erz383.

(94) Rosskopf, U.; Uteau, D.; Peth, S. Effects of Mucilage Concentration at Different Water Contents on Mechanical Stability and Elasticity in a Loamy and a Sandy Soil. *Eur. J. Soil Sci.* 2022, *73* (1), 1–14. https://doi.org/10.1111/ejss.13189.

(95) Ma, X.; Li, X.; Ludewig, U. Arbuscular Mycorrhizal Colonization Outcompetes Root Hairs in Maize under Low Phosphorus Availability. *Ann. Bot.* 2021, *127* (1), 155–166. https://doi.org/10.1093/aob/mcaa159.

(96) Jakobsen, I.; Chen, B.; Munkvold, L.; Lundsgaard, T.; Zhu, Y. G. Contrasting Phosphate Acquisition of Mycorrhizal Fungi with That of Root Hairs Using the Root Hairless Barley Mutant. *Plant, Cell Environ.* 2005, *28* (7), 928–938. https://doi.org/10.1111/j.1365-3040.2005.01345.x.

(97) Kothari, S. K.; Marschner, H.; George, E. Effect of VA Mycorrhizal Fungi and Rhizosphere Microorganisms on Root and Shoot Morphology, Growth and Water Relations in Maize. *New Phytol.* 1990, *116* (2), 303–311. https://doi.org/10.1111/j.1469-8137.1990.tb04718.x.

(98) Liu, A.; Hamel, C.; Hamilton, R. I.; Ma, B. L.; Smith, D. L. Acquisition of Cu, Zn, Mn and Fe by Mycorrhizal Maize (Zea Mays L.) Grown in Soil at Different P and Micronutrient Levels. *Mycorrhiza* 2000, *9* (6), 331–336. https://doi.org/10.1007/s005720050277.

(99) Fellbaum, C. R.; Gachomo, E. W.; Beesetty, Y.; Choudhari, S.; Strahan, G. D.; Pfeffer, P. E.; Kiers, E. T.; Bücking, H. Carbon Availability Triggers Fungal Nitrogen Uptake and Transport in Arbuscular Mycorrhizal Symbiosis. *Proc. Natl. Acad. Sci. U. S. A.* 2012, *109* (7), 2666–2671. https://doi.org/10.1073/pnas.1118650109.

(100) Gao, K.; Chen, F.; Yuan, L.; Zhang, F.; Mi, G. A Comprehensive Analysis of Root Morphological Changes and Nitrogen Allocation in Maize in Response to Low Nitrogen Stress. *Plant Cell Environ.* 2015, *38* (4), 740–750. https://doi.org/10.1111/pce.12439.

(101) Phalempin, M.; Lippold, E.; Vetterlein, D.; Schlüter, S. Soil Texture and Structure Heterogeneity Predominantly Governs Bulk Density Gradients around Roots. *Vadose Zo. J.* 2021, No. July. https://doi.org/10.1002/vzj2.20147.

(102) Chassot, A.; Stamp, P.; Richner, W. Root Distribution and Morphology of Maize Seedlings as Affected by Tillage and Fertilizer Placement. *Plant Soil* 2001, *231* (1), 123–135. https://doi.org/10.1023/A:1010335229111.

(103) Dwyer, L. M.; Stewart, D. W.; Balchin, D. Ft] Nction of Available Water

and Soil Physical Characteristics. 1988.

(104) Marin, M.; Hallett, P. D.; Feeney, D. S.; Brown, L. K.; Naveed, M.; Koebernick, N.; Ruiz, S.; Bengough, A. G.; Roose, T.; George, T. S. Impact of Root Hairs on Microscale Soil Physical Properties in the Field. *Plant Soil* 2022, No. 0123456789. https://doi.org/10.1007/s11104-022-05530-1.

(105) Qin, R.; Stamp, P.; Richner, W. Impact of Tillage and Banded Starter Fertilizer on Maize Root Growth in the Top 25 Centimeters of the Soil. *Agron. J.* 2005, *97* (3), 674–683. https://doi.org/10.2134/agronj2004.0059.

(106) Sene, M.; Vepraskas, M. J.; Naderman, G. C.; Denton, H. P. Relationships of Soil Texture and Structure to Corn Yield Response to Subsoiling. *Soil Sci. Soc. Am. J.* 1985, *49* (2), 422–427. https://doi.org/10.2136/sssaj1985.03615995004900020030x.

(107) Anderson, T. M.; Starmer, W. T.; Thorne, M. Bimodal Root Diameter Distributions in Serengeti Grasses Exhibit Plasticity in Response to Defoliation and Soil Texture: Implications for Nitrogen Uptake. *Funct. Ecol.* 2007, *21* (1), 50–60. https://doi.org/10.1111/j.1365-2435.2006.01192.x.

(108) Rogers, E. D.; Monaenkova, D.; Mijar, M.; Nori, A.; Goldman, D. I.; Benfey, P. N. X-Ray Computed Tomography Reveals the Response of Root System Architecture to Soil Texture. *Plant Physiol.* 2016, *171* (3), 2028–2040. https://doi.org/10.1104/pp.16.00397.

(109) Warnaars, B. C.; Eavis, B. W. Soil Physical Conditions Affecting Seedling Root Growth. *Plant Soil* 1972, *36* (1–3), 623–634. https://doi.org/10.1007/BF01373512.

(110) Lipiec, J.; Siczek, A.; Sochan, A.; Bieganowski, A. Effect of Sand Grain Shape on Root and Shoot Growth of Wheat Seedlings. *Geoderma* 2016, *265*, 1–5. https://doi.org/10.1016/j.geoderma.2015.10.022.

(111) Schmidt, S.; Bengough, A. G.; Gregory, P. J.; Grinev, D. V.; Otten, W. Estimating Root-Soil Contact from 3D X-Ray Microtomographs. *Eur. J. Soil Sci.* 2012, *63* (6), 776–786. https://doi.org/10.1111/j.1365-2389.2012.01487.x.

(112) Dupuy, L. X.; Mimault, M.; Patko, D.; Ladmiral, V.; Ameduri, B.; MacDonald, M. P.; Ptashnyk, M. Micromechanics of Root Development in Soil. *Curr. Opin. Genet. Dev.* 2018, *51*, 18–25. https://doi.org/10.1016/j.gde.2018.03.007.

(113) Monshausen, G. B.; Gilroy, S. The Exploring Root - Root Growth Responses to Local Environmental Conditions. *Curr. Opin. Plant Biol.*

2009, *12* (6), 766–772. https://doi.org/10.1016/j.pbi.2009.08.002.

(114) Hamilton, E. S.; Schlegel, A. M.; Haswell, E. S. United in Diversity: Mechanosensitive Ion Channels in Plants. *Annu. Rev. Plant Biol.* 2015, *66* (1), 113–137. https://doi.org/10.1146/annurev-arplant-043014-114700.

(115) Tang, W.; Lin, W.; Zhou, X.; Guo, J.; Dang, X.; Li, B.; Lin, D.; Yang, Z. Mechano-Transduction via the Pectin-FERONIA Complex Activates ROP6 GTPase Signaling in Arabidopsis Pavement Cell Morphogenesis. *Curr. Biol.* 2022, *32* (3), 508-517.e3. https://doi.org/10.1016/j.cub.2021.11.031.

(116) Kolb, E.; Legué, V.; Kolb, E.; Legué, V.; Interactions, M. B. P. R. Physical Root-Soil Interactions To Cite This Version : HAL Id : Hal-01609984 Physical Root-Soil Interactions. 2017, *14* (6).

(117) Sarquis, J. I.; Jordan, W. R.; Morgan, P. W. Ethylene Evolution from Maize (Zea Mays L.) Seedling Roots and Shoots in Response to Mechanical Impedance. *Plant Physiol.* 1991, *96* (4), 1171–1177. https://doi.org/10.1104/pp.96.4.1171.

(118) Pandey, B. K.; Huang, G.; Bhosale, R.; Hartman, S.; Sturrock, C. J.; Jose, L.; Martin, O. C.; Karady, M.; Voesenek, L. A. C. J.; Ljung, K.; Lynch, J. P.; Brown, K. M.; Whalley, W. R.; Mooney, S. J.; Zhang, D.; Bennett, M. J. Plant Roots Sense Soil Compaction through Restricted Ethylene Diffusion. *Science (80-.).* 2021, *371* (6526), 276–280. https://doi.org/10.1126/science.abf3013.

(119) Massa, G. D.; Gilroy, S. Touch Modulates Gravity Sensing to Regulate the Growth of Primary Roots of Arabidopsis Thaliana. *Plant J.* 2003, *33* (3), 435–445. https://doi.org/10.1046/j.1365-313X.2003.01637.x.

(120) Dreyer, J.; Edelmann, H. G. Root Cap-Mediated Evaluation of Soil Resistance towards Graviresponding Roots of Maize (Zea Mays L.) and the Relevance of Ethylene. *Ann. Bot.* 2018, *122* (5), 791–800. https://doi.org/10.1093/aob/mcx209.

(121) Feng, Y.; Xu, P.; Li, B.; Li, P.; Wen, X.; An, F.; Gong, Y.; Xin, Y.; Zhu, Z.; Wang, Y.; Guo, H. Ethylene Promotes Root Hair Growth through Coordinated EIN3/EIL1 and RHD6/RSL1 Activity in Arabidopsis. *Proc. Natl. Acad. Sci. U. S. A.* 2017, *114* (52), 13834–13839. https://doi.org/10.1073/pnas.1711723115.

(122) Weon, B. M.; Je, J. H.; Hwu, Y.; Margaritondo, G. Decreased Surface Tension of Water by Hard-X-Ray Irradiation. *Phys. Rev. Lett.* 2008, *100* (21), 217403. https://doi.org/10.1103/PhysRevLett.100.217403.

(123) Bouckaert, L.; Van Loo, D.; Ameloot, N.; Buchan, D.; Van Hoorebeke, L.;

Sleutel, S. Compatibility of X-Ray Micro-Computed Tomography with Soil Biological Experiments. *Soil Biol. Biochem.* 2013, *56*, 10–12. https://doi.org/10.1016/j.soilbio.2012.02.002.

(124) Schmidt, H.; Vetterlein, D.; Köhne, J. M.; Eickhorst, T. Negligible Effect of X-Ray µ-CT Scanning on Archaea and Bacteria in an Agricultural Soil. *Soil Biol. Biochem.* 2015, *84*, 21–27. https://doi.org/10.1016/j.soilbio.2015.02.010.

(125) Ganther, M.; Yim, B.; Ibrahim, Z.; Bienert, M. D.; Lippold, E.; Maccario, L.; Sørensen, S. J.; Bienert, G. P.; Vetterlein, D.; Heintz-Buschart, A.; Blagodatskaya, E.; Smalla, K.; Tarkka, M. T. Compatibility of X-Ray Computed Tomography with Plant Gene Expression Profiling, Rhizosphere Bacterial Community Composition and Enzyme Activity Analyses. *J. Exp. Bot.* 2020. https://doi.org/10.1093/jxb/eraa262.

(126) Johnson, E. L. SUSCEPTIBILITY OF SEVENTY SPECIES OF FLOWERING PLANTS TO X-RADIATION. *Plant Physiol.* 1936, *11* (2), 319–342. https://doi.org/10.1104/pp.11.2.319.

(127) Evans, H. J. Effects of Radiations on Meristematig Cells. *Radiat. Bot.* 1965, *5*.

(128) Zappala, S.; Helliwell, J. R.; Tracy, S. R.; Mairhofer, S.; Sturrock, C. J.; Pridmore, T.; Bennett, M.; Mooney, S. J. Effects of X-Ray Dose On Rhizosphere Studies Using X-Ray Computed Tomography. *PLoS One* 2013, *8* (6), e67250. https://doi.org/10.1371/journal.pone.0067250.

(129) Blaser, S. R. G. A.; Schlüter, S.; Vetterlein, D. How Much Is Too Much?—Influence of X-Ray Dose on Root Growth of Faba Bean (Vicia Faba) and Barley (Hordeum Vulgare). *PLoS One* 2018, *13* (3), 1–18. https://doi.org/10.1371/journal.pone.0193669.

(130) Gao, W.; Schlüter, S.; Blaser, S. R. G. A. G. A.; Shen, J.; Vetterlein, D.; Gao, A. W.; Schlüter, S.; Blaser, S. R. G. A. G. A.; Shen, J.; Vetterlein, D. A Shape-Based Method for Automatic and Rapid Segmentation of Roots in Soil from X-Ray Computed Tomography Images: Rootine. *Plant Soil* 2019, *441* (1–2), 643–655. https://doi.org/10.1007/s11104-019-04053-6.

(131) Gao, W.; Blaser, S. R. G. A.; Schlüter, S.; Shen, J.; Vetterlein, D. Effect of Localised Phosphorus Application on Root Growth and Soil Nutrient Dynamics in Situ – Comparison of Maize (Zea Mays) and Faba Bean (Vicia Faba) at the Seedling Stage. *Plant Soil* 2019, *441* (1–2), 469–483. https://doi.org/10.1007/s11104-019-04138-2.

(132) DOWNIE, H. F.; ADU, M. O.; SCHMIDT, S.; OTTEN, W.; DUPUY, L. X.; WHITE, P. J.; VALENTINE, T. A. Challenges and Opportunities for

Quantifying Roots and Rhizosphere Interactions through Imaging and Image Analysis. *Plant. Cell Environ.* 2015, *38* (7), 1213–1232. https://doi.org/10.1111/pce.12448.

(133) Bengough, A. G.; McKenzie, B. M.; Hallett, P. D.; Valentine, T. A. Root Elongation, Water Stress, and Mechanical Impedance: A Review of Limiting Stresses and Beneficial Root Tip Traits. *J. Exp. Bot.* 2011, *62* (1), 59–68. https://doi.org/10.1093/jxb/erq350.

(134) Colombi, T.; Torres, L. C.; Walter, A.; Keller, T. Feedbacks between Soil Penetration Resistance, Root Architecture and Water Uptake Limit Water Accessibility and Crop Growth – A Vicious Circle. *Sci. Total Environ.* 2018, *626*, 1026–1035. https://doi.org/10.1016/j.scitotenv.2018.01.129.

(135) Veen, B. W.; Boone, F. R. The Influence of Mechanical Resistance and Soil Water on the Growth of Seminal Roots of Maize. *Soil Tillage Res.* 1990, *16* (1–2), 219–226. https://doi.org/10.1016/0167-1987(90)90031-8.

(136) Dexter, A. R. Model Experiments on the Behaviour of Roots at the Interface between a Tilled Seed-Bed and a Compacted Sub-Soil. *Plant Soil* 1986, *95* (1), 123–133. https://doi.org/10.1007/BF02378858.

(137) Becher, H. H. Die Bedeutung Der Festigkeitsverteilung in Einzelaggregaten Für Den Wasser- Und Stofftransport Im Boden. *Zeitschrift für Pflanzenernährung und Bodenkd.* 1992, *155* (5), 361–366. https://doi.org/10.1002/jpln.19921550503.

(138) Logsdon, S. D. Root Effects on Soil Properties and Processes: Synthesis and Future Research Needs; 2015; pp 173–196. https://doi.org/10.2134/advagricsystmodel4.c8.

(139) Freitas, P. L.; Zobel, R. W.; Synder, V. A. Corn Root Growth in Soil Columns with Artificially Constructed Aggregates. *Crop Sci.* 1999, *39* (3), 725–730. https://doi.org/10.2135/cropsci1999.0011183X003900030020x.

(140) Flavel, R. J.; Guppy, C. N.; Tighe, M. K.; Watt, M.; Young, I. M. Quantifying the Response of Wheat (Triticum Aestivum L) Root System Architecture to Phosphorus in an Oxisol. *Plant Soil* 2014, *385* (1–2), 303–310. https://doi.org/10.1007/s11104-014-2191-9.

(141) ROBINSON, D. The Responses of Plants to Non-uniform Supplies of Nutrients. *New Phytol.* 1994, *127* (4), 635–674. https://doi.org/10.1111/j.1469-8137.1994.tb02969.x.

(142) Colombi, T.; Walter, A. Genetic Diversity under Soil Compaction in Wheat: Root Number as a Promising Trait for Early Plant Vigor. *Front. Plant Sci.* 2017, *8* (March). https://doi.org/10.3389/fpls.2017.00420.

(143) Burr-Hersey, J. E.; Mooney, S. J.; Bengough, A. G.; Mairhofer, S.; Ritz, K. Developmental Morphology of Cover Crop Species Exhibit Contrasting Behaviour to Changes in Soil Bulk Density, Revealed by X-Ray Computed Tomography. *PLoS One* 2017, *12* (7), e0181872. https://doi.org/10.1371/journal.pone.0181872.

(144) Blaser, S. R. G. A.; Koebernick, N.; Spott, O.; Thiel, E.; Vetterlein, D. Dynamics of Localised Nitrogen Supply and Relevance for Root Growth of Vicia Faba ('Fuego') and Hordeum Vulgare ('Marthe') in Soil. *Sci. Rep.* 2020, *10* (1), 15776. https://doi.org/10.1038/s41598-020-72140-1.

(145) Schüller, H. Die CAL-Methode, Eine Neue Methode Zur Bestimmung Des Pflanzenverfügbaren Phosphates in Böden. *Zeitschrift für Pflanzenernährung und Bodenkd.* 1969, *123* (1), 48–63. https://doi.org/10.1002/jpln.19691230106.

(146) Schindelin, J.; Arganda-Carreras, I.; Frise, E.; Kaynig, V.; Longair, M.; Pietzsch, T.; Preibisch, S.; Rueden, C.; Saalfeld, S.; Schmid, B.; Tinevez, J.-Y. Y.; White, D. J.; Hartenstein, V.; Eliceiri, K.; Tomancak, P.; Cardona, A. Fiji: An Open-Source Platform for Biological-Image Analysis. *Nat. Methods* 2012, *9* (7), 676–682. https://doi.org/10.1038/nmeth.2019.

(147) Rueden, C. T.; Schindelin, J.; Hiner, M. C.; DeZonia, B. E.; Walter, A. E.; Arena, E. T.; Eliceiri, K. W. ImageJ2: ImageJ for the next Generation of Scientific Image Data. *BMC Bioinformatics* 2017, *18* (1), 529. https://doi.org/10.1186/s12859-017-1934-z.

(148) Tristán-Vega, A.; García-Pérez, V.; Aja-Fernández, S.; Westin, C.-F. Efficient and Robust Nonlocal Means Denoising of MR Data Based on Salient Features Matching. *Comput. Methods Programs Biomed.* 2012, *105* (2), 131–144. https://doi.org/10.1016/j.cmpb.2011.07.014.

(149) Legland, D.; Arganda-Carreras, I.; Andrey, P. MorphoLibJ: Integrated Library and Plugins for Mathematical Morphology with ImageJ. *Bioinformatics* 2016, *32* (22), 3532–3534. https://doi.org/10.1093/bioinformatics/btw413.

(150) Otsu, N.; Smith, P. L.; Reid, D. B.; Environment, C.; Palo, L.; Alto, P.; Smith, P. L. Otsu 1979 Otsu Method. *IEEE Trans. Syst. Man. Cybern.* 1979, *C* (1), 62–66.

(151) Ollion, J.; Cochennec, J.; Loll, F.; Escudé, C.; Boudier, T. TANGO: A Generic Tool for High-Throughput 3D Image Analysis for Studying Nuclear Organization. *Bioinformatics* 2013, *29* (14), 1840–1841. https://doi.org/10.1093/bioinformatics/btt276.

(152) Phalempin, M.; Lippold, E.; Vetterlein, D.; Schlüter, S. An Improved

Method for the Segmentation of Roots from X-Ray Computed Tomography 3D Images: Rootine v.2. *Plant Methods* 2021, *17* (1), 1–19. https://doi.org/10.1186/s13007-021-00735-4.

(153) Colombi, T.; Braun, S.; Keller, T.; Walter, A. Artificial Macropores Attract Crop Roots and Enhance Plant Productivity on Compacted Soils. *Sci. Total Environ.* 2017, *574*, 1283–1293. https://doi.org/10.1016/j.scitotenv.2016.07.194.

(154) Mendiburu, F. de. Package ‘Agricolae.’ 2017.

(155) Montagu, K. D.; Conroy, J. P.; Atwell, B. J. The Position of Localized Soil Compaction Determines Root and Subsequent Shoot Growth Responses. *J. Exp. Bot.* 2001, *52* (364), 2127–2133. https://doi.org/10.1093/jexbot/52.364.2127.

(156) Materechera, S. A.; Alston, A. M.; Kirby, J. M.; Dexter, A. R. Influence of Root Diameter on the Penetration of Seminal Roots into a Compacted Subsoil. *Plant Soil* 1992, *144* (2), 297–303. https://doi.org/10.1007/BF00012888.

(157) Bengough, A. G. Root Elongation Is Restricted by Axial but Not by Radial Pressures: So What Happens in Field Soil? *Plant Soil* 2012, *360* (1–2), 15–18. https://doi.org/10.1007/s11104-012-1428-8.

(158) Ganther, M.; Vetterlein, D.; Heintz-Buschart, A.; Tarkka, M. T. Transcriptome Sequencing Analysis of Maize Roots Reveals the Effects of Substrate and Root Hair Formation in a Spatial Context. *Plant Soil* 2022, *478* (1–2), 211–228. https://doi.org/10.1007/s11104-021-04921-0.

(159) Carminati, A.; Vetterlein, D.; Koebernick, N.; Blaser, S.; Weller, U.; Vogel, H. J. Do Roots Mind the Gap? *Plant Soil* 2013, *367* (1–2), 651–661. https://doi.org/10.1007/s11104-012-1496-9.

(160) Hill, J. O.; Simpson, R. J.; Moore, A. D.; Chapman, D. F. Morphology and Response of Roots of Pasture Species to Phosphorus and Nitrogen Nutrition. *Plant Soil* 2006, *286* (1–2), 7–19. https://doi.org/10.1007/s11104-006-0014-3.

(161) Kumar, A.; Shahbaz, M.; Koirala, M.; Blagodatskaya, E.; Seidel, S. J.; Kuzyakov, Y.; Pausch, J. Root Trait Plasticity and Plant Nutrient Acquisition in Phosphorus Limited Soil. *J. Plant Nutr. Soil Sci.* 2019, *182* (6), 945–952. https://doi.org/10.1002/jpln.201900322.

(162) Wang, Y.; Lambers, H. Root-Released Organic Anions in Response to Low Phosphorus Availability: Recent Progress, Challenges and Future Perspectives. *Plant Soil* 2020, *447* (1–2), 135–156.

https://doi.org/10.1007/s11104-019-03972-8.

(163) Hoffmann, C.; Jungk, A. Growth and Phosphorus Supply of Sugar Beet as Affected by Soil Compaction and Water Tension. *Plant Soil* 1995, *176* (1), 15–25. https://doi.org/10.1007/BF00017671.

(164) Teixeira, P. P. C.; Trautmann, S.; Buegger, F.; Felde, V. J. M. N. L.; Pausch, J.; Müller, C. W.; Kögel-Knabner, I. Role of Root Hair Elongation in Rhizosheath Aggregation and in the Carbon Flow into the Soil. *Biol. Fertil. Soils* 2023, No. Jungk 2001. https://doi.org/10.1007/s00374-023-01708-6.

(165) Wen, T.-J.; Schnable, P. S. Analyses of Mutants of Three Genes That Influence Root Hair Development in Z Ea Mays (Gramineae) Suggest That Root Hairs Are Dispensable. *Am. J. Bot.* 1994, *81* (7), 833–842. https://doi.org/10.1002/j.1537-2197.1994.tb15564.x.

(166) Ganther, M.; Yim, B.; Ibrahim, Z.; Bienert, M. D.; Lippold, E.; Maccario, L.; Sørensen, S. J.; Bienert, G. P.; Vetterlein, D.; Heintz-Buschart, A.; Blagodatskaya, E.; Smalla, K.; Tarkka, M. T. Compatibility of X-Ray Computed Tomography with Plant Gene Expression, Rhizosphere Bacterial Communities and Enzyme Activities. *J. Exp. Bot.* 2020, *54*, 1–54. https://doi.org/10.1093/jxb/eraa262.

(167) Doube, M.; Klosowski, M. M.; Arganda-Carreras, I.; Cordelières, F. P.; Dougherty, R. P.; Jackson, J. S.; Schmid, B.; Hutchinson, J. R.; Shefelbine, S. J. BoneJ: Free and Extensible Bone Image Analysis in ImageJ. *Bone* 2010, *47* (6), 1076–1079. https://doi.org/10.1016/j.bone.2010.08.023.

(168) Schlüter, S.; Blaser, S. R. G. A.; Weber, M.; Schmidt, V.; Vetterlein, D. Quantification of Root Growth Patterns from the Soil Perspective via Root Distance Models. *Front. Plant Sci.* 2018, *9* (July), 1–11. https://doi.org/10.3389/fpls.2018.01084.

(169) Hendriks, L.; Claassen, N.; Jungk, A. Phosphatverarmung Des Wurzelnahen Bodens Und Phosphataufnahme von Mais Und Raps. *Zeitschrift für Pflanzenernährung und Bodenkd.* 1981, *144* (5), 486–499. https://doi.org/10.1002/jpln.19811440507.

(170) R Core Team. R: A Language and Environment for Statistical Computing. Vienna, Austria 2022.

(171) Li, T.; Lin, G.; Zhang, X.; Chen, Y.; Zhang, S.; Chen, B. Relative Importance of an Arbuscular Mycorrhizal Fungus (Rhizophagus Intraradices) and Root Hairs in Plant Drought Tolerance. *Mycorrhiza* 2014, *24* (8), 595–602. https://doi.org/10.1007/s00572-014-0578-3.

(172) Vetterlein, D.; Tarkka, M. Seeds with Low Phosphorus Content: Not so Bad after All? *J. Exp. Bot.* 2018, *69* (21), 4993–4996. https://doi.org/10.1093/jxb/ery313.

(173) Suzuki, N.; Taketa, S.; Ichii, M. Morphological and Physiological Characteristics of a Root-Hairless Mutant in Rice (Oryza Sativa L.). *Plant Soil* 2003, *255* (1), 9–17. https://doi.org/10.1023/A:1026180318923.

(174) Bailey, P. H. J.; Currey, J. D.; Fitter, A. H. The Role of Root System Architecture and Root Hairs in Promoting Anchorage against Uprooting Forces in Allium Cepa and Root Mutants of Arabidopsis Thaliana. *J. Exp. Bot.* 2002, *53* (367), 333–340. https://doi.org/10.1093/jexbot/53.367.333.

(175) Weber, N. F.; Herrmann, I.; Hochholdinger, F.; Ludewig, U.; Neumann, G. PGPR-Induced Growth Stimulation and Nutrient Acquisition in Maize: Do Root Hairs Matter? *Sci. Agric. Bohem.* 2018, *49* (3), 164–172. https://doi.org/10.2478/sab-2018-0022.

(176) Jungk, A. Root Hairs and the Acquisition of Plant Nutrients from Soil. *J. Plant Nutr. Soil Sci.* 2001, *164* (2), 121–129. https://doi.org/10.1002/1522-2624(200104)164:2<121::AID-JPLN121>3.0.CO;2-6.

(177) Ågren, G. I.; Weih, M. Plant Stoichiometry at Different Scales: Element Concentration Patterns Reflect Environment More than Genotype. *New Phytol.* 2012, *194* (4), 944–952. https://doi.org/10.1111/j.1469-8137.2012.04114.x.

(178) Lynch, J. P. Root Phenes for Enhanced Soil Exploration and Phosphorus Acquisition: Tools for Future Crops. *Plant Physiol.* 2011, *156* (3), 1041–1049. https://doi.org/10.1104/pp.111.175414.

(179) Richardson, A. E.; Hocking, P. J.; Simpson, R. J.; George, T. S. Plant Mechanisms to Optimise Access to Soil Phosphorus. *Crop Pasture Sci.* 2009, *60* (2), 124–143. https://doi.org/10.1071/CP07125.

(180) Mollier, A.; Pellerin, S. Maize Root System Growth and Development as Influenced by Phosphorus Deficiency. *J. Exp. Bot.* 1999, *50* (333), 487–497. https://doi.org/10.1093/jxb/50.333.487.

(181) Clark, L. J.; Whalley, W. R.; Barraclough, P. B. How Do Roots Penetrate Strong Soil? *Plant Soil* 2003, *255* (1), 93–104. https://doi.org/10.1023/A:1026140122848.

(182) Colombi, T.; Walter, A. Root Responses of Triticale and Soybean to Soil Compaction in the Field Are Reproducible under Controlled Conditions. *Funct. Plant Biol.* 2016, *43* (2), 114–128. https://doi.org/10.1071/FP15194.

(183) Correa, J.; Postma, J. A.; Watt, M.; Wojciechowski, T. Soil Compaction

and the Architectural Plasticity of Root Systems. *J. Exp. Bot.* 2019, *70* (21), 6019–6034. https://doi.org/10.1093/jxb/erz383.

(184) Tracy, S. R.; Black, C. R.; Roberts, J. A.; McNeill, A.; Davidson, R.; Tester, M.; Samec, M.; Korošak, D.; Sturrock, C.; Mooney, S. J. Quantifying the Effect of Soil Compaction on Three Varieties of Wheat (Triticum Aestivum L.) Using X-Ray Micro Computed Tomography (CT). *Plant Soil* 2012, *353* (1–2), 195–208. https://doi.org/10.1007/s11104-011-1022-5.

(185) Kirby, J. M.; Bengough, A. G. Influence of Soil Strength on Root Growth: Experiments and Analysis Using a Critical-State Model. *Eur. J. Soil Sci.* 2002, *53* (1), 119–127. https://doi.org/10.1046/j.1365-2389.2002.00429.x.

(186) Baluška, F.; Brailsford, R. W.; Hauskrecht, M.; Jackson, M. B.; Barlow, P. W. Cellular Dimorphism in the Maize Root Cortex: Involvement of Microtubules, Ethylene and Gibberellin in the Differentiation of Cellular Behaviour in Postmitotic Growth Zones. *Bot. Acta* 1993, *106* (5), 394–403. https://doi.org/10.1111/j.1438-8677.1993.tb00766.x.

(187) Ma, B.; He, S. J.; Duan, K. X.; Yin, C. C.; Chen, H.; Yang, C.; Xiong, Q.; Song, Q. X.; Lu, X.; Chen, H. W.; Zhang, W. K.; Lu, T. G.; Chen, S. Y.; Zhang, J. S. Identification of Rice Ethylene-Response Mutants and Characterization of MHZ7/OsEIN2 in Distinct Ethylene Response and Yield Trait Regulation. *Mol. Plant* 2013, *6* (6), 1830–1848. https://doi.org/10.1093/mp/sst087.

(188) Zhang, Y.; Du, H.; Xu, F.; Ding, Y.; Gui, Y.; Zhang, J.; Xua, W. Root-Bacteria Associations Boost Rhizosheath Formation in Moderately Dry Soil through Ethylene Responses. *Plant Physiol.* 2020, *183* (2), 780–792. https://doi.org/10.1104/pp.19.01020.

(189) Hartman, S. Trapped in the Rhizosheath: Root-Bacterial Interactions Modulate Ethylene Signaling. *Plant Physiol.* 2020, *183* (2), 443–444. https://doi.org/10.1104/pp.20.00379.

(190) Soltaninejad, M.; Sturrock, C. J.; Griffiths, M.; Pridmore, T. P.; Pound, M. P. Three Dimensional Root CT Segmentation Using Multi-Resolution Encoder-Decoder Networks. *IEEE Trans. Image Process.* 2020, *29*, 6667–6679. https://doi.org/10.1109/TIP.2020.2992893.

(191) Stubbs, C. J.; Cook, D. D.; Niklas, K. J. A General Review of the Biomechanics of Root Anchorage. *J. Exp. Bot.* 2019, *70* (14), 3439–3451. https://doi.org/10.1093/jxb/ery451.

(192) Cai, G.; Ahmed, M. A.; Abdalla, M.; Carminati, A. Root Hydraulic Phenotypes Impacting Water Uptake in Drying Soils. *Plant Cell Environ.*

2022, *45* (3), 650–663. https://doi.org/10.1111/pce.14259.

(193) Hinsinger, P. How Do Plant Roots Acquire Mineral Nutrients? Chemical Processes Involved in the Rhizosphere. In *Advances in Agronomy*; Elsevier Masson SAS, 1998; Vol. 64, pp 225–265. https://doi.org/10.1016/S0065-2113(08)60506-4.

(194) Norvell, W. A.; Cary, E. E. Potential Errors Caused by Roots in Analyses of Rhizosphere Soil. *Plant Soil* 1992, *143* (2), 223–231. https://doi.org/10.1007/BF00007877.

(195) Pflugfelder, D.; Kochs, J.; Koller, R.; Jahnke, S.; Mohl, C.; Pariyar, S.; Fassbender, H.; Nagel, K. A.; Watt, M.; Van Dusschoten, D. The Root System Architecture of Wheat Establishing in Soil Is Associated with Varying Elongation Rates of Seminal Roots: Quantification Using 4D Magnetic Resonance Imaging. *J. Exp. Bot.* 2022, *73* (7), 2050–2060. https://doi.org/10.1093/jxb/erab551.

(196) Rodionov, A.; Lehndorff, E.; Stremtan, C. C.; Brand, W. A.; Königshoven, H.-P.; Amelung, W. Spatial Microanalysis of Natural 13 C/ 12 C Abundance in Environmental Samples Using Laser Ablation-Isotope Ratio Mass Spectrometry. *Anal. Chem.* 2019, *91* (9), 6225–6232. https://doi.org/10.1021/acs.analchem.9b00892.

(197) Zaeem, M.; Nadeem, M.; Huong Pham, T.; Ashiq, W.; Ali, W.; Shah Mohioudin Gillani, S.; Moise, E. R. D.; Leier, H.; Kavanagh, V.; Galagedara, L.; Cheema, M.; Thomas, R. Development of a Hyperspectral Imaging Technique Using LA-ICP-MS to Show the Spatial Distribution of Elements in Soil Cores. *Geoderma* 2021, *385* (November 2020), 114831. https://doi.org/10.1016/j.geoderma.2020.114831.

(198) Possinger, A. R.; Zachman, M. J.; Enders, A.; Levin, B. D. A.; Muller, D. A.; Kourkoutis, L. F.; Lehmann, J. Organo–Organic and Organo–Mineral Interfaces in Soil at the Nanometer Scale. *Nat. Commun.* 2020, *11* (1), 1–11. https://doi.org/10.1038/s41467-020-19792-9.

(199) Vidal, A.; Hirte, J.; Bender, S. F.; Mayer, J.; Gattinger, A.; Höschen, C.; Schädler, S.; Iqbal, T. M.; Mueller, C. W. Linking 3D Soil Structure and Plant-Microbe-Soil Carbon Transfer in the Rhizosphere. *Front. Environ. Sci.* 2018, *6* (February), 1–14. https://doi.org/10.3389/fenvs.2018.00009.

(200) Clode, P. L.; Kilburn, M. R.; Jones, D. L.; Stockdale, E. A.; Cliff, J. B.; Herrmann, A. M.; Murphy, D. V. In Situ Mapping of Nutrient Uptake in the Rhizosphere Using Nanoscale Secondary Ion Mass Spectrometry. *Plant Physiol.* 2009, *151* (4), 1751–1757. https://doi.org/10.1104/pp.109.141499.

(201) Rohde, F.; Braumann, U. D.; Schmidt, M. Correlia: An ImageJ Plug-in to

Co-Register and Visualise Multimodal Correlative Micrographs. *J. Microsc.* 2020, *280* (1), 3–11. https://doi.org/10.1111/jmi.12928.

(202) Védère, C.; Vieublé Gonod, L.; Nunan, N.; Chenu, C. Opportunities and Limits in Imaging Microorganisms and Their Activities in Soil Microhabitats. *Soil Biol. Biochem.* 2022, *174*, 108807. https://doi.org/10.1016/j.soilbio.2022.108807.

(203) Heinrich, S.; Dippold, M. A.; Werner, C.; Wiesenberg, G. L. B.; Kuzyakov, Y.; Glaser, B. Allocation of Freshly Assimilated Carbon into Primary and Secondary Metabolites after in Situ 13C Pulse Labelling of Norway Spruce (Picea Abies). *Tree Physiol.* 2015, *35* (11), 1176–1191. https://doi.org/10.1093/treephys/tpv083.

(204) Karnovsky, M. A Formaldehyde-Glutaraldehyde Fixative of High Osmolality for Use in Electron Microscopy. *J. Cell Biol.* 1965, *27*, 137-138A.

(205) Mueller, C. W.; Kölbl, A.; Hoeschen, C.; Hillion, F.; Heister, K.; Herrmann, A. M.; Kögel-Knabner, I. Submicron Scale Imaging of Soil Organic Matter Dynamics Using NanoSIMS – From Single Particles to Intact Aggregates. *Org. Geochem.* 2012, *42* (12), 1476–1488. https://doi.org/10.1016/j.orggeochem.2011.06.003.

(206) Herrmann, A. M.; Clode, P. L.; Fletcher, I. R.; Nunan, N.; Stockdale, E. A.; O'Donnell, A. G.; Murphy, D. V. A Novel Method for the Study of the Biophysical Interface in Soils Using Nano-scale Secondary Ion Mass Spectrometry. *Rapid Commun. Mass Spectrom.* 2007, *21* (1), 29–34. https://doi.org/10.1002/rcm.2811.

(207) Bandara, C. D.; Schmidt, M.; Davoudpour, Y.; Stryhanyuk, H.; Richnow, H. H.; Musat, N. Microbial Identification, High-Resolution Microscopy and Spectrometry of the Rhizosphere in Its Native Spatial Context. *Front. Plant Sci.* 2021, *12* (July), 1–18. https://doi.org/10.3389/fpls.2021.668929.

(208) Holz, M.; Leue, M.; Ahmed, M. A.; Benard, P.; Gerke, H. H.; Carminati, A. Spatial Distribution of Mucilage in the Rhizosphere Measured with Infrared Spectroscopy. *Front. Environ. Sci.* 2018, *6* (AUG), 1–7. https://doi.org/10.3389/fenvs.2018.00087.

(209) Poczatek, C.; Kaufman, Z.; Lechene, C. *OpenMIMS ImageJ Plugin Guide.* http://nrims.harvard.edu/files/nrims/files/openmims-manual.pdf.

(210) Klein, S.; Staring, M.; Murphy, K.; Viergever, M. A.; Pluim, J. P. W. Elastix: A Toolbox for Intensity-Based Medical Image Registration. *IEEE Trans. Med. Imaging* 2010, *29* (1), 196–205. https://doi.org/10.1109/TMI.2009.2035616.

(211) Oliveira, E. M. M.; Ruiz, H. A.; Alvarez V, V. H.; Ferreira, P. A.; Costa, F. O.; Almeida, I. C. C. Nutrient Supply by Mass Flow and Diffusion to Maize Plants in Response to Soil Aggregate Size and Water Potential. *Rev. Bras. Ciência do Solo* 2010, *34* (2), 317–328. https://doi.org/10.1590/S0100-06832010000200005.

(212) Ahmed, M. A.; Zarebanadkouki, M.; Meunier, F.; Javaux, M.; Kaestner, A.; Carminati, A. Root Type Matters: Measurement of Water Uptake by Seminal, Crown, and Lateral Roots in Maize. *J. Exp. Bot.* 2018, *69* (5), 1199–1206. https://doi.org/10.1093/jxb/erx439.

(213) Veelen, A. Van; Koebernick, N.; Scotson, C. S.; Mckay-fletcher, D.; Huthwelker, T.; Borca, C. N.; Mosselmans, J. F. W.; Roose, T. Root-Induced Soil Deformation Influences Fe , S and P : Rhizosphere Chemistry Investigated Using Synchrotron XRF and XANES. 2019, No. 2010. https://doi.org/10.1111/nph.16242.

(214) Mukhtar, S.; Haswell, S. J.; Ellis, A. T.; Hawke, D. T. Application of Total-Reflection X-Ray Fluorescence Spectrometry to Elemental Determinations in Water, Soil and Sewage Sludge Samples. *Analyst* 1991, *116* (4), 333. https://doi.org/10.1039/an9911600333.

(215) Witzgall, K.; Vidal, A.; Schubert, D. I.; Höschen, C.; Schweizer, S. A.; Buegger, F.; Pouteau, V.; Chenu, C.; Mueller, C. W. Particulate Organic Matter as a Functional Soil Component for Persistent Soil Organic Carbon. *Nat. Commun.* 2021, *12* (1), 1–10. https://doi.org/10.1038/s41467-021-24192-8.

(216) Landl, M.; Haupenthal, A.; Leitner, D.; Kroener, E.; Vetterlein, D.; Bol, R.; Vereecken, H.; Vanderborght, J.; Schnepf, A. Simulating Rhizodeposition Patterns around Growing and Exuding Root Systems. *In Silico Plants* 2021, *3* (2), 1–14. https://doi.org/10.1093/insilicoplants/diab028.

(217) Kruse, J.; Abraham, M.; Amelung, W.; Baum, C.; Bol, R.; Kühn, O.; Lewandowski, H.; Niederberger, J.; Oelmann, Y.; Rüger, C.; Santner, J.; Siebers, M.; Siebers, N.; Spohn, M.; Vestergren, J.; Vogts, A.; Leinweber, P. Innovative Methods in Soil Phosphorus Research: A Review. *J. Plant Nutr. Soil Sci.* 2015, *178* (1), 43–88. https://doi.org/10.1002/jpln.201400327.

(218) Lohse, M.; Haag, R.; Lippold, E.; Vetterlein, D.; Reemtsma, T.; Lechtenfeld, O. J. Direct Imaging of Plant Metabolites in the Rhizosphere Using Laser Desorption Ionization Ultra-High Resolution Mass Spectrometry. *Front. Plant Sci.* 2021, *12* (December), 1–13. https://doi.org/10.3389/fpls.2021.753812.

(219) Vetterlein, D.; Phalempin, M.; Lippold, E.; Schlüter, S.; Schreiter, S.; Ahmed, M. A.; Carminati, A.; Duddek, P.; Jorda, H.; Bienert, G. P.;

Bienert, M. D.; Tarkka, M.; Ganther, M.; Oburger, E.; Santangeli, M.; Javaux, M.; Vanderborght, J. Root Hairs Matter at Field Scale for Maize Shoot Growth and Nutrient Uptake, but Root Trait Plasticity Is Primarily Triggered by Texture and Drought. *Plant Soil* 2022, *478* (1–2), 119–141. https://doi.org/10.1007/s11104-022-05434-0.

(220) Lohse, M.; Santangeli, M.; Steininger-Mairinger, T.; Oburger, E.; Reemtsma, T.; Lechtenfeld, O. J.; Hann, S. The Effect of Root Hairs on Exudate Composition: A Comparative Non-Targeted Metabolomics Approach. *Anal. Bioanal. Chem.* 2023, *415* (5), 823–840. https://doi.org/10.1007/s00216-022-04475-9.

(221) Baveye, P. C. Ecosystem-Scale Modelling of Soil Carbon Dynamics: Time for a Radical Shift of Perspective? *Soil Biol. Biochem.* 2023, *184* (June), 109112. https://doi.org/10.1016/j.soilbio.2023.109112.

(222) Kuppardt, A.; Vetterlein, D.; Harms, H.; Chatzinotas, A. Visualisation of Gradients in Arsenic Concentrations around Individual Roots of Zea Mays L. Using Agar-Immobilized Bioreporter Bacteria. *Plant Soil* 2010, *329* (1), 295–306. https://doi.org/10.1007/s11104-009-0154-3.

(223) ICRP. Relative Biological Effectiveness (RBE), Quality Factor (Q), and Radiation Weighting Factor (WR). *Ann. ICRP* 2003, *92* (1), 1. https://doi.org/10.1016/0146-6453(81)90127-5.

(224) Stupian, G. W. *X-Ray Dose in Microfocus Radiographic Inspections*; El Segundo, California, 2007; Vol. 2007.

List of publications

2023

Lippold, E., Schlüter, S., Mueller, C.W., Höschen, C., Harrington, G., Kilian, R., Gocke, M.i., Lehndorff, E., Mikutta, R., Vetterlein, D. (2023):
Correlative imaging of the rhizosphere ─ A multimethod workflow for targeted mapping of chemical gradients
Environ. Sci. Technol. 57 (3), 1538 – 1549, DOI: 10.1021/acs.est.2c07340

2022

Schnepf, A., Carminati, A., Ahmed, M.A., Ani, M., Benard, P., Bentz, J., Bonkowski, M., Knott, M., Diehl, D., Duddek, P., Kröner, E., Javaux, M., Landl, M., Lehndorff, E., Lippold, E., Lieu, A., Mueller, C.W., Oburger, E., Otten, W., Portell, X., Phalempin, M., Prechtel, A., Schulz, R., Vanderborght, J., Vetterlein, D. (2022):
Linking rhizosphere processes across scales: Opinion
Plant Soil 478 (1-2), 5 – 42, DOI: 10.1007/s11104-022-05306-7

Vetterlein, D., Phalempin, M., Lippold, E., Schlüter, S., Schreiter, S., Ahmed, M.A., Carminati, A., Duddek, P., Jorda, H., Bienert, G.P., Bienert, M.D., Tarkka, M., Ganther, M., Oburger, E., Santangeli, M., Javaux, M., Vanderborght, J. (2022):
Root hairs matter at field scale for maize shoot growth and nutrient uptake, but root trait plasticity is primarily triggered by texture and drought
Plant Soil 478 (1-2), 119 – 141, DOI: 10.1007/s11104-022-05434-0

Ganther, M., Lippold, E., Bienert, M.D., Bouffaud, M.-L., Bauer, M., Baumann, L., Bienert, G.P., Vetterlein, D., Heintz-Buschart, A., Tarkka, M.T. (2022):
Plant age and soil texture rather than the presence of root hairs cause differences in maize resource allocation and root gene expression in the field
Plants 11 (21), art. 2883, DOI: 10.3390/plants11212883

Lippold, E., Lucas, M., Fahrenkampf, T., Schlüter, S., Vetterlein, D. (2022):
Macroaggregates of loam in sandy soil show little influence on maize growth, due to local adaptations of root architecture to soil heterogeneity
Plant Soil 478 (1-2), 163 – 175, DOI: 10.1007/s11104-022-05413-5

Bilyera, N., Hummel, C., Daudin, G., Santangeli, M., Zhang, X., Santner, J., Lippold, E., Schlüter, S., Bertrand, I., Wenzel, W., Spielvogel, S., Vetterlein, D., Razavi, B.S., Oburger, E. (2022):
Co-localised phosphorus mobilization processes in the rhizosphere of field-grown

maize jointly contribute to plant nutrition
Soil Biol. Biochem. 165, art. 108497, DOI: 10.1016/j.soilbio.2021.108497

2021

Phalempin, M., Lippold, E., Vetterlein, D., Schlüter, S. (2021):
An improved method for the segmentation of roots from X-ray computed tomography 3D images: Rootine v.2
Plant Methods 17 , art. 39, DOI: 10.1186/s13007-021-00735-4

Lippold, E., Kleinau, P., Blaser, S.R.G.A., Schlüter, S., Phalempin, M., Vetterlein, D. (2021):
In soil measurement of radiation dose caused by X-ray computed tomography
J. Plant Nutr. Soil Sci. 184 (3), 343 – 345, DOI: 10.1002/jpln.202000276

Phalempin, M., Lippold, E., Vetterlein, D., Schlüter, S. (2021):Soil texture and structure heterogeneity predominantly governs bulk density gradients around roots
Vadose Zone J. 20 (5), e20147, DOI: 10.1002/vzj2.20147

Vetterlein, D., Lippold, E., Schreiter, S., Phalempin, M., Fahrenkampf, T., Hochholdinger, F., Marcon, C., Tarkka, M.T., Oburger, E., Ahmed, M., Javaux, M., Schlüter, S. (2021):
Experimental platforms for the investigation of spatiotemporal patterns in the rhizosphere—laboratory and field scale
J. Plant Nutr. Soil Sci. 184 (1), 35 – 50, DOI: 10.1002/jpln.202000079

Lohse, M., Haag, R., Lippold, E., Vetterlein, D., Reemtsma, T., Lechtenfeld, O.J. (2021):
Direct imaging of plant metabolites in the rhizosphere using laser desorption ionization ultra-high resolution mass spectrometry
Front. Plant Sci. 12, art. 753812, DOI: 10.3389/fpls.2021.753812

Lippold, E., Phalempin, M., Schlüter, S., Vetterlein, D. (2021):
Does the lack of root hairs alter root system architecture of *Zea mays*?
Plant Soil 467 (1-2), 267 – 286, DOI: 10.1007/s11104-021-05084-8

2020

Ganther, M., Yim, B., Ibrahim, Z., Bienert, M.D., Lippold, E., Maccario, L., Sørensen, S.J., Bienert, G.P., Vetterlein, D., Heintz-Buschart, A., Blagodatskaya, E., Smalla, K., Tarkka, M.T. (2020):
Compatibility of X-ray computed tomography with plant gene expression profiling, rhizosphere bacterial community composition and enzyme activity

analyses
J. Exp. Bot. 71 (18), 5603 – 5614, DOI: 10.1093/jxb/eraa262

Curriculum vitae

Eva Lippold

Beruflicher Werdegang

Derzeit OKTOBER 2018	Doktorandin und wissenschaftliche Mitarbeiterin am *Helmholtz Zentrum für Umweltforschung – UFZ* Arbeitsgruppe Boden-Pflanze-Interaktion des Departments Bodensystemforschung DFG Projekt: SPP 2089 “Rhizosphere spatiotemporal organization – a key to rhizosphere functions”

Ausbildung

Juni 2018	Master of science, Martin Luther Universiät Halle-Wittenberg Studiengang-Management natürlicher Ressourcen
Oktober 2015	Bachelor of science, Martin Luther Universiät Halle-Wittenberg Studiengang-Management natürlicher Ressourcen

Datum/Date Unterschrift/Signature

Eidesstattliche Erklärung / Declaration under oath

Ich erkläre an Eides statt, dass ich die Arbeit selbstständig und ohne fremde Hilfe verfasst, keine anderen als die von mir angegebenen Quellen und Hilfsmittel benutzt und die den benutzten Werken wörtlich oder inhaltlich entnommenen Stellen als solche kenntlich gemacht habe.

I declare under penalty of perjury that this thesis is myown work entirely and has been written without any help from other people. I used only the sources mentioned and included all the citations correctly both in word or content.

Datum/Date Unterschrift/Signature

Danksagung/Acknowledgement

Aus Datenschutzgründen entfernt